

Synaptic integration strategies for sound source  
localization within an excitation-inhibition circuit:  
dynamic-clamp analysis of mouse lateral superior  
olive neurons.

vom Fachbereich Biologie der Rheinland-Pfälzischen Technischen Universität  
Kaiserslautern-Landau zur Verleihung des akademischen Grades Dr. rer. nat.

genehmigte Dissertation von

**Jonas Fisch, M.Sc.**

Mündliche Prüfung: 22.08.2025

Dekan:

Promotionskommissionsvorsitzender:

Berichterstattende:

Prof. Dr. Stefan Kins

Prof. Dr. Stefan Kins

Prof. Dr. Eckhard Friauf

Prof. Dr. Felix Felmy

## Darlegung aller benutzten Hilfsmittel und Hilfestellungen

Ich erkläre hiermit, die vorliegende Dissertation selbstständig verfasst zu haben. Die verwendeten Quellen und Hilfsmittel (auch generative KI-Systeme) sind kenntlich gemacht und vollständig (d.h. mit Angabe von Version und Nutzungszweck) aufgeführt. Sofern der Einsatz von KI-Systemen über eine reine Grammatikprüfung und Stilverbesserung hinausgeht, ist der Einsatz nachvollziehbar kenntlich gemacht. Für Fehler, auch bei Übernahme aus generativen KI-Systemen, bin ich verantwortlich.

---

Kaiserslautern, 12/06/2025, Jonas Fisch

## Darlegung des Eigenanteils

Die Abbildungen 3.1 A-K zeigen Daten, welche während meiner Masterarbeit erhoben wurden und in ähnlicher Form dort präsentiert wurden (Jonas Fisch, RPTU Kaiserslautern-Landau). Die Abbildungen 3.24 bis 3.27 zeigen Daten, welche im Labor von Dr. Conny Kopp-Scheinflug durch Luna Studer erhoben wurden (Ludwig-Maximilians-Universität München). Die Daten in Abbildung 3.24 B wurden von Luna Studer analysiert und die restlichen Daten dieser Abbildungen wurden eigenständig von mir analysiert.

Die vorliegende Einschätzung über die erbrachte Leistung von Dritten wurde mit den genannten Personen einvernehmlich abgestimmt.

---

Kaiserslautern, 12/06/2025, Jonas Fisch

---

Kaiserslautern, 12/06/2025, Eckhard Friauf

“Life is like riding a bicycle.  
To keep your balance, you must keep moving.”

-Albert Einstein

## I. Summary

Excitatory and inhibitory synapses are major components of interneuronal information processing. A robust interplay between these two types is crucial in the lateral superior olive (LSO). LSO neurons integrate excitatory and inhibitory inputs from the ipsilateral and contralateral ear, respectively. They are remarkably sensitive to interaural level differences (ILDs) and interaural time differences (ITDs), making them well-suited for azimuthal sound source localization. Together with their input neurons from the cochlear nucleus and the medial nucleus of the trapezoid body, LSO neurons form an optimal circuit to investigate the mechanisms underlying behaviorally relevant synaptic integration of excitation and inhibition. The mechanisms by which the relative strength and timing of excitatory and inhibitory inputs are integrated in the LSO are not yet fully understood.

In this study, I examined synaptic integration in LSO neurons in four steps. First, I evaluated excitatory transmission by combining whole-cell voltage-clamp recordings with electrical fiber stimulations in young adult mice. LSO neurons receive up to 40 excitatory inputs, with each input contributing a synaptic weight ( $SW_{exc}$ ) of 1 nS/input. I used these values, along with four inhibitory inputs of  $SW_{inh}$  of 8 nS/input, as canonical synaptic inputs in the LSO circuit. Second, I analyzed the biophysical membrane properties of LSO neurons that underlie synaptic integration. Fast signal integration is enabled by a short membrane time constant and low input resistance along the putative tonotopic axis. Voltage sag behavior and membrane resonances indicate an extension of passive features by active conductances. Suprathreshold responses were observed as biphasic action potentials (APs), likely reflecting compartment-specific activation of voltage-gated sodium channels. Moreover, the AP threshold varied with the slope of stimulation. Third, I employed the dynamic-clamp in conjunction with an input pathway model to study synaptic integration. Upon sinusoidal stimulation, the neurons behaved as coincidence detectors. They transformed a primary-like input pattern with physiological  $SW_{exc}$  into onset responses. The onset can be employed for rate-level coding in combination with inhibition. Conversely, the sustained phase does not support rate-based level difference coding, regardless of  $SW_{exc}$  and  $SW_{inh}$  configurations. The coincidence mechanism creates band-pass filtering during sinusoidal stimulation and sets the highest sensitivity to transient activations. These activations enable robust rate-difference coding and coding of temporal disparities between excitation and inhibition. Fourth, *in vivo* data from anaesthetized mice showed that LSO neurons are highly sensitive to variations in stimulus transience and can encode these up to high modulation rates. Moreover, integration of ILDs is not impeded by such high modulation rates.

Together, my results provide a mechanistic rationale for the synaptic integration underlying the high perceptual acuity of sound source localization with transient sound signals.

## II. Zusammenfassung

Erregende und hemmende Synapsen sind zentrale Bestandteile der Informationsverarbeitung zwischen Neuronen. Ein robustes Zusammenspiel dieser beiden Typen ist von entscheidender Bedeutung in der lateralen superioren Olive (LSO). LSO Neurone integrieren erregende und hemmende Eingänge, die von dem ipsilateralen beziehungsweise kontralateralen Ohr kommen. Sie sind bemerkenswert empfindlich gegenüber interauralen Pegeldifferenzen (ILDs) und interauralen Zeitdifferenzen (ITDs), was sie besonders für die Lokalisation von Schallquellen eignet. Gemeinsam mit ihren Eingängen aus dem Nucleus cochlearis und dem medialen Trapezoidkörper bilden LSO Neurone einen optimalen Schaltkreis, um die Mechanismen von verhaltensrelevanter synaptischer Integration von Erregung und Hemmung zu untersuchen. Die Mechanismen, durch welche die relative Stärke und das zeitliche Auftreten von Erregung und Hemmung in der LSO integriert werden, sind bislang nicht vollständig verstanden.

In dieser Thesis habe ich die synaptische Integration in LSO Neuronen in vier Stufen untersucht. Erstens habe ich die erregende synaptische Transmission neu bewertet, indem ich Ganzzell-Spannungsklemmableitungen mit elektrischen Faserstimulationen bei jungen adulten Mäusen kombiniert habe. LSO Neurone erhalten etwa 40 erregende Eingänge, wobei jeder Eingang ein synaptisches Gewicht ( $SW_{exc}$ ) von 1 nS/Eingang hat. Diese Werte, zusammen mit vier hemmenden Einfängen mit einem  $SW_{inh}$  von 8 nS/Eingang, habe ich als kanonische synaptische Eingänge im LSO Schaltkreis verwendet. Zweitens habe ich die biophysikalischen Membraneigenschaften untersucht, die der synaptischen Integration in LSO Neuronen zugrunde liegen. Eine schnelle Signalverarbeitung wird durch eine kurze Membranzeitkonstante und einen niedrigen Eingangswiderstand entlang der tonotopen Achse ermöglicht. ‚Voltage Sag‘ Verhalten und Membranresonanzen weisen auf eine Erweiterung passiver Eigenschaften durch aktive Leitfähigkeiten hin. Überschwellige Antworten traten als biphasische Aktionspotentiale (APs) auf, was auf eine Kompartiment spezifische Aktivierung spannungsabhängiger Natriumkanäle hinweist. Darüber hinaus variierten die AP-Schwelle mit der Steigung des Stimulus. Drittens habe ich Dynamic-Clamp-Experimente in Kombination mit einem Model zur Simulation von Eingangsaktivität eingesetzt, um die synaptische Integration zu untersuchen. Bei sinusförmiger Stimulation verhielten sich die Neurone wie Koinzidenzdetektoren. Sie transformierten primär-ähnliche Eingangsmuster mit physiologischen  $SW_{exc}$  in Antworten im Reizbeginn. Diese Onset-Antworten können in Kombination mit Hemmung zur Kodierung von Levelunterschieden über die AP Raten verwendet werden. Die andauernde Phase hingegen unterstützt keine ratenbasierte Levelunterschiedskodierung, unabhängig von der Konfiguration von  $SW_{exc}$  und  $SW_{inh}$ . Der Koinzidenzmechanismus erzeugt eine Bandpassfilterung während sinusförmiger Stimulation

und führt zu einer höchsten Empfindlichkeit bei transienten Aktivierungen. Diese Aktivierungen ermöglichen eine robuste ratenbasierte Levelunterschiedskodierung, sowie eine Kodierung von zeitlichen Differenzen zwischen Erregung und Hemmung. Viertens zeigten *in vivo* Versuche von narkotisierten Mäusen, dass LSO Neurone sensitiv auf Veränderung der Transienz von Reizen reagieren und diese bis zu hohen Modulationsraten kodieren können. Zudem wird die Integration von ILDs durch solche die Reiztransienz nicht beeinträchtigt.

Zusammenfassend liefern meine Ergebnisse eine mechanistische Begründung für die synaptische Integration, die einer hohen Präzision in der Schallquellenlokalisierung mit transienten Schallsignalen zugrunde liegt.

### III. Index of contents

<b>I. Summary</b> .....	<b>IV</b>
<b>II. Zusammenfassung</b> .....	<b>V</b>
<b>III. Index of contents</b> .....	<b>VII</b>
<b>IV. Index of figures &amp; tables</b> .....	<b>X</b>
Figures .....	X
Tables .....	XII
<b>1. Introduction</b> .....	<b>1</b>
1.1 Sound source localization .....	1
1.2 Azimuthal sound source localization – level versus temporal coding .....	2
1.3 Neuronal representation of ILDs and ITDs in the auditory brainstem .....	4
1.4 Neuronal representation of sound in the afferent auditory pathway.....	6
1.5 Ticket to the olive: the neural pathway to lateral superior olive neurons.....	8
1.6 Activity patterns of neurons innervating the LSO .....	10
1.7 Synaptic transmission in the LSO and the effects of synaptic noise.....	11
1.8 Functional adaptations for ultra-fast information processing .....	14
1.9 Afferent and efferent projection of LSO neurons .....	16
1.10 Studying synaptic integration using virtual synapses: the dynamic-clamp method ...	16
1.11 Aims of the study .....	18
<b>2 Methods</b> .....	<b>20</b>
2.1 Animals.....	20
2.2 Brainstem slice preparation .....	20
2.3 Whole-cell patch-clamp recordings & electrical synaptic stimulation .....	20
2.3.1 Passive and active membrane properties .....	21
2.3.1.1 Recording and analysis of $V_{rest}$ , $R_{in}$ , $\tau_{mem}$ , and $C_{mem}$ .....	21
2.3.1.2 Recording and analysis of sag amplitude, rheobase, and firing pattern...	22
2.3.1.3 Recording and analysis of membrane resonance properties.....	22
2.3.1.4 Correlation analysis .....	22
2.3.1.5 Recording and analysis of slope-dependent AP initiation.....	23
2.3.1.6 Analysis of AP characteristics .....	23
2.3.2 Synaptic stimulations and recordings of excitatory postsynaptic currents.....	24
2.4 Dynamic-clamp stimulations .....	25
2.5 Modelling synaptic conductances of mimicked auditory activity. ....	27
2.5.1 Refractory function.....	28
2.5.2 Stimulus functions.....	29
2.5.3 Convolution into time-varying synaptic conductances .....	30
2.6 Analysis of DC data .....	30
2.6.1 AP occurrence and AP rates.....	30
2.6.2 Temporal analysis of AP occurrence.....	31
2.6.3 Stimulus separability .....	32

2.7	Analysis of <i>in vivo</i> data .....	32
2.8	Statistics .....	33
2.9	Data visualization .....	34
2.10	Writing .....	34
<b>3</b>	<b>Results.....</b>	<b>35</b>
3.1	Synaptic characteristics of excitatory and inhibitory synaptic inputs to LSO neurons	35
3.2	Intrinsic electrophysiological properties shape stimulus response dynamics of LSO neurons .....	39
3.2.1	Resting membrane properties of LSO neurons .....	39
3.2.2	Active membrane properties shape subthreshold integration .....	42
3.2.3	LSO neurons exhibit robust onset burst firing behavior .....	44
3.2.4	Slope-dependent modulation of AP threshold .....	46
3.2.5	Mimicked synaptic noise does not increase the frequency tuning of LSO neurons .....	50
3.3	Synaptic integration in LSO neurons stimulated with <i>in vivo</i> -like activation pattern ..	54
3.3.1	Distributing $SW_{exc}$ across multiple inputs promotes onset coding and suppresses sustained firing in response to a primary-like stimulation pattern.....	54
3.3.2	Temporal precise onset coding is enhanced by distributing $SW_{exc}$ across multiple inputs .....	59
3.3.3	Increased $V_{thr}$ constrains the ability to initiate APs in the sustained phase .....	61
3.3.4	Inhibition blocks onset APs and modulates the sustained AP rate bidirectionally .....	64
3.3.5	Sinusoidal stimulations reveal band-pass filtering of LSO neurons .....	70
3.3.6	Stimulus transients are encoded by LSO neurons at $F_{mod}$ s lower than 1000 Hz .....	74
3.3.7	Transient stimuli enable ILD computation .....	77
3.3.8	Level differences can be extracted across a wide range of time differences between excitation and inhibition. ....	81
3.3.9	Time difference coding is enabled by stimulus transience of the envelope.....	85
3.4	<i>In vivo</i> characterization reveals adaptive temporal and spatial coding strategies in LSO neurons.....	90
3.4.1	<i>In vivo</i> recordings reveal onset-dominated firing behavior of LSO neurons to pure tone acoustic stimulations .....	90
3.4.2	Enhanced ILD coding precision in stimulus onset .....	92
3.4.3	LSO neurons encode the increase of stimulus transience with increased temporal precision.....	93
3.4.4	ILD coding is maintained with increasing stimulus transience .....	96
<b>4</b>	<b>Discussion.....</b>	<b>99</b>
4.1	Excitatory synaptic convergence in the LSO: integration of many weak inputs .....	100
4.2	Passive and active membrane conductances tune LSO neurons for fast signal integration.....	101
4.3	Regulation of excitability of LSO neurons .....	103

4.3.1	Extrinsic and intrinsic regulation of excitability in LSO neuron .....	103
4.3.2	Rate-dependent AP threshold and spike initiation site in LSO neurons .....	104
4.3.3	Molecular determinants of the AP waveform .....	105
4.3.4	Excitability of LSO neurons <i>in vitro</i> and <i>in vivo</i> .....	105
4.3.5	Concluding remarks on LSO neuron excitability .....	106
4.4	Excitatory synaptic integration in LSO neurons .....	106
4.4.1	Temporal differentiation by LSO neurons via excitatory coincidence detection .....	106
4.4.2	Onset response patterns are support by physiological $SW_{exc}$ , which prevents temporally random APs in the sustained part .....	108
4.4.2.1	$SW_{exc}$ shape AP firing patterns of LSO neurons .....	108
4.4.2.2	Pre- and postsynaptic gain modulation as mechanisms to regulate excitability .....	109
4.4.2.3	Temporal correlation of onset APs but random AP firing in the sustained part .....	111
4.4.2.4	Functional classification of primary-like DC experiments based on comparison with <i>in vivo</i> findings .....	111
4.4.3	Rate-modulation coding and band-pass filtering in LSO neurons in response to sinusoidal input activity and transients .....	111
4.4.4	Temporally precise coding of the frequency modulation and the phase-locking limit of LSO neurons .....	113
4.4.5	Concluding remarks on excitatory synaptic integration .....	115
4.5	Excitation-inhibition integration in LSO neurons .....	116
4.5.1	Precise ILD coding of transients <i>in vitro</i> and <i>in vivo</i> but contrasting results in the sustained part of integration .....	116
4.5.2	Level-difference coding by transient stimulation .....	118
4.5.3	Stimulus structure defines the temporal window of effective inhibition .....	120
4.5.3.1	Limitations of the dynamic-clamp method in analyzing temporal coding of LSO neurons .....	122
4.5.3.2	Functional implications of transient ITD coding by LSO neurons .....	122
4.5.4	Concluding remarks on excitation-inhibition integration in LSO neurons .....	122
4.6	Implications for binaural coding with cochlear implants .....	123
4.7	Outlook .....	124
4.8	Conclusion .....	126
<b>5</b>	<b>Index of Abbreviations .....</b>	<b>127</b>
<b>6</b>	<b>References .....</b>	<b>129</b>
<b>7</b>	<b>Supplementary Information .....</b>	<b>149</b>
<b>8</b>	<b>Curriculum vitae .....</b>	<b>169</b>
<b>9</b>	<b>Acknowledgements .....</b>	<b>172</b>

## IV. Index of figures & tables

### Figures

Figure 1.1 Spatial information is not represented on the basilar membrane - the auditory sensory epithelium. ....	2
Figure 1.2 Azimuthal sound source localization depends on binaural auditory cues: interaural level differences and interaural time differences. ....	4
Figure 1.3 Schematic of peripheral neural representation of different sound signals. ....	7
Figure 1.4 Overview of the LSO input and output pathways and synaptic organization on LSO neurons. ....	9
Figure 1.5 Schematic of synaptic transmission and experimental setup to stimulate with simulated synaptic inputs. ....	13
Figure 1.6 Dynamic-clamp setup to study synaptic integration using virtual synapses. ....	17
Figure 2.1 Analysis of the frequency-dependent $I_{thr}$ . ....	23
Figure 2.2 Analysis of AP characteristics. ....	24
Figure 2.3 Update rate of the $I_{DC}$ . ....	26
Figure 2.4 Model procedure to generate synaptic conductances. ....	28
Figure 3.1 Unitary excitatory inputs to LSO neurons have weak synaptic weights and fast kinetics. ....	37
Figure 3.2 Estimated synaptic innervation onto LSO neurons. ....	38
Figure 3.3 Passive membrane properties are optimized for fast synaptic integration. ....	41
Figure 3.4 Active membrane properties generate resonances and shape subthreshold integration. ....	43
Figure 3.5 LSO neurons exhibit robust onset burst firing behavior. ....	45
Figure 3.6 LSO neurons exhibit a slope-dependent modulation of AP threshold. ....	47
Figure 3.7 AP initiation is determined by the current slope. ....	49
Figure 3.8 Frequency dependent modulation of AP probability is not increased by physiological synaptic noise. ....	52
Figure 3.9 Distributing $SW_{exc}$ across multiple inputs promotes onset coding and suppresses sustained firing in response to a primary-like stimulation pattern. ....	56
Figure 3.10 $SW_{exc}$ jitter increases the sustained AP rate. ....	58
Figure 3.11 Distributing $SW_{exc}$ across multiple inputs enhances temporally precise onset coding and omits randomly occurring APs in the sustained part. ....	60
Figure 3.12 $V_{thr}$ increases during the sustained part. ....	63

Figure 3.13 Inhibition effectively blocks the onset AP evoked by excitation and bidirectionally modulates the sustained AP rate.....	66
Figure 3.14 Onset reliability is minimally influenced by $SW_{inh}$ , whereas sustained rate facilitation is enhanced by large $SW_{inh}$ and suppression by small $SW_{inh}$ .....	68
Figure 3.15 Stimulus separability is reliably reached at stimulus onset, but not in the sustained part. ....	69
Figure 3.16 LSO neurons exhibit band-pass filtering in rate modulation transfer functions and low-pass filtering in temporal modulation transfer functions.....	72
Figure 3.17 Transient stimuli are reliably encoded up to $F_{mod}$ of 500 Hz. ....	77
Figure 3.18 Level difference coding is enabled by transient stimuli with highest sensitivity at $F_{mod}$ of 200 Hz. ....	78
Figure 3.19 Stimulus separability is envelope dependent and showed lowest values for high $f_{exc}$ . ....	81
Figure 3.20 Level-difference coding is maintained across a wide range of time differences.	83
Figure 3.21 Reliable time difference coding by transient stimulations.....	86
Figure 3.22 Increasing stimulus transience leads to shorter half-width and shifts the trough center.....	88
Figure 3.23 Stimulus transience increases temporal separability and limits the temporal coding range. ....	89
Figure 3.24 LSO neurons display onset-dominated firing behaviors <i>in vivo</i> .....	91
Figure 3.25 Increased ILD coding precision in onset compared to total stimulation time. ....	92
Figure 3.26 Stimulus transience increases temporal precision but decreases firing of LSO neurons <i>in vivo</i> .....	94
Figure 3.27 ILD coding is maintained with increasing stimulus transience.....	97
Figure 5.1 Firing behavior of a single neuron at different $SW_{exc}$ .....	160
Figure 5.2 Integration of excitation and inhibition during primary-like activation with $SW_{inh}$ of 4 nS/input.....	161
Figure 5.3 Integration of excitation and inhibition during primary-like activation with $SW_{inh}$ of 4 nS/input.....	162
Figure 5.4 Spike triggered averages of primary-like excitation and inhibition.....	163
Figure 5.5 Synaptic integration of sinusoidal activation patterns with four $SW_{exc}$ . ....	165
Figure 5.6 Rate modulation transfer functions at four $SW_{exc}$ . ....	166
Figure 5.7 Rate modulation transfer functions at four $SW_{exc}$ of multi firing neurons. ....	167
Figure 5.8 PSTHs of onset firing neurons and sustained firing neurons. ....	168

## Tables

Table S.1 Stimulus parameters used for primary-like-like activation shown in Fig.3.9. ....	149
Table S.2 Stimulus parameters used for primary-like activation shown in Fig.3.13.....	149
Table S.3 Stimulus parameters used for sinusoidal activation shown in Fig.3.16. ....	150
Table S.4 Stimulus parameters used for sinusoidal activation shown in Fig.3.17. ....	150
Table S.5 Stimulus parameters used for sinusoidal activation shown in Fig.3.18. ....	151
Table S.6 Statistical summary tables of Fig.3.8 (E) .....	152
Table S.7 Statistical summary tables of Fig.3.8 (F) .....	152
Table S.8 Statistical summary table of Fig.3.10 (D).....	153
Table S.9 Statistical summary table of Fig.3.12 (E).....	154
Table S.10 Statistical summary table of Fig.3.14 (C <sup>1</sup> ) .....	155
Table S.11 Statistical summary table of Fig.3.14 (C <sup>2</sup> ) .....	156
Table S.12 Statistical summary table of Fig.3.14 (C <sup>3</sup> ) .....	157
Table S.13 Statistical summary table of Fig.3.18 (F&H) .....	157
Table S.14 Statistical summary table of Fig.3.26 (F <sup>2</sup> ).....	158
Table S.15 Statistical summary table of Fig.3.26 (G <sup>2</sup> ) .....	158
Table S.16 Statistical summary table of Fig.3.26 (H <sup>2</sup> ) .....	159

# 1. Introduction

## 1.1 Sound source localization

Sensory systems are a prerequisite for orientation in a three-dimensional environment, whether it is on land, in water, or in the air. For humans, auditory orientation plays a crucial role, especially where visual information is limited or unavailable. The ability to localize sound sources is enabled by spatial hearing. Spatial hearing can be divided into three domains: sound source localization in the azimuthal plane, in elevation, and in distance. Azimuthal sound source localization refers to the ability to determine the direction of a sound source in the horizontal plane relative to the head. This skill is vital in hunting scenarios for localizing prey and, conversely, for detecting predators. Beyond this predator-prey relationship, sound source localization plays an important role in social interactions. For humans, sound source localization plays a particularly important role in recognizing danger (e.g., a rapidly passing ambulance) as well as in the separation of voices in a noisy environment. Individuals who struggle with localizing sound sources often experience the cocktail party effect, impairing their ability to follow a conversation in environments with multiple sound sources (Cherry, 1953; Bronkhorst, 2015).

Unlike other sensory systems, such as vision or somatosensation, auditory signals lack spatial information when perceived by the sensory epithelium (Fig. 1.1; Hartmann, 2021). Sound is transmitted through the auditory periphery and the middle ear to the cochlea, where a mechano-electrical transduction occurs. At this stage, the basilar membrane segregates the signal into its frequency components by a mechanical Fourier analysis, resulting in a topographic analysis of sound frequencies (tonotopic arrangement, Von Békésy, 1960; Fettiplace, 2017; Rutherford et al., 2021). Consequently, spatial information is not directly represented on the sensory epithelium. Two strategies can be employed to extract spatial information from sounds to allow the brain to create a virtual auditory map. First, spectral cues that are present monaurally are used by the central auditory system to estimate the elevation and distance of sound sources (Reiss & Young, 2005). Second, the positioning of the ears at opposite sides of the head is crucial for effective azimuthal spatial hearing, as it results in disparities in the sound reaching each ear. These differences include temporal variations (interaural time differences; ITDs) and intensity variations (interaural level differences; ILDs, Grothe et al., 2010). The physical origins and physiological effects of ITDs and ILDs are discussed in the next section.

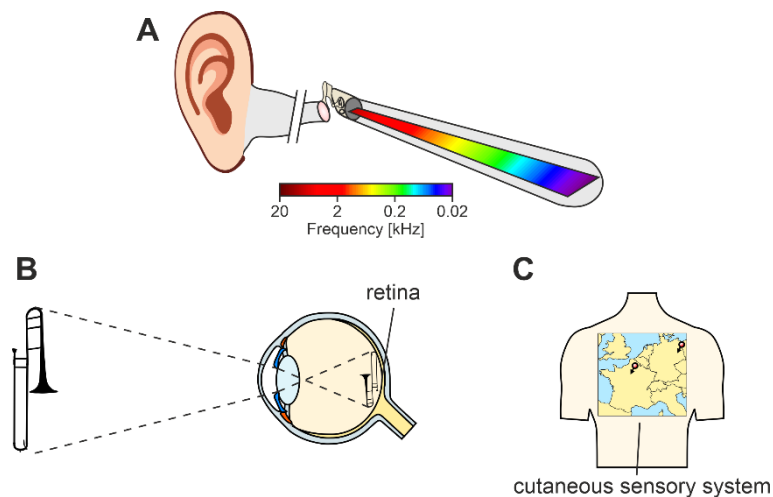


**Figure 1.1 Spatial information is not represented on the basilar membrane - the auditory sensory epithelium.**

**(A)** Auditory signals are mapped tonotopically on the basilar membrane of the cochlea, which does not encompass spatial information.

**(B)** Topographic representation on the retina. Objects like a trombone are mapped on the eye's sensory epithelium – the retina.

**(C)** The cutaneous sensory system processes topographic information for touch, pain and temperature. Humans can identify the side of stimulation represented by the two pins: Paris (left) and Berlin (right). Panels **A&B** are inspired based on standard anatomical structures, see e.g., (Kim et al., 2018, Banna et al., 2024), respectively.

## 1.2 Azimuthal sound source localization – level versus temporal coding

The significance of binaural hearing for sound source localization was recognized in the late 18th and early 19th centuries by William Charles Wells (1757–1817), and Giovanni Battista Venturi (1746–1822). Their studies concluded that the localization of sound sources necessitates an inequality of sound between the two ears (Wade & Deutsch, 2008), which we now understand to be ITDs and ILDs. I will introduce the principles of spatial coding and their underlying neurons mechanisms in the next sections. These concepts have recently been reviewed by Pecka and Encke (2020).

The use of ITDs for low-frequency sound source localization and ILDs for high-frequency sound source localization was formalized about a century later in Lord Rayleigh's duplex theory of sound localization (Rayleigh, 1909; Stevens & Newman, 1936). Sound waves shorter than the head's diameter are reflected and absorbed due to impedance differences between air and the head. Thereby, the attenuation of sound (sound shadow) creates direction-sensitive level differences at the two ears (Figs.1.2 A&D; Owruisky et al., 2021).

For humans with a head diameter of approximately 15 cm, the theoretical lower frequency limit for effective ILD computation is around 2 kHz. In contrast, for small mammals, like mice, with a head diameter of about 1.5 cm, this limit is about 20 kHz. However, empirical measurements have shown that substantial ILDs (> 10 dB) are present at frequencies of

10 kHz and higher (mouse: [Lauer et al., 2011](#); gerbil: [Maki & Furukawa, 2005](#); rat: [Koka et al., 2008](#)).

The ILDs are complemented by ITDs, which arise from the differences in arrival times of sound at each ear. When a sound source is not centered, it will first reach the ear facing the source before reaching the adverted ear. By avoiding phase ambiguities, low-frequency sound with wavelengths longer than the head diameter, enable ongoing temporal comparison of the sound between the two ears ([Grothe et al., 2010](#)). This is considered ITD analysis of the fine structure of sound ( $ITD_{fs}$ ; [Figs.1.2 B&C](#)). Hence, the head diameter limits the ITD, for humans with a head diameter of ~15 cm to a maximum of 800  $\mu$ s (1.3 kHz), while for small mammals, ITDs are in the range of up to 100  $\mu$ s ([Maki & Furukawa, 2005](#); [Benichoux et al., 2016](#); review: [Owrutsky et al., 2021](#)).

The transition between ITD and ILD dominance occurs in humans between 1 and 2 kHz, aligning well with the physical predictions ([Brughera et al., 2013](#); [Hartmann & Macaulay, 2014](#)). Mice are often considered to rely on ILD cues due to their small head diameter and low-frequency hearing limit of 1 kHz ([Markl & Ehret, 1973](#)). While phase ambiguity is not present up to frequencies of ~10 kHz (at 100  $\mu$ s, see above), ITD coding is further constrained by physiological factors. For example, auditory nerve fibers, which encode the sinusoidal structure of (pure-tone) sound, are limited to frequencies of ~1.5 kHz (further detailed in [section 1.3](#)). This establishes a biological upper boundary for ITD-based localization ([Rose et al., 1967](#); [Weiss & Rose, 1988](#); [Joris, Carney, et al., 1994](#); [Taberner & Liberman, 2005](#); review: [Joris & van der Heijden, 2019](#)). A very recent study suggests that peripheral filtering within the cochlea limits the use of ITD cues to about 1 kHz ([Goupell et al., 2024](#)).

While ITD- and ILD-based localization have limitations with pure tones, ITD cues exist in high-frequency sounds through the signal's envelope, which can be used for sound source localization ([Stecker et al., 2021](#)). For instance, the sound onset provides an important temporal cue. In human speech, temporal cues are available in the envelope structure by envelope fluctuations (2-50 Hz) and by periodicity (50-500 Hz; [Rosen, 1992](#)). Modulating the envelope enables the study of the importance of temporal cues for the localization of high-frequency sound. These can be studied systematically using sinus amplitude-modulated (SAM) tones or high-frequency filtered clicks ([Joris & van der Heijden, 2019](#); [Yin et al., 2019](#)). These high-frequency temporal cues can be categorized into:  $ITD_{onset}$ ,  $ITD_{env}$ , and  $ITD_{click}$  ([Fig.1.2 D-F](#)). In human psychophysical studies, the importance of  $ITD_{env}$  has been shown as an important cue for high-frequency sound source localization. The  $ITD_{env}$  thresholds can be as low, or even lower than for fine-structure ITDs ([Bernstein & Trahiotis, 2002](#); [Dietz et al., 2013](#)).

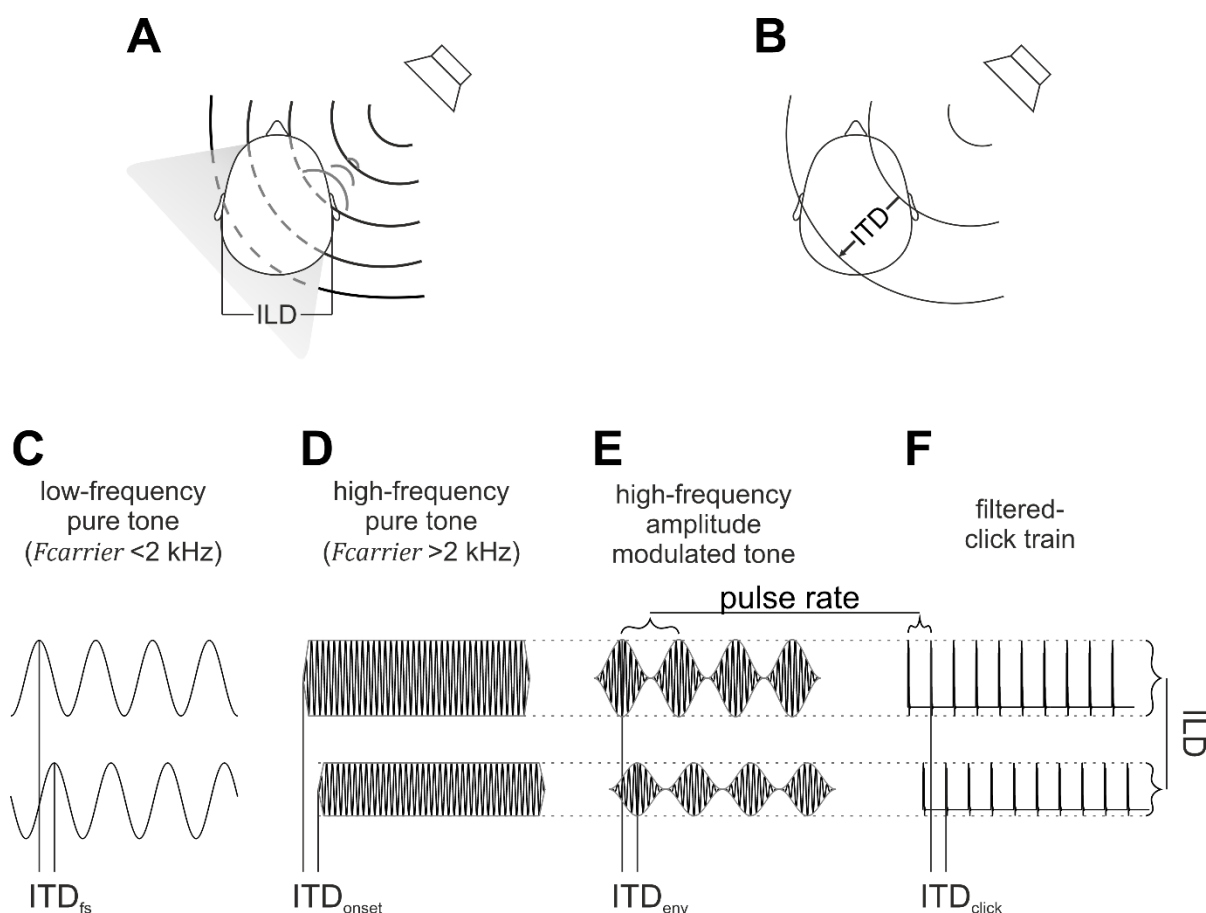


Figure 1.2 Azimuthal sound source localization depends on binaural auditory cues: interaural level differences and interaural time differences.

**(A)** Schematic of sound shadowing by a human head, creating interaural level differences (ILD). High-frequency sound ( $> 2$  kHz) is absorbed and reflected by the head as physical barrier. Panels **A&B** are adapted from Grothe et al. (2010).

**(B)** Interaural time differences (ITDs) arise from the varying differences a sound wave must travel to reach each ear.

**(C)** Visualization of ITDs in the fine structure of a low-frequency pure tone.

**(D-F)** In high-frequency sound, the ILD is the level difference with which a sound wave reaches either ear. Three sound waves commonly used in auditory neurophysiology are presented: a high-frequency pure tone (**D**), a high-frequency amplitude modulated tone (**E**; cf. Fig.1.1 A), and a filtered click train (**F**). ITDs can occur in either of these sound waves, such as at the onset (ITD<sub>onset</sub>, **B**), in phase differences in the envelope (ITD<sub>env</sub>, **F**), or in the arrival of the click (ITD<sub>click</sub>, **G**).

### 1.3 Neuronal representation of ILDs and ITDs in the auditory brainstem

The fundamental currency of information in the brain are action potentials (APs), with information encoded either through their temporal occurrence or rate of occurrence. For neurons to encode ILD and ITD information, it is essential that they receive bilateral inputs and have their AP activity modulated by these cues. The activity of neurons can be assessed by recording their APs as spikes in extracellular voltage recordings (simplified in the panel left to Fig.1.3 C<sup>1</sup>). The terms AP and spike are often used interchangeably, as they refer to the same biological observation.

ILDs are encoded in a process where the AP activity caused by sound at one ear is reduced by increasing the sound level at the other ear. According to the framework by Tollin (2003) an ideal ILD processor has to fulfill several criteria, and these criteria are reliably met by neurons in the lateral superior olive (LSO) of the auditory brainstem. LSO neurons respond with an increase in the AP rate to sounds from the ipsilateral ear, and this response decreases as the sound level at the contralateral ear rises (Boudreau & Tsuchitani, 1968; Guinan, Norris, et al., 1972; Tollin & Yin, 2002a). This information is extracted from ipsilateral excitatory (Cant & Casseday, 1986) and contralateral inhibitory inputs to the LSO (Moore & Caspary, 1983; Banks & Smith, 1992). The activity of a neuron can be displayed in peri-stimulus time histogram (PSTHs), allowing to compare the firing rate before, during, and after stimulation. Upon ipsilateral stimulation, LSO neurons exhibit a prominent onset response with little temporal jitter in the occurrence of the first AP. This is followed by a decrease in activity, and the temporal occurrence of this activity can be characterized into different firing patterns: onset, chopper, or primary-like (PL, Tsuchitani, 1982). This activity is induced by a narrow range of tone frequencies, and the frequency range that inhibits LSO neurons by contralateral stimulation aligns with the excitatory range (Boudreau & Tsuchitani, 1968; Caird & Klinke, 1983). This implies that the neurons innervating a given LSO neuron have very similar frequency tuning. The frequency sensitivity of LSO neurons is tonotopically ordered. Neurons in the lateral limb of the LSO are sensitive to low-frequency sound, and neurons in the medial part of the LSO to high-frequency sound (Fig.1.4 B, Caird & Klinke, 1983; Sanes & Rubel, 1988).

Computation of ITDs is classically assigned to neurons in the medial superior olive (MSO). These neurons are excited by low-frequency tone stimulations of either ear. The AP probability of MSO neurons depends on the ITD of the stimulus, and they only fire APs in a narrow temporal window, enabling microsecond ITD coding (Goldberg & Brown, 1969). This is achieved through a coincidence detection of excitatory inputs from both hemispheres. They activate cyclically with the stimulus phase, which MSO neurons can follow up to frequencies of about 1.5 kHz (Yin & Chan, 1990). This sets the upper frequency limit for ITD computation by MSO neurons (Brughera et al., 2013). Importantly, the excitatory inputs are accompanied by bilateral inhibitory inputs that can modulate the coincidence detection window and thereby shift the preferred ITD for coincidence detection (Brand et al., 2002; Pecka et al., 2008; Myoga et al., 2014). The intricate mechanisms of ITD coding of MSO neurons are further elaborated in a recent review (Grothe et al., 2019). In the following, I will focus on a second mechanism of ITD coding.

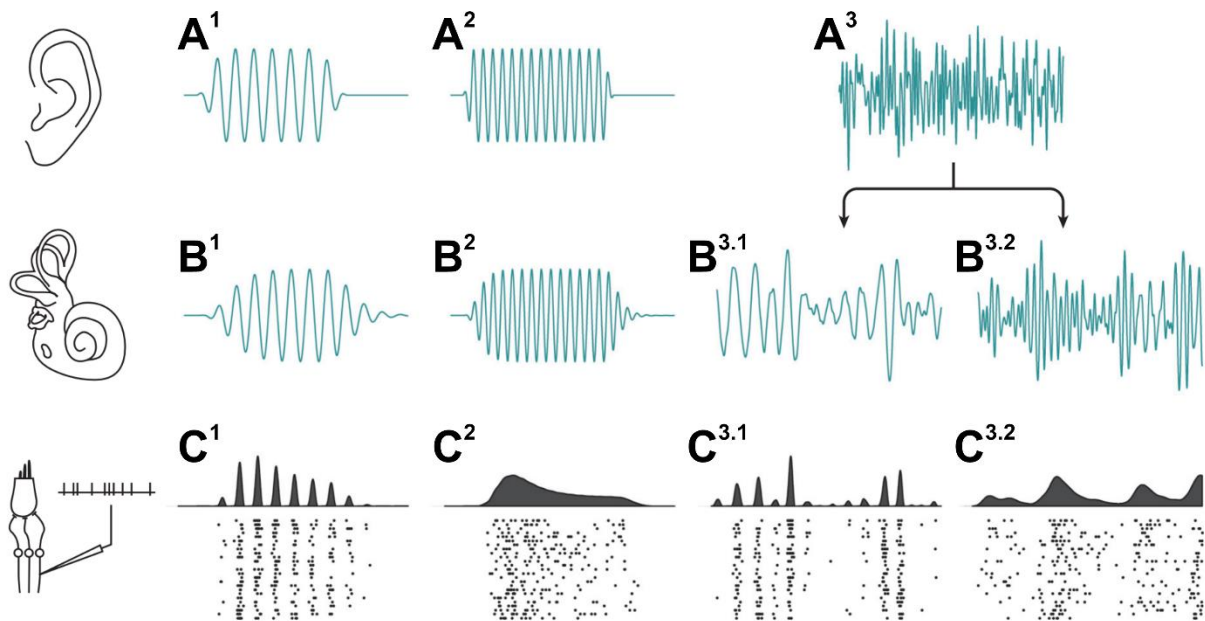
Despite LSO neurons fulfilling several criteria that allow ILD computation, this does not imply that ILD computation is the exclusive coding regime of these neurons. LSO neurons

exhibit an exclusive high sensitivity to ITDs of click stimulation (cf.  $ITD_{click}$ , Fig.1.2 F, Beiderbeck et al., 2018; Franken et al., 2021). In contrast to MSO neurons, the ipsi-excitatory, contra-inhibitory nature of the LSO inputs leads to an anti-coincidence detection. They fire APs when ipsilateral and contralateral inputs are not in temporal register. Thus, APs are suppressed in an anti-coincidence detection window (Joris & Yin, 1995). The dual sensitivity to ILDs and ITDs led to the hypothesis of time-intensity trading, in which the presence of one cue can be compromised by the second (Grothe & Park, 1995; Park et al., 1996). In pure-tone stimulations, the onset response of LSO neurons is suppressed by both ITDs and ILDs, while the sustained part is primarily sensitive to ILDs (Irvine et al., 2001). However, low-frequency sensitive LSO neurons are described to be activated cyclically, following the low-frequency stimulus phase like MSO neurons, and show ITD sensitivity throughout the stimulus (Finlayson & Caspary, 1991; Tollin & Yin, 2005). Cyclic activation can also be achieved by an ipsilateral high-frequency SAM tone. The APs of the neuron then follow the low-frequency sinusoid of the modulation (Joris & Yin, 1995; Batra et al., 1997). Combined with contralateral inhibition, the activity is sensitive to  $ITD_{env}$  (Joris, 1996). In humans, the ITD sensitivity for  $ITD_{env}$  can even surpass the  $ITD_{fs}$  sensitivity (Bernstein & Trahiotis, 2002; Dietz et al., 2013), and rats have been shown to behaviorally be able to use the  $ITD_{env}$  for sound source localization (Li et al., 2019). The synaptic integration mechanisms by which LSO neurons achieve dual sensitivity to ILDs and ITD with high perceptual acuity remain largely unknown and were the focus of my research.

## 1.4 Neuronal representation of sound in the afferent auditory pathway

Understanding how the brain decodes ITDs and ILDs requires comprehension of the mechanisms by which sound is transformed into both temporal and rate-based representations of APs. Therefore, I will introduce how the nervous system encodes sound in the early afferent pathway.

The Fourier analysis of the basilar membrane spatially separates sound frequencies in the cochlea (cf. Fig.1.1). The movement of the basilar membrane, along with the tectorial membrane, stimulates activity in two types of hair cells: outer hair cells, which serve as a reinforcement mechanism, and inner hair cells, which synaptically activate spiral ganglion neurons (SGNs) through their peripheral processes (Rutherford et al., 2021). Together with the central processes of the bipolar SGNs, these projections are collectively referred to as auditory nerve fibers (ANFs). ANFs target various neural populations within the cochlear nucleus complex (CN), the brain's gate for auditory information (Oertel et al., 2019). Consequently, all information required for subsequent sound processing, including ITD and ILD information, must be encoded via the timing and/or rate of APs in the ANFs.



**Figure 1.3 Schematic of peripheral neural representation of different sound signals.**

**(A)** Illustration of the sound pressure profile of a low-frequency pure tone (**A<sup>1</sup>**), a high-frequency pure tone (**A<sup>2</sup>**) and a complex sound (wideband noise, **A<sup>3</sup>**).

**(B)** Schematics of basilar membrane oscillations induced by the sounds patterns in **A**. According to **Fig.1.1 (A)**, the oscillations shown in **B<sup>1</sup>** would be at an apical position, whereas those of **B<sup>2</sup>** would be at a basal position in the cochlea. The sound in **A<sup>3</sup>** would undergo a Fourier analysis and the oscillations in low-frequency areas are shown in **B<sup>3.1</sup>** and those of high-frequency areas in **B<sup>3.2</sup>**.

**(C)** Neural representation of the sound patterns in **A**. The panel to the left of **C<sup>1</sup>** illustrates a recording from spiral ganglion neurons. Their activity is drawn in panels **C<sup>1</sup>-C<sup>3</sup>** in spike raster plots (bottom), where the dots mark the occurrence of APs. Each row is a single representation of the same sound. These can then be summarized in peri-stimulus time histograms (top panels), i.e., by counting the number of dots that fall into a single bin.

Figure is redrawn from (Joris & van der Heijden, 2019).

Low-frequency sound (**Fig.1.3 A<sup>1</sup>**) induces cyclic displacements of the basilar membrane (**Fig.1.3 B<sup>1</sup>**), and ANFs generate APs when the membrane is positively displaced. Thus, the temporal pattern of APs follows the temporal structure of the sound (**Fig.1.3 A<sup>1</sup>-C<sup>1</sup>**). Because they lock their AP activity to the phases of stimulation, this phenomenon is called phase locking (Goldberg & Brown, 1969; Joris & Smith, 2008). The oscillations of high-frequency sounds are too fast for the neural system to follow (**Fig.1.3 A<sup>1</sup>-C<sup>1</sup>**; Joris & van der Heijden, 2019). Instead, the AP activity of ANFs follows the envelope of the stimulus (**Fig.1.3 C<sup>2</sup>**; Joris, Carney, et al., 1994). Complex sound signals include multiple frequency domains. These are separately analyzed, and their low-pass filtered component can again reliably be encoded by phase locking. The encoding of the high-pass filtered component is characterized by phase locking to the envelope of the signal (**Fig.1.3 A<sup>3</sup>-C<sup>3</sup>**).

## 1.5 Ticket to the olive: the neural pathway to lateral superior olive neurons

In order to extract ILD and ITD information from high-frequency sound, the neural architecture of the LSO circuitry must support the ipsi-excitatory and contra-inhibitory coding principle. This architecture provides the anatomical basis for understanding the mechanisms of synaptic integration in the LSO.

After sound is perceived in the cochlea by mechano-electrical transduction in the inner hair cells, the information is transmitted to the CN via ANFs. These ANFs have multiple functional classes that activate at different sound levels and span a range of rate-level functions, enabling sound level computation over a wide range (Taberner & Liberman, 2005; Pyott & von Gersdorff, 2020). They innervate bushy cells (BCs) in the anteroventral cochlear nucleus (AVCN), in an ANF-subtype independent manner, presumably allowing BCs to integrate rate-level information over a wide range (Wong et al., 2025). BCs are contacted via exceptionally large synapses, named endbulb of Held, which engulf the soma of their postsynaptic partners (Held, 1893). The number of ANFs converging on a given BC is low, with functional estimates being 1-13 (Cao & Oertel, 2010) and anatomical estimates being 5-12 (Spirou et al., 2023, both in mice). BC display sharp frequency sensitivity and follow a tonotopic arrangement within the AVCN (Fig.1.4 B, review: Oertel et al., 2019). They are categorized into three classes, based on their somatodendritic morphology and auditory brainstem targets. (NB: in mice these differences are less prominent (Lauer et al., 2013), and not taken into account by some author (Zhuang et al., 2020)). Large spherical BCs (SBCs) are situated ventrally, respond to low-frequency sound, and send excitatory projections to the MSO in both brainstem hemispheres (Stotler, 1953; Osen, 1969; Lindsey, 1975; Smith et al., 1993). Small SBCs are situated more dorsally and show sensitivity to higher sound frequencies. These neurons project to neurons in the ipsilateral LSO (Fig.1.4 C, Cant & Casseday, 1986; Friauf & Ostwald, 1988). The ipsilateral excitatory inputs are opposed by glycinergic inhibitory inputs emanating from neurons of the homolateral medial nucleus of the trapezoid body (MNTB, Moore & Caspary, 1983; Bledsoe et al., 1990; Sommer et al., 1993), which in turn are innervated by globular BCs (GBCs, Tolbert & Morest, 1982).

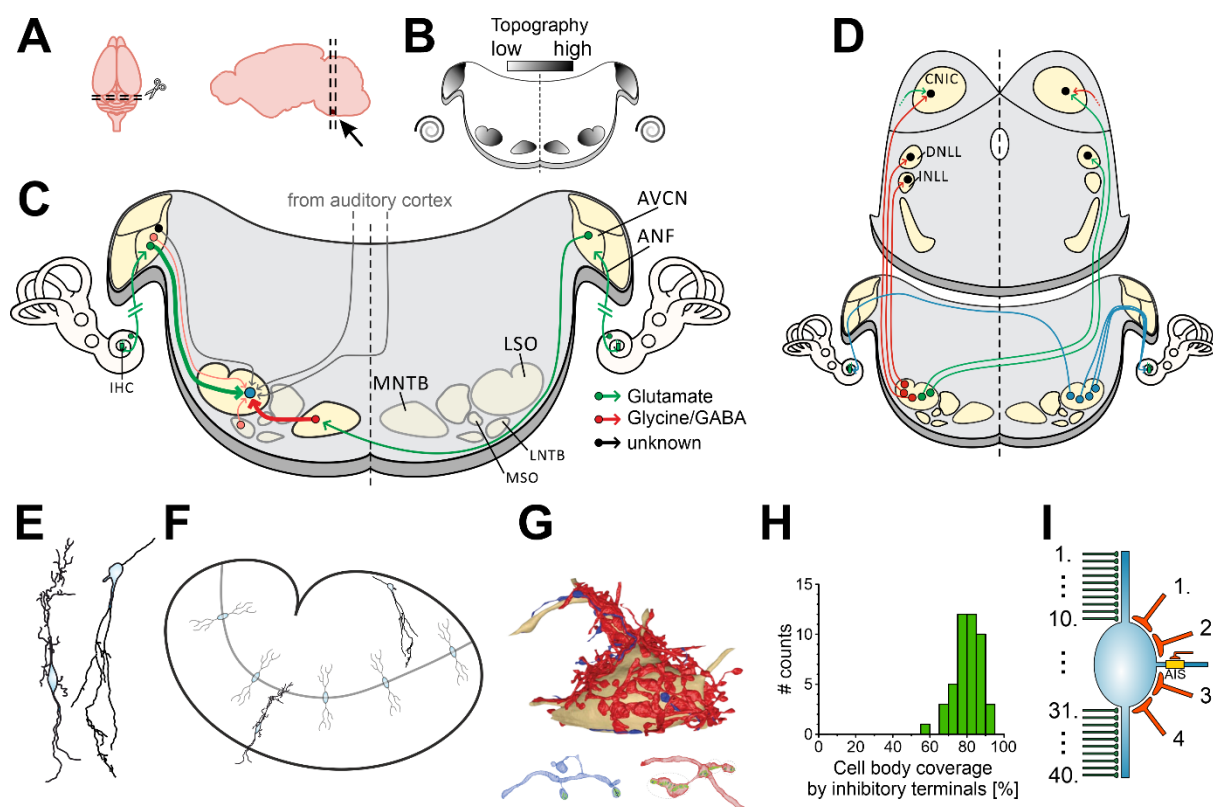


**Figure 1.4 Overview of the LSO input and output pathways and synaptic organization on LSO neurons.**

**(A)** The location of the LSO within the mouse brain seen from a dorsal view and in a sagittal brain slice. In the sagittal slice, the LSO is indicated in red (arrow to ventral section) but is hard to see due to its small size.

**(B)** Topographic arrangement of the LSO pathway in a coronal section.

**(C)** Cartoon depicting a coronal brainstem section indicating the input pathways to LSO principal neurons. The major binaural innervations are drawn in bold, while innervations considered modulatory or with unknown function are drawn light (drawn for completeness, but not further addressed). Panels **C&D** are modified from (Friauf et al., 2019).

**(D)** Cartoon depicting the output pathways of LSO principal neurons (left) and lateral olivocochlear (LOC) neurons (right – drawn for completeness, but not further addressed). Dotted lines ending in arrows in the central nucleus of the inferior colliculus (CNIC) indicate ipsilateral excitatory projections from LSO neurons, and contralateral inhibitory projection (see section 1.9).

**(E)** Somatodendritic morphology of two stereotypical LSO neurons (redrawn from Rietzel & Friauf, 1998).

**(F)** Somatodendritic orientation of LSO neurons within the nucleus follow the tonotopic axis. The two neurons from **E** are approximately positioned at their location shown in Rietzel & Friauf (1998).

**(G)** Synaptic arrangement onto an LSO neuron soma and proximal dendrites. Red: presumed inhibitory synapses, blue: presumed excitatory synapses. Modified from (Gjoni, Aguet, et al., 2018).

**(H)** Histogram of cell body coverage by inhibitory terminals. Modified from (Franken et al., 2018).

**(I)** Synaptic inputs onto an LSO neuron. Green excitatory inputs, red inhibitory inputs. Numbers of inputs are based on (Gjoni, Zenke, et al., 2018).

Abbreviations: IHC: inner hair cell, AVCN: anteroventral cochlear nucleus, LSO: lateral superior olive, MNTB: medial nucleus of the trapezoid body, LNTB: lateral nucleus of the trapezoid body, INLL: intermediate nucleus of the lateral lemniscus, DNLL: dorsal nucleus of the lateral lemniscus, CNIC, central nucleus of the inferior colliculus.

The axons of the GBCs run through the ventral acoustic stria to innervate MNTB neurons by another giant synapse: the calyx of Held (Held, 1893). The calyceal synapse enwraps the MNTB soma and is the virtually exclusive spike-driving input to MNTB neurons (review: Yu & Goodrich, 2014). MNTB neurons form conventional inhibitory boutons predominantly on the soma of LSO neurons. An impressive 80 % of the soma area are covered by inhibitory terminals (Fig.1.4 G&H, Helfert & Schwartz, 1987; Franken et al., 2018; Gjoni, Aguet, et al., 2018). Functional estimates suggest that ~4-8 MNTB neurons are the source of these innervations (Gjoni, Zenke, et al., 2018; Müller, Jovanovic, et al., 2019). During development, inhibitory synaptic innervations are pruned, enhancing the frequency selectivity of inhibition onto LSO neurons (Kim & Kandler, 2003; Müller, Sonntag, et al., 2019). This process aligns the frequency selectivity of excitation and inhibition (Caird & Klinke, 1983; Sanes & Rubel, 1988). Since the soma is predominantly covered in inhibitory terminals, it is deduced that excitatory synapses target LSO neurons on their dendrites (Fig.1.4 I). In contrast to the MSO, there is no polarity in the excitatory and inhibitory afferents to the LSO, i.e., they target both dendrites extending from the soma (Glendenning et al., 1985). The number of excitatory converging synapses onto LSO neurons varies across studies. Recent studies suggest that multiple (~40) weak excitatory inputs converge on a single LSO neuron, and each input contributes about 50 pA (~0.7 nS; optogenetical stimulation, Gjoni, Zenke, et al., 2018). Others report a smaller number of innervating inputs with higher unitary strength (Case et al., 2011; Felix & Magnusson, 2016; Haragopal et al., 2025). These differences will be addressed in my study.

LSO neurons have a spindle-shaped soma and extend their dendritic tree in orthogonally to the tonotopic axis (Fig.1.4 E-F, Scheibel & Scheibel, 1974; Cant, 1984; Helfert & Schwartz, 1987; Williams et al., 2022). It is supposed that this allows excitatory inputs to form frequency-selective laminar sheets of innervation to LSO neurons to effectively increase the frequency selectivity of LSO neurons (Williams et al., 2022).

These excitatory and inhibitory innervations form the canonical innervation of LSO neurons, thus aligning well with concepts of subtraction-like ILD computation (review: Friauf et al., 2019). The rate-based ILD sensitivity reflects this computation, with AP rate increasing in response to ipsilateral stimulation and progressively decreasing by increasing contralateral stimulation (Boudreau & Tsuchitani, 1968; Moore & Caspary, 1983; Tollin & Yin, 2002b; Tsai et al., 2010).

## 1.6 Activity patterns of neurons innervating the LSO

To understand how LSO neurons compute ILDs and ITDs, it is essential to consider the activation dynamics of their primary inputs. I now turn to the activation pattern of BCs and MNTB neurons, which forms the conceptual basis for ILD and ITD coding in LSO neurons.

The activity of ANFs is further processed by BCs and MNTB neurons before being transmitted to the LSO. In response to high-frequency pure tones, BCs and MNTB neurons show PL activation patterns (Rhode & Smith, 1986). These PL patterns are sensitive to the sound level and the AP rate is increased with increasing level. The peak firing rate is ~300 APs/s (Rhode et al., 1983; Winter & Palmer, 1990; Postolache et al., 2024). However, non-monotonic effects due to inhibition are also described (Kopp-Scheinflug et al., 2002; Kuenzel et al., 2011; Kuenzel et al., 2015). Computational studies often simplify input rate-level coding to a monotonic increase when investigating the ILD and ITD coding in LSO neurons (e.g.: Wang & Colburn, 2012; Bures & Marsalek, 2013; Ashida et al., 2021; Dietz & Ashida, 2021).

In addition to level coding, BCs and MNTB neurons exhibit remarkable temporal precision, such as at the onset of a sound. To ensure that the temporally precise activity of excitation and inhibition is in temporal register (Joris & Yin, 1998), structural and functional axonal specializations compensate for the additional synapse in the contralateral pathway (Ford et al., 2015; Stange-Marten et al., 2017). Furthermore, the input neurons phase-lock their APs to the sound of low-frequency pure tones with enhanced temporal precision (Joris, Carney, et al., 1994; Joris, Smith, et al., 1994). Similarly, the ANFs provide phase-locked inputs in response to SAM tones with a high-frequency carrier, which are encoded with high precision in both BCs and MNTB neurons (BC: Müller, Sonntag, et al., 2019, MNTB: Kopp-Scheinflug et al., 2003; Tolnai et al., 2008, interaction in the LSO: Joris & Yin, 1998). The transience of the stimulus can be increased by using transposed tones, compared to SAM tones. Such stimulations lead to a further increase in temporal precision of ANFs (Dreyer & Delgutte, 2006), but have not been tested so far on BCs or MNTB neurons. The highest temporal precision is achieved when stimulating with clicks. Even at stimulations with inter-click intervals of 500 Hz, BCs and MNTB neurons exhibit remarkable temporal coding (Müller et al., 2023). Collectively, high temporal precision is considered to elicit synchronous activation of inputs to LSO neurons, which decreases with decreasing temporal structure of the sound envelopes. How such synchrony affects the rate-level and temporal coding in LSO neurons is poorly understood. Therefore, a central aim of my study was to investigate how excitatory and inhibitory inputs are processed, which vary in their temporal correlation, and how this affects the sensitivity to ILD and ITD cues.

## 1.7 Synaptic transmission in the LSO and the effects of synaptic noise

Synaptic transmission enables interneuronal communication. LSO neurons process ipsilateral excitation along with contralateral inhibition for sound source localization, as described in the former paragraph. The ipsilateral excitatory and contralateral inhibitory nature of inputs was confirmed in *in vitro* brainstem slice studies (Sanes, 1990; Wu & Kelly, 1992;

Kandler & Friauf, 1995). Excitatory inputs from multiple SBC converge onto LSO neurons and form glutamatergic synapses. These elicit fast AMPA ( $\alpha$ -amino-3-hydroxy-5-methyl-4-isoxazolepropionic acid) receptor-mediated currents with decay time constants  $< 1$  ms (Pilati et al., 2016). The AMPA receptor subunits' expression of the fast-gating GluR4 subunits increases developmentally (Caicedo & Eybalin, 1999; Vitten et al., 2004; Pilati et al., 2016). NMDA (N-methyl-D-aspartate) receptor-mediated currents are reported, however, they decrease with age (Pilati et al., 2016). These excitatory inputs are contrasted by glycinergic inhibitory innervations from the MNTB, which are also reported to be fast at  $\sim 1$  ms (Pilati et al., 2016; Müller, Sonntag, et al., 2019). Their strength varies across inputs, but are about  $\sim 10$ -fold stronger than the excitatory inputs ( $\sim 8$  nS; Garcia-Pino et al., 2017; Gjoni, Zenke, et al., 2018; Müller, Sonntag, et al., 2019). As mentioned earlier, there are about 40 excitatory inputs converging onto a given LSO neuron, and about 4-8 inhibitory inputs.

Synaptic integration refers to the process of translating synaptic activity into changes in the postsynaptic membrane potential ( $V_{\text{mem}}$ ). When an excitatory input is active, it triggers an excitatory postsynaptic conductance (EPSC). I will refer to the peak conductance elicited by the activity of a single input as its  $SW$  ( $SW_{\text{exc}}$  in case of an excitatory input), and the sum of all excitatory inputs is the compound  $SW_{\text{exc}}$  ( $cSW_{\text{exc}}$ ). The  $SW_{\text{exc}}$ , by which a neuron is innervated, is a key player in shaping its synaptic integration strategy. If multiple weak inputs converge onto a neuron, substantial spatio-temporal summation is necessary to trigger APs. Conversely, if the  $SW_{\text{exc}}$  is large, a unitary input may dictate the firing behavior of the neuron, such as in the MNTB.

Temporally correlated inputs yield high EPSC peaks, while uncorrelated inputs produce a broader, dispersed EPSC profile (cf. Fig.1.5 C<sup>1</sup>). Synchronous inputs maximize the EPSC peak by summing individual peaks, which are integrated into a postsynaptic depolarization (EPSP) that, if sufficient, triggers an AP (Fig.1.5 A). The initiation of the AP can be blocked by adding inhibition (Fig.1.5 B). The scenarios outlined above describe the integration of EPSC from multiple synaptic partners. Their combined effect on the  $V_{\text{mem}}$  is typically referred to as spatial summation. The second form of integration is temporal summation, referring to the integration of synaptic inputs that occur in rapid succession at the same synapse. In this case, the time interval between the activations is too short to allow the  $V_{\text{mem}}$  to repolarize back to its resting level, allowing successive EPSPs to summate temporally.

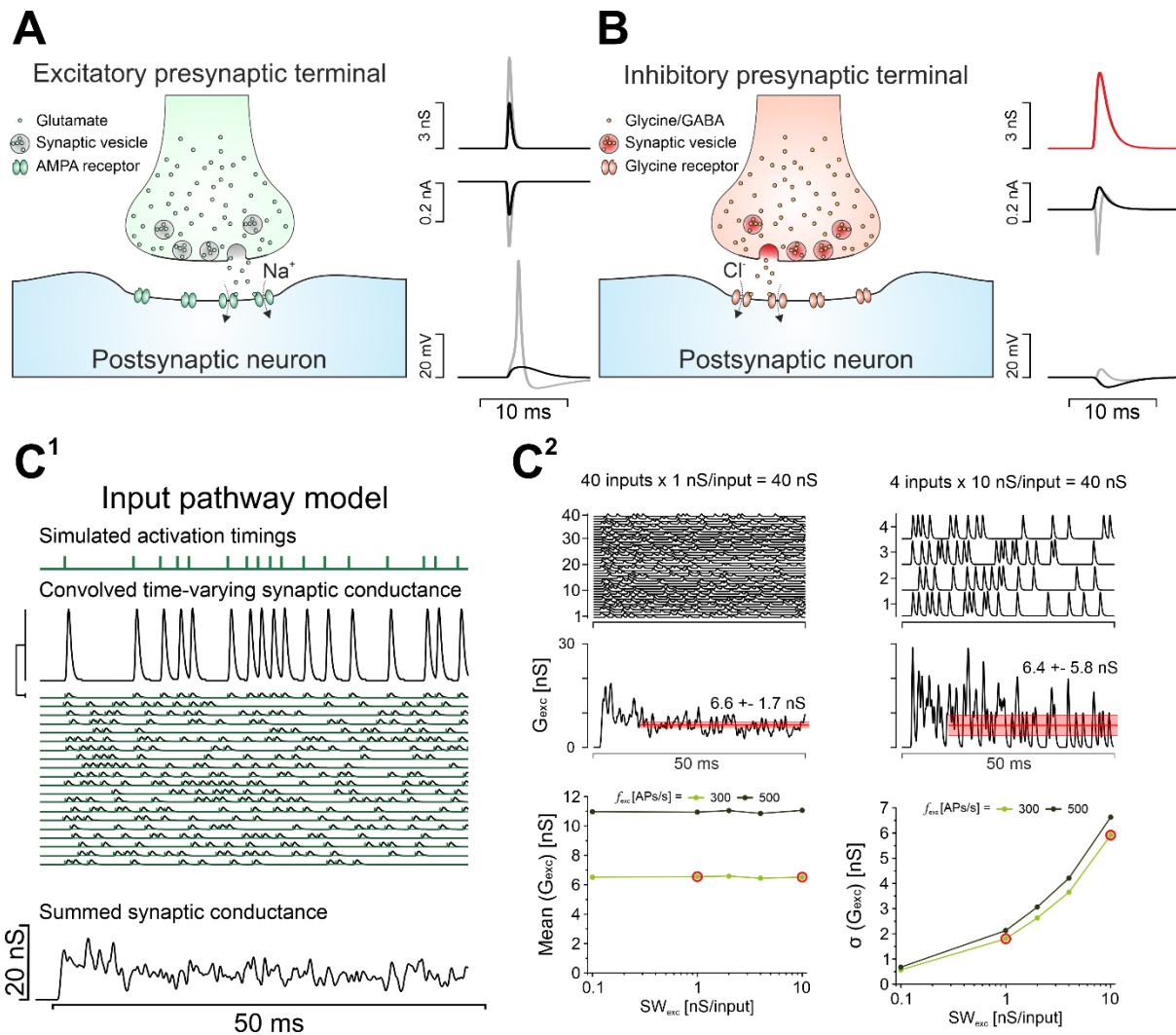


**Figure 1.5 Schematic of synaptic transmission and experimental setup to stimulate with simulated synaptic inputs.**

**(A)** Schematic of glutamatergic excitatory synaptic transmission (left). The right shows a synaptic conductance (top), its corresponding synaptic current (middle) and the voltage change in the postsynaptic neuron (bottom; black: subthreshold, grey: suprathreshold).

**(B)** Same as **A** but for glycinergic inhibitory synaptic transmission. The grey traces to the right, show the combination of the suprathreshold excitation from **A** with the hyperpolarizing inhibition (black in **B**) that prevents the initiation of an AP.

**(C)** The influence of distributing the compound  $SW$  on different number of inputs. **C<sup>1</sup>** depicts the summation of 40 converging inputs, each contributing 1 nS/input. The summed excitatory conductance ( $G_{exc}$ ) shows a mean steady-state conductance (starting 10 ms after onset) of  $6.6 \pm 1.7$  nS (**C<sup>2</sup>** left). In case of a convergence of four inputs (right) the mean is similar (6.4 nS) but the SD increases (5.8 nS, **C<sup>2</sup>** right). The bottom panels in **C<sup>2</sup>** quantify this effect by plotting the mean  $G_{exc}$  (left) as function of  $SW_{exc}$  for two different activation frequencies ( $f_{exc}$ ; top panels show traces for  $f_{exc}$  of 300 APs/s). The right plot shows the same for the SD ( $\sigma(G_{exc})$ ). See [Silver \(2010\)](#) for further details on ‘neural arithmetics’.

When multiple inputs converge onto a neuron and transmit the same type of signal, they are considered to act in parallel. This concept relies on the assumption that the synapses are functionally similar, particularly in their molecular composition, such as postsynaptic receptor

subtypes. The conductances of these parallelly connected synapses would linearly summate to create a summed synaptic conductance (Fig.1.5 C<sup>1</sup>-C<sup>2</sup>). An important feature of such summed PSG is the time-averaged conductance and its deviations from the mean (here termed synaptic noise; while further sources of synaptic noise are summarized by Faisal et al., 2008). Several studies have shown that such noise is an important carrier of information and can reliably be encoded in auditory neurons (Street & Manis, 2007; Gai et al., 2009). The noise of the summed PSG is a product of the  $SW$  each synapse contributes and their activation rate. Fig.1.5 (C<sup>2</sup>) shows two scenarios to illustrate these effects. On the left, 40 inputs converge onto a given neuron, with each of the inputs contributing a  $SW_{exc}$  of 1 nS/input. They sum to a  $cSW_{exc}$  of 40 nS. The same 40 nS can be reached by distributing the 40 nS to only four inputs, resulting in  $SW_{exc}$  of 10 nS/input. While both scenarios have a very similar mean steady-state conductance of ~6.5 nS, they differ in the noise ( $\sigma(G_{exc})$ ) of the EPSG (Fig.1.5 C<sup>2</sup>, bottom panels). These changes can be explained by Campbell's theorem connecting the frequency of randomly occurring, fast decaying signals to their time averaged mean and standard deviation (Campbell, 1909; Silver, 2010). The summed EPSG will be majorly altered if there is temporal correlation between converging inputs. Therefore, the temporal activity patterns of the synaptic inputs are major determinants for encoding of level and temporal information. How variations in the  $SW_{exc}$  and  $SW_{inh}$  influence the computations for ILD and ITD coding in LSO neurons is not known. To this end, I used the dynamic-clamp (DC) method in combination with an input pathway model to study synaptic integration in LSO neurons. This method will further be subject in section 1.10.

## 1.8 Functional adaptations for ultra-fast information processing

The bilateral LSO brainstem circuit shows several adaptations, functionally as well as morphologically, that allow for exquisite temporal coding. A very recent review covers structural and functional adaptations of neurons across the auditory brainstem (Keine & Englitz, 2025), while I will focus on adaptations of LSO neurons that shape synaptic integration.

Important features of synaptic integration are intrinsic membrane properties as well as active conductances. The latter result from the activity of voltage-gated channels that contribute to changes in the membrane potential, causing non-linear current-voltage relationships. Auditory neurons typically exhibit low input resistances ( $R_{in}$ ) that result in short membrane time constants ( $\tau_{mem}$ , Keine & Englitz, 2025). These are determined by passive and active channels and are major determinants for high-frequency membrane resonances, which allow fast synaptic integration (Fischer et al., 2018; Leao, 2019).

Neurons of the bilateral auditory pathways utilize different sub-threshold active channels. The two most well-described are low-threshold voltage-gated potassium (Kv) channels of the Kv1 family and hyperpolarization-activated cyclic nucleotide-gated (HCN) channels, which are expressed (Maraslioglu-Sperber et al., 2024) and functionally described in the LSO (HCN: Leao et al., 2006; Kv1: Karcz et al., 2011; review: Leao, 2019). Kv1.1 channels show fast activation due to depolarizations, and they slowly inactivate. They conduct a hyperpolarizing current, and play an important role in limiting the number of APs in response to a current step stimulation and to influence a rate- or slope threshold for AP initiation (McGinley & Oertel, 2006; Cao et al., 2007). Furthermore, neurons utilizing Kv1 channels exhibit a band-pass filtering behavior in combination with stochastic resonance when cyclically activated (Gai et al., 2009; Gai et al., 2010; Johnston et al., 2010). While the activity of these channels has been described in BCs and MNTB neurons (Manis & Marx, 1991; Brew & Forsythe, 1995), the influence of their activity in response to sinusoidal activation has so far not been tested in LSO. The second channel family, HCN channels (HCN1-4), activates due to hyperpolarization, and the current they conduct has an equilibrium potential of about -50 mV (Wahl-Schott & Biel, 2009). Therefore, their activation can have a depolarizing or hyperpolarizing effect depending on the  $V_{mem}$  of the neuron. LSO neurons primary utilize HCN1-channels, which have the fastest kinetics of the four subtypes (Leao et al., 2006; Hassfurth et al., 2009; Kopp-Scheinflug et al., 2015). A functional role in dendritic integration has been attributed, in that they effectively dampen the integration of unsynchronous excitatory input signals (Leao et al., 2011). In combination, the overlapping activation curves of low-threshold Kv conductance and HCN conductances contribute to the resting  $R_{in}$  of a neuron (Golding & Oertel, 2012). Together, they shape coincidence detection of excitatory inputs by influencing a slope-dependent AP threshold (Cao et al., 2007; Golding & Oertel, 2012). In the LSO, a post-inhibitory facilitatory effect is most likely influenced by the intricate interplay of some of these voltage-gated currents (Kv1- and HCN-mediated) in combination with voltage-gated sodium (Nav) channels (Dodla et al., 2006; Beiderbeck et al., 2018).

Further low-threshold Kv conductances were recently described in the LSO, by means of single cell expression analysis and immunohistochemistry: Kv7.2, Kv7.3 and Kv11.3 (Maraslioglu-Sperber et al., 2024). The activation of the Kv7 channels hyperpolarizes LSO neurons and contributes to enhance onset AP firing by preventing multiple firing. Similar functions are attributed to Kv11.3 channels in BCs and MNTB neurons (Hardman & Forsythe, 2009; Yildirim & Bal, 2018). The function of this channel for synaptic integration in LSO neurons is so far unknown.

## 1.9 Afferent and efferent projection of LSO neurons

The projection patterns of LSO neurons are introduced briefly here, to provide anatomical context and allow for functional interpretations in the results and discussion sections.

The neuronal pathway described so far, is the innervation pathway onto the principal neurons in the LSO. These neurons are part of the ascending auditory pathway. Besides principal neurons, the LSO harbors neurons of the lateral olivocochlear (LOC) system (Romero & Trussell, 2022). As the LOC neurons will not be further subject in this study, the wording is simplified to LSO neurons regarding the main neuron type. These can be further subdivided into excitatory and inhibitory neurons, which project to several target nuclei in the ascending auditory pathway. Ipsilateral projections terminate in the intermediate and dorsal nucleus of the lateral lemniscus (INLL and DNLL, respectively) as well as neurons in the central nucleus of the inferior colliculus (CNIC). Contralaterally projecting LSO neurons terminate in the DNLL and CNIC (Friauf et al., 2019; Williams et al., 2022) (Fig.1.4 D). Whether there is a strict segregation of excitatory LSO neurons projecting contralaterally and inhibitory ipsilaterally, or if the two types project bilaterally is currently under debate (Mellott et al., 2022; Williams et al., 2022; Haragopal et al., 2023; Williams & Ryugo, 2024) and species-specific differences are discussed by Williams et al. (2022). The temporal dynamics of the activation patterns of LSO neurons are thought to contribute to temporal coding in CNIC neurons (Ono et al., 2020). These show sensitivity to  $ITD_{env}$  of high-frequency modulated tones. This strongly suggests that the temporal firing patterns of LSO neurons are important factors in the ascending auditory pathway. The temporal activation patterns of LSO neurons in response to different synaptic integration paradigms are another focus of my study.

## 1.10 Studying synaptic integration using virtual synapses: the dynamic-clamp method

Synaptic integration is mediated by various intricate mechanisms, including the intensity and timing of input signals, temporal jitter in synaptic vesicle release, neuromodulation during continuous stimulations, and voltage-gated conductances of postsynaptic neurons. In monosynaptically innervated neurons, like MNTB neurons, synaptic integration can be studied by electrically stimulating the input and recording  $V_{mem}$  changes. In contrast, this is complicated in poly-innervated neurons, such as in the LSO. Electrical stimulation of the excitatory, respectively inhibitory pathway unavoidably activates presynaptic inputs simultaneously. This prevents to study the influence of temporally uncorrelated inputs within either pathway.

To address these limitations, the DC method can be employed. This approach was initially utilized by two groups (Robinson & Kawai, 1993; Sharp et al., 1993) to examine the impact of virtual conductances in real-time in neurons. In this method, a conventional patch-clamp setup

is augmented with a DC interface, which may consist of an additional computer or a microcontroller (Prinz et al., 2004; Yang et al., 2015). Synthetic conductances are transmitted through the patch-clamp setup to the DC interface. The interface then computes the resulting current based on the conductance, the instantaneous  $V_{mem}$  obtained from current-clamp (CC) recordings, and the reversal potential of the conductance. This calculated current is subsequently applied via the patch-clamp amplifier (Fig.1.6 A&B).

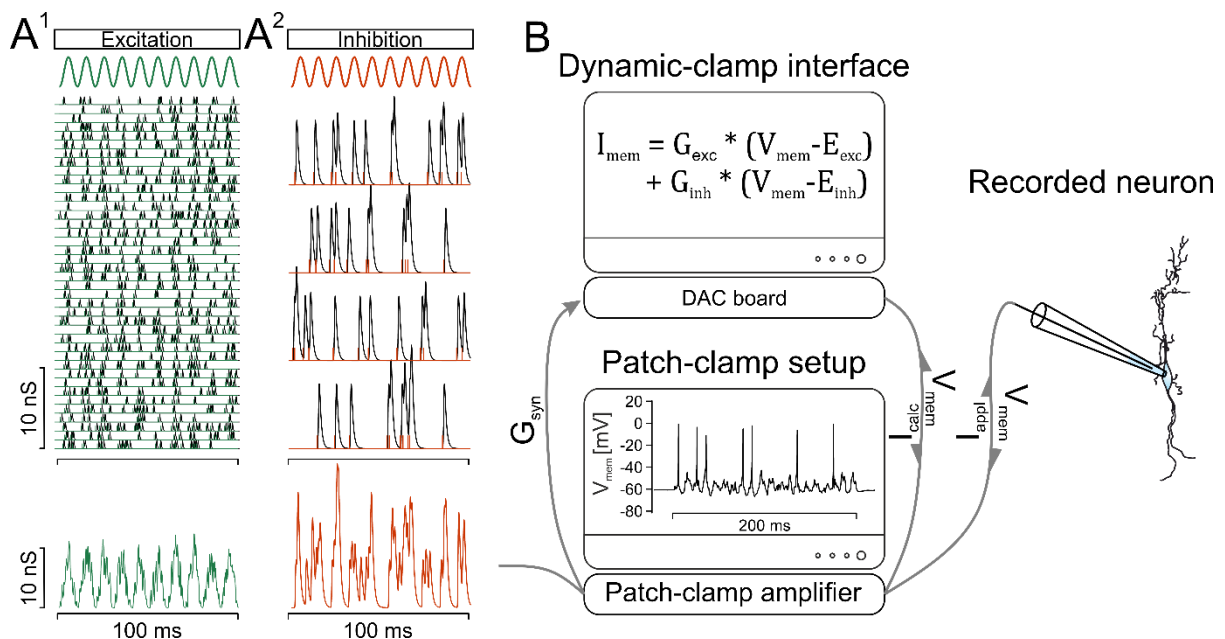


**Figure 1.6 Dynamic-clamp setup to study synaptic integration using virtual synapses.** (A) The process of creating simulated synaptic conductances for excitation is shown in A<sup>1</sup> and for inhibition in A<sup>2</sup>. First, activation timings are created for each input that follow a stimulus function (green and red sinusoid and digitized green and red traces overlaying the black traces in the top panel). A unitary conductance of either input is then positioned at each timing to create the time-varying conductance of a unitary input. The sum of those reflects the summed excitatory and inhibitory conductance that can be used for dynamic-clamp (DC) stimulations (bottom). (B) Experimental setup to stimulate neurons with simulated synaptic inputs. A classical patch-clamp setup is extended by a DC interface. This calculates in real-time the current which results from the conductances in combination with the reversal potential of each synapse and the momentary  $V_{mem}$ . This current is applied to the neuron, via the patch-clamp amplifier. For details of the DC interface see (Yang et al., 2015).

The relative timing and strength of each input can be modeled in a manner akin to computational experiments (Rothman et al., 1993; Ashida et al., 2017). As illustrated in Fig.1.6 A, the timings of excitatory and inhibitory synapses are simulated using an inhomogeneous Poisson process, which utilizes a sinusoidal stimulus function. At each generated input timing for a specified input, a unitary conductance is assigned to produce a time-varying conductance for each input. The sum of all inputs can then be applied via the DC interface to study different effects of synaptic integration. Thereby, a key advantage of this experimental setup is the precise control over input strength and timings. This permits isolation

of the intrinsic response properties of the postsynaptic neuron to defined synaptic parameter. Such manipulation enables bridging the gap between *in vivo* and *in vitro* approaches and provide mechanistic insights into principles of synaptic integration.

### 1.11 Aims of the study

This thesis aims to enhance our understanding of synaptic integration mechanisms in LSO neurons. The goals can be split into four parts:

- 1.) As outlined in the introduction, there is disagreement in the literature of the synaptic innervations of excitatory synaptic inputs to LSO neurons. To this end, I reevaluated the excitatory synaptic inputs to LSO neuron with a focus on the  $cSW_{exc}$ , the  $SW_{exc}$  and the kinetics of synaptic inputs. These will be used as a physiological reference, to allow the interpretation of the influence of different synaptic parameters on synaptic integration in LSO neurons.
- 2.) Intrinsic membrane properties form the basis for synaptic integration and are reported to vary with the position of the neurons along the putative tonotopic axis of the LSO of rats and guinea pig (Barnes-Davies et al., 2004; Remme et al., 2014, respectively). Therefore, I analyzed the following aspects:
  - i. What are the basic subthreshold membrane properties of LSO neurons?
  - ii. Do these properties vary along the tonotopic axis?
  - iii. What are the intrinsic AP properties of LSO neurons and do LSO neurons express a slope-dependent AP threshold?

This characterization provides valuable insights into how intrinsic membrane properties are set for synaptic integration and are important for the interpretations on mechanisms of synaptic integration in LSO neurons.

- 3.) The primary objective of this thesis was to assess mechanisms of synaptic integration of LSO neurons under *in vivo* like stimulation patterns. This was studied in several aspects. The primary questions were as follows:
  - i. A coincidence detector role for LSO neurons was proposed by a modeling study (Ashida et al., 2016) and auditory neurons are reported to exhibit stochastic resonance (Gai et al., 2010). Do LSO neurons exhibit such a coincidence detection mechanism?
  - ii. How does the  $SW_{exc}$  influence rate and temporal coding of LSO neurons and how do the temporal dynamic of input activation influence this?
  - iii. How do LSO neurons extract level-difference information from PL input patterns, characteristic for pure-tone stimulation?
  - iv. How does stimulus transience, modeled by increasing temporal correlation, affect synaptic integration for rate-level coding?

- v. I hypothesized that temporal correlation is a major determinant for temporal coding in LSO neurons and analyzed the influence of temporal disparities on the rate-level coding, as well as the influence of stimulus transience on the coding of temporal disparities.
- 4.) To characterize the functional importance of the *in vitro* findings in an *in vivo* situation, a cooperation with the group of Dr. Conny Kopp-Scheinflug was established. Here we wanted to address the following objective:
- i. Does stimulus transience increase temporal coding in LSO neurons, potentially restricting APs to shorter time windows?
  - ii. Does stimulus transience negatively affect rate-level coding in LSO neurons?

## 2 Methods

### 2.1 Animals

Animal breeding and experiments were approved by the regional councils of Rhineland-Palatia according to the German Animal Welfare Act (TSchG §4/3) and followed the guidelines for the protection and welfare of laboratory animals. C57BL/6J mice, bred and housed in the animal facility of the University of Kaiserslautern-Landau, were used for *in vitro* experiments. Animals of both sexes aged > 27 postnatal days were analyzed.

### 2.2 Brainstem slice preparation

Brainstem slices were prepared similarly as described (Müller, Sonntag, et al., 2019). Briefly, mice were decapitated, and the brain was quickly removed into an ice-cold preparation solution containing (in mM): 93 N-methyl-D-glucamine, 93 HCl, 30 NaHCO<sub>3</sub>, 25 glucose, 20 HEPES, 10MgCl<sub>2</sub>, 5 L-ascorbic acid, 3 myo-inositol, 3 sodium pyruvate, 2.5 KCl, 1.2 NaH<sub>2</sub>PO<sub>4</sub>, 0.5 CaCl<sub>2</sub> (pH 7.4 when oxygenated with carbogen; 300 ± 10 mOsm/l; final solution was stored for a maximum of three days). The forebrain and cerebellum were cut off the brainstem, which was glued with the caudal side onto a magnetic plate. This was inserted into a Leica VT 1200S (Leica Microsystems, Wetzlar, Germany) and brainstem slice (270 µm) were cut ventral to dorsal at low speed (0.01-0.03 mm/s). The presence of the 7<sup>th</sup> cranial nerve (facial nerve) stump indicated the presence of the LSO. Accordingly, this slice, along with one above and one below were collected. These were subsequently incubated in preparations solution at 36°C for 7-8 mins. The slices were then transferred to artificial cerebrospinal fluid (ACSF) at room temperature, containing (in mM): 125 NaCl, 2.5 KCl, 1 MgCl<sub>2</sub>, 1.25 NaH<sub>2</sub>PO<sub>4</sub>, 2 sodium pyruvate, 3 myo-inositol, 0.44 L-ascorbic acid, 25 NaHCO<sub>3</sub>, 10 D-glucose, 2 CaCl<sub>2</sub> (pH 7.4 when oxygenated with carbogen; 295 ± 5 mOsm/l) and stored up to 6 h at room temperature, before recordings were made.

### 2.3 Whole-cell patch-clamp recordings & electrical synaptic stimulation

LSO neurons were patched under a Nikon FN1 upright microscope (Nikon GmbH, Düsseldorf, Germany), equipped with a 4x (Nikon, Plan 4x/0.10 ∞/- WD 40) and 60x (Nikon NIR Apo 60x/1.0W DIC N2 ∞/0 WD2.8) objective. The bath was perfused with ACSF at a rate of ~1ml/min, and the temperature was maintained at 35-37°C using a TC07 temperature controller (Luigs&Neumann, Ratingen, Germany). Data acquisition was performed using a Heka EPC 10 double amplifier (Heka, Lambrecht, Germany) at sampling frequencies of 20-100 kHz with PatchMaster (Heka, version, v2x90.3) software run on Fujitsu Esprimo P95894+ computer (Fujitsu, Minato, Japan) with Windows 10 operating system. The LSO was

identified by its bean-like structure in the ventral brainstem (Fig.3.1 A<sup>2</sup>, Friauf et al., 2019) and LSO principal neurons were identified by their spindle-shaped soma. Patch pipettes were pulled from borosilicate glass (GB 150F-8P; Science products, Hofheim am Taunus, Germany) with a horizontal puller (P-1000 micropipette puller, Sutter instruments, Novato, USA). The patch pipettes had a resistance of 0.8-4.5 M $\Omega$  when filled with an internal solution containing (in mM): 10 HEPES, 5 EGTA, 1 MgCl<sub>2</sub>, 140 K-Gluconate (pH 7.2). A SM10 micromanipulator (Luigs&Neumann) was used to control the patch pipette. Liquid junction potential of 15.4 mV was corrected online, and offset potentials were corrected. Successfully patched LSO neurons were identified as principal neuron by fast membrane kinetics, voltage sag in response to hyperpolarizing current injection, and short-latency APs at rheobase and distinguished from LOC neurons (Sternborg et al., 2010; Maraslioglu-Sperber et al., 2024). Voltage-clamp (VC) recordings were low-pass filtered by a 2.9 kHz Bessel filter. Series resistance ( $R_s < 17$  M $\Omega$ ; determined by a 200-ms hyperpolarization from -70 mV to -72 mV) was compensated by 60-70 % online. CC recordings were 100 % bridge-balanced and recorded at a sampling frequency of 100 kHz (not filtered online). A 4x micrograph was taken for analysis of the recording position, after terminating the recording. The location of the neurons within the LSO was determined from 4x micrograph. To this end, the tip of the recording electrode was orthogonally traced to the midline of the LSO, and its position calculated along the LSOs tonotopic axis (medial = 0 %, lateral = 100; Fig.3.3 F). This analysis was performed by tracing the tonotopic axis in Corel Draw (2021, version 23.1.0.389, Ottawa, ON, Canada).

### 2.3.1 Passive and active membrane properties

A set of VC and CC protocols were applied on each recorded neuron before starting with specific experiments. These were used to ensure recording quality and characterize the passive and active membrane properties of the neurons. Data analysis was performed by custom IgorPro 9 scripts (latest version: 9.0.5.1, WaveMetrics Inc., Lake Oswego, OR, USA). The VC protocol to determine  $R_s$  is mentioned above. All CC recordings were filtered with a 10 kHz low-pass filter prior to analysis, unless otherwise specified.

#### 2.3.1.1 Recording and analysis of $V_{rest}$ , $R_{in}$ , $\tau_{mem}$ , and $C_{mem}$

In CC, 40 repeats of a 50-ms depolarizing current step (10-pA or 20-pA) were applied to determine the resting membrane potential ( $V_{rest}$ ),  $R_{in}$ , the  $\tau_{mem}$ , and the membrane capacitance ( $C_{mem}$ ).  $V_{rest}$  values were determined as the mean  $V_{mem}$  of a 10-ms phase preceding the current step. The amplitude of the peak depolarization was used to calculate  $R_{in}$ , according to Ohm's law. An exponential fit from the start depolarization to the peak depolarization was used to

determine  $\tau_{mem}$ . Fig.3.3 A illustrates these analyses.  $C_{mem}$  was calculated by the relation

$$C_{mem} = \frac{\tau_{mem}}{R_{in}}.$$

### 2.3.1.2 Recording and analysis of sag amplitude, rheobase, and firing pattern

A second CC protocol included current step stimulations of -200 pA to 1.5 nA in 50-pA steps, resulting in 35 steps (200 ms duration). The -100-pA stimulation was used to determine the sag amplitude. This was determined as the difference between the peak hyperpolarization and the steady state hyperpolarization (last 10 ms of stimulation; cf. Fig.3.3 J). APs were detected by  $V_{mem}$  crossing -30 mV. The rheobase was defined as the current step amplitude at which the first AP was elicited. The AP latency was determined by the peak location.

### 2.3.1.3 Recording and analysis of membrane resonance properties

A sinusoidal current with exponentially increasing frequency (ZAP-current; 2.5 to 2000 Hz over 60 s) was used to analyze membrane resonance properties. A subthreshold current amplitude was used for stimulation (200-400 pA, cf. Fig.3.4). Membrane impedance (Z) was calculated on cycle-by-cycle basis (difference between peak de- and hyperpolarization divided by the current amplitudes) as this resulted in less noise compared to an analysis in the frequency domain. The instantaneous Z ( $Z_{inst}$ ) was defined as the Z, average across the first three cycles. The impedance was smoothed by a moving average (five points) across cycles, and the resonant Z ( $Z_{res}$ ) was the maximal Z. The frequency at which this maximum occurred was defined as the resonance frequency ( $f_{res}$ ). The Q factor resulted from the division of  $Z_{res}$  by  $Z_{inst}$ .

### 2.3.1.4 Correlation analysis

A correlation analysis of the active and passive membrane properties was performed in Microsoft excel (version: 2105, Microsoft Corporation, Redmond, WA, USA). The Pearson correlation coefficient ( $\rho$ ) was calculated by a build-in function and the standard error (SE) and the t statistic, used to determine the p value, were calculated as follows:

$$SE = \sqrt{\frac{1 - \rho^2}{n - 2}}; \quad t = \frac{\rho * \sqrt{n - 2}}{\sqrt{1 - \rho^2}} \quad (1)$$

The t value was then used to extract the p value with a build-in function in Microsoft excel. The membrane resonance properties were employed for a correlation analysis in the same way.

### 2.3.1.5 Recording and analysis of slope-dependent AP initiation

Sinusoidal current stimulations of a single cycle were used to analyze the slope-dependent AP initiation. The sinusoidal current was in form of a raised sine, and modulation frequencies ( $F_{mod}$ ) of 5-2000 Hz were tested:

$$I(t) = A * (\sin(2\pi F_{mod} * t) + 1) \quad (2)$$

With  $A$  describing the amplitude of the sinusoid. The amplitude varied for each  $F_{mod}$  between 0.1 nA and 3 nA, in 0.1 nA steps (30 steps in total), resulting in 270 combinations (9 x 30). The presentation of these combinations was randomized for each neuron. The recording was accepted for analysis if the  $R_{in}$  (determined in CC) changed by less than 30 % throughout the time course of the experiment, and  $R_s$  was below 16 M $\Omega$  and changed by less than 25 %. The minimal current amplitude at a given  $F_{mod}$ , at which an AP was triggered, was considered the current threshold ( $I_{thr}$ ). The frequency dependency of this  $I_{thr}$  was further analyzed by the preferred frequency ( $F_{pref}$ ) and the bandwidth 3 dB above threshold (bandwidth<sub>3dB</sub>). The  $F_{pref}$  is the frequency at which  $I_{thr}$  was lowest, or the geometric mean, if two  $F_{mod}$ s had the same  $I_{thr}$  (Fig.2.1).

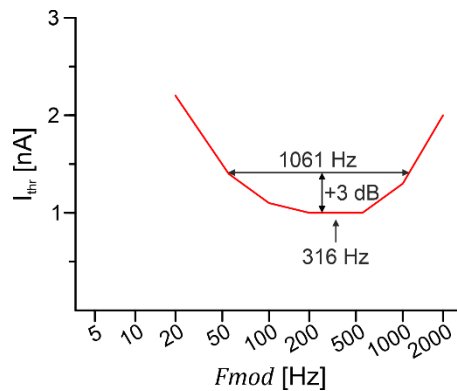
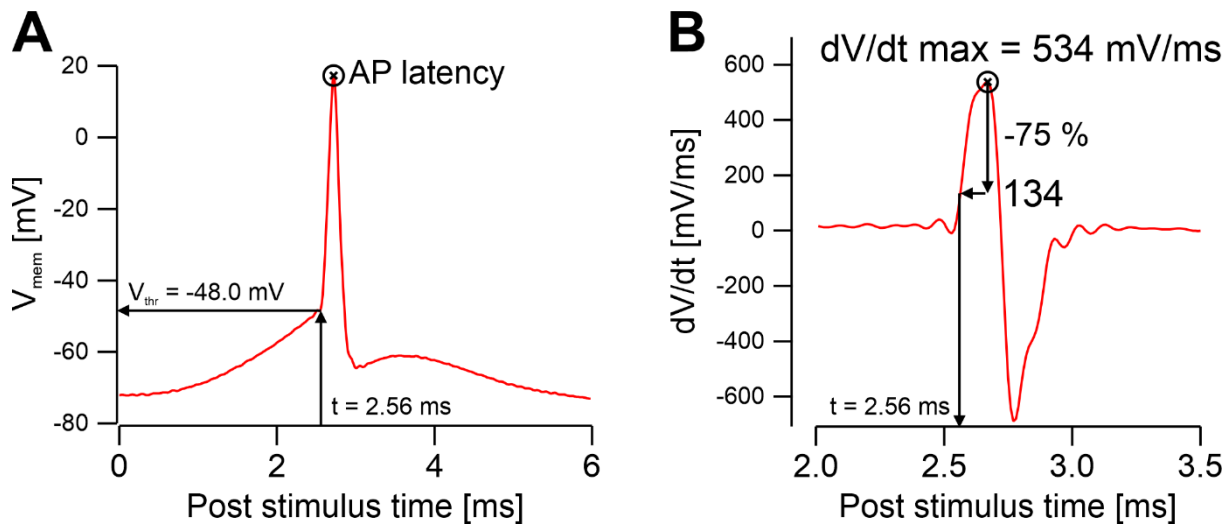


Figure 2.1 Analysis of the frequency-dependent  $I_{thr}$ .

The  $I_{thr}$  as a function of  $F_{mod}$  of an exemplary neuron. The  $F_{pref}$  was the geometric mean of 200 Hz and 500 Hz (316 Hz), and the bandwidth<sub>3dB</sub> was 1061 Hz.

### 2.3.1.6 Analysis of AP characteristics

To extract the voltage threshold ( $V_{thr}$ ) of the APs, the first derivative of  $V_{mem}$  was used. Starting from the AP latency, the signal was searched backward in time, and the point at which the derivative reached 25 % of its maximum amplitude was determined. The corresponding  $V_{mem}$  value at this time point was defined as the  $V_{thr}$  (Fig.2.2). The rate of current presentation was extracted from the peak of its first derivative. Phase-plane plots were created from the  $V_{mem}$  without prior filtering, and the number of phases was visually identified



**Figure 2.2 Analysis of AP characteristics.**

**(A)** Time course of an AP. APs were detected by crossing a -30-mV threshold. The AP latency was calculated from the peak position. The  $V_{thr}$  was extracted from the x-position of 25 % of the peak of the first derivative **(B)**.

**(B)** The first derivative of  $V_{mem}$ , illustrating the extraction of the time point of the  $V_{thr}$ .

The relation of the  $V_{thr}$  with the max rate of current (current slope) was evaluated by sigmoid fitting, using OriginLab's build-in Boltzman fit (Origin2018G, version b9.5.0.193, OriginLab Corporation, Northampton, MA, USA). The amplitude values were further used as  $V_{thr,1}$  and  $V_{thr,2}$ , for the more positive and more negative amplitude, respectively.

### 2.3.2 Synaptic stimulations and recordings of excitatory postsynaptic currents

Evoked excitatory postsynaptic currents (eEPSCs) were recorded at a membrane potential ( $V_{mem}$ ) of -70 mV and isolated from inhibitory postsynaptic currents (IPSCs) by applying 1  $\mu$ M strychnine (Sigma-Aldrich, St. Louis, MO, USA). A subset of experiments was performed by adding QX-314 (5 mM, Sigma Aldrich) to the internal solution. A stimulation electrode (~10  $\mu$ m tip) was placed on the slice just medial to the 7<sup>th</sup> nerve stump to stimulate the fibers in the ventral acoustic stria (VAS, Fig.3.1 A<sup>1</sup>-A<sup>2</sup>). Electrical stimulation was generated by a stimulus isolator (STG 4002, Multi-Channel Systems, Reutlingen, Germany) at 0.5 Hz. Stimulation pulses had a duration of 100  $\mu$ s and were gradually increased by 5  $\mu$ A every 10 stimuli, up to 300  $\mu$ A, and by 10  $\mu$ A every five stimuli from 300-1200  $\mu$ A. Recordings were terminated if the  $R_{in}$  changed more than 30 % (determined by 200-ms hyperpolarization from -70 mV to -72 mV, just before every synaptic stimulation), or if the stimulus directly activated the neuron, as indicated by a fast inward current that occurred immediately after the stimulation artifact.

Peak eEPSC amplitudes were analyzed with custom IgorPro 9 routines (including a subset from Dr. A. U. Fischer and mafPC, a courtesy of Dr. M. A. Xu-Friedman) and were used for

k-means-based cluster analysis (Dr D. J. Weingarten, Univ. Kaiserslautern) in MatLab (MathWorks, Natick, MA, USA). For a detailed description of the cluster analysis, see (Müller, Sonntag, et al., 2019). eEPSC kinetics of minimal stimulation were determined by means of the decay time constant ( $\tau_{decay}$ ) of a single exponential fit and averaged across the first ten eEPSCs for each neuron. To generate synaptic conductance templates (alias synaptic kernels), the graphical average of the first ten rise<sub>50</sub> aligned eEPSCs was fit by a bi-exponential function (Nielsen et al., 2004):

$$y = A_{rise} * \left(1 - e^{\frac{-x-xc}{\tau_{rise}}}\right)^n * A_{decay} * e^{\frac{-x-xc}{\tau_{decay}}} \quad (3)$$

with  $A_{rise}$  and  $A_{decay}$  being the peaks of the two exponential functions and  $xc$  the  $x$  value of the peaks.  $n$  describes a scaling factor.  $\tau_{rise}$  and  $\tau_{decay}$  describing the time constants of the rising and decaying functions, respectively.

## 2.4 Dynamic-clamp stimulations

The DC is an extension of the CC configuration that allows the application of artificial conductance, and thereby stimulating neurons with simulated synaptic conductances (Robinson & Kawai, 1993; Sharp et al., 1993; Prinz et al., 2004). All DC experiments have been performed with the setup that I established in my master's thesis (Fisch, 2021), and the DC system is adapted from Yang et al. (2015). I simulated excitatory synaptic conductances and inhibitory synaptic conductances to analyze feed-forward excitatory synaptic integration, in conjunction with feed-forward inhibitory synaptic integration in LSO neurons (see below). The artificial synaptic current (dynamic-clamp current ( $I_{DC}$ )) is calculated as follows:

$$I_{DC} = G_{exc} * (V_{mem} - E_{exc}) + G_{inh} * (V_{mem} - E_{inh}) \quad (4)$$

Where  $V_{mem}$  is the membrane potential of the neuron,  $G_{exc}$  and  $G_{inh}$  are the excitatory and inhibitory synaptic conductances, respectively.  $E_{exc}$  and  $E_{inh}$  are the associated reversal potentials and were set to 0 mV ( $E_{exc}$ ) and -85 mV ( $E_{inh}$ ). The latter was chosen as the glycine reversal potential in LSO neurons is approximately -82 mV at P11 (Ehrlich et al., 1999). Predetermined conductances were read by the Heka EPC10/2 amplifier and sent to a separate computer (Fujitsu Esprimo P958/94+ computer) via a National Instruments 6321 PCIe card (National Instruments Corporation, Austin, TX, USA). The current was calculated in real-time in IgorPro 9 running mafPC, generously provided by Dr. Matthew Xu-Friedman (<https://www.xufriedman.org/mafpc>). A detailed description of the DC setup can be found in my master's thesis (Fisch, 2021).

The DC recordings were performed at a sampling rate of 100 kHz. However, the update rate of the  $I_{DC}$  is inevitably lower. The update rate was tested by running the “testmode” in mafPC, for presenting only a  $G_{exc}$  and for presenting a  $G_{exc}$  along with  $G_{inh}$  (Yang et al., 2015). The fast Fourier transformation (FFT) of these signals is displayed in Fig.2.3 A&B, and the update rates were determined as the peaks of the FFT, which were 28.0 kHz and 17.3 kHz, for the two settings, respectively.

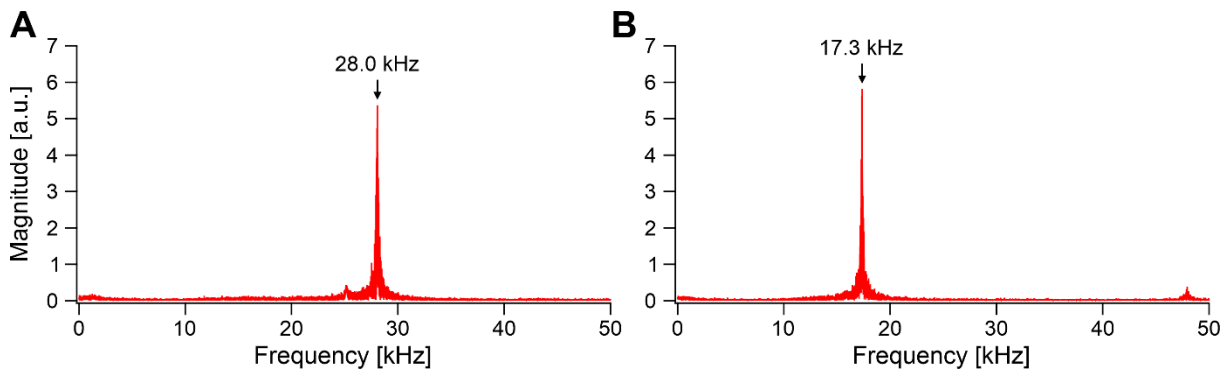


**Figure 2.3 Update rate of the  $I_{DC}$ .**

**(A)** A fast Fourier transformation (FFT) of a single presentation of the “testrun” of mafPC with only a  $G_{exc}$  activated. The peak of the FFT can be used to estimate the update rate of the DC interface (28.0 kHz).

**(B)** Same as **A**, but with a  $G_{exc}$  and a  $G_{inh}$  activated.

The DC experiments were performed under blockers for glutamatergic excitatory synaptic transmission (10  $\mu$ M, CNQX, Abcam, Cambridge, UK) and glycinergic inhibitory synaptic transmission (1 $\mu$ M, strychnine). For DC recordings, patch pipettes with a  $R_{pip} < 3.5$  M $\Omega$  were used, and recordings were restricted to  $R_s < 17$  M $\Omega$  and less than 25 % change in  $R_s$  and less than 30 % in  $R_{in}$ , throughout the experiment. The  $R_{in}$  was monitored using the same protocol mentioned earlier (40 repeats of a 50-ms, 10- or 20-pA step current stimulation). All DC recordings were 100 % bridge-balanced and a low-frequency VC was used to set the  $V_{mem}$  to -60 mV (update rate  $\sim$ 1 Hz), as a close approximation of the  $V_{mem}$  of LSO neurons recorded *in vivo* (Franken et al., 2021), and to maintain the same driving force for synaptic conductances across experiments.

Occasionally, the DC interface produced stimulation errors ( $< 1$  % of stimulations), due to interruptions by the operating system. These were detected semi-automatically by the sum of squared residuals of the recorded  $I_{DC}$  and the theoretical  $I_{DC}$ , as per equation (4). The distribution of these was used to detect stimulation errors. These recordings were restricted from further analysis.

In DC experiments, where the conductance stimulations are large, recording and stimulating through the same electrode can cause large errors in the current presented and lead to oscillations in the recorded  $V_{mem}$ . To circumvent this limitation, a subset of experiments was

performed by dual patch-clamp experiments. Here, a neuron was patched with two patch-pipettes, allowing it to record  $V_{\text{mem}}$  with one electrode (also monitored by the DC interface) and apply the currents with the second electrode (Yang et al., 2015). For these experiments, I used electrodes with  $R_{\text{pip}} < 5 \text{ M}\Omega$ . The  $R_{\text{in}}$  was monitored throughout the experiment in the same way as for single-electrode DC experiments. To successfully patch neurons with two electrodes, I first performed a giga seal with both electrodes before breaking through the membrane. Two-electrode DC experiments were performed in experiments of Fig.3.8, Fig.3.20 and Fig.3.21/3.22.

## 2.5 Modelling synaptic conductances of mimicked auditory activity.

I used a model to create artificial input AP timings, to simulate the activity of BCs and MNTB neurons. These were then used to generate synaptic conductances of the innervating pathway for DC stimulations. The model is adapted from Rothman et al. (1993).

In a first step an inhomogeneous Poisson process was used to model the AP timings of the synthetic input. The probability of an AP occurring at a given timing is determined by two interacting components: a stimulus function and a refractory function (Fig.2.4).

The stimulus function models the AP dynamics of the BCs and MNTB neurons to tonal stimulations, such as PL firing behavior or sinusoidal activity in form of phase locking to a SAM stimulation. The refractory function accounts for the refractory period after an AP was initiated, preventing APs from occurring too closely together and ensuring realistic inter AP intervals. The product of the stimulus and refractory functions is integrated until the integral reaches a random variable drawn from a standard exponential distribution. The ordinary differential equations were solved by IgorPro 9's build-in fifth order Runge-Kutta-Fehlberg integration with a step size of  $10 \mu\text{s}$ . Together, these components regulated the AP generation process, allowing the model to produce AP trains that resemble *in vivo* AP recordings of BCs and MNTB in response to auditory stimulations (Fig.2.4). The model was implemented in IgorPro 9 and the scripts to create artificial AP timings are available in the supplementary information in digital format ("Input AP timing model", IgorPro 9 file). Furthermore, all DC stimulation files are available in the digital supplements.

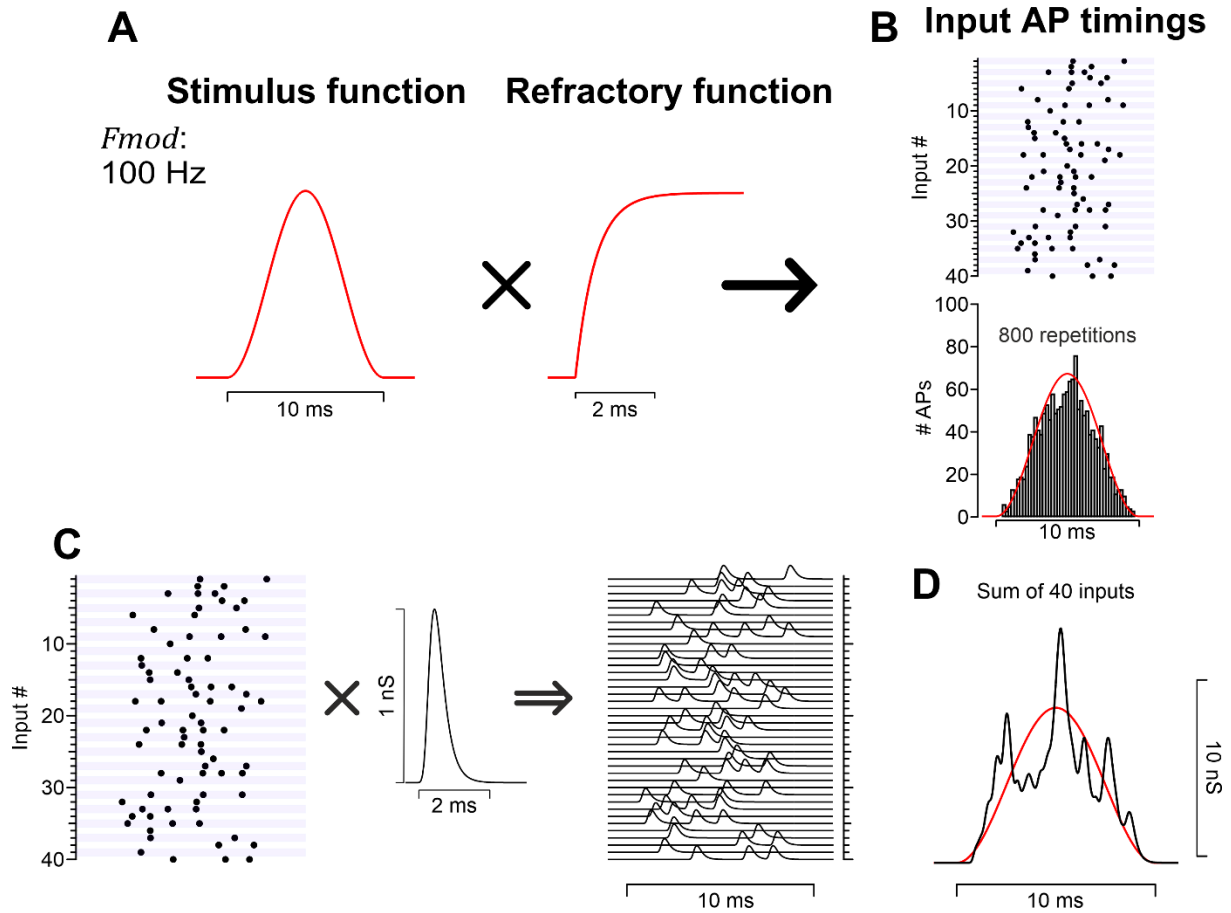


**Figure 2.4 Model procedure to generate synaptic conductances.**

**(A)** Two functions regulated the generation of input AP timings: a stimulus function and a refractory function. These are used in an inhomogeneous Poisson process to generate the Input AP timings. The stimulus function was adapted depending on the experiment, and consisted of PL functions, sinusoidal functions or pulsed-sinusoidal functions.

**(B)** AP timings follow the stimulus function (here, a single cycle sinusoid) and the inter AP intervals are constrained by the refractory function. The histogram of 800 repetitions depicts how AP timings resemble the stimulus function.

**(C)** AP timings are used in conjunction with a unitary synaptic conductance to be convolved into time-varying synaptic conductances for each of the modeled synaptic inputs.

**(D)** Summing the individual inputs, leads to the synaptic conductance used for stimulations.

### 2.5.1 Refractory function

The refractory function follows the equation:

$$R(t) = 1 - \frac{1}{\left(1 + e^{\frac{f \cdot 10 \cdot (t - (t_{AP,n-1} + t_d))}{0.001}}\right)^{\frac{1}{100}}} \quad (5)$$

Where  $f$  is the mean AP frequency, which was varied to fit the target rates (50-500 Hz).  $t_{spike,n-1}$  is the AP time of the  $n^{th}-1$  AP, and  $t_d$  is an absolute refractory period of 0.7 ms. Therefore, the

function consisted of two components, an absolute refractory period of 0.7 ms and a relative refractory period.

### 2.5.2 Stimulus functions

The stimulus function controlled the temporal dynamics of AP occurrence. A PL function ( $P(t)$ ) was used to model AP firing behavior in response to pure tones of BCs and MNTB neurons:

$$P(t) = \begin{cases} \left(1 - e^{-\frac{t-t_{on}}{\tau_q}}\right) * \left(R_r * e^{-\frac{t-t_{on}}{\tau_r}} + R_{st} * e^{-\frac{t-t_{on}}{\tau_{st}}} + R_{ss}\right) & , \text{if } t_{on} \leq t \leq t_{off} \\ 0 & , \text{otherwise} \end{cases} \quad (6)$$

Where  $R_x$  are rate constants and  $\tau_x$  are time constants.  $t_{on}$  and  $t_{off}$  describe the onset and offset of stimulations, and were set to  $t_{on} = 0.05$  s,  $t_{off} = 0.25$  s, respectively. Thus, the stimulus duration was 200 ms.  $R_{ss}$  was varied to simulate level-dependent rate coding in the sustained part of the stimulus (last 190 ms of the stimulus). The values for  $R_{ss}$  and the resulting average AP frequencies can be found in supplementary tables (Table S.1 & Table S.2). The remaining parameters were kept constant:  $\tau_q = 0.2$  ms;  $\tau_r = 3$  ms;  $\tau_{st} = 10$  ms;  $R_r = 600$ ;  $R_{st} = 200$ .

The sinusoidal function ( $S(t)$ ) is set up to allow for different sinusoidal modulations ( $F_{mod}$ ), to repeat either at  $F_{mod}$  or at a lower rate, denoted as pulse frequency ( $F_{pulse} = N * F_{mod}$ ;  $\{N = 1, 2, 3, \dots\}$ ). This is realized by a cosine function and a gating condition, which is written as follows:

$$S(t) = \begin{cases} \left(1 - \cos(2\pi * (t * F_{env} - \Delta\varphi))\right) * \frac{A_{sin}}{2} & , \text{if } t_{on} \leq t \leq t_{off} \wedge \text{mod}\left(t - \frac{\Delta\varphi}{F_{mod}}, \frac{1}{F_{pulse}}\right) \leq \frac{1}{F_{env}} \\ 0 & , \text{otherwise} \end{cases} \quad (7)$$

where  $\Delta\varphi$  describes a phase shift in multiples of the envelope phase duration, thus  $t = \Delta\varphi * \frac{1}{f_{env}}$ , and  $A_{sin}$  is the amplitude that controls the rate at which the synthetic input is activated (100-500 Hz; Table S.3, Table S.4 & Table S.5). Reducing  $t_{off}$  to  $\frac{1}{F_{mod}}$  allows to model single cycle sinusoids as presented in Fig.3.8. In this experiment, the synaptic model stimulations and the sinusoidal conductance stimulations were scaled to match in their integral. To this end, the integral of the unitary EPSP was multiplied by the theoretical number of APs

occurring in a single cycle  $\left(\frac{f_{exc}}{F_{mod}} * number\ inputs\right)$  and the sinusoidal conductance was scaled to match this number.

### 2.5.3 Convolution into time-varying synaptic conductances

The next process involves convolving the input AP timings with the predefined synaptic templates, i.e., a synaptic template is positioned at each input AP timing to produce a time-varying synaptic conductance (Fig.2.4 C). The templates are provided in the digital supplementary file (“Input AP timing model”, IgorPro 9 file). This process is repeated for the number of inputs, and the resulting conductances are summed to yield the total synaptic conductance used for DC stimulation. This process is performed separately for excitation ( $G_{exc}$ ) and inhibition ( $G_{inh}$ ). To analyze the effect of different  $SW$ , I maintained the  $cSW$  across different stimulation constant (i.e., 40 nS for excitation and 32 nS for inhibition) but distributed it across different number of converging inputs. To model a more naturalistic  $SW_{exc}$  distribution, the  $SW_{exc}$  of 40 inputs were drawn from a gamma distribution, with  $\alpha = 0.6$ ,  $\beta = 1$ . If the drawn value was below 0.3 nS/input, it was rejected and a new one drawn. 0.3 nS/input was chosen as lower limitation as it calculates to a current that reflects about the quantal size of excitatory synaptic transmission (at  $V_{hold}$  of -70 mV and  $E_{exc}$  of 8 mV:  $0.3\ nS * (-70\ mV - 8\ mV) \approx -23\ pA$ ). The drawn  $SW_{exc}$  resulted in a mean  $\pm$  SD of  $1.0 \pm 0.7$  nS/input (Fig.3.9).

The stimulations were 200 ms in duration, presented at 1 Hz (therefore, 800 ms interval in between stimulations), and repeated ten (or twenty) times for every stimulus configuration. To minimize possible time-dependent changes in the results of AP probabilities in LSO neurons, the configurations were presented in semi-random order, i.e., the presentation of the combinations was randomized across the repeats but maintained in the same order for each neuron.

## 2.6 Analysis of DC data

Analysis of the DC data was performed in IgorPro 9 and Microsoft Excel. The data were low pass filtered (10kHz cutoff) and analyzed for stimulation errors.

### 2.6.1 AP occurrence and AP rates

APs were detected by  $V_{mem}$  crossings of -30 mV. Peak AP latencies were extracted and further processed in Microsoft Excel. The occurrence of APs was calculated in different ways. In the single cycle sinusoidal stimulations (Fig.3.8), the entrainment was calculated, which describes if the stimulation was responded with APs or not, independent on the number of APs.

The AP timings in the PL stimulations were analyzed for the onset probability. Specifically, the probability of AP occurrence within the first 10 ms of stimulation was calculated (independent of the number of APs) and the mean across multiple (5-10) repeats was the onset probability. The AP rate of the remaining stimulus duration was calculated by dividing the number of APs by 0.19 s. I introduce the modulation index (MI) to quantify the effect of inhibition on the AP rate:

$$MI = \frac{R_{f_{inh}} - R_{f_{inh}=0} \text{ APs/s}}{R_{max}} \quad (8)$$

This normalizes the AP rate to the AP rate at  $f_{inh} = 0$  ( $R_{f_{inh}=0}$  APs/s) and allowed us to statistically assess both facilitation and suppression of the AP rate.

The AP rate in sinusoidal stimulations (Fig.3.16-Fig.22) are reported as the number of APs divided by the stimulus duration (0.2 s).

The -3 dB bandwidth was calculated for rate modulation transfer functions (rMTF), with the gain calculated as follow:

$$gain = 20 * \log\left(\frac{R}{R_{max}}\right) \quad (9)$$

Where  $R$  is the AP rate, and the  $R_{max}$  the maximal AP rate for a given stimulation configuration.

## 2.6.2 Temporal analysis of AP occurrence

The AP timings were used for temporal analyses, which were performed in IgorPro 9. The PL stimulations were subject to two temporal analyses. The 1<sup>st</sup> AP latency jitter was calculated as the standard deviation of the 1<sup>st</sup> AP's latency. The spike-triggered average (STA) of the 1<sup>st</sup> AP was constructed by aligning the 1<sup>st</sup> APs at the position of  $V_{thr}$  and averaging the  $V_{mem}$  across the number of repeats.

In the second analysis, I created shuffled auto correlograms (SACs) and extracted the correlation index (CI) according to (Joris et al., 2006). The SAC is constructed as the between repeats cross-correlation and is normalized by  $N(N - 1)R^2\omega D$ ;  $N$  was the number of repeats,  $R$  was the mean AP rate,  $\omega$  was the coincidence window (0.5 ms) and  $D$  was the stimulus duration (200 ms). The CI represented the correlation value at a delay of 0 ms.

Another metric of temporal coding is the vector strength (VS). The VS was only determined for sinusoidal stimulations as it relies on knowledge of the stimulus phase. The VS was calculated to create temporal modulation transfer functions (Goldberg & Brown, 1969):

$$VS = \frac{\sqrt{(\sum_n \cos(\alpha))^2 + (\sum_n \sin(\alpha))^2}}{n} \quad (10)$$

Where  $\alpha$  is the angular phase of the AP latency in regards to the stimulus phase, and  $n$  the number of APs. The VS was then used to compute Rayleigh statistics (RS, [Mardia & Jupp, 1999](#); [Sayles et al., 2013](#)):

$$RS = 2n * VS^2 \quad (11)$$

### 2.6.3 Stimulus separability

To estimate the influence of stimulus parameters on the AP rates of LSO neurons, I calculated the standard separation ([Sakitt, 1973](#)), and refer to it as 'separability'. The separability (D) calculates as follow:

$$D = \frac{|\bar{x}_{ref} - \bar{x}_{test}|}{\sqrt{\sigma_{ref} * \sigma_{test}}} \quad (12)$$

where,  $\bar{x}_{ref}$  and  $\bar{x}_{test}$  refer to the means of the reference and test condition, respectively, and  $\sigma_{ref}$  and  $\sigma_{test}$  to their corresponding standard deviations (performed in Microsoft excel).

To assess the influence of inhibition, the reference condition was always the AP rate at  $f_{inh} = 0$  APs/s, representing the condition of pure excitation. Test conditions were the AP rates, elicited at various  $f_{inh}$ .

Separability in the hemispheric rate difference model was calculated as described ([Müller et al., 2023](#)). In this case, the reference condition corresponded to the AP rate at  $\Delta t_n$ , and the test conditions to the AP rate at  $\Delta t_{n+1}$ . The resulting separability values were smoothed by a triangular weighted average with a fixed kernel of  $[\frac{12}{41}, \frac{17}{41}, \frac{12}{41}]$ , and no boundary conditions at the edges.

## 2.7 Analysis of *in vivo* data

A cooperation with the laboratory of Dr. Conny Kopp-Scheinpflug (Devison of Neurobiology, Faculty of Biology, Ludwig-Maximilians-University Munich, Germany) was initiated and *in vivo* recordings were performed by Luna Studer. For full methodological details on the recording procedure, please see ([Stancu et al., 2024](#)). This section focuses on the stimuli and analysis of the *in vivo* data, as performed by me. Amplitude-modulated pulsed-sine tone followed equation (7) and had a duration of 400 ms. Pure-tone stimulations were presented with a 5 ms

linear ramped on- and offset (stimulus duration 100 ms). Auditory stimuli were presented through hollow ear bars to anaesthetized C56/BL6J mice, with an inter-stimulus interval of 450 ms. Neurons located in the superior olivary complex that responded with an increase in AP activity to ipsilateral sound stimulations and a decrease in AP activity to contralateral sound stimulations, were considered LSO neurons. They provided the data of recorded AP timings from these tentative LSO neurons (Fig.3.24-Fig.3.27), which I used for further analysis. The data was imported to IgorPro 9 and rate and temporal analysis was performed as described for the DC data. The AP rates were determined within the stimulation period for each ILD and the resulting ILD functions were fitted with a build-in sigmoid fit in IgorPro 9:

$$Sigmoid(x) = \frac{A}{1 + \exp\left(\frac{ILD_{50} - x}{k}\right)} \quad (13)$$

where A is the amplitude of the sigmoid function,  $ILD_{50}$  the midpoint of the sigmoid and k is a slope parameter. The dynamic range was defined as the difference in ILD values at which the sigmoid reached 95 % and 5 % of A.

The temporal analysis of AP occurrences was performed as described above, while the CI is referred to as reproducibility, in accordance with (Müller, Sonntag, et al., 2019) and to differentiate it from the *in vitro* data. Furthermore, the modulation depth was extracted from the SACs, as the difference in correlation at delay of 0 ms and a delay of half a cycle of  $F_{pulse}$ .

## 2.8 Statistics

Statistics were applied in Microsoft Excel and IgorPro 9. Data was tested for normality by a Kolmogorov-Smirnov test, and normal distribution was accepted if  $p > 0.05$ . For datasets that consisted of multiple stimulus condition, normality was assessed for each condition, and the data were considered normally distributed if more than 95 % of the conditions met the criteria for normality. Otherwise, a non-normal distribution was assumed. This approach avoids mixing different statistical tests within a dataset and represents a conservative decision criterion. In case of normal distribution, the mean  $\pm$  SD is presented in the figures, while non-normal distributed data is displayed as median  $\pm$  median absolute deviation of the median (MAD). Details on the descriptive statistics and the statistical tests applied are provided in the figure legends. Significances are indicated as: \* ( $p < 0.05$ ); \*\* ( $p < 0.01$ ); \*\*\* ( $p < 0.001$ ), and n.s. ( $p \geq 0.05$ ). Critical  $\alpha$  levels were post hoc corrected (Bonferroni correction) for multiple comparisons, and the critical level surpassed is indicated in the figure legends or the accompanying supplementary tables.

Data in the frequency domain (e.g.: Fig.3.6 E&F) was averaged by the geometric mean. Specifically, the mean and SD were calculated on ln-transformed data and then back-transformed for presentation.

## 2.9 Data visualization

Data was visualized in IgorPro 9 and in OriginLab and further processed in CorelDraw 2021 (version: 23.1.0.389, Corel Corporation, Ottawa, ON, Canada).

## 2.10 Writing

Parts of the manuscript were refined with the assistance of writing tools (Microsoft Copilot Pro (in Microsoft Word version 2504), ChatGPT (version: GPT-4o, OpenAI, San Francisco, CA, USA), and Grammarly (version 14.1232.0, Grammarly Inc., San Francisco, CA, USA)) to improve grammar, clarity, and conciseness. All scientific content and interpretations were developed by me. An early draft of this manuscript was proofread by my supervisor Dr. Eckhard Friauf.

## 3 Results

### 3.1 Synaptic characteristics of excitatory and inhibitory synaptic inputs to LSO neurons

The strength and time course of synaptic inputs are major determinants for temporal and spatial synaptic integration, and majorly influence synaptic noise (Campbell, 1909; Silver, 2010). Therefore, the first experiment was designed to determine three synaptic characteristics: the  $cSW$ , the contribution of unitary synaptic input to the total synaptic strength (the  $SW_{exc}$ ), and the kinetics of synaptic inputs. The synaptic current was later used to create a template for DC experiments.

LSO neurons were patch-clamped and recorded in VC to record synaptic currents. A stimulation electrode was placed on the VAS to evoke EPSCs from BCs in the AVCN (Fig.3.1 A<sup>1</sup>&A<sup>2</sup>). The stimulation protocol was identical to the one determining synaptic characteristics of eIPSCs in LSO neurons from a prior study (Fig.3.1 B, Müller, Sonntag, et al., 2019, see methods for details).

Stimulation at low stimulus intensity typically elicited no eEPSCs in LSO neurons, as observed for the exemplary neuron for intensities up to 45  $\mu$ A (Fig.3.1 C&D). The first eEPSCs recorded (minimal eEPSCs) were small, often < 100 pA and increasing stimulation amplitudes resulted in an increase in the amplitude of the eEPSCs (Fig.3.1 C). Plotting the eEPSC amplitude against the stimulus intensity indicated increases of the eEPSC amplitudes with increasing stimulus intensity (Fig.3.1 D). A k-means-based cluster analysis enabled to assign individual eEPSC amplitudes to clusters, reflecting the recruitment of input fibers. This allowed me to determine the number of converging inputs and the amplitudes with which each input contributed to the compound eEPSC. In the exemplary neuron depicted in Fig.3.1 C&D, minimal stimulation elicited eEPSCs with a cluster mean of -79 pA, increasing to -267 pA after recruiting an additional fiber. The additional fiber thus contributed to the compound eEPSC by an amplitude of -188 pA. The neuron ran into direct stimulation after a stimulus intensity of 100  $\mu$ A, and thus, the recording was terminated (see Methods 2.3.2, Fig.3.1 D). Minimal eEPSCs were small in most neurons, with a mean of  $-94 \pm 12$  pA (Fig.3.1 E). At maximal stimulation, i.e., the stimulus intensity that elicited the largest eEPSC amplitudes, the eEPSC amplitudes increased to  $-292 \pm 72$  pA. Most neurons (13/15) did not exceed -500 pA, with only one neuron surpassing -1000 pA (Fig.3.1 E). This increase was caused by the recruitment of 1-4 fibers, and a total of 37 input fibers terminating onto 15 LSO neurons were found, resulting in a mean of  $2.5 \pm 0.9$  fibers per LSO neuron (Fig.3.1 F).

To evaluate the strength with which each input fiber drives excitatory currents in the LSO, the  $SW_{exc}$  was determined. To this end, I pooled the data from 37 inputs. The current

amplitudes were converted to a conductance amplitude by equation (4) with a  $V_{rev}$  of +8 mV (empirically determined  $V_{rev}$ , Fisch, 2021). The resulting  $SW_{exc}$ s were small with most values barely reaching 1.0 nS/input and only four  $SW_{exc}$ s reached values > 2.5 nS. The median  $SW_{exc}$  was 1.0 nS (mean: 1.5 nS), a value highly comparable with the estimates of 0.7 nS from Gjoni, Zenke, et al. (2018).

The brain slice methodology, in combination with electrical stimulation, sets inherent limitations to determine the total synaptic strength (cut axons during slice preparation or too long distance to the stimulation electrode). Thus, the number of recruited input fibers reported here arguably reflects the lower end of the range. Indeed, Gjoni, Zenke, et al. (2018) report a considerably higher number of convergences of ~10-40. I subsequently reassessed the compound eEPSC by including QX-314 in the patch pipette, blocking Nav channels and thereby increasing the voltage clamp. The minimal eEPSCs from these experiments are comparable with the first assessment (mean:  $-108 \pm 23$  pA compared to  $-94 \pm 12$  pA,  $p = 0.58$ , unpaired t-test). The maximal eEPSCs increased to values between -469 pA to -2313 pA (median: -731 pA). The data of eight neurons are shown in Fig.3.1 L. A linear increase in eEPSC amplitudes was observed across a broad range of stimulus intensities for all neurons. I avoided k-means clustering, due to its limitation in handling small steps across a large range. Notably, the linear increase was accompanied by single, distinct stepwise increase in half of the neurons (4/8, Fig.3.1 L). Assuming a  $SW_{exc}$  of 1 nS, the convergence ranges between 6 and 30 inputs (median: 9.4). These findings may still represent a conservative approximation of the number of converging inputs. Therefore, I followed the suggestion by Gjoni, Zenke, et al. (2018) and a convergence of 40 inputs, each with a  $SW_{exc}$  of 1 nS/input serves as the basis for the subsequent experiments. This relates to a  $cSW_{exc}$  of 40 nS.

In the next step, I analyzed the  $\tau_{decay}$  as a measure for synaptic kinetics. To this end, the first ten eEPSCs were averaged for each neuron, thus reflecting the kinetics of minimal stimulation. eEPSCs decayed rapid, with a  $\tau_{decay}$  of  $0.47 \pm 0.03$  ms (Fig.3.1 H). A neuron with slightly faster than mean kinetics ( $\tau_{decay} = 0.39$  ms) was chosen to serve as the source to create a conductance template. 30 minimal eEPSCs from the representative neuron were peak aligned, averaged and fitted with a biexponential function according to equation (3) ( $R^2 > 0.99$ ), resulting in the EPSC template for subsequent DC stimulations (Fig.3.1 I).

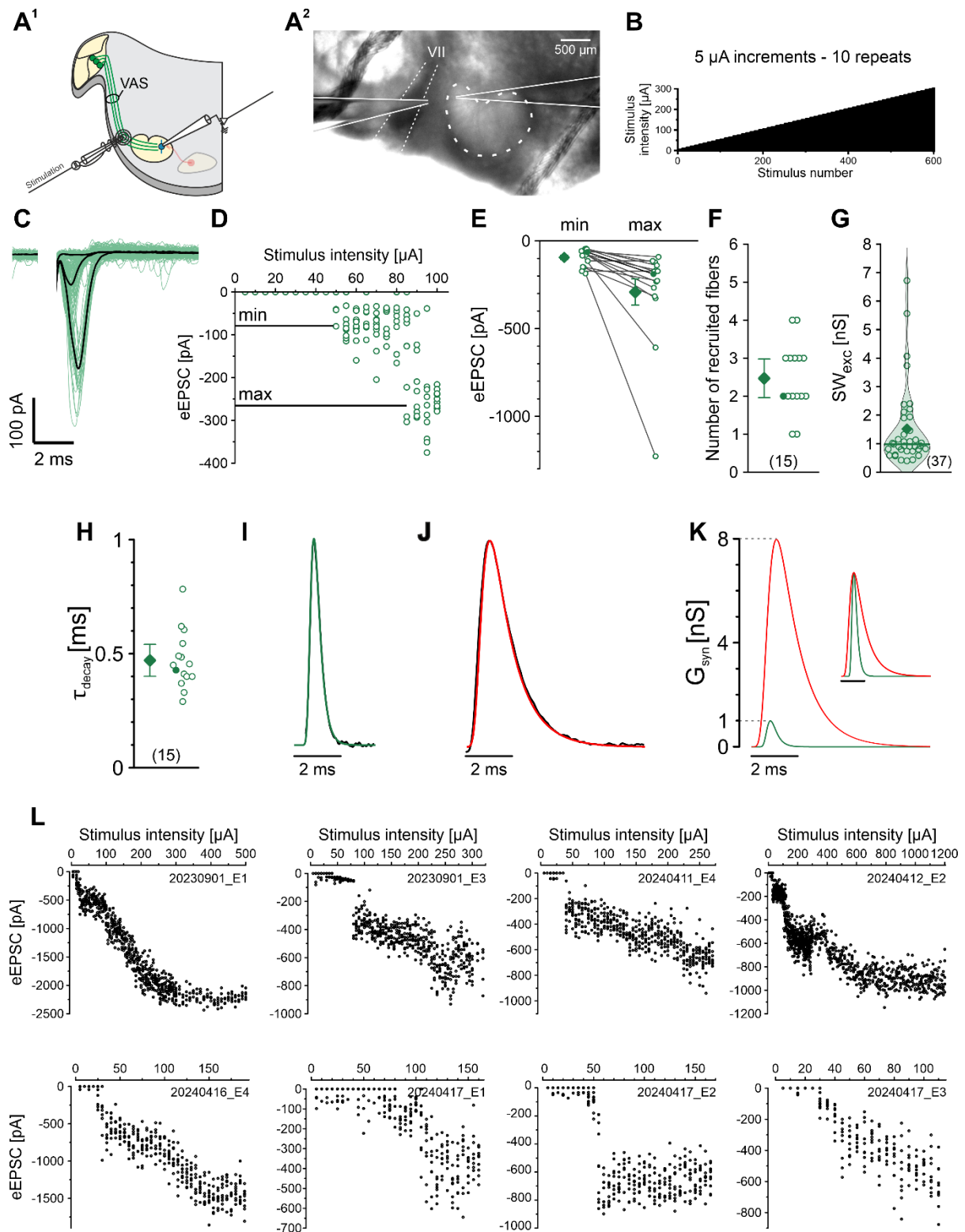


**Figure 3.1** Unitary excitatory inputs to LSO neurons have weak synaptic weights and fast kinetics.

**(A)** Voltage-clamp (VC) recording from an exemplary LSO neuron and synaptic stimulation of excitatory input fibers running in the ventral acoustic stria (VAS). **A<sup>1</sup>** is a schematic drawing, whereas **A<sup>2</sup>** is a photomicrograph. The stimulation electrode was positioned medially to the 7th nerve (**A<sup>2</sup>**).

**(B)** The stimulation intensity was increased in increments of 5  $\mu\text{A}$  following each ten repeats, up to a maximum of 600  $\mu\text{A}$ . In some cases, the intensity was increased further in increments of 10  $\mu\text{A}$  after

each ten repeats up to a maximum of 1200  $\mu$ A.

(C) Evoked excitatory post-synaptic currents (eEPSCs) from an exemplary neuron. Individual eEPSCs are shown as thin green lines, whereas black lines represent the mean of each cluster.

(D) eEPSC peak amplitudes as a function of the stimulation intensity (open dots) and the cumulative mean amplitude of each cluster (black lines). Same neuron as in C.

(E) Minimum and maximum eEPSC amplitudes (mean  $\pm$  SEM, green diamonds) for 15 neurons. The filled dots denote the data from the exemplary neuron from C and D. The same designation is used in F and H.

(F) Number of recruited input fibers calculated by cluster analysis.

(G) Excitatory synaptic weight ( $SW_{exc}$ ) of all recorded fibers ( $n = 37$ ; sum of F). Corresponding violin plot is superimposed.

(H) Same as F, but for the decay time constant ( $\tau_{decay}$ ).

(I) Minimal eEPSCs (black trace) from a neuron with slightly faster-than-average kinetics (filled dot in H;  $\tau_{decay} = 0.4$  ms) fitted with a two-exponential waveform function to generate the excitatory postsynaptic conductance (EPSC) with an arbitrary amplitude (green trace). The peak amplitude of the EPSC was set to fit the median  $SW_{exc}$  of 1 nS/input shown in G.

(J) Same as I, but for an evoked inhibitory postsynaptic current (eIPSC; black trace) and the corresponding IPSC template (red trace). The peak amplitude was set to 8 nS. Data were reanalyzed from Müller, Sonntag, et al. (2019).

(K) Overlay of EPSC and IPSC templates to illustrate the differences in  $SW$  and in kinetics. Inset shows peak-aligned templates to emphasize the differences in kinetics. These templates were used to generate synaptic conductances ( $G_{syn}$ ) of the excitatory inputs ( $G_{exc}$ ) and the inhibitory inputs ( $G_{inh}$ ).

(L) Same as D but for eight neurons, which were recorded with QX-314 in the patch pipette.

Panels A-K were presented in a similar form in my master thesis (Fisch, 2021).

To obtain a template for inhibitory MNTB-LSO synapses, data reported by Müller and colleagues was reexamined (Müller, Sonntag, et al., 2019). Again, minimal eIPSCs from a representative MNTB-LSO stimulation were peak aligned, averaged and fitted by a biexponential function (Fig.3.1 J). The fit results describe the eIPSC waveform very well with  $R^2 > 0.99$ . The  $SW_{inh}$  reported by Müller et al. is markedly higher than the excitatory one determined here ( $\sim 8$  nS vs. 1 nS, Fig.3.1 K) and shows slower kinetics ( $\tau_{decay} = 1.2$  ms). The authors report a 4:1 convergence of inhibitory input fibers onto LSO neurons, similar to Gjoni, Zenke, et al. (2018) ( $\sim 4-8$ ).

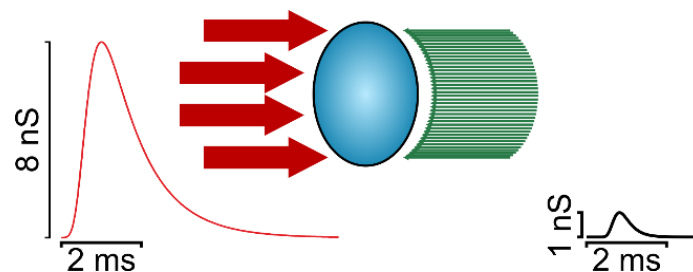


Figure 3.2 Estimated synaptic innervation onto LSO neurons.

This model summarizes the findings from Fig. 3.1 with few strong inhibitory inputs and 40 weak excitatory inputs converging onto an LSO neuron. The  $SW_{inh}$  is 8 nS/input and the  $SW_{exc}$  is 1 nS/input.

These results provided the basis for modeling the LSO circuit for DC stimulations. In conclusion, 40 excitatory inputs converge onto a given LSO neuron with a  $SW_{exc}$  of 1 nS/input. This is contrasted by a few strong inhibitory inputs, namely four inputs each with a  $SW_{inh}$  of 8 nS/input. The  $cSW_{exc}$  and  $cSW_{inh}$  are in a similar range with  $cSW_{exc} = 40$  nS and  $cSW_{inh} = 32$  nS (Fig.3.2).

## 3.2 Intrinsic electrophysiological properties shape stimulus response dynamics of LSO neurons

The intrinsic membrane properties of neurons dynamically shape the integration of synaptic inputs. Together they form the mechanisms that dictate the excitability of neurons and the kinetics of stimulus response dynamics. To this end, I characterized the intrinsic membrane properties of LSO neurons.

### 3.2.1 Resting membrane properties of LSO neurons

Neurons integrate the electrical charges transferred by synaptic transmission into changes in  $V_{mem}$ . The rate and magnitude of change are determined by passive and active membrane properties and thereby determine how incoming synaptic inputs are spatially and temporally integrated. The passive properties set the basis for synaptic integration and includes the  $R_{in}$  and the  $C_{mem}$  of a neuron, setting up the RC circuit. Together they determine the  $\tau_{mem}$ . These parameters were determined before every CC experiment offering a dataset of passive membrane properties of  $n = 106$  LSO neurons, recorded under physiological conditions.

To determine the resting membrane properties, a small current step stimulation (10 or 20 pA) was used and the resulting changes in  $V_{mem}$  analyzed to determine aforementioned parameters (Fig.3.3 A). The  $R_{in}$  of LSO neurons was low, spanning values of 21.7 – 94.7 M $\Omega$  (mean:  $46.3 \pm 18.1$  M $\Omega$ , median: 39.5 M $\Omega$ , Fig.3.3 B). The  $\tau_{mem}$  was fast, with a mean of  $1.5 \pm 0.7$  ms, and only three neurons displayed values above 3 ms (Fig.3.3 C). The  $C_{mem}$ , derived from the previous two measurements, yielded an average value of  $34.7 \pm 11.7$  pF. The violin plot indicates that most values lie within the range of 15 to 40 pF, with an additional distribution observed at ~50 pF (Fig.3.3 D). The  $V_{rest}$  also influences synaptic integration by influencing the increase in  $V_{mem}$  necessary to reach the AP threshold ( $V_{thr}$ ). The neurons showed a  $V_{rest}$  of  $-70.0 \pm 4.3$  mV (Fig.3.3 E), well in the reported range for auditory brainstem neurons.

Differences in membrane properties of LSO neurons along the tonotopic axis were reported for different species (rat: Barnes-Davies et al., 2004, guinea pig: Remme et al., 2014), and thus suggest differences between the synaptic integration of low-frequency and high-frequency coding LSO neurons. *In vivo* experiments and immunohistochemical analysis do not suggest such gradients in mouse LSO neurons, based on Kv.1.1 channels

(Karcz et al., 2011), but the hypothesis of the absence of tonotopic effects has so far not been tested in mice *in vitro*. To this end, I determined the tonotopic location of the recording site and performed a correlation analysis between the determined membrane properties ( $R_{in}$ ,  $\tau_{mem}$ ,  $C_{mem}$ , and  $V_{mem}$ ) and the recording site (Fig.3.3 F-H). Plotting the  $R_{in}$  as function of the tonotopic position reveals no linear correlation as indicative by a low Pearson correlation coefficient ( $\rho = -0.01$ ;  $p = 0.88$ ; Pearson correlation test; Fig.3.3 G). Neither of the remaining parameters showed a significant correlation, with  $\rho$ s of -0.04 for  $C_{mem}$  ( $p = 0.71$ ), -0.04 for  $\tau_{mem}$  ( $p = 0.70$ ) and -0.03 for  $V_{mem}$  ( $p = 0.73$ , Fig.3.3 H). This leads to the conclusion that mouse LSO neurons possess fast intrinsic membrane properties that are consistently set along the tonotopic axis.

Furthermore, correlation tests between  $V_{mem}$  and the remaining parameters showed a significant link with  $R_{in}$  and  $\tau_{mem}$ , but not with  $C_{mem}$  ( $\rho (V_{mem}, R_{in})$ : -0.59,  $p < 9e-15$ ;  $\rho (V_{mem}, \tau_{mem})$ : -0.55,  $p < 6e-12$ ;  $\rho (V_{mem}, C_{mem})$ : 0.02,  $p = 0.84$ ; Fig.3.3 I). Since  $C_{mem}$  is mainly determined by the neuron's membrane area, the absence of correlation was hypothesized. The dependency of the three parameters through  $\tau_{mem} = R_{in} * C_{mem}$  suggests a voltage-dependent influence on  $R_{in}$ , indicating low-threshold conductances like Kv1 and HCN channels. Given the proportional relationship between  $\tau_{mem}$  and  $R_{in}$ , the correlation between  $V_{rest}$  and  $\tau_{mem}$  may be accounted for by voltage-dependent changes of  $R_{in}$  (Fig.3.3 I).

LSO principal neurons are often characterized by an HCN channel-mediated current ( $I_h$ ) dependent voltage sag in response to hyperpolarizing current injections. An exemplary voltage sag evoked by a -100-pA current injection is shown in Fig.3.3 J, resulting in a sag amplitude of 2.5 mV. Across the population, the mean sag amplitude was 2.0 mV, with a median of 1.8 mV (Fig.3.3 K). Because of the constant stimulus amplitude, the ohmic relation leads to a bigger hyperpolarization for neurons with higher  $R_{in}$ s, which in turn may activate a larger  $I_h$ . A linear correlation between the sag amplitude and  $R_{in}$  is in line with this mechanism ( $\rho (sag, R_{in})$ : 0.79,  $p = 4e-24$ ; Fig.3.3 L). This relationship is accompanied by correlations between the sag amplitude and  $\tau_{mem}$  ( $\rho (sag, \tau_{mem})$ : 0.58,  $p = 6e-11$ ) and  $V_{mem}$  ( $\rho (sag, V_{mem})$ : -0.56,  $p = 4e-10$ ), but not with  $C_{mem}$  ( $\rho (sag, C_{mem})$ : -0.20,  $p = 0.04$ ; Fig.3.3 M). Moreover, no significant correlation was observed between sag amplitude and tonotopic position (Fig.3.3 M).

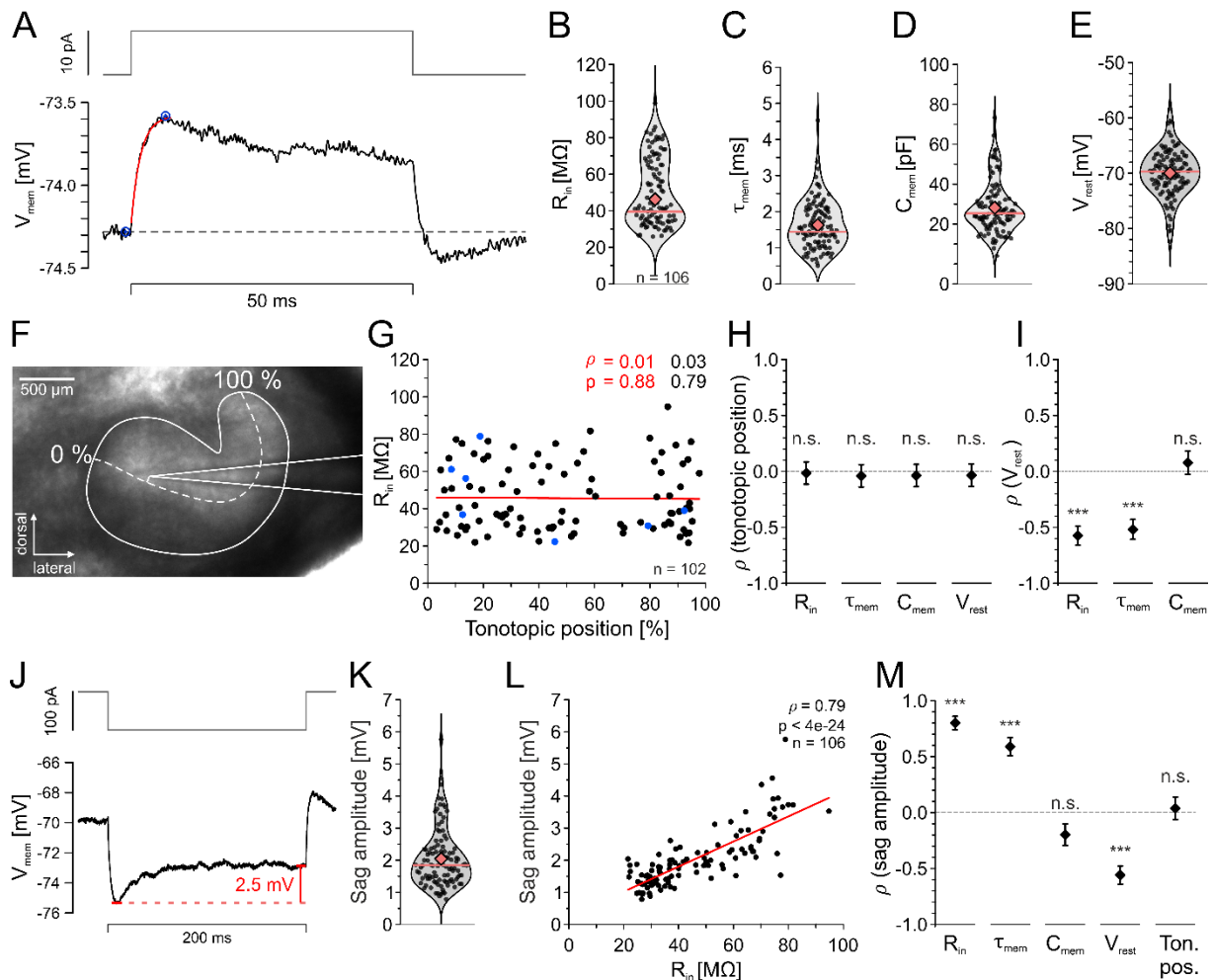


**Figure 3.3** Passive membrane properties are optimized for fast synaptic integration.

**(A)** Voltage deflection from rest (dotted line in lower trace) to a 10-pA current step stimulation (upper trace). Membrane potential ( $V_{mem}$ ) is the average over 40 repeats. The blue dots indicate the x- and y-positions used to calculate the input resistance ( $R_{in}$ ). The red line displays an exponential fit to the depolarizing phase of the voltage deflection.

**(B)**  $R_{in}$  of all neurons reported in this thesis as violin plot, including single cell data (black circles). The red diamond represents the mean, and the red line represents the median.  $n$  indicates the number of neurons analyzed.

**(C)** Same as **B** but for the membrane time constant ( $\tau_{mem}$ ).

**(D)** Same as **B** but for the membrane capacitance ( $C_{mem}$ ).

**(E)** Same as **B** but for resting membrane potential ( $V_{rest}$ ).

**(F)** Example of tonotopic position analysis from a 4x micrograph of the LSO including the recording electrode (medial: 0 %, lateral: 100 %, scale bar in the top left).

**(G)** Scattered plot of  $R_{in}$  as a function of tonotopic position for  $n = 102$  neurons. Onset firing neurons are presented as black circles, and multi-firing neurons as blue circles (see Fig.3.5 for assignments of firing type). The red line indicates a linear fit, and the associated Pearson correlation coefficient ( $\rho$ ) along with its p-value are displayed in red. The black values indicate the results of a linear fit excluding the multiple firing neurons.

**(H)**  $\rho$  of the correlation between the tonotopic position and the four parameters analyzed above:  $R_{in}$ ,  $\tau_{mem}$ ,  $C_{mem}$ , and  $V_{rest}$ . Diamonds show  $\rho \pm SE$  and statistics are indicated above each value (see Methods for details of calculations).

**(I)** Similar to **H**, but for the correlation between  $V_{rest}$  and the remaining parameters. No further correlation was analyzed as these parameters are dependent through  $\tau_{mem} = R_{in} * C_{mem}$ .

**(J)** A -100-pA current step stimulation was used to calculate the voltage sag amplitude. The difference between the peak hyperpolarization (left red line) and the steady state  $V_{mem}$  (right red line) were subtracted to calculate the sag amplitude.

**(K)** Same as **B** but for the sag amplitude

**(L)** Scattered plot of the sag amplitude as a function of  $R_{in}$  for  $n = 106$  neurons. Linear fit (red line) statistics from the correlation analysis are indicate.

**(M)** Same as **I**, but for the correlation analysis between the sag amplitude and the remaining parameters.

Bonferroni-corrected significance thresholds for six comparisons were set as follows:  $p < 0.0083$  (\*);  $p < 0.0017$  (\*\*);  $p < 0.00017$  (\*\*\*)

---

Finally, a correlation analysis was performed between the parameters and the postnatal age (P) of the animal. Although previous reports suggested changes in  $R_{in}$  and  $C_{mem}$  (Dagostin & von Gersdorff, 2022), I did not find influence here (data not illustrated;  $\rho$  (P,  $R_{in}$ ): -0.12,  $p = 0.25$ ;  $\rho$  (P,  $C_{mem}$ ): -0.04,  $p = 0.71$ ). The same holds true for correlations of  $\tau_{mem}$ , and  $V_{mem}$  with the postnatal age ( $\rho$  (P,  $\tau_{mem}$ ): -0.14,  $p = 0.15$ ;  $\rho$  (P,  $V_{mem}$ ): 0.10,  $p = 0.34$ ).

### 3.2.2 Active membrane properties shape subthreshold integration

The passive membrane properties described above are accompanied by active membrane properties (see Introduction 1.8). Subthreshold voltage-gated ion channels, such as HCN and low threshold Kv channels, play a significant role in this process and both channel types are described in LSO neurons (HCN1: Leao et al., 2006, Kv1.1: Karcz et al., 2011; review: Leao, 2019). The opening and closing of these channels dynamically adjust neuronal excitability by altering the momentary  $R_{in}$ , which also affects  $\tau_{mem}$  (Izhikevich, 2006). Moreover, the  $V_{mem}$  can be affected, depending on the sum of conducted 'active' currents. Besides regulating neuronal excitability, the activity of the channels can create subthreshold resonances, leading to preferential input frequencies in oscillatory inputs (Remme et al., 2014; Mikiel-Hunter et al., 2016; Fischer et al., 2018; review: Hutcheon & Yarom, 2000).

The activity of subthreshold active membrane properties and the favored input frequency of oscillatory inputs can be analyzed by applying a sinusoidal current with exponentially increasing frequency (ZAP-current; Puil et al., 1986; Fischer et al., 2018) in a CC recording (Fig.3.4 A). The resulting changes in  $V_{mem}$  (Fig.3.4 B) can be used to determine the frequency dependent Z, which was analyzed for four factors: the instantaneous Z ( $Z_{inst}$ ), the resonating Z ( $Z_{res}$ ), the Q factor and the  $f_{res}$  (Fig.3.4 C). Since  $Z_{inst}$  is related to  $R_{in}$  (for low stimulation frequencies  $Z \approx R_{in}$ , Izhikevich, 2006), the values of  $Z_{inst}$  embed in the range of  $R_{in}$  with a mean of  $34.8 \pm 14.2$  M $\Omega$  (Fig.3.4 D). All analyzed neurons showed an increase from  $Z_{inst}$  to  $Z_{res}$ , elevating the impedance to  $46.5 \pm 15.5$  M $\Omega$  (Fig.3.4 E) and resulting in a Q factor of  $1.4 \pm 0.2$  (Fig.3.4 F). The  $f_{res}$ s associated with the  $Z_{res}$ s range from 18.4 to 45.5 Hz (mean:  $29.1 \pm 8.1$ , Fig.3.4 G), a value considerably low for auditory neurons, but well in range with previous reports (Fischer et al., 2018).

Given that active subthreshold membrane properties significantly impact synaptic integration, a tonotopic location analysis was performed. Neither the Q factor (Fig.3.4 H) nor the  $f_{res}$  (Fig.3.4 I) showed a significant correlation with the mediolateral position ( $\rho$  (tonotopic position, Q factor): 0.44,  $p = 0.16$ ;  $\rho$  (tonotopic position,  $f_{res}$ ): -0.26,  $p = 0.46$ ; Fig.3.4 J). Similarly, no tonotopic effect was found on  $Z_{inst}$  and  $Z_{res}$  ( $\rho$  (tonotopic position,  $Z_{inst}$ ): -0.3,  $p = 0.37$ ;  $\rho$  (tonotopic position,  $Z_{res}$ ): -0.20,  $p = 0.58$ ; Fig.3.4 J). This implies no differences in active subthreshold membrane properties between LSO neurons responsible for low and high sound frequency encoding.

Taken together, the analysis of passive and active subthreshold membrane properties indicates that mouse LSO neurons possess membrane kinetics required for fast auditory signal processing and do not vary along the tonotopic axis of the LSO.

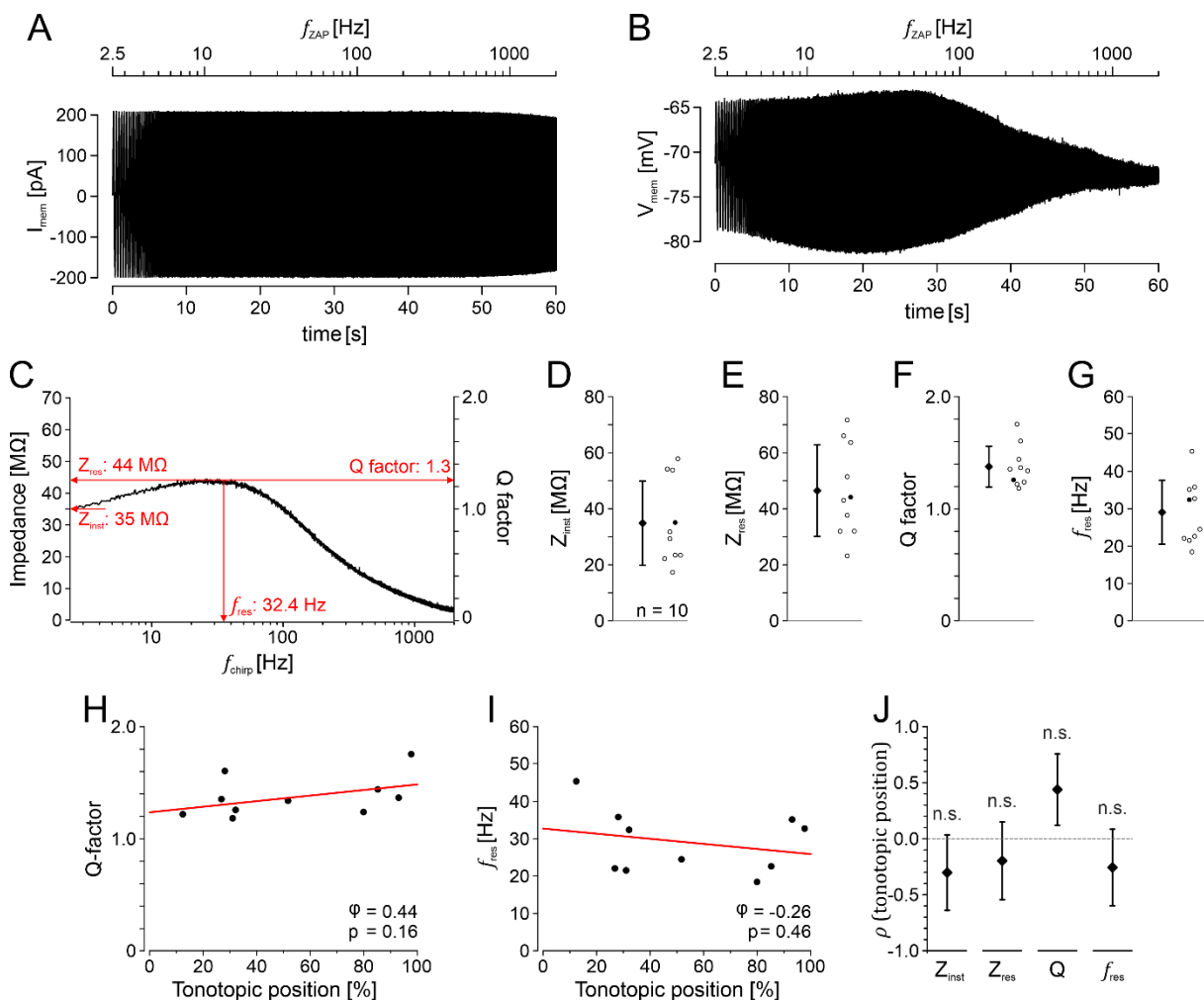


**Figure 3.4 Active membrane properties generate resonances and shape subthreshold integration.**

**(A)** A sinusoidal current with exponentially increasing frequency (2.5 Hz to 2000 Hz over 60 s; ZAP-current) was used for stimulation.

**(B)**  $V_{mem}$  response to the stimulus in **A**.

**(C)** The membrane impedance ( $Z_{mem}$ , left y-axis) and Q factor (right y-axis) as a function of  $f_{chirp}$ . The

quantifications of  $Z_{inst}$ ,  $Z_{res}$ , Q factor, and  $f_{res}$  are illustrated in red.

**(D)** The  $Z_{inst}$  is shown for ten LSO neurons. The value of the neuron shown in **C** is highlighted as filled circle.

**(E)** Same as **D** but for the  $Z_{res}$ .

**(F)** Same as **D** but for the Q-factor.

**(G)** Same as **D** but for the  $f_{res}$ .

**(H)** The Q factor as a function of the mediolateral recording position. The red trace shows a linear regression used for correlation analysis.

**(I)** Same as **H** but for  $f_{res}$  as a function of the mediolateral position.

**(J)**  $\rho$  of the correlation between the tonotopic position and the four parameters quantified in **D-G**.

---

### 3.2.3 LSO neurons exhibit robust onset burst firing behavior

The AP firing response of neurons to current-step stimulation is commonly employed to classify neurons as either differentiators or integrators and they fall into three classes of excitability (Hodgkin, 1948; Izhikevich, 2006). Auditory neurons often exhibit class 3 excitability, firing either a single AP, or a brief burst of APs at the onset of a constant current stimulation (Yang et al., 2016). Class 1 and 2 excitability show increasing firing rate with increasing stimulus amplitude, either continuous (class 1) or discontinuous (class 2). LSO principal neurons are reported to display class 1 and 3 excitability, while the latency of the first AP can reliably be used to differentiate them from the co-resident LOC neurons (Stereberg et al., 2010; Haragopal & Winters, 2023; Maraslioglu-Sperber et al., 2024). *In vivo* recordings from LSO neurons reported onset burst firing behavior (Franken et al., 2018). In order to examine the intrinsic AP firing behavior of LSO neurons, and to characterize their excitability class, I stimulated the neurons with depolarizing step currents, increasing the applied current from 0 to 1.5 nA in 0.05 nA steps (31 steps, Fig.3.5 A). Typically, LSO neurons fired a single AP at the rheobase, i.e., the smallest current step that induced APs (Fig.3.5 A&B). At higher stimulation amplitudes, this often transitioned into a brief burst of APs at the onset of stimulation, characteristic for class 3 excitability (Fig.3.5 B&C). Most neurons follow this feature, with bursts comprising 1-9 APs (mean: 3 APs, Fig.3.5 D). A subset of neurons (7/106; 7 %) increased their AP firing frequency with rising current amplitude. These neurons can be distinctly identified by the maximal number of APs evoked by the stimulation protocol, exceeding 100 APs within the 200 ms pulse (Fig.3.5 D). According to this criterion, 99 out of 106 neurons (93.4 %) are classified as onset burst firing neurons, and seven (6.6 %) are identified as multiple firing neurons exhibiting ‘class 1 excitability’ (Fig.3.5 D&E).

Contrary to rat and guinea pig LSO neurons, the mouse LSO neurons tested here, showed no signs of tonotopic differentiation based on their passive or active subthreshold membrane properties. To test if AP triggering and suprathreshold mechanisms order tonotopically, I first determined the rheobase to analyze the excitability of neurons. The mean rheobase value is  $0.65 \pm 0.18$  nA (Fig. 3.5 F). Similar to the above findings, no tonotopic organization was found, indicated by a low Pearson  $\rho$  of 0.05 ( $p = 0.60$ ; Fig.3.5 G). Finally, the increase in the number

of APs evoked at each current step was analyzed. The mean number of APs increased monotonically for the population of onset LSO neurons. It started to increase at 0.45 nA and the average neuron fired three APs at the highest stimulation intensity tested (1.5 nA; Fig. 3.5 H).

Collectively, these results demonstrate that most LSO neurons show onset burst firing behavior across the entire tonotopic axis. Thereby, the neurons show intrinsic properties to function as temporal differentiators.

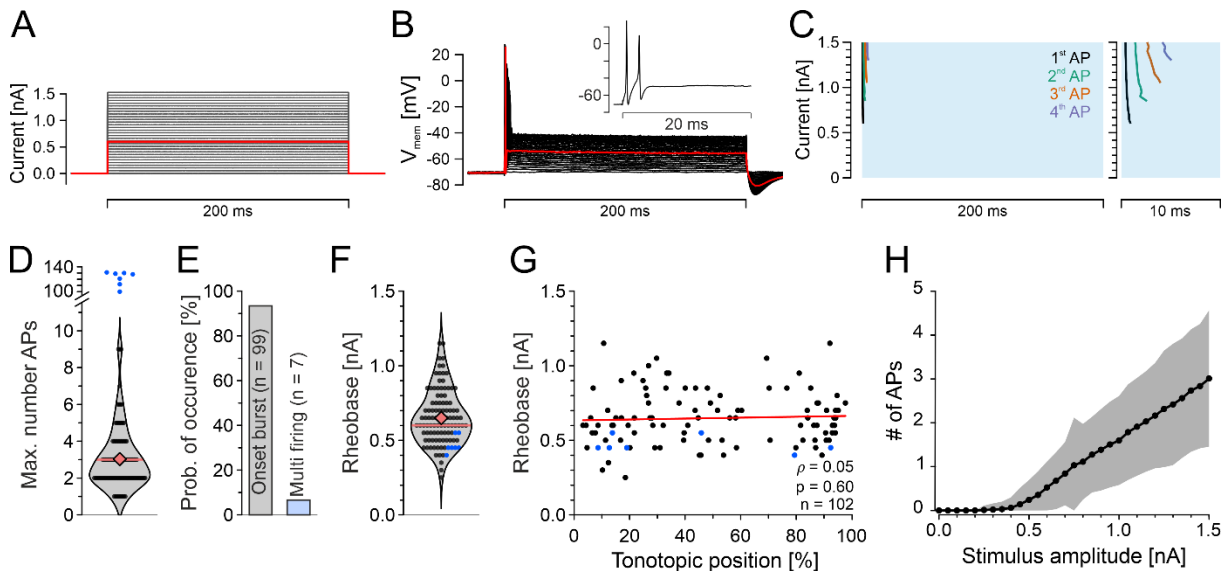


**Figure 3.5 LSO neurons exhibit robust onset burst firing behavior.**

**(A)** LSO neurons were stimulated with a 200-ms step current protocol to analyze sag behavior and AP firing characteristics. Current steps increased in steps of 0.05 nA from -0.2 nA to 1.5 nA (35 steps). The hyperpolarizing currents were used for sag amplitude analysis (Fig. 3.3 J-M). Rebound APs were not observed in any of the recordings, consequently only 0-1.5 nA stimulations (31 steps) were analyzed for APs and are displayed here. The red trace shows the rheobase stimulation of the exemplary neuron shown in **B** (0.6 nA).

**(B)** Overlaid voltage responses of an exemplary LSO neuron to the 31 current stimulations shown in **A**. The red trace illustrates the AP at rheobase stimulation. The neuron displayed an onset burst AP firing with a maximum of four APs. The inset shows a zoom-in of the time course of  $V_{mem}$ , stimulated at 0.85 nA (0.25 nA above rheobase).

**(C)** Temporal occurrence of APs of the exemplary neuron at different current stimulation amplitudes. The APs are differentiated in color by their sequence (1<sup>st</sup> to 4<sup>th</sup>). The blue box indicates the period of stimulation (left) and is truncated in the zoom-in of the first 10 ms on the right.

**(D)** Violin plot illustrating the maximum number of APs triggered by the step stimulation protocol. Multi firing neurons (blue dots) showed a different magnitude in the maximal number of APs compared to onset firing neurons (black dots), leading to an interruption of the y-axis. Mean (red diamond) and median (red line) were calculated excluding the multi firing neurons.

**(E)** Probability of occurrence of onset burst firing neurons and multi firing neurons. Numbers of neurons in each category are indicated.

**(F)** Violin plot of the rheobase values for  $n = 106$  LSO neurons. Single cell data is shown as black dots, the mean is indicated by the red diamond and the median by the red line.

**(G)** Scattered plot of the rheobase values as a function of the tonotopic recording position. Black dots represent data from onset burst firing neurons, and blue dots represent data from multiple firing neurons. Red line indicates a linear fit, with the Pearson correlation coefficient ( $\rho$ ) displayed along with

the corresponding p-value.

**(H)** The mean number of APs of onset burst firing neurons as a function of stimulation amplitude. The SD is shown as gray shaded area.

---

### 3.2.4 Slope-dependent modulation of AP threshold

The results that LSO neurons exhibit subthreshold resonances and fire onset burst APs are highly suggestive of a differentiator function. Differentiating neurons are characterized by a slope-dependent AP threshold (McGinley & Oertel, 2006; Gai et al., 2009). In auditory neurons, this mechanism aids in detecting rapidly changing signals and creates a high-pass filter to suppress slowly changing input signals (Gai et al., 2010). As the role of LSO neurons as differentiators or integrators is under debate (e.g.: Franken et al., 2018), I tested if LSO neurons also express such a mechanism.

To explore a slope-dependent AP threshold, I used sinusoidal stimulations, similar to (Lehnert et al., 2014). Nine stimulation frequencies ( $F_{\text{mod}}$ : 5, 10, 20, 50, 100, 200, 500, 1000, 2000 Hz) were tested with stimulus amplitudes from 0.1 nA to 3 nA in 0.1 nA steps (resulting in  $9 * 30 = 270$  stimulus combinations, Fig.3.6 A). Stimulating at 100 Hz resulted in no APs in the exemplary neuron at low stimulus amplitudes of up to 0.7 nA (Fig.3.6 B<sup>1</sup> ①). Increasing the stimulus amplitude to 0.8 nA resulted in a single AP ②. The number of APs increased with increasing stimulus amplitude to a maximum of four APs elicited by stimulus amplitudes  $\geq 2.4$  nA (Fig.3.6 B<sup>1</sup>&C ⑤). Similar effects were also seen at  $F_{\text{mod}}$  of 50 and 200 Hz (Fig.3.6 C).

For frequencies  $> 200$  Hz only single APs were elicited, likely due to temporal limitations of the stimulus (Fig.3.6 C). Specifically, the number of APs elicited at a constant stimulus amplitude varied depending on  $F_{\text{mod}}$ . At 0.6 nA, the neuron fired an AP exclusively at  $F_{\text{mod}} = 200$  Hz. Increasing the stimulus amplitude up to 1.3 nA increased the  $F_{\text{mod}}$ s that elicited APs (100-2000 Hz), but still only a single AP was triggered by each stimulus. At stimulus amplitude of up to 1.3 nA, only a single AP/stimulus was observed at  $F_{\text{mod}}$ s  $\geq 100$  Hz. Stimulations with  $F_{\text{mod}}$ s  $< 50$  Hz did not trigger an AP in the neuron regardless of the stimulus amplitude (Fig.3.6 B<sup>2</sup> ⑥, Fig.3.6 C). At this stimulus level, the number of APs decreased with increasing  $F_{\text{mod}}$ s at frequencies  $> 50$  Hz (Figs.3.6 B<sup>2</sup>&C ⑦-⑨).

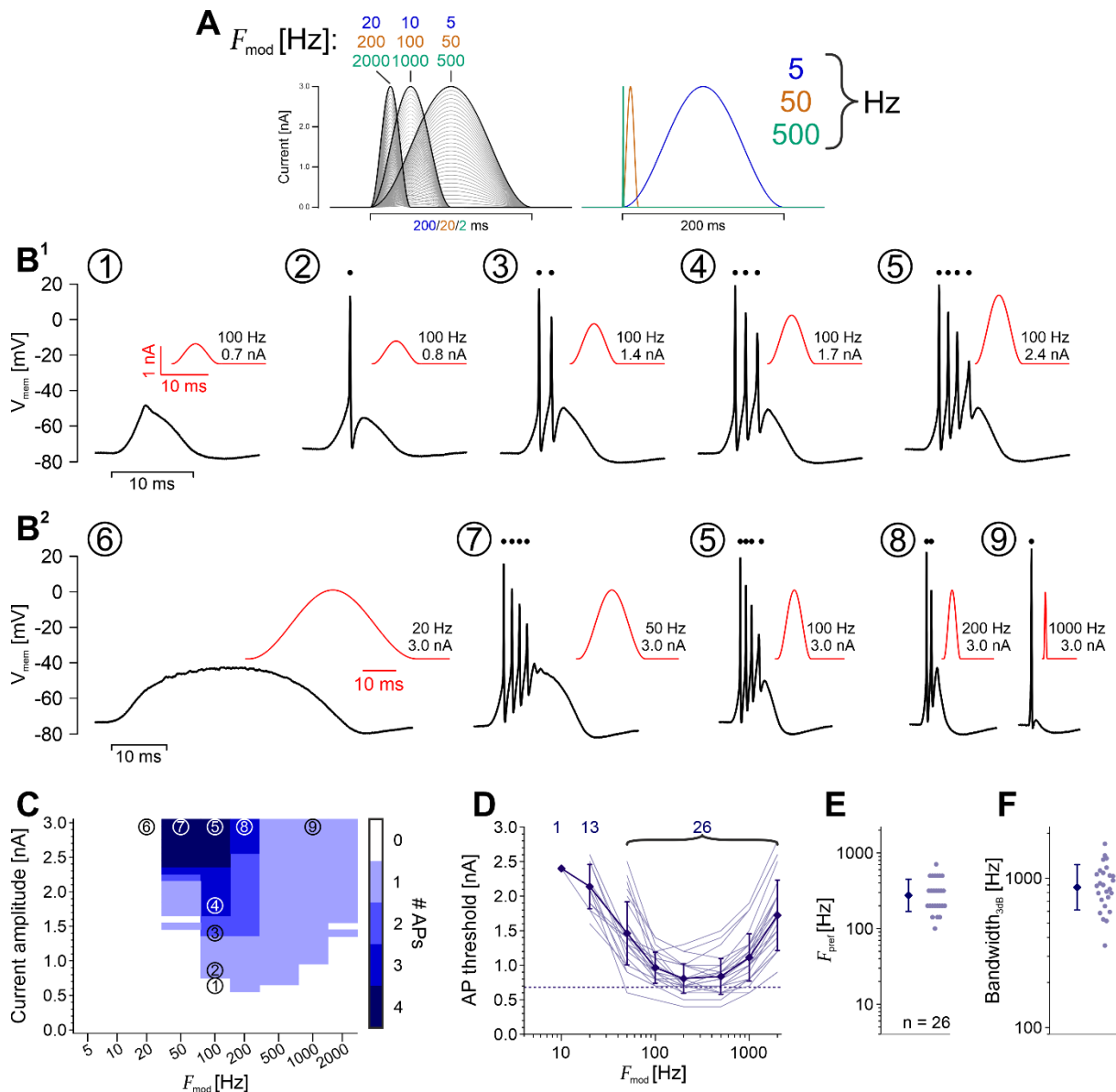


**Figure 3.6 LSO neurons exhibit a slope-dependent modulation of AP threshold.**

**(A)** Stimulus paradigm to analyze slope dependent modulation of AP threshold. The sinusoidal frequency ( $F_{mod}$ ) was presented at nine different frequencies (5, 10, 20, 50, 100, 200, 500, 1000, and 2000 Hz) and an amplitude of 100 pA to 3000 pA in 100 pA steps (i.e., 30 steps), resulting in a total of 270 stimulus combinations. The left panel shows the stimulation waveforms at each amplitude step, plotted across three time scales (x-axis scaling either 200, 20, or 2 ms). The right panel illustrates three  $F_{mods}$  (5, 50, and 500 Hz), representing one example from each time domain.

**(B<sup>1</sup>)**  $V_{mem}$  recordings (black traces) from an exemplary LSO neuron in response to stimulations at  $F_{mod} = 100$  Hz and five stimulus amplitudes (0.7 nA – 2.4 nA; red traces). Each AP is marked with a dot above its peak. With increasing current amplitude (700 pA – 2400 pA), the number of APs was increased (①-⑤).

**(B<sup>2</sup>)** Same as **B<sup>1</sup>** but for stimulation amplitude of 3 nA and five  $F_{mod}$ s (20 Hz to 1000 Hz; ⑤-⑨).

**(C)** The number of APs per stimulus (color-coded) as a function of current amplitude and  $F_{mod}$  for the neuron shown in **B<sup>1</sup>-B<sup>2</sup>**. The situations depicted in **B** are highlighted in the plot (①-⑨).

**(D)** The AP threshold as a function of  $F_{mod}$ . Blue diamonds represent mean  $\pm$  SD, while faded lines represent single-cell data. The dotted line is the average rheobase value for the neurons analyzed in this experiment. Numbers on top indicate how many neurons responded with an AP to the specified

$F_{mod}$ . The total number of neurons tested was  $n = 26$  (see **E**).

**(E)** The preferred frequency ( $F_{pref}$ ) of LSO neurons. Blue diamond represents the geometric mean  $\pm$  SD and dots represent single-cells data of  $n = 26$  neurons.

**(F)** Same as **E** but for the bandwidth<sub>3dB</sub>.

---

Subsequently, the current necessary to initiate spiking (i.e.,  $I_{thr}$ ) was determined at each  $F_{mod}$ s. The resulting graph exhibited a frequency-dependent  $I_{thr}$  (Fig. 3.6 D). The  $I_{thr}$  was lowest at  $F_{mod}$ s of 100–500 Hz, with the average curve indicating the lowest threshold at 200 Hz ( $0.80 \pm 0.21$  pA; mean  $\pm$  SD; Fig.3.6 D). Even at this optimized stimulus frequency, the threshold did not fall below the average rheobase value of  $0.68 \pm 0.20$  nA for those neurons. For  $F_{mod}$ s exceeding 200 Hz, a slight increase in the  $I_{thr}$  at 500 Hz (0.84 nA) was observed, followed by a steeper increase thereafter. For  $F_{mod}$ s below 200 Hz, the  $I_{thr}$  also increased slightly to 0.97 nA at 100 Hz and more pronouncedly to 1.46 nA at 50 Hz. At frequencies below 50 Hz, the number of neurons responding with an AP decreased, highlighting an increase in the threshold. At an  $F_{mod}$  of 10 Hz, only one neuron fired an AP at a stimulus amplitude of 2.4 nA (Fig.3.6 D). To quantify the frequency at which the  $I_{thr}$  was lowest, the preferred frequency ( $F_{pref}$ ) was introduced. The  $F_{pref}$  ranged from 100–707 Hz, with an average of  $275 \pm 141$  Hz (Fig. 3.6 E). The frequency tuning of the neurons was quantified at a cutoff of 3 dB and can be used as a measure of the bandwidth of the tuning (bandwidth<sub>3dB</sub>). All neurons showed low- and high-frequency cutoffs and were thus characterized by a band-pass filtering behavior. The bandwidth<sub>3dB</sub> ranged from 353 to 1700 Hz with an average at  $868 \pm 311$  Hz (Fig.3.6 F). These results demonstrate that LSO neurons exhibit a slope-dependent modulation of the  $I_{thr}$  and are most sensitive to input signals with a  $F_{mod}$  of 275 Hz and a bandwidth of 868 Hz. These adaptations help LSO neurons to better encode fast fluctuations in auditory stimuli.

To get a deeper understanding of the mechanisms behind the slope dependent  $I_{thr}$  changes, I analyzed the  $V_{thr}$ . Fig.3.7 (A) shows two APs elicited by stimulation at the respective  $I_{thr}$ s and  $F_{mod}$ s of 50 Hz (1red, 1.9 nA), and 200 Hz (black, 0.7 nA). There is a notable difference in the slope of the  $V_{mem}$  rise, and the APs were initiated at different  $V_{thr}$ . While  $V_{thr}$  was -48.0 mV at the 200 Hz stimulation (black), the  $V_{thr}$  at the 50 Hz stimulation was markedly higher -32.4 mV (Fig.3.7 A). I performed a phase-plane analysis to further characterize the APs. This analysis revealed clear differences between the AP waveforms elicited by 50 Hz and 200 Hz stimulations (Fig.3.7 B). The 200 Hz stimulation led to a biphasic AP. The two phases are described to be the activation of Nav channels at different locations, with the first (left) phase being caused by the activation of somatodendritic Nav channels and the second (right) phase the activation of Nav channels in the axon initial segment (AIS, Bean, 2007). In contrast, the AP caused by the 50 Hz stimulation showed a monophasic AP, probably because of the inactivation of somatodendritic Nav channels (Fig.3.7 B). In the phase-plane analysis, the

threshold can be determined by the sudden increase in the first derivative of the  $V_{\text{mem}}$  ( $dV/dt$ ) (see arrows in Fig.3.7 B). Plotting the  $V_{\text{thr}}$  as a function of the maximal slope of the current ( $dI/dt_{\text{max}}$ ) reveals a smooth transition between two  $V_{\text{thr}}$  states. At low  $dI/dt_{\text{max}}$ , the  $V_{\text{thr}}$  is about 20 mV more positive than at high  $dI/dt_{\text{max}}$ . A sigmoidal function can well be used to describe the data ( $R^2 = 0.76$ ), and the two amplitude values  $V_{\text{thr},1}$  and  $V_{\text{thr},2}$  are used to quantify the effect (Fig.3.7 C). Threshold elevation occurred in 81 % (21/26) of the neurons analyzed, with a significantly higher  $V_{\text{thr},1}$  compared to  $V_{\text{thr},2}$  ( $V_{\text{thr},1}$ :  $-32.5 \pm 4.2$  mV,  $V_{\text{thr},2}$ :  $-49.4 \pm 3.8$  mV; mean  $\pm$  SD,  $p = 1.5e-17$ ; Fig.3.7 E). The increase in threshold amounts to  $16.9 \pm 2.7$  mV (mean  $\pm$  SD; Fig.3.7 F).

The rate-dependent change in  $V_{\text{thr}}$  suggests that the AP initiation zone can vary in an activity-dependent manner, which creates a high-pass filter in LSO. In other words, with decreasing  $F_{\text{mod}}$  the threshold for AP initiation increases, because the availability of Nav channels in the somatodendritic compartment decreases.

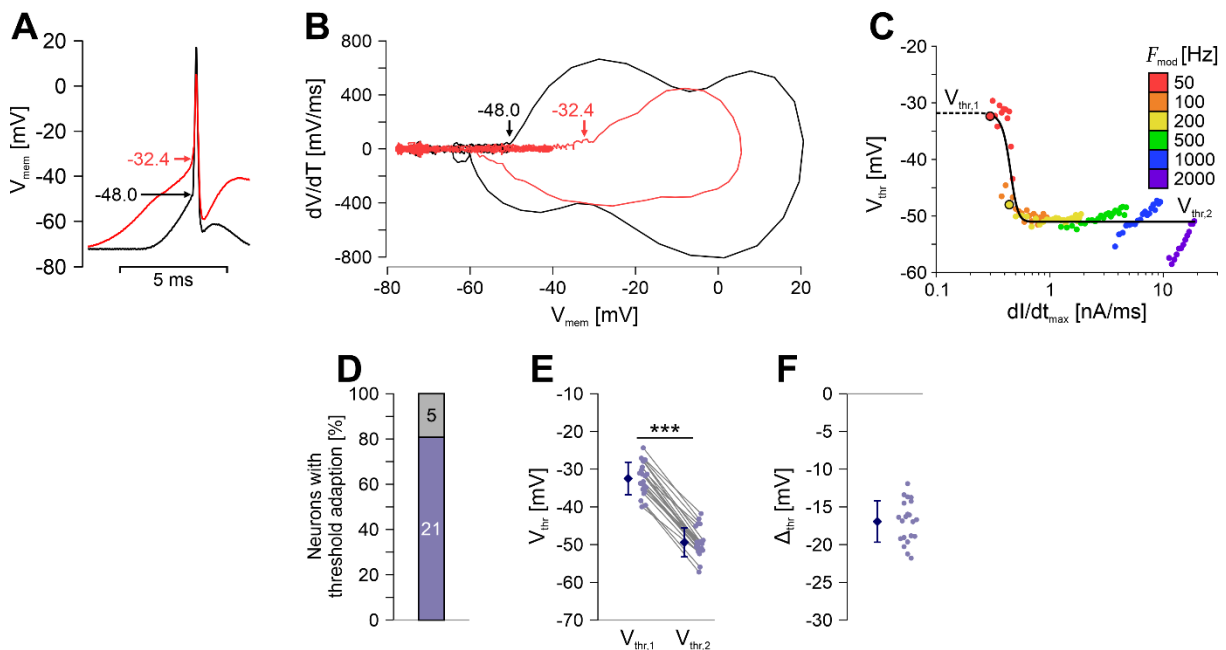


**Figure 3.7 AP initiation is determined by the current slope.**

**(A)** Time course of two APs of an exemplary neuron, elicited by stimulations at 50 Hz, 1.9 nA (red trace) and at 200 Hz, 0.7 nA (black trace). The arrows mark the  $V_{\text{thr}}$  of the APs ( $-32.4$  mV and  $-48.0$  mV, respectively).

**(B)** Same APs as in **A** shown in a phase-plane plot. The phase-plane plot shows the first derivative of  $V_{\text{mem}}$  ( $dV/dt$ ) as function of  $V_{\text{mem}}$ . The arrows again mark  $V_{\text{thr}}$ . While the phase-plane plot for the AP evoked by the 200 Hz stimulus clearly shows two phases (black trace), the phase-plane plot for the AP evoked by the 50 Hz stimulus barely shows a second phase.

**(C)** The  $V_{\text{thr}}$  of the neuron displayed in **A&B**, as a function of the maximal current slope ( $dI/dt_{\text{max}}$ ). The different stimulation frequencies are color-coded. As  $dI/dt$  is influenced by  $F_{\text{mod}}$  and current amplitude, multiple  $F_{\text{mod}}$ -current amplitude pairs correspond to the same  $dI/dt$  (each x-value can have multiple y-values). The two situations shown in **A&B** are marked by larger circles. The black line represents a sigmoidal fit used to extract  $V_{\text{thr},1}$  and  $V_{\text{thr},2}$ , while the dotted line indicates the extrapolation of the resulting function.

(D) Number of LSO neurons that exhibit a threshold adaptation.

(E)  $V_{thr,1}$  for the 21 LSO neurons exhibiting threshold adaptation. Blue diamonds represent mean  $\pm$  SD, and dots represent single-cell data. Statistics were evaluated by a paired t-test,  $p = 1.5e-17$ .

(F)  $\Delta_{thr}$  between  $V_{thr,2}$  and  $V_{thr,1}$  for the neurons presented in E.

---

### 3.2.5 Mimicked synaptic noise does not increase the frequency tuning of LSO neurons

The above findings, based on CC experiments, showed that LSO neurons exhibit a slope-dependent modulation of the AP threshold. Such experiments are suitable for describing the intrinsic spiking properties of the neurons, but they ignore two important factors from the neuron's physiological environment. First, a neuron does not experience ohmic currents as input signals; rather, the input signals are in the form of synaptic conductances. One consequence is that the current dynamically adjusts according to the driving force of the conductance ( $V_{mem} - E_{exc}$ , for an excitatory conductance), leading to a less effective depolarization if  $V_{mem}$  approaches  $E_{exc}$ . Second, synaptic noise due to the summation of multiple inputs is running on top of sinusoidal waveforms (like an AC component), which might initiate spiking by fast changes in the  $G_{exc}$ .

To test if physiological synaptic noise is capable of triggering APs in LSO neurons and thereby increasing the frequency coding range, I switched to DC experiments in combination with an input pathway model to mimic synaptic noise. The modeled input consists of 40 converging inputs, each having a  $SW_{exc}$  of 1 nS/input, thus matching the physiological estimates (Fig.3.8 A). Input AP timings were modeled for each of the inputs, which were generated by an inhomogeneous Poisson process that followed sinusoidal stimulus functions (see Methods 2.5). The same nine  $F_{mod}$ s as earlier were used (5-2000 Hz; Fig.3.6) and the amplitude of  $G_{syn}$  was varied by increasing the input activation rate ( $f_{exc}$ ) (NB: at  $F_{mod} = 500$  Hz and  $f_{exc} = 500$  APs/s, there will be on average one presynaptic spike/input/stimulus. Consequently, at  $F_{mod} = 500$  Hz and  $f_{exc} = 100$  APs/s, the probability of an input being active within the 2 ms ( $\frac{1}{500 \text{ Hz}}$ ) is 20 %, reducing the number of active inputs effectively to eight). The synaptic model stimulations were compared to an idealized sinusoidal conductance (hereafter referred to as sinusoidal conductance), which was scaled to match in integrated conductance.

Low levels of stimulation ( $f_{exc} = 100$  Hz) led to a depolarization that was insufficient to initiate APs in the exemplary neuron at a  $F_{mod} = 500$  Hz (Fig.3.8 B<sup>1</sup>, top and bottom panel) for the sinusoidal conductance, and for the synaptic model stimulation (red and blue, respectively). The same was true for each of 16 repeats, leading to a response probability/stimulus (entrainment, independent of the number of APs) of 0 % for both conditions (Fig.3.8 B<sup>1</sup>, middle panel). Increasing the stimulus amplitude by raising  $f_{exc}$  to 200 APs/s (Fig. 3.8 B<sup>2</sup>) was sufficient to trigger an AP with the sinusoidal conductance, but not with the synaptic model.

The entrainment, increased to 37.5 % and 18.75 %, respectively. Further increasing  $f_{exc}$  increased the entrainment to 100 % (Figs.3.8 B<sup>3</sup>-B<sup>4</sup>). The neuron responded to each synaptic model stimulus with a single AP at  $f_{exc} = 500$  APs/s, but increased to AP doublets at  $f_{exc} = 1000$  APs/s.

Stimulating the neuron at low  $F_{mod}$ s (< 50 Hz) did not trigger APs in response to sinusoidal conductances (Fig.3.8 B<sup>5</sup> (red), C<sup>1</sup>). Interestingly, the fast fluctuations in the synaptic model were insufficient to initiate APs, (Fig.3.8 B<sup>5</sup> (blue), Fig.3.8 D<sup>1</sup>), resulting in an entrainment of 0 % for both stimulation conditions. These results resemble the high-pass filtering observed in Fig. 3.6 and the synaptic noise could not bypass the filter.

The lowest  $F_{mod}$  at which APs occurred was 50 Hz at  $f_{exc} = 500$  Hz, with entrainment values of 13 % and 31 % for sinusoidal stimulation and synaptic model simulations, respectively (Fig.3.8 B<sup>6</sup>). At all  $F_{mod}$ s > 50 Hz, the entrainment was 100 %, except at 2000 Hz where the entrainment of the synaptic model decreased to 38 % (Fig.3.8 B<sup>7</sup>-B<sup>11</sup>). It should be mentioned that the  $G_{exc}$  at 2000 Hz had a much lower amplitude for the synaptic model compared to the sinusoidal conductance because the synaptic kernel reflects a frequency of ~500 Hz (see high overlap in both conductances in Fig.3.8 B<sup>9</sup>), thus the scaling increases the amplitude of sinusoidal conductance, while the synaptic model is limited. At lower  $f_{exc}$  (200 APs/s), only  $F_{mod}$ s of 500 and 1000 Hz (sinusoidal conductance), or 200 – 1000 Hz (synaptic model) were capable of initiating APs (Fig.3.8 C<sup>1</sup>-D<sup>1</sup>), probably caused by similar mechanisms underlying the slope-dependent threshold adaptations observed before (Fig.3.7). These results were qualitatively similar for all 14 neurons tested (Fig.3.8 C<sup>2</sup>-D<sup>2</sup>).

To capture AP firing beyond entrainment, I next analyzed the number of APs per stimulation at two  $f_{exc}$ , 200 and 500 APs/s (Fig.3.8 E, light and bold traces, respectively). At  $f_{exc} = 500$  APs/s, the average number of APs sharply increased at  $F_{mod}$ s > 50 Hz. On average, about one AP per stimulus was elicited for  $F_{mod}$ s of 100 – 1000 Hz, for both the sinusoidal conductance stimulation and the synaptic model stimulation. The synaptic model stimulations showed a number of APs/stimulus at an  $F_{mod}$  of 2000 Hz compared to sinusoidal stimulations, reflecting the previously observed decrease in AP probability (Fig.3.8 B<sup>11</sup>&E). At  $f_{exc} = 200$  APs/s, similar  $F_{mod}$ s were encoded by the neuron of 100 – 1000 Hz. However, the sinusoidal stimulation showed an elevated number of APs at  $F_{mod}$ s of 200 and 500 Hz compared to the synaptic model stimulations (Fig.3.8 E).

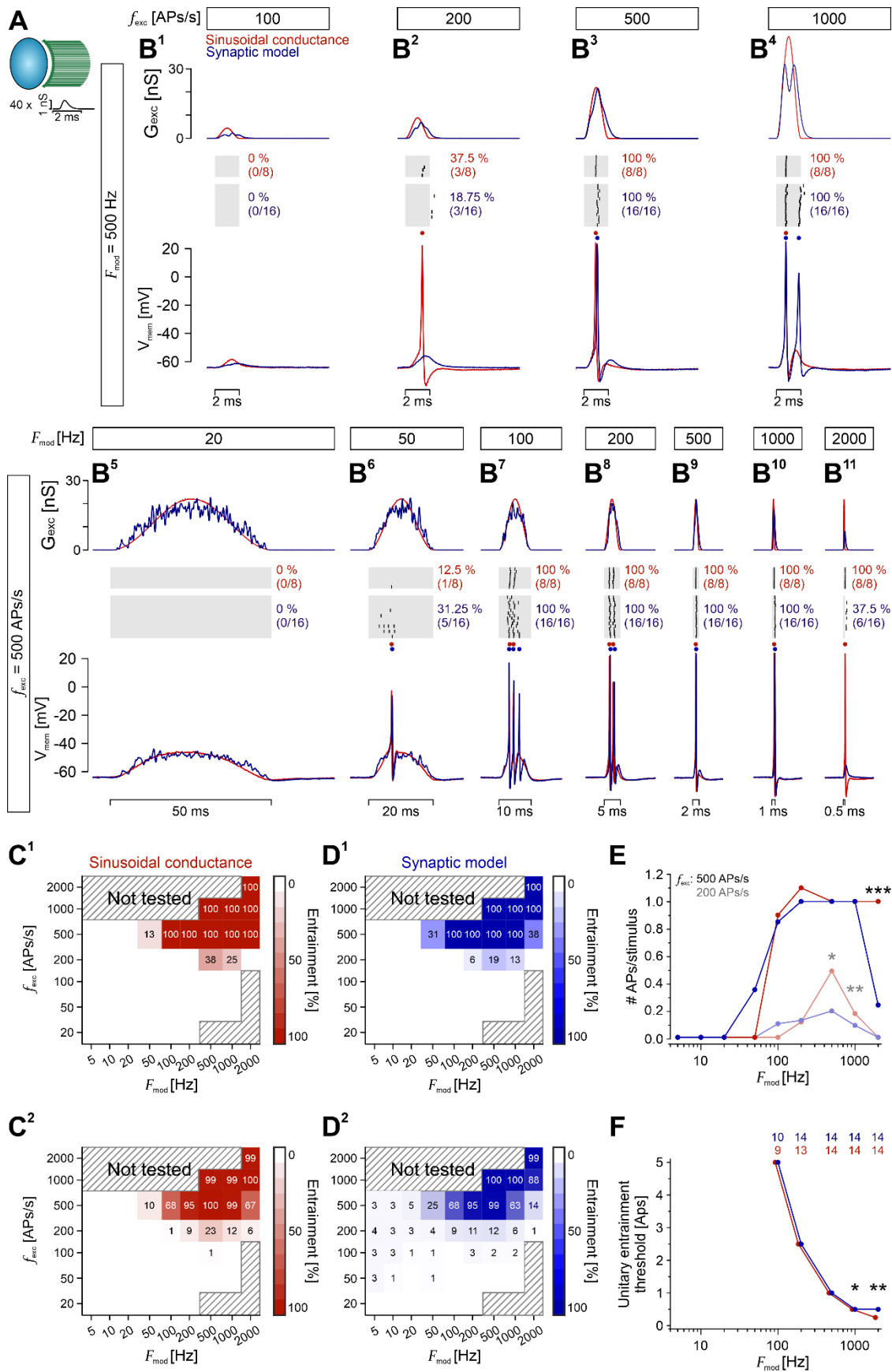


Figure 3.8 Frequency dependent modulation of AP probability is not increased by physiological synaptic noise.

**(A)** The cartoon illustrates the simulated excitatory synaptic convergence and the associated  $SW$  onto an LSO neuron chosen to match the physiological situation.

**(B)** DC stimulations of an exemplary LSO neuron with synaptic model (blue traces) and idealized sinusoidal conductance stimulations (referred to as sinusoidal conductance; red traces). Each panel consists of three subpanels: the top subpanels display the time-varying conductance stimulus ( $G_{exc}$ ) with either varying the  $f_{exc}$  (**B<sup>1</sup>-B<sup>4</sup>**) or the  $F_{mod}$  (**B<sup>5</sup>-B<sup>11</sup>**). The two stimulus types were designed to match in integrated conductance (as the model is probabilistic, trial-to-trial differences may have occurred). The voltage response of an example neuron to the two stimulus types are shown in the lower subpanels, with each AP marked by a dot. The middle subpanels display the occurrence of AP over multiple repeats (spike raster plots), with 16 repeats for the synaptic model and 8 repeats for the sinusoidal conductance. The grey boxes indicate the phase duration of the sinusoidal stimulus. The numbers next to them provides the entrainment, i.e., how many of the stimuli were responded with an AP (top in percent, bottom in counts). Note that in **B<sup>1</sup>-B<sup>4</sup>**,  $F_{mod}$  was constant (500 Hz) and  $f_{exc}$  increases from left to right (100-1000 APs/s). In **B<sup>5</sup>-B<sup>11</sup>** the  $F_{mod}$  increases from left to right (20-2000 Hz) at a constant  $f_{exc}$  (500 APs/s).

**(C<sup>1</sup>)** The entrainment (color coded) as a function of  $f_{exc}$  and  $F_{mod}$  for the sinusoidal conductance of the neuron shown in **B**. Grey boxes indicate stimulation combinations that were not tested.

**(C<sup>2</sup>)** Same as **C<sup>1</sup>** but the average of 13 neurons.

**(D<sup>1</sup>)** Same as **C<sup>1</sup>** but the synaptic model.

**(D<sup>2</sup>)** Same as **D<sup>1</sup>** but the average of 13 neurons.

**(E)** The median number of APs/stimulus as a function of  $F_{mod}$  for the sinusoidal conductance stimulations (red; saturated trace shows the data for  $f_{exc}$  of 500 APs/s, and faded traces at  $f_{exc}$  of 200 APs/s) and the synaptic model stimulations (blue). The synaptic model and sinusoidal conductance stimulations were compared at either  $f_{exc}$ , but not across  $f_{exc}$ . Statistics were evaluated by Wilcoxon-signed-rank test. Details on statistics are provided in the supplements ([Table S.6](#)).

**(F)** The median unitary entrainment threshold as function of  $F_{mod}$  for the sinusoidal conductance stimulations and the synaptic model stimulations. The unitary entrainment threshold calculates as  $\frac{f_{exc}}{F_{mod}}$ , e.g.:  $\frac{500 \text{ APs/s}}{200 \text{ s}^{-1}} = 2.5 \text{ APs}$ . Numbers on top indicate how many neurons responded with an AP to the specified stimulation. The data of the sinusoidal conductance (red) was shifted to the left for visibility. Statistics between the two stimulus types was tested by Wilcoxon-signed-rank test. Details on statistics are provided in the supplements ([Table S.7](#)).

In the next step, I calculated the unitary entrainment threshold as a measure of how often a single input must be active in one cycle of stimulation to trigger spiking with an entrainment  $> 50\%$  ([Fig.3.8 F](#)). At a  $F_{mod}$ s of 50 Hz, entrainment of 50% was only exceeded in three neurons (3/14, 21%) by synaptic model stimulation and only one neuron (1/14, 7%) by sinusoidal conductance stimulation. Thus, they were not further considered for analysis. At  $F_{mod}$ s = 100 Hz the threshold was crossed mostly at  $f_{exc} = 500$  Hz, leading to a unitary entrainment threshold of 5 APs ( $\frac{f_{exc}}{F_{mod}}$ , e.g.:  $\frac{500 \text{ APs} \cdot \text{s}^{-1}}{100 \text{ s}^{-1}} = 5 \text{ APs}$ ; [Fig.3.8 F](#)). At  $F_{mod} = 200$  and 500 Hz the threshold was exceeded at  $f_{exc}$  of 500 Hz, leading to a unitary entrainment threshold of 2.5 and 1. At higher  $F_{mod}$ s, the synaptic model stimulation showed an increased unitary entrainment threshold compared to the sinusoidal stimulation. Synaptic model stimulations resulted in a unitary entrainment threshold of 0.5 for both  $F_{mod} = 1000$  Hz and 2000 Hz, while the sinusoidal stimulation further decreased from 0.5 to 0.25 ([Fig.3.8 F](#)).

To put this in perspective with other studies, the temporal jitter (latency SD of the inputs) caused by the sinusoid can be estimated. In a Gaussian distribution, six times the SD covers > 99 % of values, therefore, dividing the sinusoidal wavelength by six provides a good estimate of temporal dispersion. Considering  $F_{mod} = 100$  Hz as the lowest encoded  $F_{mod}$ , the maximal temporal dispersion an LSO neuron allows can be approximated to  $\frac{1}{\frac{100 \text{ Hz}}{6}} = \frac{10 \text{ ms}}{6} = 1.67 \text{ ms}$ . The sensitivity of the LSO neurons increases up to frequencies of 200-500 Hz, relating to temporal windows of 0.83 and 0.33 ms. If the temporal jitter is lower (0.17 ms and 0.01 ms for 1000 Hz and 2000 Hz, respectively) the sensitivity of the neurons decreases.

Together, this experimental series demonstrates that mimicking synaptic inputs to the LSO does not increase the coding range of the LSO neurons. Auditory stimuli are thus encoded by the temporal envelope of the inputs to LSO neurons, rather than the fast conductance dynamics on top of the envelopes. This implies that LSO neurons prioritize temporally structured inputs over randomly occurring inputs, improving signal discrimination, and suggesting a coincidence mechanism for excitatory inputs.

### 3.3 Synaptic integration in LSO neurons stimulated with *in vivo*-like activation pattern

In the previous chapters, I described biophysical properties of LSO neurons that help to encode temporally structured inputs. In the next experimental series, I aimed to simulate the activity of presynaptic inputs to LSO neurons with *in vivo*-like stimulation patterns. The objective was to analyze the sensitivity of LSO neurons to various aspects of these input patterns. One major aspect in synaptic information transfer is the  $SW$  (Silver, 2010; Wu et al., 2024). I systematically varied these from the empirically determined  $SW$  ( $SW_{exc}$ : 1 nS/input,  $SW_{inh}$ : 8 nS/input) to infer the functional consequences on LSO neurons' coding. To achieve this, I employed the previously described synaptic model (Fig. 3.8). I generated stimulation patterns using different stimulus functions to mimic the firing behavior of the two main input populations, BCs and MNTB neurons. This approach allows to connect cellular coding mechanisms to *in vivo*-like synaptic dynamics.

#### 3.3.1 Distributing $SW_{exc}$ across multiple inputs promotes onset coding and suppresses sustained firing in response to a primary-like stimulation pattern

In the first experimental series, I stimulated LSO neurons with excitatory conductances to analyze the AP driving capabilities of different PL stimulation patterns. These reflect the typical spiking activity of *in vivo* recorded BCs and MNTB neurons when stimulated with high-frequency pure tones (see Introduction 1.6). The inputs were activated over a 200-ms period, and the  $f_{exc}$  was used as a proxy for sustained sound level coding. The  $f_{exc}$  was varied between

50 – 500 APs/s, in 50 APs/s increments, and reflects the rate coding of sound pressure levels observed in the innervating excitatory pathway (see [Introduction 1.6](#)). Moreover, I analyzed the influence of five levels of  $SW_{exc}$  on LSO neurons' coding. Beside the physiological most relevant situation (40 inputs X 1 nS/input), the remaining either aimed to decrease the synaptic noise (400 inputs X 0.1 nS/input) or increase the synaptic noise (20 inputs X 2 nS/input, 10 inputs X 4 nS/input, and 4 inputs x10 nS/input; three configurations are shown in [Fig.3.9 A](#)). All patterns have a  $cSW_{exc}$  of 40 nS. Together, five  $SW_{exc}$  and ten  $f_{exc}$  were tested, resulting in  $5 \times 10 = 50$  stimulation combinations.

When stimulated with a small  $SW_{exc}$  of 0.1 nS/input and an  $f_{exc}$  of 300 APs/s, the exemplary neuron shown in [Fig.3.9 \(B<sup>1</sup>-B<sup>3</sup>\)](#), responded with a reliable onset AP in each of ten repeats. I quantified this by the onset reliability (spiking probability within the first 10 ms of stimulation), resulting in an onset reliability of 100 % ([Fig.3.9 B<sup>1</sup>](#), black). Throughout the remaining 190 ms of stimulation, no further AP was observed (sustained rate = 0 APs/s, [Fig.3.9 B<sup>1</sup>](#), blue). Increasing the  $SW_{exc}$  to the physiological equivalent of 1 nS/input, the onset reliability was maintained at 100 % and the sustained rate showed a negligible increase to 3 APs/s ([Fig.3.9 B<sup>2</sup>](#)). Further increasing the  $SW_{exc}$  to 10 nS/input initiated a high AP rate in the sustained part of stimulation with 281 APs/s (53 APs/190 ms) and maintained the high onset reliability of 100 % ([Fig.3.9 B<sup>3</sup>](#)).

The exemplary neuron showed an onset reliability of 100 %, irrespective of  $SW_{exc}$ , and for all ten  $f_{exc}$  tested ([Figs.3.9 C<sup>1</sup>-C<sup>5</sup> & D<sup>1</sup>](#)). Corroborating findings were observed for the sample of ten neurons ([Fig.3.9 D<sup>2</sup>](#)). A small  $SW_{exc}$  of 0.1 nS/input was not able to initiate APs in the sustained part, independent of  $f_{exc}$  ([Figs.3.9 C<sup>1</sup>&E<sup>1</sup>](#)). A low sustained rate of < 15 APs/s was obtained upon stimulation with  $SW_{exc}$  of 1 nS/input, even at the highest  $f_{exc}$  of 500 APs/s ([Figs.3.9 C<sup>2</sup>&E<sup>1</sup>](#)). Further increasing  $SW_{exc}$  to levels  $\geq 2$  nS/input, the sustained rate showed level dependent increases, with a saturating, or even oversaturating effect. The maximal sustained rate for stimulations with  $SW_{exc}$  of 2 nS/input (70 APs/s) was achieved at  $f_{exc} = 350$  APs/s and decreased with higher  $f_{exc}$  ([Fig.3.9 E<sup>1</sup>](#)). Both,  $SW_{exc}$  of 4 and 10 nS/input, achieved maximal sustained rates at  $f_{exc}$  of 450 APs/s (173 and 316 APs/s, respectively; [Figs.3.9 \(C<sup>3</sup>-C<sup>5</sup> & E<sup>1</sup>\)](#)). These findings were qualitatively confirmed by the sample of ten neurons ([Fig.3.9 E<sup>2</sup>](#)).

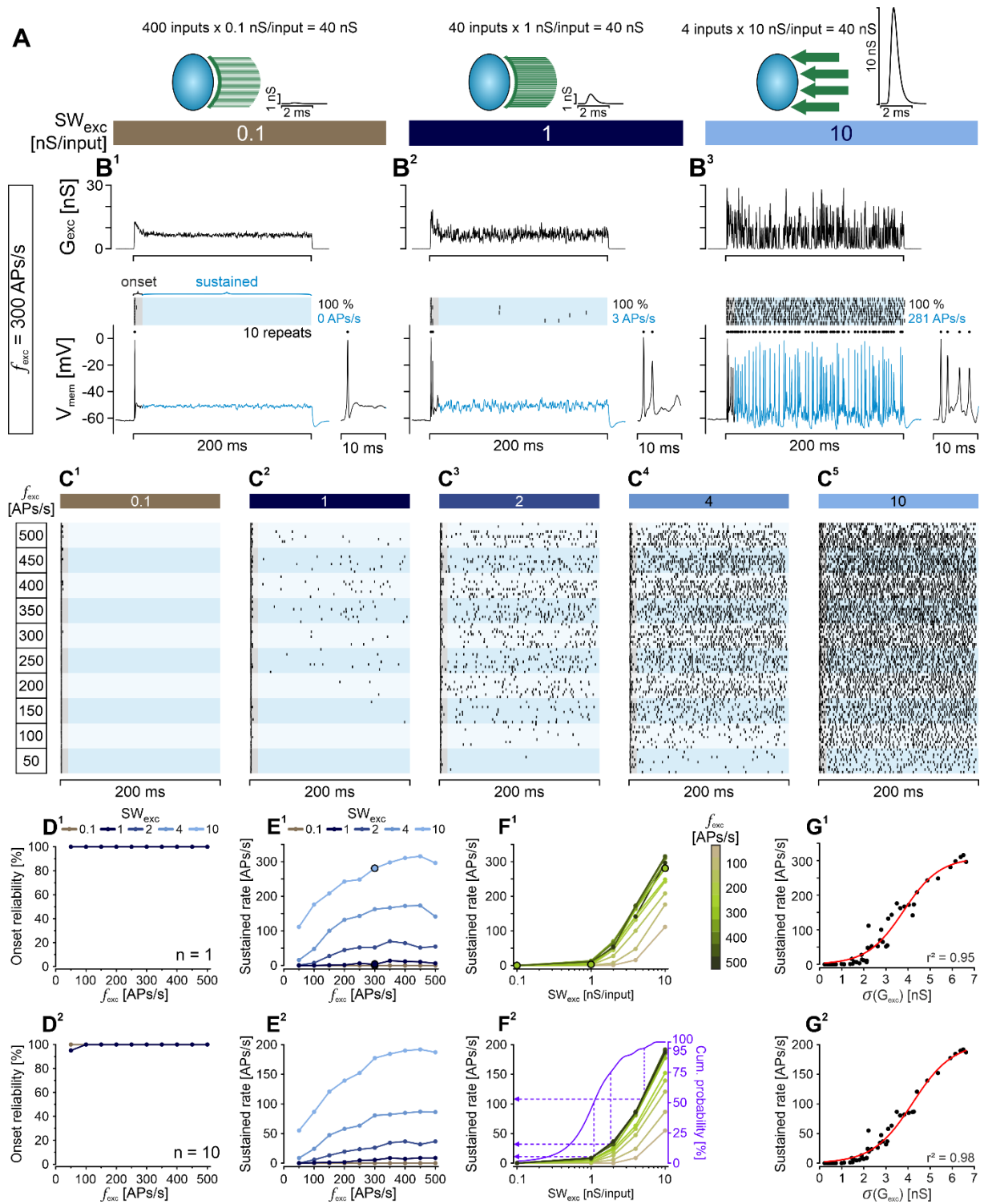


**Figure 3.9** Distributing  $SW_{exc}$  across multiple inputs promotes onset coding and suppresses sustained firing in response to a primary-like stimulation pattern.

**(A)** Three cartoons illustrate simulated excitatory synaptic convergence and associated  $SW_{exc}$  onto an LSO neuron. The number of inputs varied inversely with  $SW_{exc}$ , resulting in a  $cSW_{exc}$  of 40 nS.

**(B)** Integration of  $SW_{exc}$  0.1 nS/input (**B<sup>1</sup>**), 1 nS/input (**B<sup>2</sup>**), 10 nS/input (**B<sup>3</sup>**) at  $f_{exc}$  of 300 APs/s. The subpanels follow the same structure as **Fig.3.8 (B)**: Top: Time-varying conductance stimulation, bottom: voltage response of an exemplary neuron, middle: spike raster plots over 10 repeats. The 200 ms stimulation was divided into a 10 ms onset phase (black, magnified at the right) and the subsequent 190 ms represents the sustained phase (blue). The numbers next to the spike raster plot provide the

onset reliability (black) and the sustained AP rate (blue).

(C) Spike raster plots of five  $SW_{exc}$  (0.1, 1, 2, 4, 10 nS/input) and ten  $f_{exc}$  (50 – 500 Aps/s in 50 APs/s steps, see left scale). Each combination shows ten repeats.

(D) The onset reliability in dependence of  $f_{exc}$  for five  $SW_{exc}$  (color-coded brown to light blue) of the neuron shown in B-C is illustrated in D<sup>1</sup>, and the median of ten neurons is shown in D<sup>2</sup>. Note that the onset reliability is 100 % for all conditions in D<sup>1</sup> leading to an overlap of all curves. In D<sup>2</sup>,  $SW_{exc}$  of 2 nS/input and 4 nS/input are at 95 % at  $f_{exc} = 50$  APs/s.

(E) The sustained AP rate in dependence of  $f_{exc}$  for five  $SW_{exc}$  (color-coded brown to light blue) of the neuron shown in B-C is illustrated in E<sup>1</sup>, and the mean of ten neurons is shown in E<sup>2</sup>. In E<sup>1</sup>, the larger circles illustrate the results depicted in B.

(F) The sustained firing rate as a function of  $SW_{exc}$  for ten  $f_{exc}$  (color-coded beige to green; scale to the right of F<sup>1</sup>). F<sup>1</sup> illustrates the results for the neuron shown in B-C, and the median of ten neurons is shown in F<sup>2</sup>. In F<sup>1</sup>, the larger circles illustrate the results depicted in B. The distribution of empirically determined  $SW_{exc}$  from Fig. 3.1 (G) is redrawn as a cumulative probability function (purple) and the sustained rates at the 50<sup>th</sup>, 75<sup>th</sup> and 95<sup>th</sup> percentiles are highlighted by dotted lines.

(G) The sustained AP rate in dependence of the SD of the excitatory conductance ( $\sigma(G_{exc})$ ). G<sup>1</sup> illustrates the results for the neuron shown in B-C, and the median of ten neurons is shown in G<sup>2</sup>.

---

Fig.3.9 F<sup>1</sup> displays the sustained rate of the exemplary neuron as a function of the  $SW_{exc}$ . This reveals an exponential increase in the sustained rate with increasing  $SW_{exc}$  for all  $f_{exc}$ . To determine the relationship between the  $SW_{exc}$  and the sustained rate on the sample level, I incorporated the empirically determined cumulative distribution of  $SW_{exc}$  in the sample plot (Fig.3.9 F<sup>2</sup>). This allows a direct assessment of the influence of  $SW_{exc}$  on the sustained rate. The median  $SW_{exc}$  of 1 nS/input resulted in a maximal sustained rate of 11 APs/s, and an increase of the  $SW_{exc}$  to the 75<sup>th</sup> percentile (1.8 nS/input) is connected to a sustained rate to 32 APs/s. A further increase to the 95<sup>th</sup> percentile (5.2 nS/input) is connected to a sustained rate of 108 APs/s (Fig.3.9 F<sup>2</sup>). When considering an arbitrary threshold of 50 APs/s as threshold for ‘sustained firing’ this was achieved by  $SW_{exc} \geq 2.5$  nS/input (86<sup>th</sup> percentile) and increasing the threshold to 100 APs/s was reached by stimulation with  $SW_{exc} \geq 4.7$  nS/input (94<sup>th</sup> percentile). Plotting the sustained rate against the SD ( $\sigma$ ) of the sustained  $G_{exc}$  ( $\sigma(G_{exc})$ ) confirmed that the sustained rate mainly depended on the noise in the input signal, with higher noise levels fostering sustained firing behavior ( $r^2 = 0.98$ ; Fig3.9 (G<sup>1</sup>&G<sup>2</sup>) review: Silver, 2010).

The  $SW_{exc}$ s tested so far were uniformly-distributed across the number of inputs ( $uSW_{exc}$ ). Next, I tested, if a physiologically more plausible scenario with jitter in the distribution of  $SW_{exc}$  ( $jSW_{exc}$ ) increases the coding range of LSO neurons. To this end, the  $SW_{exc}$ s of 40 inputs were drawn from a gamma distribution to simulate jitter in the  $SW_{exc}$ . The minimal  $SW_{exc}$  was 0.3 nS/input and the largest 3.2 nS/input. The mean  $SW_{exc}$  was 1 nS/input, thus reflecting the physiologically relevant scenario (Fig.3.10 (A), right). The traces emerge from the same exemplary neuron as in Fig.3.9. The neuron reliably fired onset APs in response to both  $uSW_{exc}$  and  $jSW_{exc}$  stimulations (100 % onset reliability, Figs.3.10 B<sup>1</sup>&B<sup>2</sup>). The sustained rate of this neuron increased ten times comparing  $uSW_{exc}$  and  $jSW_{exc}$  stimulations (3 APs/s and 30 APs/s,

respectively). The onset reliability was independent of  $f_{exc}$ , but the increase in the sustained rate became apparent in the raster plots in Figs.3.10 (C<sup>1</sup> & C<sup>2</sup>). On the population level (n = 10), the neurons showed a significant increased sustained rate in 5/10  $f_{exc}$ s tested (at  $f_{exc}$  = 150, 200, 250, 350 and 400 APs/s; Fig.3.10 D, Table S.8). The dynamic range, as quantified by the minimal sustained rate subtracted from the maximal sustained rate (independent of  $f_{exc}$ ), also showed a significant increase ( $uSW_{exc}$ :  $12 \pm 15$  APs/s vs.  $jSW_{exc}$ :  $27 \pm 35$  APs/s, p = 0.04; Fig.3.10 E). This increase was mainly driven by half the population of neurons, while the dynamic range for the remaining five neurons increased by  $\leq 5$  APs/s. This indicates that, at least within a subpopulation of neurons, jitter in the  $SW_{exc}$  can substantially enhance the coding range of LSO neurons.

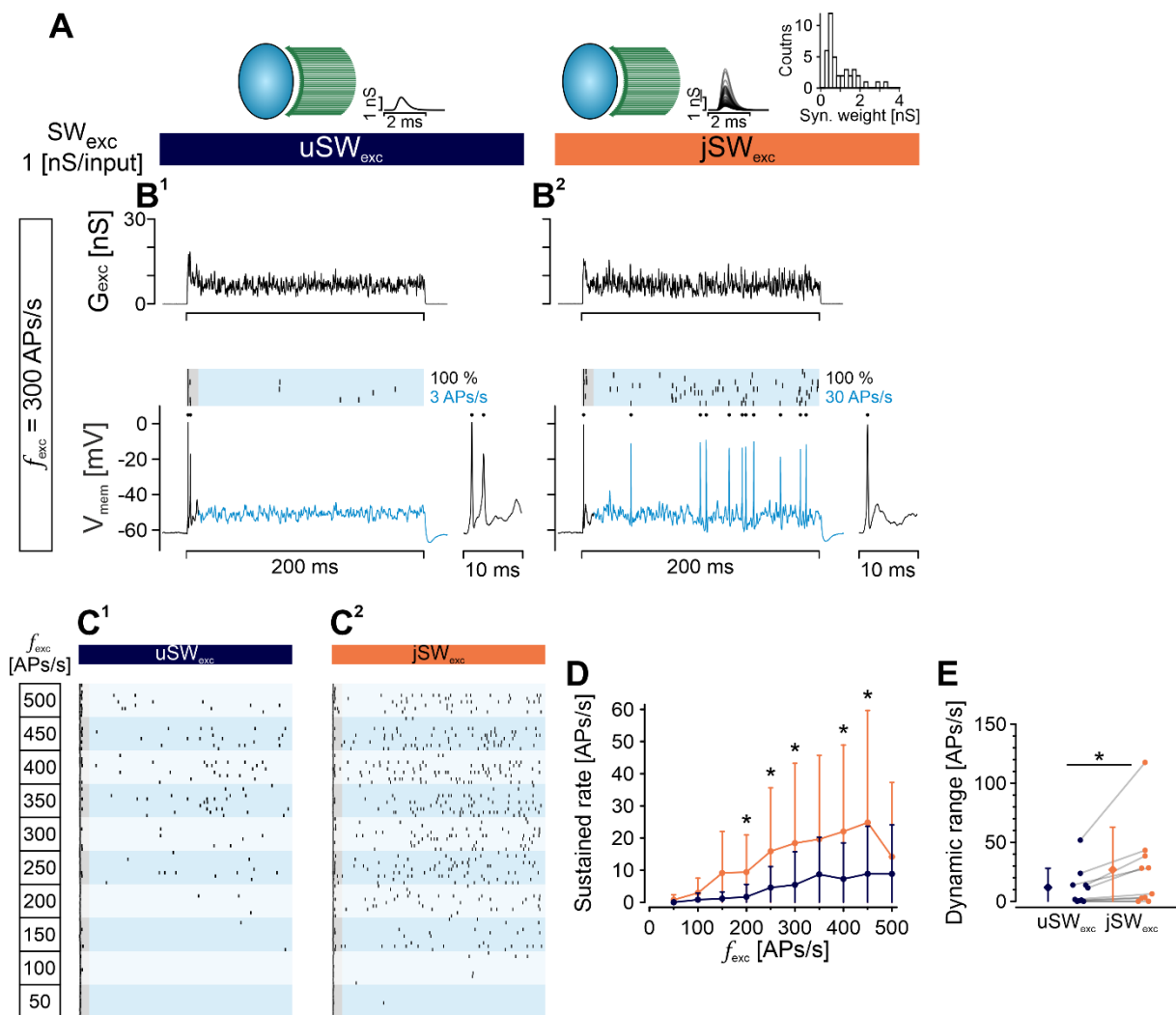


**Figure 3.10**  $SW_{exc}$  jitter increases the sustained AP rate.

**(A)** Similar to Fig.3.9 A. In the left cartoon the  $SW_{exc}$  is uniform with 1 nS/input ( $uSW_{exc}$ ). In the situation on the right  $SW_{exc}$  jitter ( $jSW_{exc}$ ) is introduced by drawing the  $SW_{exc}$  of the 40 inputs from a gamma distribution. The histogram shows the distribution of  $SW_{exc}$  (mean  $\pm$  SD:  $1.0 \pm 0.7$ ).

**(B)** Same as Fig.3.9 (B), but for the stimulation paradigm shown in A.

**(C)** Same as Fig.3.9 (C), but for the stimulation paradigm shown in A.

**(D)** The sustained spiking rate as a function of  $f_{exc}$  for  $uSW_{exc}$  and  $jSW_{exc}$ . Statistics were evaluated by

paired t-test. Details on statistics are provided in the supplements (Table S.8).

(E) The dynamic range of the sustained rate, compared between the  $uSW_{exc}$  and  $jSW_{exc}$ . Statistics were evaluated by paired t-test,  $p = 0.041$ .

Note: Figs.3.10 (B<sup>1</sup>-C<sup>1</sup>) are replotted from Fig.3.9 for comparison with the  $jSW_{exc}$ .

---

### 3.3.2 Temporal precise onset coding is enhanced by distributing $SW_{exc}$ across multiple inputs

Temporal precision is a hallmark of the central auditory system, and LSO neurons provide temporally structured input pattern to IC neurons (Ono et al., 2020). To analyze the temporal coding capabilities of LSO neurons under the PL stimulation paradigm, I conducted a temporal analysis of the onset APs and the sustained APs. The onset phase was analyzed by the temporal jitter in the latency of the first AP (Fig.3.11 A). The onset latency jitter was low, rarely exceeding 0.2 ms, for  $SW_{exc} \leq 2$  nS/input. At  $f_{exc} \geq 300$  APs/s, the jitter dropped below 0.12 ms (Fig.3.11 B). Stimulating with a  $SW_{exc}$  of 4 nS/input resulted in higher onset latency jitter of ~0.3 ms, which halved to ~0.15 ms when  $f_{exc}$  exceeded 300 APs/s. Stimulations with  $SW_{exc}$  of 10 nS/input resulted in the highest onset latency jitter, which showed peaks for distinct  $f_{exc}$  (Fig.3.11 B).

Plotting the onset latency jitter as function of  $SW_{exc}$  supports the finding that jitter increased with increasing  $SW_{exc}$  (Fig.3.11 C). To disentangle the contribution to the onset latency jitter of the intrinsic AP generating mechanism from the temporal jitter in the stimulus ( $G_{exc}$ ), I generated STAs of the  $V_{mem}$  (STA  $V_{mem}$ ) of the first AP (Fig.3.11 D). When aligned at  $V_{thr}$ , the STA  $V_{mem}$  curves of all  $SW_{exc}$  stimulations virtually overlapped. Since the intrinsic AP generating mechanism contributed minimally to the jitter, I examined the contribution of the input latency on onset latency jitter. I defined input latency as the time, at which  $G_{exc}$  exceeded 5 nS. The onset AP latency of the exemplary neuron highly depended on the input latency jitter, as evident by  $R^2$  of 0.98 of a linear fit, with a slope equivalent to unity (Fig.3.11 E). The ordinate value of 0.53 ms measures the latency from input latency to the AP peak.

To assess temporal structure in the occurrence of APs within the 200 ms of stimulation, I conducted an analysis of the normalized SACs, (Joris et al., 2006). The data presented in Figs. 3.11 (F,G<sup>1</sup>&H) originates from the example neuron presented in Figs.3.9 & Fig.3.10. If all APs are perfectly synchronized across the ten repeats, the SAC shows a straight line at 0 ms delay. If they occur randomly, the SAC forms a triangle, approaching zero at a delay equal to the stimulus duration (Fig.3.11 F<sup>1</sup>). If APs are temporally structured, the SACs display side peaks at delays matching the inter-AP interval (Lim & Capranica, 1994). The SACs showed a high degree of synchronization for small  $SW_{exc}$  of 0.1 and 1 nS/input (Figs.3.11 F<sup>2</sup>&F<sup>3</sup>), while for larger  $SW_{exc}$  the SACs showed a progressive increase in randomly occurring APs, as indicated by a progressive transition to a triangle (Figs.3.11 F<sup>4</sup>-F<sup>6</sup>).

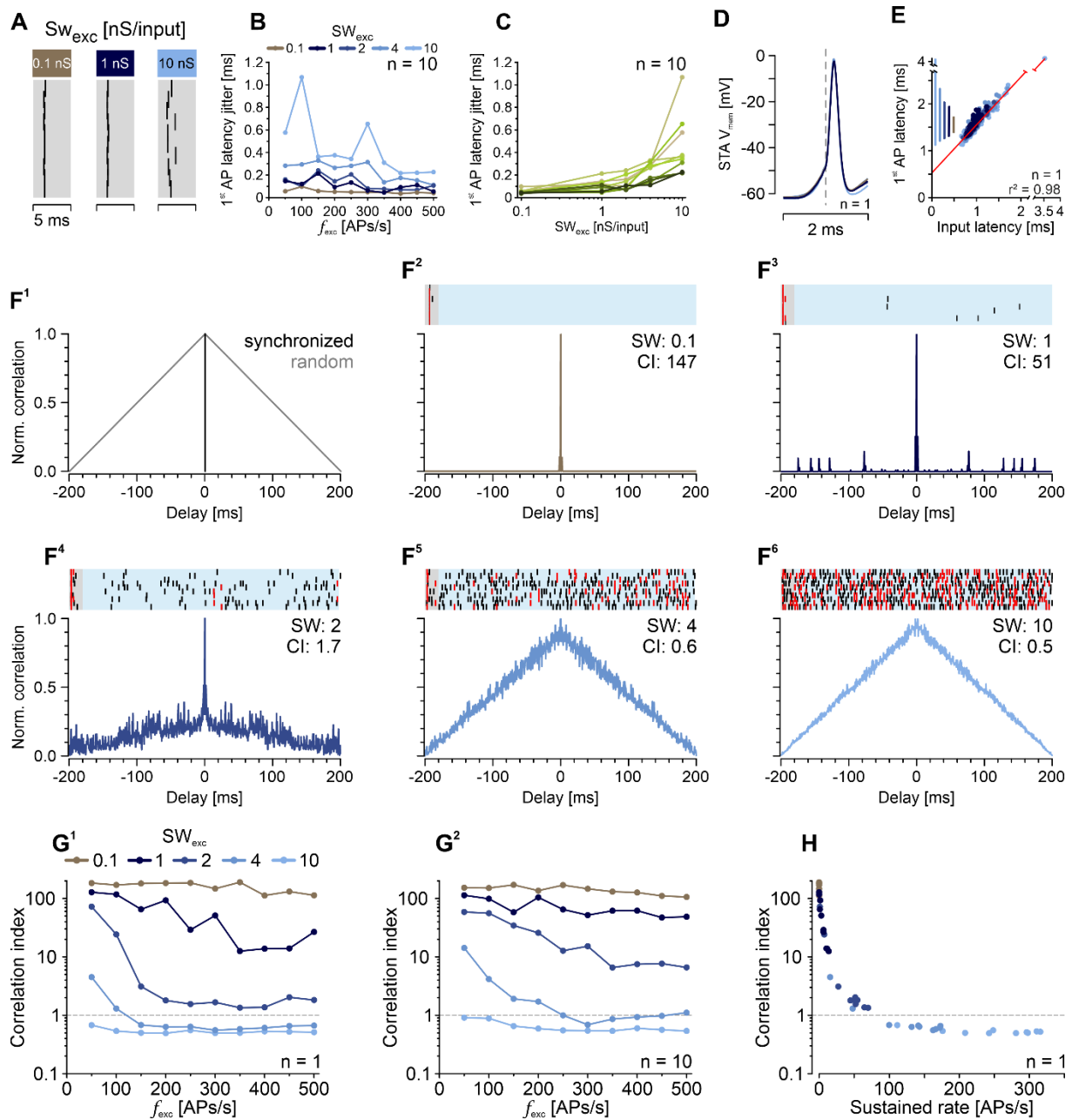


**Figure 3.11** Distributing  $SW_{exc}$  across multiple inputs enhances temporally precise onset coding and omits randomly occurring APs in the sustained part.

**(A)** Spike raster plot of the onset for three  $SW_{exc}$  (0.1, 1, 10 nS/input) from an exemplary neuron. The plots are redrawn from the spike raster plots in Fig.3.9 (B).

**(B)** 1<sup>st</sup> AP peak latency jitter as a function of  $f_{exc}$  for five  $SW_{exc}$ .

**(C)** 1<sup>st</sup> AP peak latency jitter as a function of  $SW_{exc}$  for ten different  $f_{exc}$ .

**(D)** Spike-triggered average (STA) of the 1<sup>st</sup> AP across ten repeats for all  $SW_{exc}$ . Same neuron as in A. APs were temporally aligned at the  $V_{thr}$  (dashed line). The STAs of the five  $SW_{exc}$  show a high degree of overlap and start to deviate during the afterhyperpolarization.

**(E)** The 1<sup>st</sup> AP latency as a function of the input latency. Plotted are all values for the neuron depicted in A when an onset AP was elicited, resulting in 100 dots/ $SW_{exc}$  (10  $f_{exc}$  x 10 repeats). The red line shows a linear fit, demonstrating a high degree of correlation ( $R^2 = 0.98$ ). The lines to the right of the y-axis indicate the range of 1<sup>st</sup> AP latencies for each  $SW_{exc}$ .

**(F)** Normalized shuffled auto correlograms (SAC) of five  $SW_{exc}$  at  $f_{exc} = 300$  APs/s. Two special cases of SACs are illustrated in F<sup>1</sup>: when APs occur in perfect temporal alignment across repetitions, only a line

is visible at delay = 0. The SAC results in a triangle that approaches 0 at the stimulus duration if APs occur randomly over time during the stimulus and are not temporally aligned across repeats. **F<sup>2</sup>-F<sup>6</sup>** depict the SACs for five  $SW_{exc}$  at  $f_{exc} = 300$  APs/s (bottom graphs). The numbers to the right of each panel represent the correlation index (CI). The spike raster plot is redrawn for each of the depicted situations with synchronously occurring APs marked in red (at least 2 APs in a temporal register of 0.2 ms across repeats; same data as in **Fig.3.9 (B)**)

**(G)** The CI as a function of  $f_{exc}$  for all  $SW_{exc}$  for a single neuron (**G<sup>1</sup>**) and for the sample median of ten neurons **G<sup>2</sup>**.

**(H)** The CI as a function of the sustained rate for the neuron show in **A**. The results from different  $SW_{exc}$  follow the same color-code as in **G**.

---

The peak of the SAC at 0 ms delay, is quantified as the CI (**Joris et al., 2006; Brette et al., 2007**). If  $CI > 1$ , APs are temporally correlated across repeats. The exemplary neuron showed the highest CI values for  $SW_{exc}$  of 0.1 nS/input for all  $f_{exc}$  (**Fig.3.11 G<sup>1</sup>**). At  $SW_{exc} = 1$  nS/input, the CI decreased with increasing  $f_{exc}$  but still showed very high correlation with all CI values being  $> 10$ . A similar course was observed at  $SW_{exc} = 2$  nS/input, eventually decreasing to values slightly above 1, which suggested only minor temporal correlation. For  $SW_{exc}$  of 4 and 10 nS/input most CI values are smaller than 1 (18 of 20 values; 90 %), indicating no temporal correlation, thereby emphasizing the result that APs occur temporally random (**Fig.3.11 G<sup>1</sup>**). The ensemble showed higher CI values compared to the exemplary neuron, resulting in a high degree of correlation for  $SW_{exc}$  of 2 nS/input at all  $f_{exc}$  (**Fig.3.11 G<sup>2</sup>**). The finding that most APs occurred randomly at  $SW_{exc}$  4 and 10 nS/input was affirmed by the ensemble (**Fig.3.11 G<sup>2</sup>**). Plotting the CI against the sustained rate revealed an exponential dependence of the CI on the sustained rate, suggesting that the high degree of correlation results from the onset APs (**Fig.3.11 H**).

These findings collectively illustrate a remarkable level of temporal precision of APs from LSO neurons when stimulated with physiological  $SW_{exc}$ . An increase in  $SW_{exc}$  elevates the onset latency jitter and causes APs that are initiated during the sustained phase, to appear temporally random.

### 3.3.3 Increased $V_{thr}$ constrains the ability to initiate APs in the sustained phase

The analysis of the rate of APs and their temporal occurrence (**Figs. 3.9 & Fig.3.11**, respectively) described the coding mechanisms of LSO neurons. Subsequently, I analyzed the data to identify biological mechanisms that could explain the observed phenomena. One mechanism observed in the literature is that the AP threshold varies with the amount of noise in the stimulus (**Higgs & Spain, 2011; Lubejko et al., 2019**). Therefore, in the next step, I analyzed the  $V_{thr}$  of the APs. **Fig. 3.12 (A)** depicts the  $V_{mem}$  of the exemplary neuron, stimulated with five  $SW_{exc}$ , as previously presented in **Fig.3.9 (B)**, and the  $V_{thr}$  of each AP is marked by a red dot. The  $V_{thr}$  of the first AP is also indicated as a red dotted line, for comparison with the  $V_{thr}$  of APs in the sustained part of stimulation. At large  $SW_{exc}$  of 10 nS/input, APs with  $V_{thr}$  both

higher and lower than the first AP occurred (Fig. 3.12 A<sup>1</sup>&B<sup>1</sup>). In the next step, I subtracted the  $V_{thr}$  of the 1<sup>st</sup> AP from the APs in the sustained phase of stimulation ( $\Delta_{thr}$ ). A normalized histogram of  $\Delta_{thr}$  indicates the distribution of the  $V_{thr}$  in respect to the  $V_{thr}$  of the first AP. For large  $SW_{exc}$  of 10 nS/input, the data distributed around zero, with a mean of  $1.0 \pm 3.4$  mV (Fig. 3.12 C<sup>1</sup>). With smaller  $SW_{exc}$ , the  $V_{thr}$  of the sustained APs gradually shifts to more depolarized values compared to the  $V_{thr}$  of the 1<sup>st</sup> AP (Figs.3.12 A<sup>2</sup>-A<sup>4</sup> & B<sup>2</sup>-B<sup>4</sup>). The distributions of  $\Delta_{thr}$  confirmed this observation by a depolarizing shift from zero with decreasing  $SW_{exc}$  ( $SW_{exc}$  4 nS/input:  $4.1 \pm 2.5$  mV;  $SW_{exc}$  2 nS/input:  $6.0 \pm 2.5$  mV;  $SW_{exc}$  4 nS/input:  $8.7 \pm 2.0$  mV; Fig.3.12 C<sup>2</sup>-C<sup>4</sup>). This analysis was not possible at the lowest  $SW_{exc}$  of 0.1 nS/input, as there were no APs in the sustained part of stimulation (Fig. 3.12 A<sup>5</sup>-C<sup>5</sup>).

The observed shift in  $\Delta_{thr}$  was not due to changes in the  $V_{thr}$  of the 1<sup>st</sup> AP, as this was highly comparable between all  $SW_{exc}$  tested at  $f_{exc}$  of 300 APs/s. Similarly, no statistical significance of  $SW_{exc}$  on the  $V_{thr}$  of the 1<sup>st</sup> AP was found at any  $f_{exc}$  tested (data not shown). As the average level of depolarization increased with increasing  $f_{exc}$ , the  $\Delta_{thr}$  was analyzed across  $f_{exc}$ . The results from the exemplary neuron indicate that the  $\Delta_{thr}$  increased for all  $SW_{exc}$  tested with increasing  $f_{exc}$  (Fig.3.12 E<sup>1</sup>). The exemplary neuron also exhibited hyperpolarizing shifts of  $V_{thr}$  at large  $SW_{exc}$  of 10 nS/input and low  $f_{exc}$  of 50 – 200 APs/s. This phenomenon was otherwise observed only at  $SW_{exc}$  of 4 nS/input and  $f_{exc} = 50$  APs/s (Fig.3.12 E<sup>1</sup>). The shift in  $\Delta_{thr}$  for low  $SW_{exc}$  of 1 nS/input, was large with values ranging from 2.3 mV at  $f_{exc} = 150$  APs/s to the highest value observed of 8.7 mV at  $f_{exc} = 400$  APs/s. These results were corroborated by the sample median (Fig. 3.12 E<sup>2</sup>). At larger  $SW_{exc}$  of 10 nS/input, three significant hyperpolarizing shifts were detected at  $f_{exc} = 50, 100,$  and 200 APs/s. The intermediate  $SW_{exc}$  of 4 nS/input did not show any significant deviations from zero in  $\Delta_{thr}$ , however smaller  $SW_{exc}$  of 2 and 1 nS/input show various significant depolarizing shift (Fig. 3.12 E<sup>2</sup>).

Together, these results indicate that at the physiological  $SW_{exc}$  (1 nS/input), an increase in  $f_{exc}$  shifted the  $V_{thr}$  of APs during sustained integration to depolarized levels, thereby constraining the neurons from initiating APs. For  $SW_{exc}$  of > 4 nS/input this phenomenon would flip and the shifts in  $V_{thr}$  became negative, potentially adding a facilitatory effect on the AP rate.

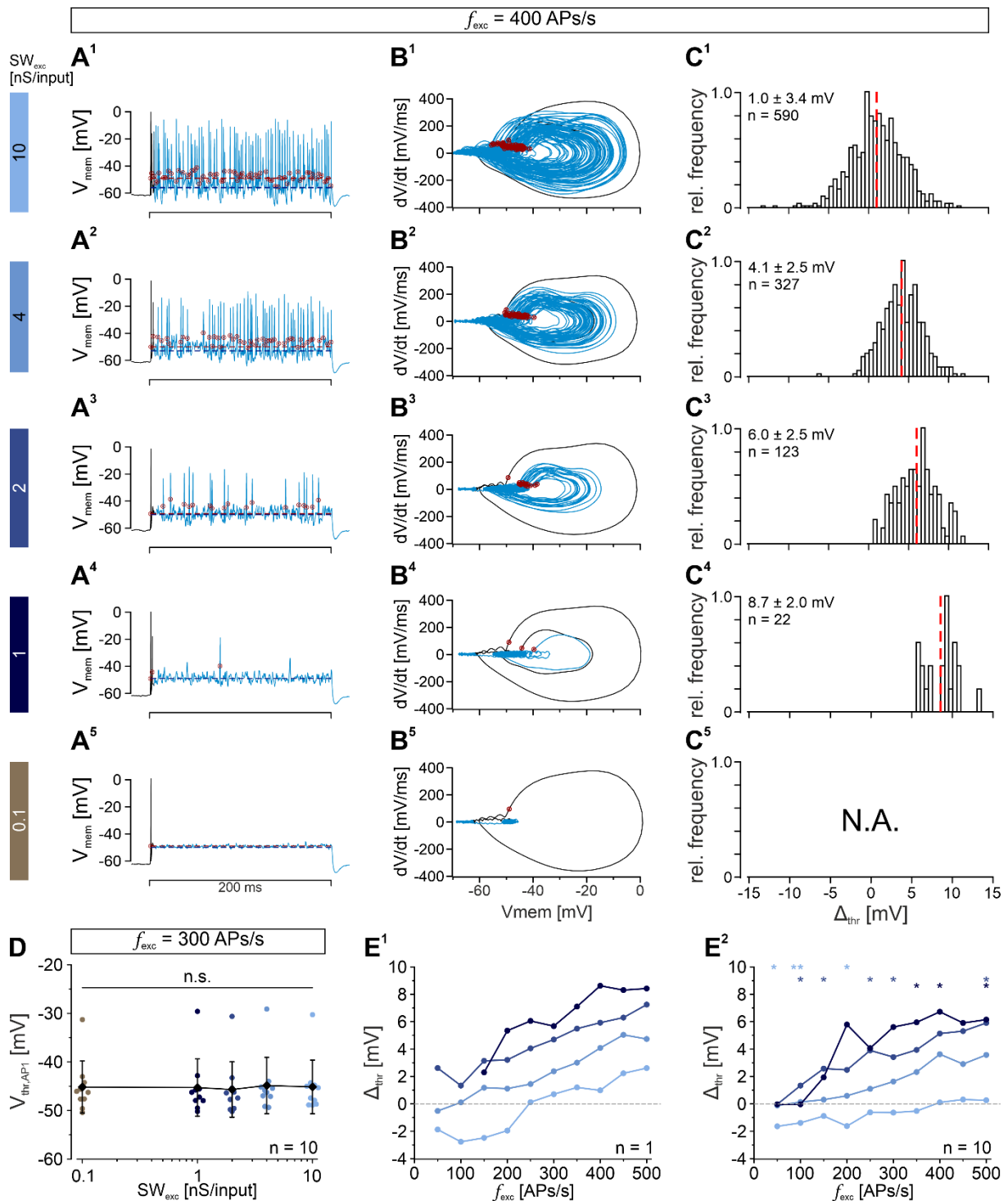


**Figure 3.12**  $V_{thr}$  increases during the sustained part.

**(A)** Time course of  $V_{mem}$  of an exemplary neuron to a stimulation at  $f_{exc}$  of 400 AP/s at five  $SW_{exc}$  (indicated to the left). In each trace the  $V_{thr}$  of each AP is marked by a red dot. The red dotted line depicts the  $V_{thr}$  of the 1<sup>st</sup> AP, and the blue dotted line the average  $V_{mem}$  during the sustained part of the trace.

**(B)** Phase-plane plots of the  $V_{mem}$  displayed in **A**. The red dots mark the  $V_{thr}$ .

**(C)** The difference in  $V_{thr}$  between the 1<sup>st</sup> AP and remaining ones ( $\Delta_{thr}$ ) displayed in normalized histograms, of all APs extracted from ten repeats. Red dotted lines mark the mean  $\Delta_{thr}$  for each condition. Note the increase of  $\Delta_{thr}$ , indicated by a shift of the red dotted line to the right across the plots.

(D) The  $V_{thr}$  of the 1<sup>st</sup> AP as a function of  $SW_{exc}$  at  $f_{exc} = 300$  APs/s. Black diamonds represent mean  $\pm$  SD, while dots represent single cell data. Statistics were evaluated by a one-way ANOVA ( $p > 0.99$ ).

(E) The  $\Delta_{thr}$  as a function of  $f_{exc}$  for five  $SW_{exc}$ . **E<sup>1</sup>** represent the results from the neuron shown above and **E<sup>2</sup>** shows the sample median. Statistics were evaluated by a one-sample Wilcoxon signed-rank test (comparison against zero). Details on statistics are provided in the supplements (Table S.9).

---

### 3.3.4 Inhibition blocks onset APs and modulates the sustained AP rate bidirectionally

Ipsilateral sound stimulations increase the AP rate of *in vivo* recorded LSO neurons, and an increase in the contralateral sound level, successively decrease the AP rate. Excitation-inhibition synaptic integration in LSO neurons has been assessed in multiple studies using the *in vitro* brainstem slice preparation. They either used electrical or optical input fiber stimulations (e.g.: Sanes, 1990; Wu & Kelly, 1992; Gjoni, Zenke, et al., 2018) or DC stimulations (e.g.: Beiderbeck et al., 2018; Franken et al., 2021). In these experiments the excitatory, respectively inhibitory inputs, were collectively activated but did not consider temporal jitter within an input pathway. Such a high degree of synchronization is rarely achieved in a naturally condition. To assess the effects of inhibitory inputs on the onset firing and the sustained AP rate, as well as to understand the mechanisms underlying rate coding during bilateral stimulation, I extended the excitatory stimulation model with an inhibitory component. To achieve this, I combined the semi-natural PL stimulation paradigm with simulations of the inhibitory pathway in the same way.

I tested the excitation-inhibition integration by stimulating at a constant  $f_{exc}$  of 300 APs/s while varying the inhibitory activation rate ( $f_{inh}$ ) from 0 to 300 APs/s in increments of 50 APs/s, which resulted in seven levels. The influence of  $SW_{exc}$  and  $SW_{inh}$  was evaluated using three values each ( $SW_{exc}$ : 1 nS/input, 4 nS/input, 10 nS/input;  $SW_{inh}$ : 2 nS/input, 4 nS/input, 8 nS/input; the two values considered physiological are underlined, compared Fig.3.1 & Fig.3.2).

In the absence of inhibitory activity ( $f_{inh}$  of 0 APs/s), excitatory stimulation produced results that aligned with those observed in Fig. 3.9. Specifically, stimulation with small  $SW_{exc}$  resulted in exclusive onset responses for the exemplary neuron (onset reliability of 100 %) and a sustained AP rate of 0 APs/s (Fig.3.13 B<sup>1</sup>). As  $SW_{exc}$  increased, the onset reliability remained at 100 %, while the sustained AP rate increased to 52 and 164 APs/s for  $SW_{exc}$  of 4 and 10 nS/input, respectively (Figs.3.13 C<sup>1</sup>&D<sup>1</sup>). Adding inhibition at a rate of  $f_{inh} = 200$  APs/s reduced the onset reliability to 30 % when combined with  $SW_{exc}$  of 1 nS/input. Paradoxically, by adding inhibition the neuron fired APs in the sustained stimulation phase with a rate of 17 APs/s (Fig.3.13. B<sup>2</sup>). APs emerged by adding inhibition at levels as low as 50 APs/s as illustrated in the raster plot in Fig. 3.13 (E<sup>1</sup>). At a  $SW_{exc}$  of 4 nS/input, the reduction in onset reliability was less pronounced (50 %), and the paradoxical facilitating effect of inhibition was also seen (increase from 52 APs/s to 71 APs/s, Figs.3.13 C<sup>1</sup>-C<sup>2</sup> & E<sup>2</sup>). At the largest  $SW_{exc}$ , adding

inhibition minorly decreased the onset reliability (by 10 %), while showing a suppressive effect on the sustained rate (reduction from 164 APs/s to 142 APs/s, Figs.3.13 D<sup>1</sup>-D<sup>2</sup> & E<sup>3</sup>).

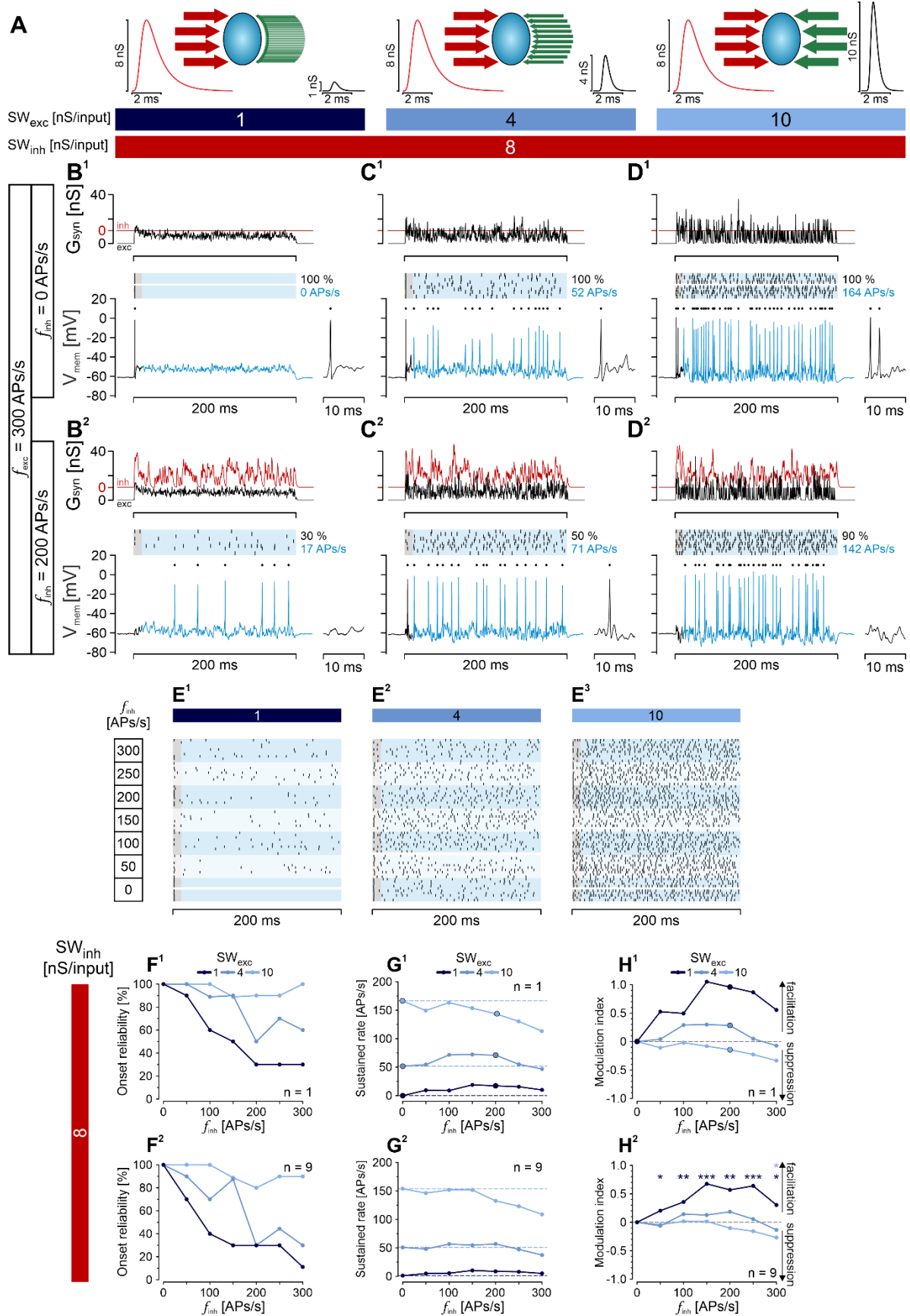


Figure 3.13 Inhibition effectively blocks the onset AP evoked by excitation and bidirectionally modulates the sustained AP rate.

**(A)** Similar to the cartoon in Fig.3.9 (A). The stimulation paradigm is indicated in the cartoon with the number of converging inputs and the  $SW$  for both, excitation and inhibition. The  $cSW_{inh}$  of 32 nS was distributed across 4 inputs, resulting in a  $SW_{inh}$  of 8 nS/input.

**(B-D)** Integration of simulated synaptic inhibition ( $G_{inh}$ ) with  $G_{exc}$  for three different  $SW_{exc}$  (1 nS/input **(B)**, 4 nS/input **(C)**, and 10 nS/input **(D)**). The panels essentially follow the same structure as Fig.3.9 (B). The rate of inhibition ( $f_{inh}$ ) varied between 0 APs/s **(B<sup>1</sup>-D<sup>1</sup>)** and 300 APs/s **(B<sup>2</sup>-D<sup>2</sup>)** shows  $f_{inh} = 200$  APs/s. The  $f_{exc}$  was kept constant at 300 APs/s. The PL functions were modeled the same way for excitation and inhibition, without a time difference between the two functions. Note that stimulation errors occurred, which were excluded from analysis (white box in raster plots in **B<sup>1</sup>&D<sup>1</sup>**).

**(E)** Spike raster plots for the stimulation paradigms shown in **A**, at seven different  $f_{inh}$ . Each stimulation condition was presented ten times.

**(F)** The onset reliability as a function of  $f_{inh}$  for three  $SW_{exc}$ . **F<sup>1</sup>** displays the results of the exemplary neuron shown in **B-E**, and **F<sup>2</sup>** the median of the sample ( $n = 9$ ). Large dots depict the situations shown in **B-D**.

**(G)** Same as **F** but for the sustained rate. **G<sup>2</sup>** displays the mean sustained rate. Horizontal dotted lines indicate the sustained rate at  $f_{inh} = 0$  APs/s to indicate sustained rate suppression and facilitation.

**(H)** Same as **G** but for the modulation index (MI). The MI normalizes the sustained rate to the value at  $f_{inh} = 0$  APs/s. The equation is provided in the text body. Statistics were evaluated by a one-sample two-tailed t-test. Details on statistics are provided in the supplements ([Table S.10](#), [Table S.11](#), and [Table S.12](#)).

---

Inhibition was most effective in reducing the onset APs triggered by  $SW_{exc}$  of 1 nS/input. An onset AP probability of 30 % was achieved by inhibition at a rate of 150 APs/s ([Figs.3.13 F<sup>1</sup>-F<sup>2</sup>](#)). Inhibition was less effective in reducing the onset APs induced by  $SW_{exc}$  4 nS/input stimulations, with the lowest level achieved of ~30 % at  $f_{inh} \geq 200$  APs/s. Conversely, inhibition had limited impact on the onset AP probability induced by stimulations with  $SW_{exc}$  of 10 nS/input, with the lowest onset reliability recorded at 80% ([Figs.3.13 F<sup>1</sup>-F<sup>2</sup>](#)). This demonstrates that large  $SW_{inh}$  (8 nS/input) are most effective in reducing the onset reliability, when paired with a small  $SW_{exc}$  of 1 nS/input.

The bidirectional modulation of the sustained rate (suppression and facilitation) became increasingly evident when evaluating the effect across various  $f_{inh}$  levels. The physiologically most relevant combination displayed an elevation in the sustained AP rate at all levels of  $f_{inh}$ , for both the example neuron and the ensemble ([Figs.3.13 G<sup>1</sup>-G<sup>2</sup>](#)). The higher sustained rate elicited by stimulation with  $SW_{exc}$  of 4 nS/input increased, when combined with intermediate levels of inhibition ( $f_{inh}$  of 100-200 APs/s) before returning to its initial value ([Fig.3.13 G<sup>1</sup>](#)). At the ensemble level, this effect appeared to be diminished, and adding inhibition minimally affected the sustained AP rate ([Fig.3.13 G<sup>2</sup>](#)). Finally, high sustained AP rates, triggered by  $SW_{exc}$  4 nS/input stimulation, were suppressed when adding inhibition at  $f_{inh} \geq 200$  APs/s ([Figs.3.13 G<sup>1</sup>-G<sup>2</sup>](#)).

To statistically assess the AP rate suppression and facilitation, the sustained AP rate was normalized by the MI, which calculates as  $MI = \frac{R_{f_{inh}} - R_{f_{inh}=0 \text{ APs/s}}}{R_{max}}$ . Positive values indicate an increase in the sustained rate, compared to the rate elicited at  $f_{inh} = 0$  APs/s, while negative values indicate a decrease in the sustained rate. The sustained rate of the exemplary neuron changed from 52 APs/s to 71 APs/s in Figs.3.13 (B<sup>1</sup>-B<sup>2</sup>) ( $SW_{exc}$ : 4 nS/input;  $SW_{inh}$ : 8 nS/input;  $f_{inh}$  0 and 200 APs/s). The maximal rate of 74 APs/s was induced by  $f_{inh} = 150$  APs/s. The equation solves as  $MI = \frac{71 \text{ APs/s} - 52 \text{ APs/s}}{74 \text{ APs/s}} = 0.26$  (Fig. 3.13 H<sup>1</sup>). The effects observed before are reflected in this analysis and adding inhibition reliably and significantly increased the sustained rate across all  $f_{inh}$  when combined with  $SW_{exc}$  of 1 nS/input (Fig.3.13 H<sup>2</sup>). In contrast, significant suppression of the sustained rate only occurred at the largest  $SW_{exc}$  (10 nS/input) in combination with the highest  $f_{inh}$  of 300 APs/s. Although significant the effect of suppression was moderate, reducing the sustained rate only by -0.27 (Fig.3.13 H<sup>2</sup>).

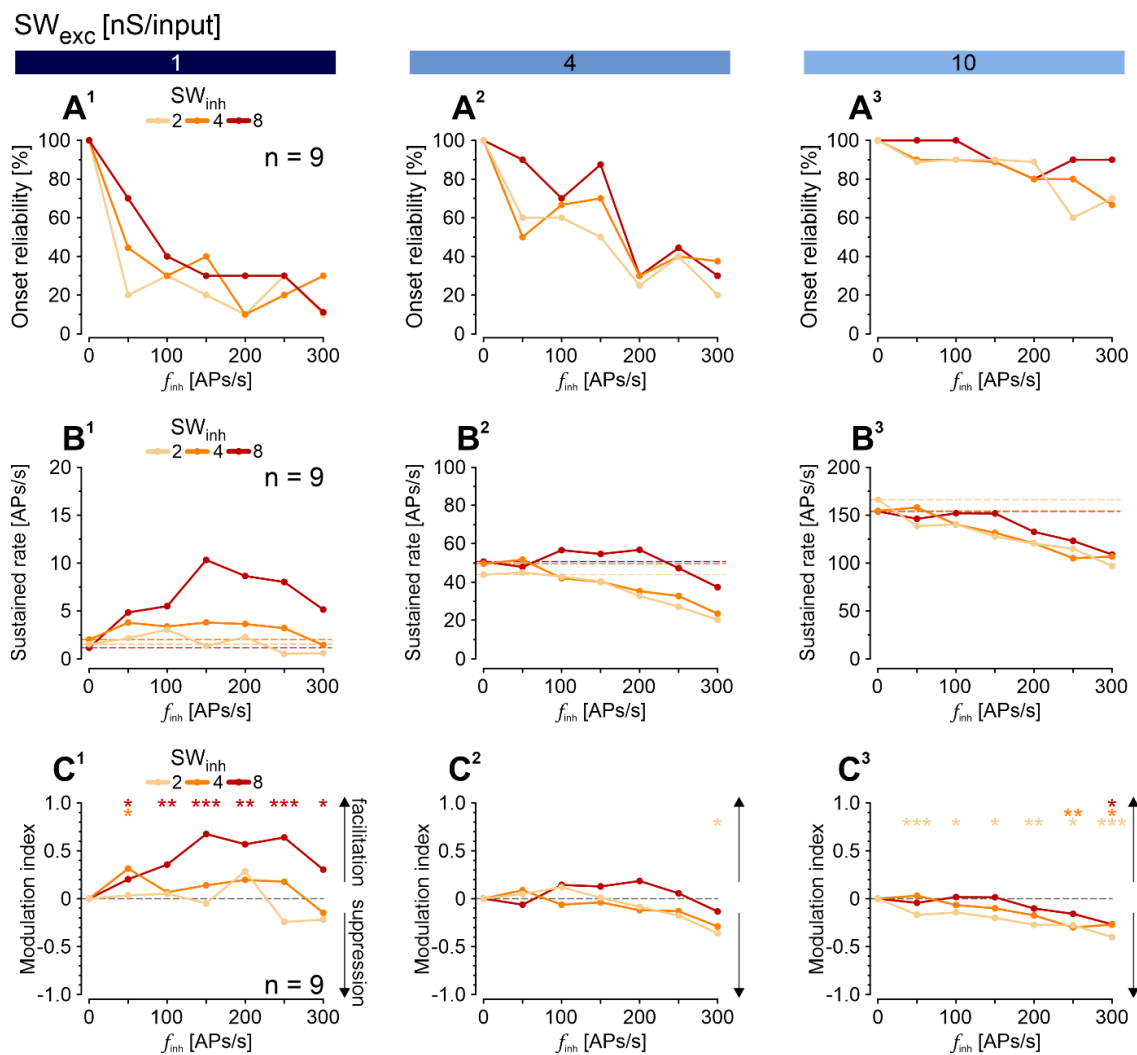


Figure 3.14 Onset reliability is minimally influenced by  $SW_{inh}$ , whereas sustained rate facilitation is enhanced by large  $SW_{inh}$  and suppression by small  $SW_{inh}$ .

**(A)** The median onset reliability as function of  $f_{inh}$  for three  $SW_{inh}$ . Besides the physiologically relevant 8 nS/input, two smaller  $SW_{inh}$  of 4 nS/input and 2 nS/input were tested. **A<sup>1</sup>** depicts the plot for  $SW_{exc}$  of 1 nS/input, **A<sup>2</sup>** for  $SW_{exc}$  of 4 nS/input, and **A<sup>3</sup>** for  $SW_{exc}$  of 10 nS/input. Accompanying figures similar to **Figs.3.13 (A-D)** can be found in the supplementary material (**Fig.5.2** & **Fig.5.3**). The figure presents results from nine neurons (same for **B&C**).

**(B)** Same as **A**, but for the mean sustained rate. Horizontal dotted lines indicate the sustained rate at  $f_{inh} = 0$  APs/s to indicate sustained rate suppression and facilitation. **B<sup>1</sup>-B<sup>3</sup>** show the results in the same way for  $SW_{exc}$  of 1, 4, and 10 nS/input.

**(C)** Same as **B** but for the MI. Significances were tested by a one-sample t-test against zero (dotted gray line).

Statistics were evaluated by a one-sample two-tailed t-test. Details on statistics are provided in the supplements (**Table S.10**, **Table S.11**, and **Table S.12**).

---

The above section described the results of physiological  $SW_{inh}$ . In the next step, I analyzed the effect of decreasing  $SW_{inh}$ . Three levels of  $SW_{inh}$  were tested: 2 nS/input, 4 nS/input, and 8 nS/input (**Fig.3.14**, **Fig.5.2**, and **Fig.5.3**). The onset reliability was reduced to levels of ~20-30% by all  $SW_{inh}$  tested (**Fig.3.14 A<sup>1</sup>**). To assess the inhibitory frequency that was necessary to reduce the AP rate effectively, I calculated the population separability against  $f_{inh} = 0$  APs/s (**Figs.3.15 A<sup>1</sup>-A<sup>3</sup>**, **Sakitt, 1973**). A threshold of one was chosen to determine the  $f_{inh}$  necessary for the population to detect the reduction. For  $SW_{exc}$  of 1 nS/input, this threshold was crossed by adding inhibition at levels as small as 8 APs/s ( $SW_{inh}$  of 2 nS/input), 9 APs/s ( $SW_{inh}$  of 4 nS/input), and 18 APs/s ( $SW_{inh}$  of 8 nS/input; **Fig.3.15 A<sup>1</sup>**). At larger  $SW_{exc}$  of 4 nS/input, the reduction in onset reliability was less pronounced compared to  $SW_{exc}$  of 1 nS/input and reached levels of ~30-40% at the highest  $f_{inh}$  (**Figs.3.14 A<sup>1</sup>-A<sup>2</sup>**). The  $f_{inh}$ s to cause separability accompanying these stimulation combinations were low, with values of 13 APs/s ( $SW_{inh}$  of 2 nS/input), 11 APs/s ( $SW_{inh}$  of 4 nS/input), and 30 APs/s ( $SW_{inh}$  of 8 nS/input; **Fig.3.15 A<sup>2</sup>**). Onset reliability, induced by the largest  $SW_{exc}$  was only slightly reduced, even when paired with the highest  $f_{inh}$  of 300 APs/s (67%-90%; **Fig.3.14 A<sup>3</sup>**). This reduction followed a similar trend for all  $SW_{inh}$  (**Fig.3.14 A<sup>3</sup>**). However, the small reductions in the onset reliability were still detectable by means of the separability analysis (29 APs/s ( $SW_{inh} = 2$  nS/input), 25 APs/s ( $SW_{inh} = 4$  nS/input), and 116 APs/s ( $SW_{inh} = 8$  nS/input); **Fig.3.15 A<sup>3</sup>**). Due to the relatively minor differences in onset reliability, separability is primarily achieved through comparable values of onset reliability across the recorded neurons. In all  $SW_{exc}$  conditions, onset separability was highest for large  $SW_{inh}$  (8 nS/input) and decreased with decreasing  $SW_{inh}$  (**Figs.3.15 A<sup>1</sup>-A<sup>3</sup>**). Collectively, the  $SW_{exc}$  had a more pronounced effect on the rate computation of the onset (**Figs.3.14 A<sup>1</sup>-A<sup>3</sup>**), while  $SW_{inh}$  also influenced the stimulus separability (**Figs.3.15 A<sup>1</sup>-A<sup>3</sup>**).

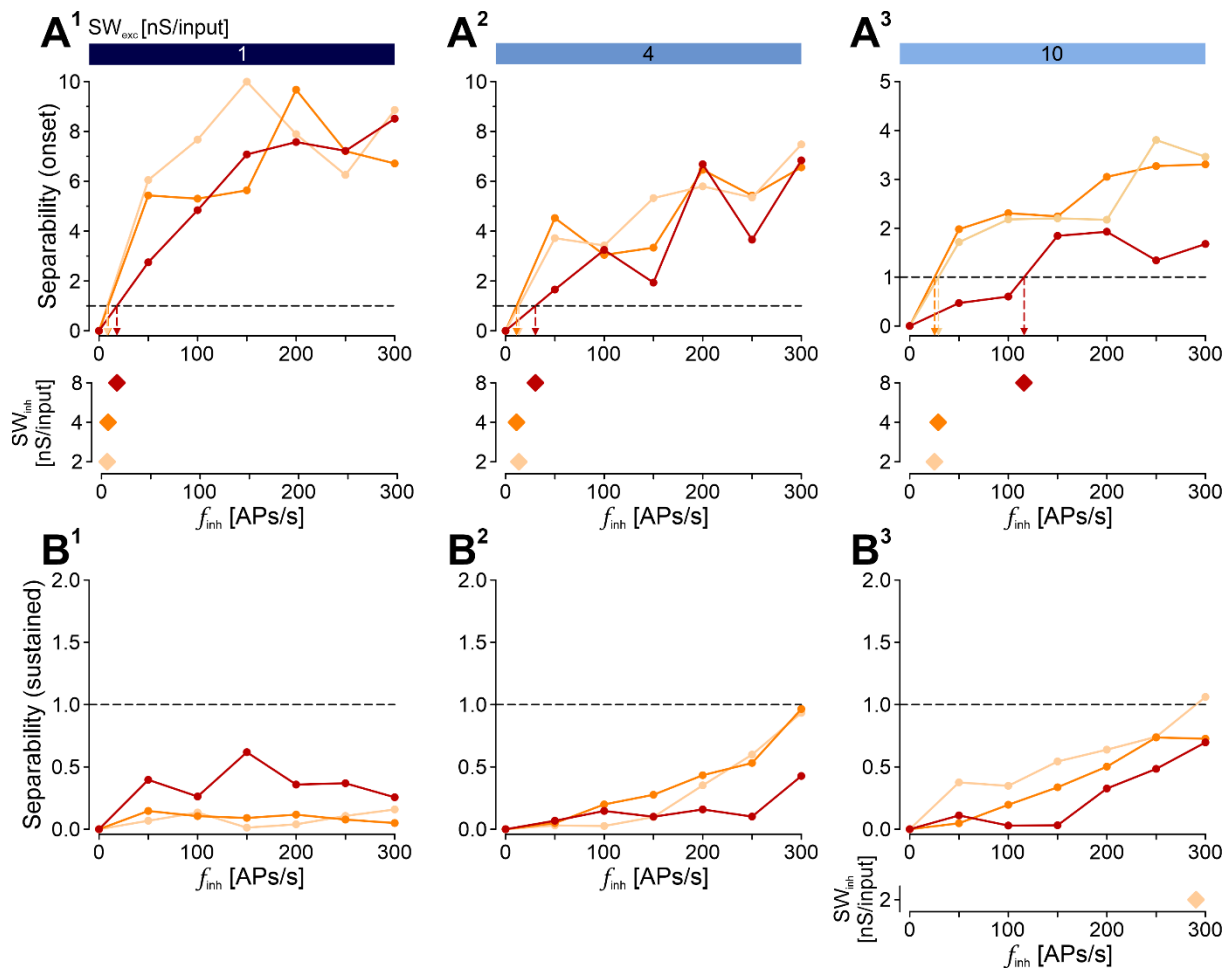


**Figure 3.15** Stimulus separability is reliably reached at stimulus onset, but not in the sustained part.

**(A)** The separability of the onset for three  $SW_{inh}$  levels (4, 8, and 16 nS/input) is shown as a function of  $f_{inh}$ . A threshold of one indicated separable means (grey dotted line). The  $f_{inh}$  crossing this threshold represents the required inhibitory drive to separate the conditions. Separability is assessed for three  $SW_{exc}$  configurations: 1 nS/input (**A<sup>1</sup>**), 4 nS/input (**A<sup>2</sup>**), and 10 nS/input (**A<sup>3</sup>**).

**(B)** Similar as **(A)** but for the stimulus' sustained part. Note that only one  $SW$  configuration crossed the separability threshold (**B<sup>3</sup>**).

The sustained part of the stimulation was analyzed using the mean AP rate and the modulation index (Figs. 3.14 B-C). The above observations (Figs.3.13 F-H) indicated that adding inhibition often resulted in an increased AP rate, rather than demonstrating a suppressive effect. This facilitating effect was strongest, when weak  $SW_{exc}$ s (1 nS/input) were combined with strong  $SW_{inh}$  (8 nS/input; Figs.3.14 B<sup>1</sup>&C<sup>1</sup>). This gradually changed to suppressive inhibition with increasing  $SW_{exc}$  and decreasing  $SW_{inh}$  (Figs.3.14 B<sup>1</sup>-B<sup>3</sup> & C<sup>1</sup>-C<sup>3</sup>). More generally, AP rate facilitation was promoted by small  $SW_{exc}$  and large  $SW_{inh}$ , and the opposite was true for AP rate suppression. Intermediate  $SW$  levels minorly influenced the sustained rate of LSO neurons (Figs.3.14 B<sup>2</sup>&C<sup>2</sup>). I utilized the population separability to assess, whether the modulation of the AP rate through inhibition had functional significance. The separability remained low across all conditions (Figs. 3.15 B<sup>1</sup>-B<sup>3</sup>) and only exceeded the

threshold of one in a single case, when weak inhibition was combined with strong excitation, i.e., unphysiologically large  $SW_{exc}$  and small  $SW_{inh}$ . This illustrates that despite bidirectional significant changes in the sustained rate, these changes cannot be employed for rate-level coding in LSO neurons.

Collectively, these findings (Fig.3.13, Fig.3.14 & Fig.3.15) indicate that a rate-level code can be employed at the onset of stimulation, when the innervating conductances exhibit the greatest deviations due to the temporally correlated recruitment of numerous inputs. The onset rate-level coding is promoted by small  $SW_{exc}$ , while the  $SW_{inh}$  shows only minor effects. Conversely, sustained integration of temporally uncorrelated input activity is ineffective for extracting rate-level information. In stimulation conditions that elicited a low sustained AP rate (small  $SW_{exc}$ ), adding inhibition paradoxically increased the sustained rate. High sustained rates, induced by large  $SW_{exc}$ , were suppressed by about 30 %. Despite these bidirectional changes, the separability analysis revealed that the AP rate modulations by inhibition were insufficient to induce functional significant changes. This underscores the significance of temporally aligned input patterns for rate-level coding in LSO neurons, such as at the onset of stimulation. In essence, this highlights the critical role of temporal structure in the innervating synaptic conductances.

### 3.3.5 Sinusoidal stimulations reveal band-pass filtering of LSO neurons

The results of the preceding section (section 3.3.4) show that LSO neurons can barely extract any rate-based ILD information from the sustained part of PL stimulations. This part is characterized by temporally uncorrelated (randomly) activity within the excitatory and inhibitory input pathway. Correlated activity of the innervating pathway can be induced by stimulations with amplitude-modulated sound with a high frequency carrier, such as SAM tones, transposed tones, or click stimulations (Joris, 1996; Kopp-Scheinflug et al., 2003; Tolnai et al., 2008; Müller, Jovanovic et al., 2019; reviews: Joris & Trussell, 2018; Owrutsky et al., 2021). In the following setup, I used sinusoidal stimulation patterns to mimic synchronization in the input pathways, to analyze the synaptic integration of temporally correlated inputs in LSO neurons (Fig.3.16 A).

In the first step, I tested the AP driving capacity of excitatory stimulations following sinusoidal activation pattern. To this end, I tested nine  $F_{mod}$ : 5, 10, 20, 50, 100, 200, 500, 1000, and 2000 Hz (Fig. 3.16 A presents three). To analyze how different  $SW_{exc}$ s affect rate and temporal coding, I tested four  $SW_{exc}$  levels: 0.1 nS/input, 1 nS/input, 2 nS/input and 4 nS/input. In such experiments, the coding of the neuron at different  $F_{mod}$  is typically analyzed in two ways: the AP rate is quantified in rMTFs, and the temporal precision of the APs, in means of the VS is quantified in temporal modulation transfer functions (tMTFs).

When stimulating LSO neurons with physiological  $SW_{exc}$  of 1 nS/input, and at a low  $F_{mod}$  of 10 Hz, an exemplary neuron exhibited APs at a rate of 2 APs/s (Fig.3.16 B<sup>1</sup>). The AP rate increased at intermediate  $F_{mod}$ s of 100-500 Hz, peaking at 200 Hz with 93 APs/s, before decreasing towards zero at 1000-2000 Hz (Figs.3.16 C<sup>1</sup>&D<sup>1</sup>, quantified Fig.3.16 E<sup>1</sup>). This indicates that the neuron exhibited band-pass filtering behavior at this low  $SW_{exc}$ . At an elevated  $SW_{exc}$  of 4 nS/input, the same neuron demonstrated an increased rate of 72 APs/s, when stimulated with a 10 Hz sinusoid. At intermediate frequencies, this rate further increased to 134 APs/s at 100 Hz modulation, and at high  $F_{mod}$ s, the rate decreased to 87 APs/s (Figs.3.16 B<sup>2</sup>-D<sup>2</sup> & E<sup>1</sup>), revealing the band-pass filtering effect again. The band-pass filtering was also observed at  $SW_{exc}$  of 2 nS/input, with AP rates falling between those previously mentioned. The lowest  $SW_{exc}$  of 0.1 nS/input resulted in a low AP rate peaking at 33 APs/s at  $F_{mod} = 200$  Hz, yet the band-pass filtering remained appreciable (Fig.3.16 E<sup>1</sup>). A similar firing pattern was observed in 14 neurons, with the mean rMTF reflecting a response trajectory comparable to that of the representative neuron (Fig. 3.16 E<sup>2</sup>). The normalized rMTF functions have been used to quantify the bandwidth, indicating the range of  $F_{mod}$ s the neuron responded to. In other words, it quantifies the sharpness of frequency tuning (Fig.3.16 F). The sharpest frequency tuning was achieved by stimulations with  $SW_{exc}$  of 0.1 nS/input (0.9 octaves), which increased depending on the  $SW_{exc}$  (Fig. 3.16 G). At the physiological level of  $SW_{exc} = 1$  nS/input, the bandwidth was 1.5 octaves, corresponding to frequency cutoffs of ~90 Hz to 320 Hz. At  $SW_{exc}$  of 2 nS/input and 4 nS/input, the bandwidth increased to 2.2 and 2.8 octaves, respectively (Fig. 3.16 G). The results suggest that LSO neurons exhibit highly selective frequency tuning, which is promoted by small  $SW_{exc}$ . This is an important feature for extracting information from rapidly changing signals and implies that LSO neurons play a crucial role in processing amplitude modulations in natural sounds.

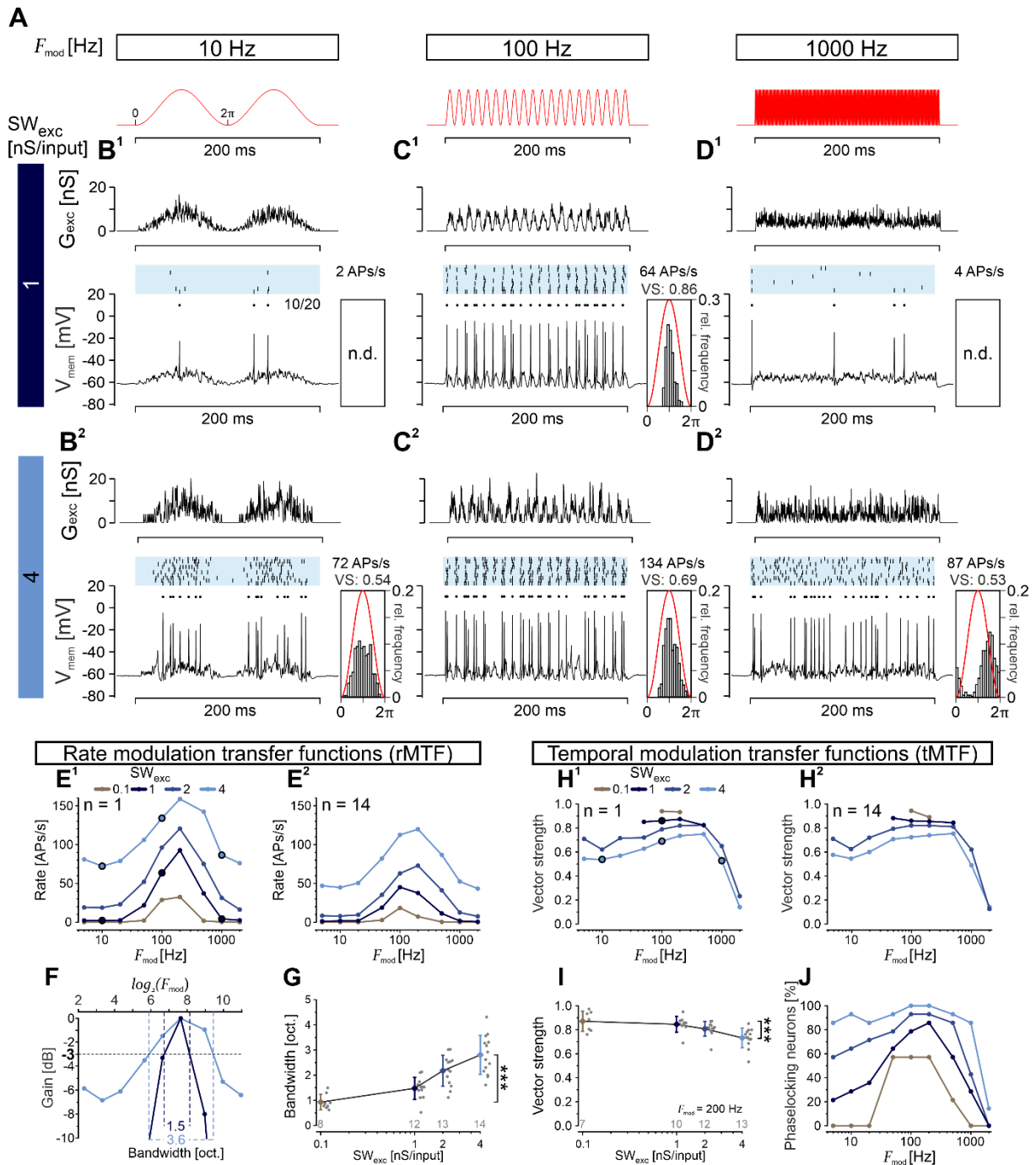


**Figure 3.16** LSO neurons exhibit band-pass filtering in rate modulation transfer functions and low-pass filtering in temporal modulation transfer functions.

**(A)** Sinusoidal functions used to simulate input timings with various  $F_{mod}$ . Depicted are three (10, 100, 1000 Hz) out of nine  $F_{mod}$ s (5-2000 Hz). Further traces are shown in the supplements (Fig.5.5), as well as the rMTFs of single neurons (Fig.5.6).

**(B-D)** Sinusoidal stimulations at three  $F_{mod}$  values depicted in **A** at two  $SW_{exc}$  (1 and 4 nS/input; **B<sup>1</sup>-D<sup>1</sup>** and **B<sup>2</sup>-D<sup>2</sup>**, respectively). The panels essentially follow the same structure as Fig. 3.9 (B). For space reasons, the raster plots show the first 10 of 20 repeats. The panels have been extended by phase histograms, above which the vector strength (VS) is indicated. In instances where the number of APs was less than 20, the VS was not calculated (n.d.).

**(E)** Rate modulation transfer functions (rMTFs) display the evoked AP rate as a function of  $F_{mod}$  tested

at four  $SW_{exc}$  (brown to light blue, see legend in **E**<sup>1</sup>). **E**<sup>1</sup> illustrates the results for the neuron shown above, with larger circles showing the situations depicted in **B-D**. **E**<sup>2</sup> illustrates the sample median of 14 neurons. The analysis was restricted to onset neurons, and five neurons exhibiting multi firing behavior have been excluded from the analysis, as this firing type was rarely observed (**Fig.3.5 E**). The rMTFs of these neurons can be found in the supplement (**Fig.5.7**).

**(F)** Normalized rMTF of  $SW_{exc}$  1 and 4 nS/input from **E**<sup>1</sup> for the calculation of the bandwidth at a cutoff of -3 dB. The values are indicated for both rMTFs. NB:  $\log_2(100) \approx 6.6$  indicates the left dark blue line.

**(G)** The bandwidth as a function of  $SW_{exc}$ . Diamonds show the sample mean  $\pm$  SD, and dots show single cell data. The numbers above the x-axis indicate the number of neurons (out of 14) for which it was possible to calculate a bandwidth. The effect of  $SW_{exc}$  on the bandwidth was tested by a one-way ANOVA,  $p = 3.4e-7$ .

**(H)** Temporal modulation transfer functions (tMTFs) display the VS as a function of  $F_{mod}$  tested at four  $SW_{exc}$ . The panels follow the same structure as in **E**. In cases where fewer than six neurons showed a VS ( $< 20$  APs; see **B-D**), the analysis was omitted.

**(I)** Same as **G** but for the VS determined at  $F_{mod}$  of 200 Hz. The effect of  $SW_{exc}$  on the VS was tested by a one-way ANOVA,  $p = 5.7e-4$ .

**(J)** Similar to **E**<sup>2</sup> and **H**<sup>2</sup> but for the percentage of phase-locking neurons, according to the Rayleigh statistics.

---

The temporal occurrence of APs represents another mode for information transfer. To assess the temporal coding capabilities of LSO neurons, I utilized the VS, and constructed tMTFs. The highest VS, exceeding values of 0.9 was observed for the smallest  $SW_{exc}$  tested (0.1 nS/input), both in an example neuron and across the population (**Figs.3.16 H**<sup>1</sup>-**H**<sup>2</sup>). Stimulations with  $SW_{exc}$  of 1 nS/input exhibited a minor decrease in VS, with values between 0.82 and 0.87 for the example neuron and between 0.84 and 0.88 for the ensemble. VS measurements were feasible only for  $F_{mod}$ s of 100-200 Hz with 0.1 nS/input and 50-500 Hz with 1 nS/input stimulations, because of the low AP rates. At higher  $SW_{exc}$  of 2 nS/input and 4 nS/input, the tMTFs exhibited low-pass filtering behavior (**Figs.3.16 H**<sup>1</sup>-**H**<sup>2</sup>). At a  $SW_{exc}$  of 2 nS/input, the VS values increased slightly from  $F_{mod}$  of 5 Hz (0.71), to reach a peak at 500 Hz (0.82), before abruptly decreasing towards zero at  $F_{mod}$ s of 1000 Hz and 2000 Hz (**Figs.3.16 H**<sup>1</sup>-**H**<sup>2</sup>). For both, the example neuron, and the ensemble, the tMTF of  $SW_{exc}$  of 2 nS/input is  $\sim 0.08$  VS values higher, compared to VS reached by  $SW_{exc}$  of 4 nS/input, indicating higher temporal precision. Statistical influence of the  $SW_{exc}$  on the VS was tested for  $F_{mod}$  of 200 Hz (**Fig.3.16 I**) and for 100 Hz (data not shown). At both  $F_{mod}$ s an increase in  $SW_{exc}$  resulted in a significant decrease in the VS. This indicates that temporal precision is increased by stimulations with many neurons and small  $SW_{exc}$ .

In the final step, I determined the RS to quantify the number of neurons exhibiting significant phase locking (**Mardia & Jupp, 1999; Sayles et al., 2013**). The RS becomes significant when a sufficient number of APs occur in a temporal register within a phase. Therefore, it combines both rate and temporal codes and weights to ensure that an adequate number of APs with temporal precision are present. Across all  $F_{mod}$ s, the highest number of neurons showing significant RS were observed at  $SW_{exc}$  of 4 nS/input, and consistently decreased with smaller

$SW_{exc}$  (Fig.3.16 J). At  $SW_{exc}$  of 4 nS/input, the function exhibited a low-pass filtering profile and transitioned to a band-pass filtering profile with smaller  $SW_{exc}$ . At the  $SW_{exc}$  level of 1 nS/input, most neurons are selective for  $F_{mod}$ s between 50-500 Hz, showing that LSO neurons are well suited to extract amplitude modulations from natural sound.

Together, the above results demonstrate that LSO neurons act as strong band-pass filters for sinusoidal excitatory inputs, with the bandwidth of this filter depending on the  $SW_{exc}$ . Specifically, increasing  $SW_{exc}$  broadens the filter bandwidth, while decreasing it enhances frequency selectivity. This indicates that LSO neurons are particularly sensitive to temporally synchronized inputs within a modulation range of 100 – 500 Hz. They effectively suppress unsynchronized activity. At the physiological  $SW_{exc}$  of 1 nS/input, LSO neurons exhibit sharp frequency tuning, suggesting that this low  $SW_{exc}$  may represent an adaptation to enhance frequency selectivity. In parallel, the tMTFs show that AP precision increases with decreasing  $SW_{exc}$  and thereby enhances the temporal fidelity of LSO neurons' output.

### 3.3.6 Stimulus transients are encoded by LSO neurons at $F_{mod}$ s lower than 1000 Hz

I showed that LSO neurons are capable of following high-frequency sinusoidal activation of 50-500 Hz. However, both the rate coding and the temporal coding decrease at higher  $F_{mod}$ s (see section 3.3.5). The low-pass filtering behavior raises the question of whether this limitation is imposed by the increasing repetition rate of the cycles (i.e., 1 ms at 1000 Hz). Such fast modulations may exceed the neuron's  $\tau_{mem}$ , consequently causing it to integrate over multiple cycles of the stimulus. This is disentangled by a stimulation pattern that maintains the repetition rate but increases the stimulus transience. Such input activity can be caused by click trains, where the repetition rate (here modeled as  $F_{pulse}$ ) is set by the inter-click intervals. The inputs are activated highly synchronously (Müller et al., 2023), which can be modeled by a high  $F_{mod}$  ( $\geq 500$  Hz). Thereby, the transience in the stimulus increases while maintaining the  $F_{pulse}$ .

To test if the stimulus transience limits the coding of LSO neurons, I presented four  $F_{mod}$ s of 100 Hz, 200 Hz, 500 Hz, and 1000 Hz at a  $F_{pulse}$  of 100 Hz (Fig. 3.17 A). For instance, a stimulus with  $F_{mod}$  of 500 Hz and  $F_{pulse}$  of 100 Hz repeats every 10 ms, resulting in an 8 ms pause without stimulation between cycles. In this experiment, I tested a  $SW_{exc}$  of 1 nS/input for the four  $F_{mod}$ s at  $f_{exc}$  (100 – 500 APs/s, in increments of 100 APs/s). Higher  $F_{mod}$ s restrict the APs to occurred in shorter temporal window, thereby increasing summation in the conductance amplitudes. To test LSO neurons with similar conductance amplitudes across  $F_{mod}$ s,  $f_{exc}$  was scaled:  $scaled\ f_{exc} = f_{exc} * \frac{F_{mod}}{F_{pulse}}$ , e.g.,  $20\ APs/s * \frac{500\ Hz}{100\ Hz} = 100\ APs/s$ . I refer to it as  $f_{exc}$  in the text body, while the figure indicates that it is “scaled”.

At the lowest  $f_{exc}$  of 100 APs/s, neurons exhibited very low AP rates across all  $F_{mod}$ s (1-3 APs/s; Figs.3.17 B<sup>1</sup>-E<sup>1</sup> & Figs.3.17 F<sup>1</sup>&F<sup>2</sup>). Due to the insufficient number of APs, determining the VS was not feasible. When  $f_{exc}$  increased to 300 APs/s, the example neuron responded with AP rates approaching 100 APs/s for all  $F_{mod}$ s, except for 1000 Hz (Figs.3.17 B<sup>2</sup>-E<sup>2</sup> & F<sup>1</sup>). At this highest  $F_{mod}$  tested, it fired only 53 APs/s, which was consistent with ensemble observations (Fig.3.17 F<sup>2</sup>). Temporal precision was remarkable at this level, with VS values (based on  $F_{pulse}$ ) exceeding 0.98 for  $F_{mod}$ s of 200-500 Hz, and 0.92 at an  $F_{mod}$  of 100 Hz (Figs.3.17 G<sup>1</sup>&G<sup>2</sup>). The AP rate peaked at 100 APs/s at  $f_{exc}$  of 500 APs/s for  $F_{mod}$ s of 500 and 1000 Hz. For  $F_{mod}$ s of 100 and 200 Hz, there was an increase up to approximately 150 APs/s, indicating multiple APs per sinusoidal cycle (Figs.3.17 B<sup>3</sup>-E<sup>3</sup> & Figs.3.17 F<sup>1</sup>-F<sup>2</sup>). This led to a slight decrease in VS to 0.88 for the example neuron. The ensemble showed exceptional temporal precision for stimulations with  $F_{mod}$ s of 500 and 1000 Hz, resulting in VS values > 0.99. At  $F_{mod}$ s of 200 Hz and 100 Hz, the VS values were still high, ranging from 0.85 to 0.88 for  $F_{mod}$  of 100 Hz and from 0.90 to 0.96 for  $F_{mod}$  of 200 Hz (Fig.3.17 G<sup>2</sup>).

The excitatory rate-level functions of the ensemble (Fig.3.17 F<sup>2</sup>) demonstrated a  $f_{exc}$ -dependent increase in the AP rate for all  $F_{mod}$ s, with the highest  $F_{mod}$  of 1000 Hz showing a right-shifted rate-level function. Replotting the data as a function of  $F_{mod}$ , at  $f_{exc}$  of 200 and 300 APs/s, revealed a significant change in the AP rate depending on  $F_{mod}$  (Figs.3.17 H&J). To quantify the number of neurons responsive to a given stimulus level, I introduced a threshold of 30 APs/s and quantified the number of neurons crossing this value. At a level of  $f_{exc} = 200$  APs/s, more than 80% of the LSO neurons exceeded the value for  $F_{mod}$ s of 100-200 Hz (Fig.3.17 H&I). At  $F_{mod}$  of 500 Hz, half of the neurons remained responsive, while at  $F_{mod}$  of 1000 Hz only 2/12 (17%) were responsive. The number of neurons that crossed this value increased at  $f_{exc} = 300$  APs/s, with > 90 % of neurons showing responsiveness at  $F_{mod}$ s of 100-500 Hz. At  $F_{mod}$  of 1000 Hz, less than 50 % of the neurons were responsive to the stimulus (Fig.3.17 J&K).

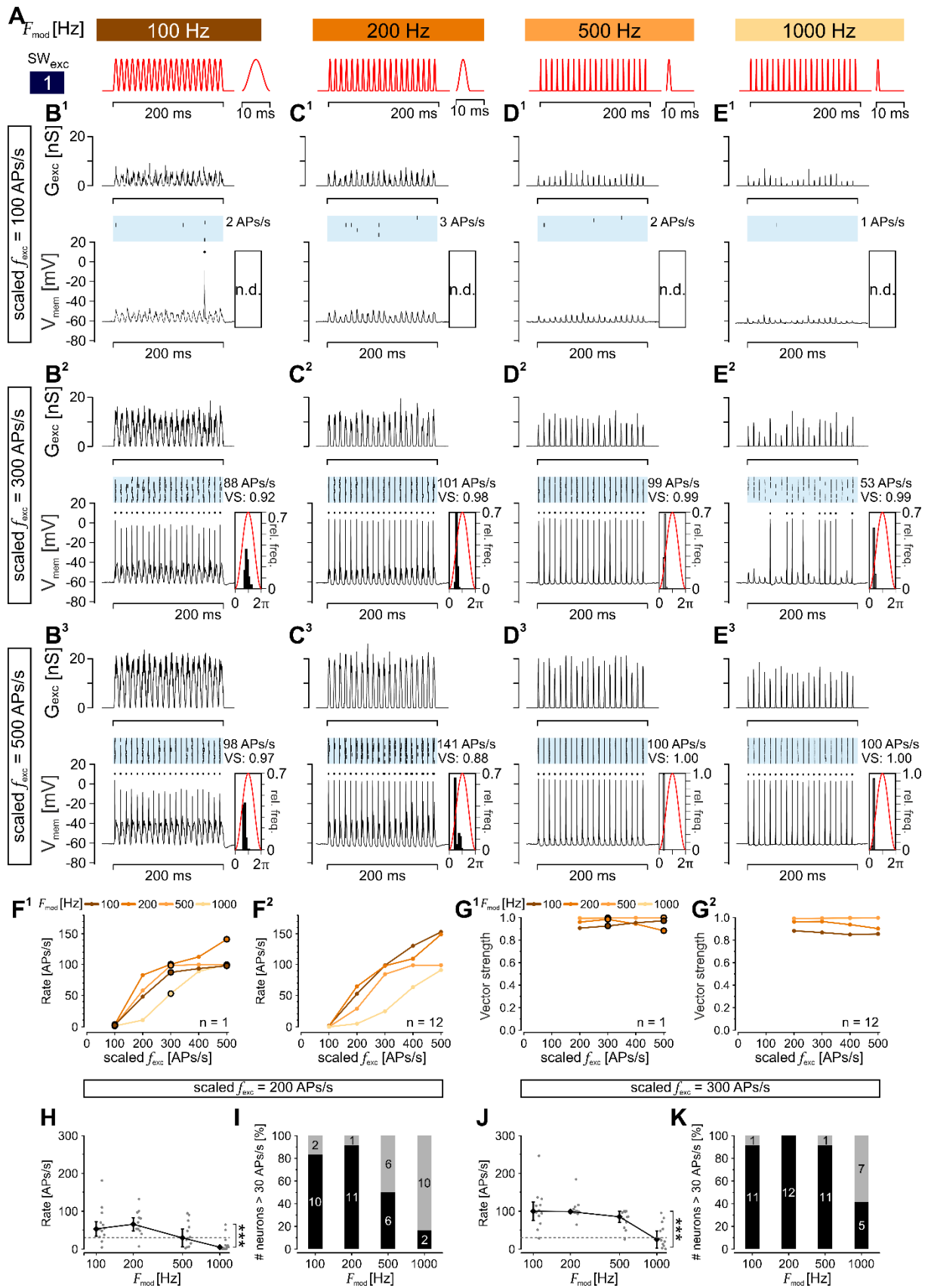


### Figure 3.17 Transient stimuli are reliably encoded up to $F_{mod}$ of 500 Hz.

**(A)** Sinusoidal functions used to simulate input timings with various  $F_{mod}$ s at constant  $F_{pulse}$  of 100 Hz. This  $F_{pulse}$  corresponds to a peak difference of 10 ms. Four  $F_{mod}$  were tested: 100 Hz; 200 Hz, 500 Hz and 1000 Hz. A  $SW_{exc}$  of 1 nS/input was tested. The insets to the right display a single phase of the stimulus to show increasing transientness with increasing  $F_{mod}$ .

**(B-E)** Excitatory rate-level coding tested at five different  $f_{exc}$  (shown are three, 100, 300 and 500 APs/s) at four  $F_{mod}$ s (**B<sup>1</sup>-B<sup>3</sup>** 100 Hz, **C<sup>1</sup>-C<sup>3</sup>** 200 Hz, **D<sup>1</sup>-D<sup>3</sup>** 500 Hz, and **E<sup>1</sup>-E<sup>3</sup>** 1000 Hz). The panels follow the same structure as Fig. 3.16 (B-D), with the same criteria to analyze phase locking.

**(F)** Excitatory rate-level functions show the AP rate as a function of scaled  $f_{exc}$  at four  $F_{mod}$ s. The scaling of  $f_{exc}$  was done to normalize the conductance stimulation to the same amplitude:  $scaled\ f_{exc} = f_{exc} * \left(\frac{F_{mod}}{F_{pulse}}\right)$ . **F<sup>1</sup>** depicts the results of the exemplary neuron shown above, and **F<sup>2</sup>** the sample median of  $n = 12$  neuron. Large circles depict the situations shown above.

**(G)** Same as **F** but for the VS.

**(H)** rMTF at a  $f_{exc}$  of 200 APs/s. Black diamonds show mean  $\pm$  SD and grey circles the single cell data. The grey line highlights the AP rate of 30 APs/s, a value chosen for the analysis in **I**. (NB: at a rate of 30 APs/s ~every third phase was responded with an AP.) A one-way ANOVA was performed to assess statistical influence of the  $F_{mod}$  on the AP rate ( $p = 1.5e-4$ ).

**(I)** Black bars represent the percentage of neurons exceeding 30 APs/s at the four  $F_{mod}$ s, with the white numbers indicating the neuron counts. The grey bars, along with the black numbers, show the percentage of neurons not exceeding this value.

**(J-K)** Same as **H-I** but for a  $f_{exc}$  of 300 APs/s. A one-way ANOVA was performed to assess statistical influence of the  $F_{mod}$  on the AP rate in **J** ( $p = 6.5e-5$ ).

---

The findings showed that stimulus transience can be consistently encoded in LSO neurons, if the input neurons synchronize their AP to modulation frequencies  $\leq 500$  Hz. This implies that optimal encoding by LSO neurons does not occur when excitatory inputs are perfectly synchronized, but rather, when there is a certain degree of temporal variability among the different inputs. Importantly, the sensitivity of LSO neurons decreases for sinusoidal activations with  $F_{mod} \geq 1000$  Hz. The temporal coding of LSO neurons to such stimulation is superior, with a high degree of phase locking at all  $F_{mod}$ s.

### 3.3.7 Transient stimuli enable ILD computation

In the preceding section (see section 3.3.6), I demonstrated that LSO neurons are capable of coding transient amplitude-modulated input signals at high  $F_{pulse}$  of 100 Hz. However, this does not imply that the neurons can extract meaningful information for ILD computation. Prior observations showed that separability values were low when stimulated with a PL stimulation pattern, even when AP rates triggered by excitation were high (see section 3.3.4). To determine whether LSO neurons are more sensitive to level-difference cues when stimulated with amplitude-modulated input signals, pulsed-sinusoidal innervation patterns of excitation and inhibition were presented together.

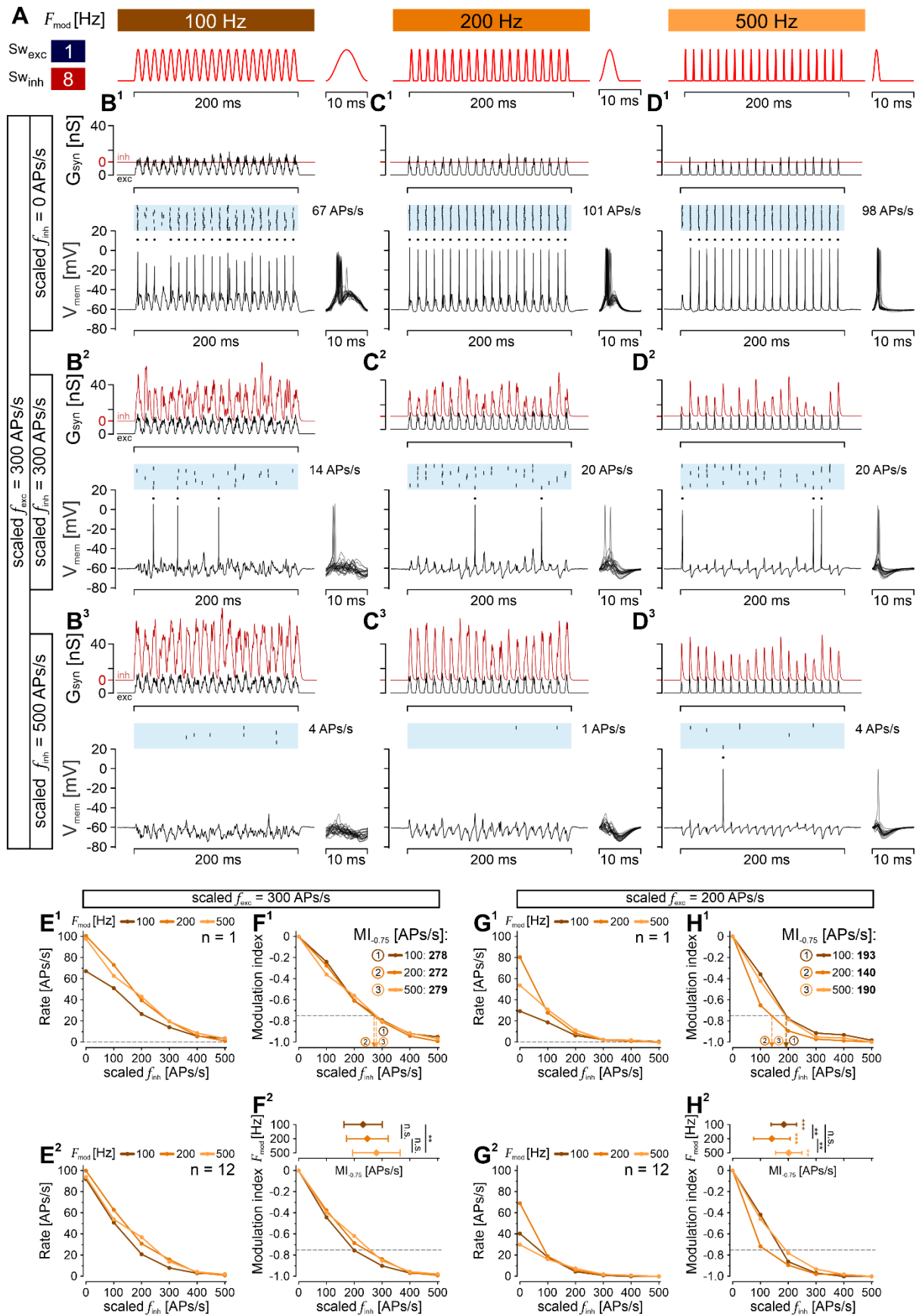


Figure 3.18 Level difference coding is enabled by transient stimuli with highest sensitivity at  $F_{mod}$  of 200 Hz.

**(A)** Excitation-inhibition integration was analyzed using  $SW_{exc} = 1$  nS and  $SW_{inh} = 8$  nS. The same  $F_{mod}$  and  $F_{pulse}$  conditions as in Fig.3.17 were tested. Analysis of  $F_{mod} = 1000$  Hz was omitted as explained in the results.

**(B-D)** Excitation-inhibition integration at three different  $F_{mod}$ s of 100, 200 and 500 Hz. The panels essentially follow the same structure as Fig.3.17 (B-E) but include the inhibitory conductances and phase overlays of  $V_{mem}$  to show AP sparseness and increasing hyperpolarization. A  $f_{exc}$  (300 APs/s) was tested against six levels of inhibition ( $f_{inh} = 0, 100, 200, 300, 400$  and  $500$  APs/s; shown are 0, 300 and 500 APs/s). Inhibition advanced excitation by 0.2 ms, to be more effective.

**(E)** The impact of inhibition is shown by the AP rate as a function of  $f_{inh}$  for three  $F_{mod}$ s. The  $f_{exc}$  was constant at 300 APs/s. **E<sup>1</sup>** presents the results of the neuron depicted above, while **E<sup>2</sup>** presents the sample median of 12 neurons.

**(F)** The MI plotted as a function of  $f_{inh}$  at a  $f_{exc}$  of 300 APs/s. Only negative MI values were observed. **F<sup>1</sup>** displays the results for the exemplary neuron shown in **B-D** and includes the quantification of the MI-<sub>0.75</sub> ( $f_{inh}$  at which a MI of -0.75 is reached) value for the three  $F_{mod}$ s tested. The MI-<sub>0.75</sub> for the three  $F_{mod}$ s is indicated in the panel. **F<sup>2</sup>** illustrates the sample median (lower plot) of  $n = 12$  neurons. The upper plot shows the MI-<sub>0.75</sub> values for the three  $F_{mod}$ s tested. Diamonds show mean  $\pm$  SD. Black statistics show the within-group comparison and brown to yellow statistics indicate comparison with a lower  $f_{exc}$  of 200 APs/s (**H<sup>2</sup>**). A two-way ANOVA followed by paired t-tests was performed, and alpha levels were corrected for three-way comparison using Bonferroni correction. Details on statistics can be found in the supplements (Table S.13).

**(G-H)** Same as (E-F) but at an excitatory rate of  $f_{exc} = 200$  APs/s.

To evaluate the impact of inhibition on APs triggered by transient excitation, I tested the transient stimulation paradigm in conjunction with physiological  $SW_{exc}$ s and  $SW_{inh}$ s (1 nS/input and 8 nS/input, respectively; Fig.3.18 A). Three levels of  $f_{exc}$  (100 APs/s, 200 APs/s, and 300 APs/s) were examined against six levels of  $f_{inh}$  (0-500 APs/s, in increments of 100 APs/s). The amplitude modulation was presented at a  $F_{pulse}$  of 100 Hz, and four  $F_{mod}$ s were assessed: 100 Hz, 200 Hz, 500 Hz, and 1000 Hz. Combinations, in which neurons showed low responsiveness to an isolated excitatory stimulus were excluded from the analysis. This pertained to all conditions of  $f_{exc}$  of 100 APs/s and to the  $F_{mod}$  was 1000 Hz (Fig.3.17).

Stimulating an exemplary neuron with excitation at  $f_{exc}$  of 300 APs/s, and no inhibition ( $f_{inh} = 0$  APs/s) recapitulated previous findings from Fig. 3.17, with minor differences. Stimulation with  $F_{mod}$  of 100 Hz yielded the lowest AP rate of 67 APs/s (Fig.3.18 B<sup>1</sup>). Both  $F_{mod}$ s of 200 Hz and 500 Hz produced rates of approximately 100 APs/s (Figs.3.18 C<sup>1</sup>&D<sup>1</sup>). The ensemble data were consistent with the previous experiment, indicating that stimulation at all three  $F_{mod}$ s resulted in rates near 100 APs/s (Figs.3.18 E<sup>1</sup>&E<sup>2</sup>). Introducing inhibition alongside excitation at  $f_{inh}$  of 300 APs/s decreased the AP rate by ~80%, irrespective of  $F_{mod}$  ( $F_{mod}$  100 Hz:  $\frac{14 \text{ APs/s}}{67 \text{ APs/s}} = 21 \%$ ;  $F_{mod}$  200 Hz:  $\frac{20 \text{ APs/s}}{101 \text{ APs/s}} = 20 \%$ ;  $F_{mod}$  500 Hz:  $\frac{20 \text{ APs/s}}{98 \text{ APs/s}} = 20 \%$ ; Figs.3.18 B-D & E<sup>1</sup>). At the highest  $f_{inh}$  (500 APs/s), AP occurrence was sparse, reducing the rates to 1-4 APs/s (Figs.3.18 B<sup>3</sup>-D<sup>3</sup>). The decrease in AP rate with increasing  $f_{inh}$  occurred monotonically for both the example neuron and the ensemble data, indicating that inhibition effectively suppressed the AP rate (Figs.3.18 E<sup>1</sup>-E<sup>2</sup>). To assess inhibition efficiency statistically, I calculated the MI,

followed by the calculation of the  $MI_{0.75}$  value. This value represents the  $f_{inh}$ , at which the AP rate was reduced by 75 %. For the example neuron, this occurred for  $F_{mod}$  of 100 Hz at 278 APs/s,  $F_{mod}$  of 200 Hz at 272 APs/s, and  $F_{mod}$  of 500 Hz at 279 APs/s (Fig.3.18 F<sup>1</sup>). At the ensemble level, the value slightly increased with higher  $F_{mod}$ s, resulting in values of  $232 \pm 66$  APs/s for  $F_{mod}$  of 100 Hz,  $247 \pm 72$  APs/s for  $F_{mod}$  of 200 Hz, and  $280 \pm 82$  APs/s for  $F_{mod}$  of 500 Hz, showing a significant increase between  $F_{mod}$ s of 100 Hz and 500 Hz ( $p = 0.001$ ; Fig.3.18 F<sup>2</sup>).

The experiment was also conducted at a lower  $f_{exc}$  of 200 APs/s. At this level, an  $F_{mod}$  of 200 Hz triggered APs most effectively (69 APs/s), while  $F_{mod}$ s of 100 Hz and 500 Hz resulted in lower values (41 APs/s and 30 APs/s, respectively; Fig.3.18 G<sup>2</sup>). This indicates that the highest excitatory drive occurred at an  $F_{mod}$  of 200 Hz, consistent with the results shown in Fig. 3.17. The calculation of  $MI_{0.75}$  values revealed the lowest values for  $F_{mod}$  of 200 Hz ( $141 \pm 63$  APs/s), which were significantly lower compared to  $F_{mod}$  of 100 Hz ( $184 \pm 44$  APs/s,  $p = 0.0006$ ) and  $F_{mod}$  of 500 Hz ( $202 \pm 45$  APs/s,  $p = 0.0007$ ; Fig.3.18 H<sup>2</sup>). This demonstrated that inhibition most effectively blocked APs at  $F_{mod}$  of 200 Hz. All three values were significantly smaller for  $f_{exc}$  levels of 200 APs/s compared to 300 APs/s, indicating that increased excitation must be countered by stronger inhibition (statistic in Table S.13, Figs.3.18 F<sup>2</sup>&H<sup>2</sup>).

Finally, I analyzed the separability to determine whether this stimulus paradigm offers level-difference cues that can be employed by the LSO neurons. The separability was determined for the six stimulation combinations mentioned above, two  $f_{exc}$  (200 and 300 APs/s) and for three  $F_{mod}$ s (100, 200 and 500 Hz; Figs.3.19 A<sup>1</sup>-A<sup>3</sup>). A separability threshold of one was reached at  $f_{inh}$  levels of  $\leq 150$  APs/s in all situations. At  $F_{mod}$  of 100 Hz, stimulations at  $f_{exc}$  of 200 APs/s showed a higher  $f_{inh}$  necessary to reach stimulus separability, compared to  $f_{exc}$  of 300 APs/s (separability reached at  $f_{inh} = 133$  and 115 APs/s for  $f_{exc}$  of 200 and 300 APs/s, respectively; Fig.3.19 A<sup>1</sup>). Similar results were found at  $F_{mod}$  of 500 Hz (separability reached at  $f_{inh} = 147$  and 77 APs/s for  $f_{exc}$  of 200 and 300 APs/s, respectively; Fig.3.19 A<sup>3</sup>). At  $F_{mod}$  of 200 Hz, separability was reached at considerably lower  $f_{inh}$  values of 53 and 66 APs/s for the two  $f_{exc}$  of 200 and 300 APs/s, respectively (Fig.3.19 A<sup>2</sup>). This again highlights the enhanced ILD computation capability at a  $F_{mod}$  of 200 Hz.

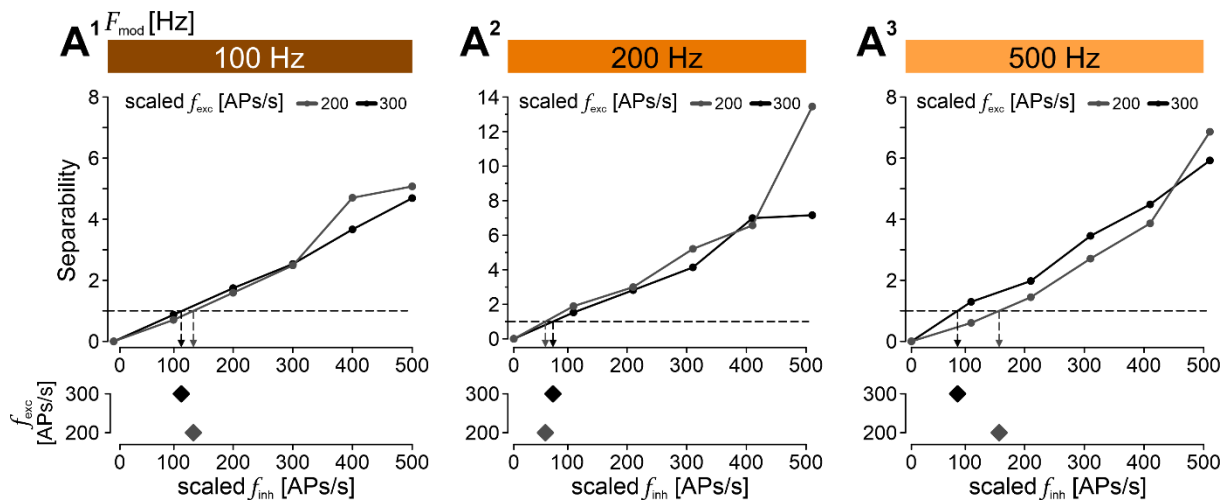


Figure 3.19 Stimulus separability is envelope dependent and showed lowest values for high  $f_{exc}$ .

(A) Separability as a function of the inhibitory rate for two levels of excitation ( $f_{exc}$ : 200, and 300 APs/s). The separability was analyzed on three envelope configurations of  $F_{mod}$ : 100 Hz (A<sup>1</sup>), 200 Hz (A<sup>2</sup>) and 500 Hz (A<sup>3</sup>). A threshold of one was set to achieve stimulus separability, as shown in the lower panels for the different  $f_{exc}$ .

Collectively, these experiments (Fig.3.18 and Fig.3.19) demonstrate effective inhibition when APs are triggered by transient stimulations within a temporally restricted time frame. This indicates that LSO neurons exhibit increased sensitivity to ILD cues, when stimulated with amplitude-modulated signals, potentially enhancing ILD-based sound source localization. The system's adaptive nature requires stronger inhibition to counter higher excitation, ensuring that APs are elicited in ipsilateral LSO neurons when a sound source is lateralized. Conversely, the reduced excitatory drive in contralateral LSO neurons may render their susceptibility to suppression of AP rates through inhibition.

### 3.3.8 Level differences can be extracted across a wide range of time differences between excitation and inhibition.

ILDs as azimuthal sound source localization cues are inevitably connected with ITDs. A change in the horizontal position leads to a change in the level difference, and at the same time entails a change in the arrival times at both ears (Introduction 1.2). These external delays are further increased by internal delays, as described by the “latency hypothesis” (e.g.: Grothe & Park, 1995). Therefore, the rate-based level differences are inevitably connected to differences in the arrival time of excitation and inhibition.

As of now, the experiments were designed to analyze the sensitivity of LSO neurons to changes in rate-based level differences. To understand how level difference coding interacts with time differences imposed on top, I varied both factors in the next experimental setting. The stimulations were presented with a  $F_{mod}$  of 100 Hz, as temporally structured activation of

the inputs is a necessity for temporal coding (Joris & Yin, 1995; Irvine et al., 2001). I tested an excitatory level of 200 APs/s to drive APs in LSO neurons. This excitation was combined with six levels of inhibition ( $f_{inh} = 0, 20, 50, 100, 200,$  and  $500$  APs/s), which I presented at seven time differences ( $\Delta t$ s). Inhibition preceding excitation at  $\Delta t$ s of 0, 0.1, 0.2, 0.5, 1, 2, and 5 ms was tested. According to conventions, positive  $\Delta t$ s refer to inhibition preceding excitation. It has been shown that LSO neurons possess exquisite mechanisms to extract  $\Delta t$ s with preceding inhibition (Beiderbeck et al., 2018). I only tested positive  $\Delta t$ s, to minimize stimulation combinations, reducing recording time and ensuring all combinations could be successfully recorded.

Similar to results presented earlier in this thesis (Fig.3.16), excitation ( $f_{exc}$  of 200 Hz) presented without inhibition at  $F_{mod}$  of 100 Hz resulted in an AP rate of 24 APs/s for the example neuron (Figs.3.20 B<sup>1</sup>&E<sup>1</sup>). Adding inhibition at levels of 100 APs/s reduced the AP rate by 33 %, to 16 APs/s (Fig.3.20 B<sup>2</sup>). Increasing inhibition to 200 and 500 APs/s further decreased the AP rate to 9 APs/s and 1 AP/s, respectively (Figs.3.20 B<sup>3</sup>-B<sup>4</sup>). This monotonic level decrease reflects the previous results of Fig.3.18. Figs.3.20 (C&D) extends this analysis by adding temporal disparities. At a constant  $f_{inh}$  of 100 APs/s, the LSO neurons' AP rate changed minorly, when inhibition preceded excitation by up to 2 ms (16 APs/s at  $\Delta t = 0$  ms; 14 APs/s at  $\Delta t = 0.2$  ms; 13 APs/s at  $\Delta t = 1$  ms; 17 APs/s at  $\Delta t = 2$  ms; Figs.3.20 D<sup>1</sup>-D<sup>3</sup> & G<sup>1</sup>). Further increasing the  $\Delta t$  to 5 ms resulted in a tremendous facilitation of the AP rate to 68 APs/s (>400 % compared to  $\Delta t$  of 0 ms; Fig.3.20 D<sup>4</sup>).

These observations are corroborated by the rate-(inhibitory) level functions of the exemplary neuron for the seven  $\Delta t$ s. The rate-level functions of  $\Delta t = 0$  ms up to  $\Delta t = 2$  ms decreased nearly monotonically with increasing  $f_{inh}$ , and followed a highly similar course, indicating similar inhibitory effectiveness (Figs.3.20 E<sup>1</sup>&F<sup>1</sup>). In strong contrast, the rate-level function at  $\Delta t = 5$  ms showed increased AP rates already at the smallest  $f_{inh}$  tested (20 APs/s). The AP rate increased up to  $f_{inh}$  of 200 APs/s, before it decreased slightly at the highest  $f_{inh}$  tested (Figs.3.20 E<sup>1</sup>&F<sup>1</sup>). Supporting findings were observed at the ensemble level (Figs.3.20 E<sup>2</sup>&F<sup>2</sup>). Swapping the  $f_{inh}$  on the x-axis against  $\Delta t$  further highlights the observed effects. Here the functions for all  $f_{inh}$  showed nearly flat lines of AP rates for  $\Delta t = 0$  to 2 ms and an increased at  $\Delta t = 5$  ms (Fig.3.20 G<sup>1</sup>). The sample median demonstrates a strong resemblance of these results, showing a lot of overlap for the rate-level function of  $\Delta t = 0$  to 2 ms and the facilitatory effect at  $\Delta t = 5$  ms (Figs.3.20 E<sup>2</sup>-G<sup>2</sup>).

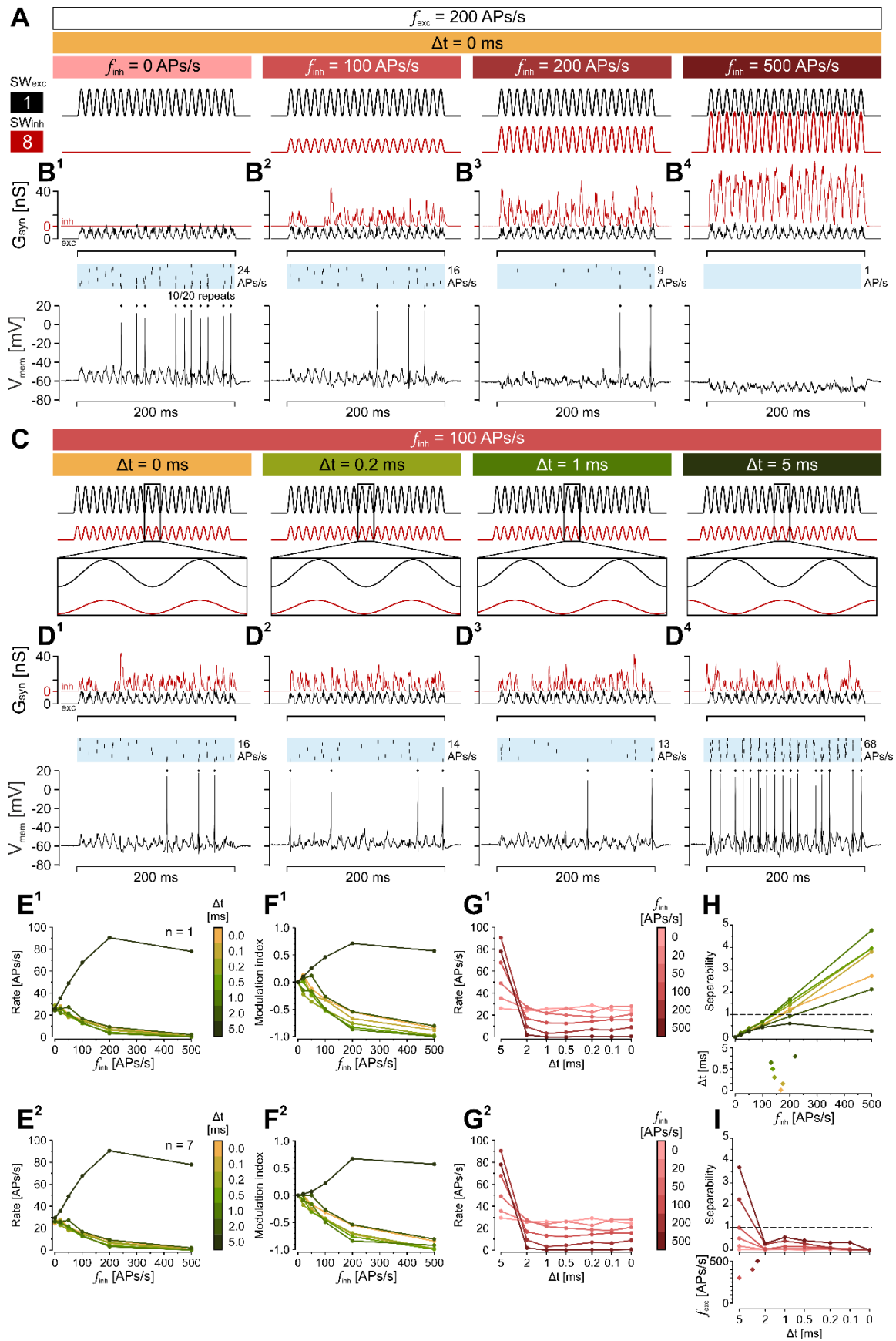


Figure 3.20 Level-difference coding is maintained across a wide range of time differences.

**(A)** Schematics illustrating the stimulation paradigm. A sinusoidal stimulation at  $F_{mod}$  of 100 Hz was employed to analyze level differences (**A**) in conjunction with time differences ( $\Delta t$ , **(C)**). Six levels of  $f_{inh}$  were tested (0 ; 20; 50; 100; 200; 500 APs/s) at a fixed  $\Delta t$  of 0 ms. The  $SW_{exc}$  &  $SW_{inh}$  were used based on physiological values (1 nS/input and 8 nS/input, respectively).

**(B)** Synaptic integration at a constant excitation with varying levels of inhibition ( $f_{inh} = 0$  APs/s (**B**<sup>1</sup>), 100 APs/s (**B**<sup>2</sup>), 200 APs/s (**B**<sup>3</sup>), 500 APs/s (**B**<sup>4</sup>)). The panels follow the same structure as in Fig.3.18 (B-D). Phase overlays were omitted for space reasons. As mentioned above, the stimulation combinations depicted in **B** had a  $\Delta t$  of 0 ms between the excitatory and inhibitory sinusoids. 10/20 repeats of an exemplary neuron are presented in the raster plots.

**(C)** Same as **A** but for various  $\Delta t$ s at a fixed  $f_{inh}$  of 100 APs/s. Seven  $\Delta t$ s were tested (0, 0.1, 0.2, 0.5, 1, 2, and 5 ms). The panels include 20 ms zoom-ins (bottom) to improve visibility of the time difference between the sinusoidal functions. By convention leading inhibition is presented by positive  $\Delta t$  values.

**(D)** Same as **B** but for four  $\Delta t$ s at a fixed  $f_{inh}$  of 100 APs/s. Four of seven  $\Delta t$ s are displayed (0 ms (**D**<sup>1</sup>), 0.2 ms (**D**<sup>2</sup>), 1 ms (**D**<sup>3</sup>), 5 ms (**D**<sup>4</sup>)).

**(E)** The AP rate as function of  $f_{inh}$  for seven  $\Delta t$ s (yellow to dark green; color scale on the right to the plot). The results from the neuron shown in **B** & **D** are displayed in **E**<sup>1</sup> and the median of the sample ( $n = 7$ ) is displayed in **E**<sup>2</sup>. Note that most function follow a similar course, leading to overlap. Only  $\Delta t = 5$  ms stands out clearly (dark green curve).

**(F)** Same as **E** but for the MI.

**(G)** The AP rate as a function of  $\Delta t$  for six different  $f_{inh}$  (pink to dark red; color scale on the right to the plot). The diagrams show the same data as in **E**, but essentially, the x-axis and the color axis are swapped. **G**<sup>1</sup> displays the results from the exemplary neuron, while **G**<sup>2</sup> displays the sample median ( $n = 7$ ).

**(H)** The population separability displayed against  $f_{inh}$  for seven  $\Delta t$ s. The threshold of one was used to extract the  $f_{inh}$  leading to separability and the bottom plot displays these values for each  $\Delta t$ -function that reached separability.

**(G)** Population separability was also calculated against  $\Delta t$  for six  $f_{inh}$ . The  $\Delta t$  at which separability occurred was computed using the same threshold of one. This was only true for three values ( $f_{inh}$  of 100, 200, and 500 APs/s).

---

Moreover, I calculated the population separability for both the rate-level functions and  $\Delta t$  functions. The  $f_{inh}$  and the  $\Delta t$  values crossing the separability threshold of one describe the values necessary to observe a difference to the control situation of either  $f_{inh} = 0$  APs/s or  $\Delta t = 0$  ms. Separable differences in rate-level functions were observable in a range of  $f_{inh}$  of 100 to 250 APs/s (Fig.3.20 H). Although  $\Delta t$ s had a minor influence on the  $f_{inh}$  required for separability, the analysis revealed that inhibition was most effective in suppressing the AP rate when preceding excitation by 1 ms in a 100 Hz modulated input signal (separability at  $f_{inh} = 131$  APs/s; Fig.3.20 H). The separability function for  $\Delta t = 5$  ms did not cross the threshold, suggesting that this  $\Delta t$  cannot be used for reliable ILD coding.

The result that  $\Delta t$  barely influenced the AP rate was reflected in a  $\Delta t$ -separability analysis. An  $f_{inh}$  of  $\geq 100$  APs/s was necessary to detect separable  $\Delta t$ s ( $f_{inh} = 100, 200, \text{ and } 500$  APs/s; Fig.3.20 I). In all three cases, these  $\Delta t$  amounted to  $> 2$  ms (Fig.3.20 I). This suggests that  $\Delta t$ s  $> 2$  ms are necessary to have an impactful influence on the rate-level coding of LSO neurons.

Together, these results demonstrate that LSO neurons can maintain rate-level sensitivity across a wide range of temporal disparities between the activity of excitatory and inhibitory inputs.

### 3.3.9 Time difference coding is enabled by stimulus transience of the envelope

The preceding experimental series (section 3.3.8) analyzed the level-difference coding capability across a range of time differences for a 100 Hz sinusoidal stimulation. The results suggest that temporal disparities do not increase the coding capabilities of level-difference extraction for a wide range of  $\Delta t$ s. This contrasts with the extensive literature, demonstrating high ITD sensitivity of LSO neurons (Park et al., 1996; Irvine et al., 2001; Beiderbeck et al., 2018; Franken et al., 2018; Franken et al., 2021). It must be reflected that the 100 Hz sinusoidal stimulation reflects a temporal input activation pattern, which correlates across a 10 ms cycle. The ITD sensitivity is often tested by transient stimulation with clicks, which elicit a high degree of synchronization in the innervating pathway (Müller et al., 2023). Therefore, I tested the effect of increased temporal precision (increased transience) in the innervating pathway on the time difference coding in the following experimental series.

To analyze the influence of increasing transience on the temporal coding in LSO neurons, I used similar sinusoidal patterns as in Fig.3.17 & Fig.3.18 to simulate excitatory and inhibitory input activations ( $f_{exc}$  and  $f_{inh}$  were 200 APs/s for  $F_{mod}$ s of 100 and 200 Hz, and 100 APs/s for  $F_{mod}$ s of 500 and 1000 Hz). A constant pulse rate of  $F_{pulse} = 100$  Hz was combined with four  $F_{mod}$ s (100, 200, 500, and 1000 Hz). Temporal disparities between excitation and inhibition were tested across a full cycle of  $F_{pulse}$ , specifically  $\pm 5$  ms (every 0.5 ms between 5 and 2 ms and 0.25 ms between 2 and 0 ms, resulting in 29  $\Delta t$ s). Fig.3.21 presents the results of an exemplary neuron at  $F_{mod} = 200$  Hz and lists all  $\Delta t$ s (Fig.3.21 C). Seven stimulation conditions are highlighted, including stimulations from  $\Delta t = 3$  to -3 ms (Figs.3.21 A&B). At positive  $\Delta t$ s (preceding inhibition), inhibition was not effective in reducing the AP rate much below 100 APs/s for  $\Delta t$ s of 5 to 3 ms. Across the next  $\Delta t$ s tested, the AP rate decreased, and only 6 APs/s were observed at  $\Delta t = 1.5$  ms (Figs.3.21 B<sup>1</sup>-B<sup>3</sup> & C). This low AP rate was maintained up to a  $\Delta t$  of -0.5 ms (15 APs/s), before increasing again, reaching levels of  $\geq 100$  APs/s at a  $\Delta t$  of -2 ms.

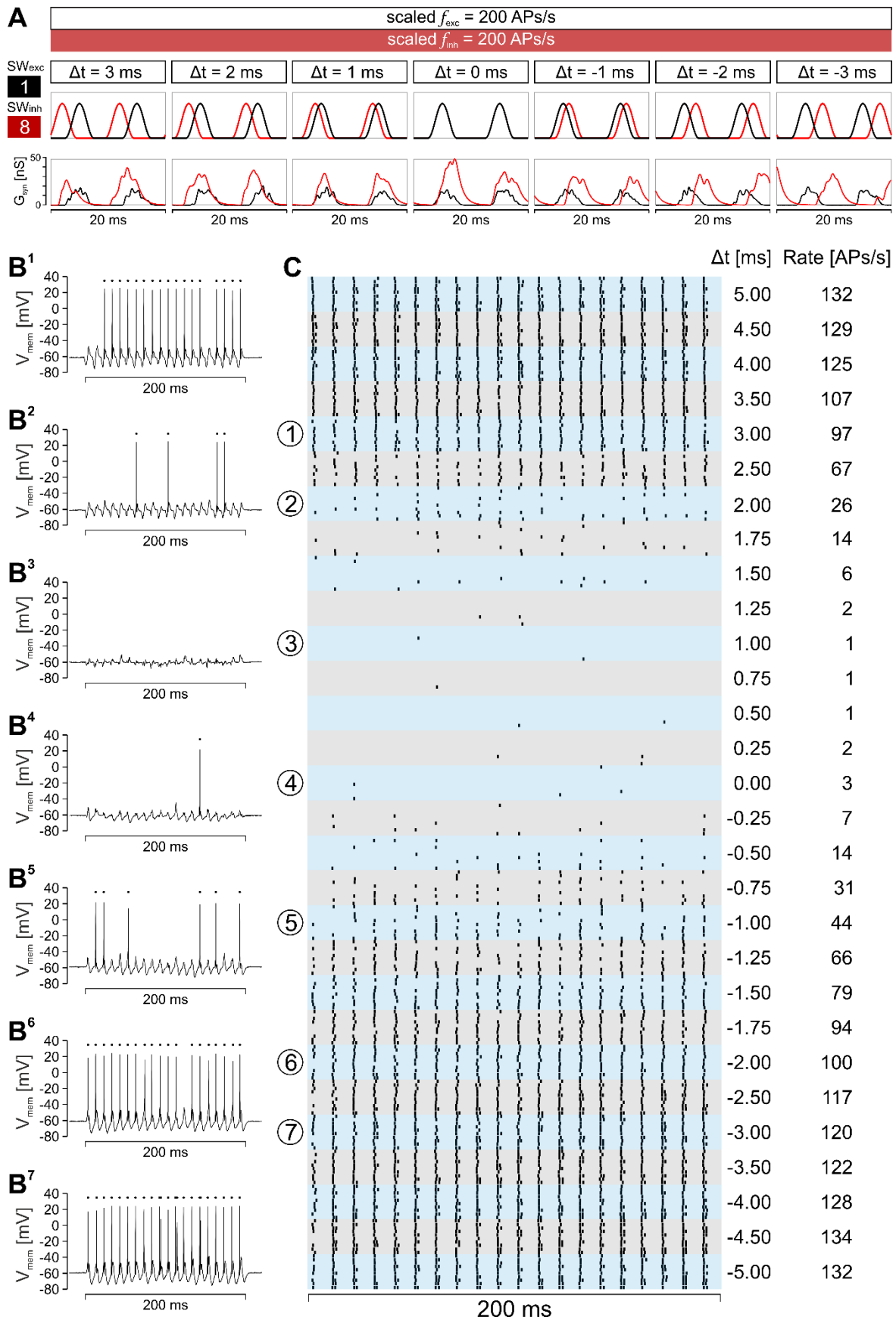


Figure 3.21 Reliable time difference coding by transient stimulations.

**(A)** Schematic of the stimulation protocol analyzing time difference coding. The stimulation duration was 200 ms, but only 20 ms is shown for clarity. Four  $F_{mod}$ s (100, 200, 500 and 1000 Hz) were tested at a fixed  $F_{pulse}$  of 100 Hz, with the synaptic integration of  $F_{mod}$  of 200 Hz depicted here. 29  $\Delta t$  values were tested between excitation and inhibition (seven shown) combined with physiological  $SW_{exc}$  and  $SW_{inh}$ . A total of  $4 \times 29 = 116$  combinations were assessed.

**(B)** Time course of  $V_{mem}$  during the 200 ms of stimulation for the seven  $\Delta t$  values tested (**B<sup>1</sup>-B<sup>7</sup>**). APs elicited by the neuron are marked by dots.

**(C)** Spike raster plots of ten repetitions for the 16  $\Delta t$  values tested at a  $F_{mod}$  of 200 Hz. The numbers on the left assign the situations shown in **B**.  $\Delta t$  is shown right of the raster plots with resulting AP rates next to it.

---

When plotting the AP rate as a function of  $\Delta t$ , the results demonstrated characteristic trough-like functions (Figs.3.22 A&B, Galambos et al., 1959; Joris & Yin, 1995; Franken et al., 2021). In the example neuron, these can be appreciated for  $F_{mod}$  of 200, and 500 Hz (Fig.3.22 A<sup>1</sup>), and after normalization at  $F_{mod}$  of 100 Hz (due to low rate, Fig.3.22 B<sup>1</sup>). At  $F_{mod} = 1000$  Hz, inhibition was not effective in reducing the AP rate of the exemplary neuron below 88 APs/s. In the sample median, inhibition was effective to reduce the trough to 31 APs/s at  $F_{mod}$  of 1000 Hz, and to values close to 0 APs/s for all remaining  $F_{mod}$ s (Fig.3.22 A<sup>2</sup>&B<sup>2</sup>). I analyzed two metrics to characterize the ITD coding of the trough-like functions: the trough half-width and the trough center (center value of the half-width). The trough half-width served as a measure of the effective temporal window of inhibition, while the trough center estimated the  $\Delta t$  of maximal inhibitory effectiveness. Both are indicated for the example neuron in Fig.3.22 B<sup>1</sup>. The neuron demonstrated a decreasing half-width, and trough center, with increasing  $F_{mod}$ . The ensemble showed the highest half-width at  $F_{mod}$  of 100 Hz with  $6.6 \pm 0.7$  ms (mean  $\pm$  SD; Fig.3.22 C). This value decreased exponentially with increasing  $F_{mod}$  to values of  $3.8 \pm 0.8$  ms ( $F_{mod} = 200$  Hz),  $2.1 \pm 1.1$  ms ( $F_{mod} = 500$  Hz) and to  $1.3 \pm 1.3$  ms ( $F_{mod} = 1000$  Hz; Fig.3.22 C). This illustrates that the increase in  $F_{mod}$ , and therefore the increasing transience in the stimulus envelope, can reliably be used by the neurons to sharpen the ITD trough function. The trough center also decreased with increasing  $F_{mod}$  (Fig.3.22 D).

These results revealed that inhibition is very effective in reducing the AP rate, when in temporal register with excitation and the window of effective inhibition is strongly influenced by the temporal synchronization in the inputs. In other words, when excitation and inhibition are highly synchronized, there is a very sharp dependency on the input timings to modulate the AP rate of LSO neurons. When the inputs are less synchronized (as for example in the  $F_{mod} = 100$  Hz situation), the dependency of the temporal occurrence decreases.

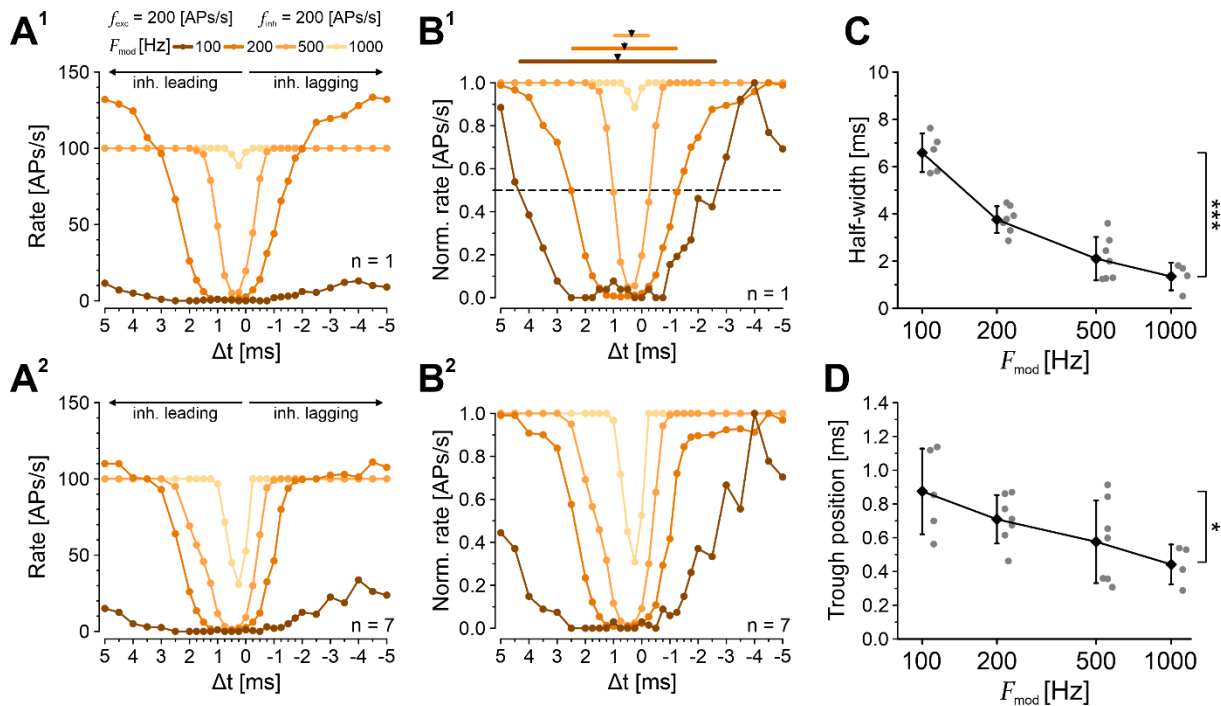


**Figure 3.22** Increasing stimulus transience leads to shorter half-width and shifts the trough center.

**(A)** AP rates based on relative time difference ( $\Delta t$ ) between excitatory and inhibitory inputs for four different  $F_{mod}$ s (100, 200, 500, 1000 Hz) at a  $F_{pulse}$  of 100 Hz. At  $F_{mod}$ s of 100 and 200 Hz,  $f_{exc}$  and  $f_{inh}$  were 200 APs/s, while at  $F_{mod}$ s of 500 and 1000 Hz,  $f_{exc}$  and  $f_{inh}$  were 100 APs/s. **A<sup>1</sup>** displays the results of an example neuron, whereas **A<sup>2</sup>** shows the median of seven neurons. Positive  $\Delta t$  values indicate leading inhibition in relation to excitation, and negative values indicate lagging inhibition.

**(B)** Similar as **A** but for normalized AP rates. In **B<sup>1</sup>**, the dotted line marks the 50 % value, which was used to determine the suppression window's half-width (trough). The bars above indicate this half-width, and triangles mark the trough center. **B<sup>2</sup>** shows the normalized AP rates of the median of seven neurons.

**(C)** Suppression window half-width (mean  $\pm$  SD; black diamonds) as a function of  $F_{mod}$ . Grey dots represent individual neurons. Statistics were evaluated by a one-way ANOVA,  $p = 5.4e-9$ .

**(D)** Same as **C** but for the trough center. Statistics were evaluated by a one-way ANOVA,  $p = 0.02$ .

The data was then tested using a hemispheric ITD coding model (Klug et al., 2020; Pecka & Encke, 2020; Müller et al., 2023). This model assumes that the ITD trough function of an LSO neuron is mirrored by an LSO neuron in the other hemisphere (Fig.3.23 A<sup>1</sup>). The model calculates a separability index based on the differences in AP rates between hemispheres (Figs.3.23 A<sup>2</sup>). Results showed peak separability at an  $F_{mod}$  of 500 Hz, and 200 Hz, while 1000 Hz also yielded high values (Figs.3.23 B<sup>1</sup>&B<sup>2</sup>). The  $F_{mod}$  of 100 Hz crossed the separability threshold, but reached smaller values compared to the other  $F_{mod}$ s. Importantly, the normalized rate difference in the model is very low for  $F_{mod}$ s of 100 and 1000 Hz, which might reduce the impact of the high separability values (Fig.3.23 A<sup>2</sup>). A second metric, extractable of the hemispheric rate difference model, is the  $\Delta t$  coding range, i.e., the range of  $\Delta t$ s that can be used to extract meaningful rate differences from the two populations of LSO

neurons. This was assessed as the  $\Delta t$  values, where the separability functions crossed a threshold of one. The  $\Delta t$  coding range, was highest for  $F_{mod}$  of 200 Hz and decreased in both directions (Fig.3.23 C). Importantly at 200 Hz, the  $\Delta t$  coding range exceeded 1.0 ms, which is a very high value compared to the ITDs naturally occurring for mice (up to 100  $\mu$ s, see Introduction 1.2).

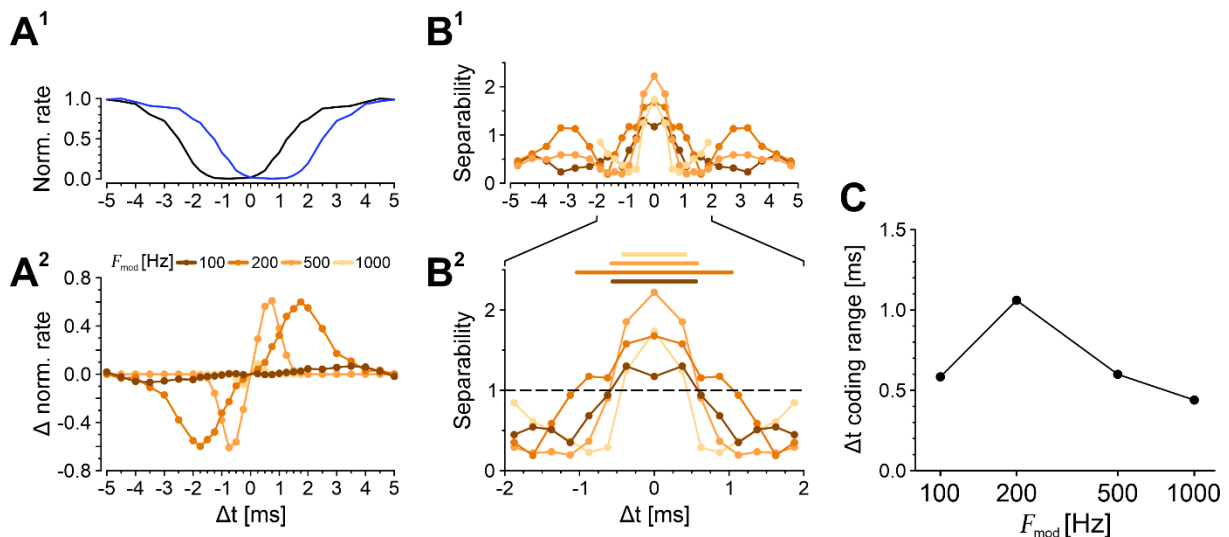


Figure 3.23 Stimulus transience increases temporal separability and limits the temporal coding range.

(A) Hemispheric rate- $\Delta t$  functions for four  $F_{mod}$ s, simulating increasing stimulus transience. Hemispheric rate- $\Delta t$  functions are created by mirroring the rate- $\Delta t$  functions (A<sup>1</sup>) and subtracting them (A<sup>2</sup>). The example in A<sup>1</sup> displays the median normalized rate- $\Delta t$  function from Fig.3.22 (A<sup>2</sup>) of  $F_{mod} = 200$  Hz and A<sup>2</sup> the hemispheric rate- $\Delta t$  functions for all  $F_{mod}$ s.

(B) Separability as a function of  $\Delta t$  for four  $F_{mod}$ s across a full cycle of  $F_{pulse} = 100$  Hz (10 ms; B<sup>1</sup>) and a zoom-in of  $\pm 2$  ms (B<sup>2</sup>). A separability of one was again chosen as coding threshold. The lines on top of the separability functions in B<sup>2</sup> indicate the  $\Delta t$  coding range for each  $F_{mod}$ .

(C) The  $\Delta t$  coding range as a function of  $F_{mod}$ .

These results demonstrate LSO neurons' capability of time difference coding. They suggest that the synchronization in the innervating pathway is a major determinant of temporal coding. Sound transients that elicit a high synchronization in the inputs to LSO neurons can be used reliably for time difference coding, with the best coding capabilities if the inputs are not perfectly coincident but follow a  $F_{mod}$  of 200 - 500 Hz.

### 3.4 *In vivo* characterization reveals adaptive temporal and spatial coding strategies in LSO neurons

The *in vitro* findings are highly suggestive of LSO neurons performing a combined sound source localization strategy, employing time differences and rate-based level differences coding. The results highlight that synchronized activity of the innervating neurons majorly influences the temporal coding. However, such activity also supports level coding. To test if these results are observable in the functional intact LSO circuit, a set of *in vivo* experiments was conducted. The response of LSO neurons to different sound stimuli were tested in cooperation with the group of Dr. Conny Kopp-Scheinflug (Ludwig-Maximilians-Universität Munich) and the recordings were performed by Luna Studer.

#### 3.4.1 *In vivo* recordings reveal onset-dominated firing behavior of LSO neurons to pure tone acoustic stimulations

LSO neurons were stimulated *in vivo* with several stimulation protocols. The first protocol involved pure-tone stimulation at characteristic frequency (CF) to identify the firing type of the neuron. LSO neurons are reported to cover all firing types stereotypical for auditory neurons found in the CN. These include PL, PL with notch, chopper and onset firing behavior (Tsuchitani, 1977; Caird & Klinke, 1983; Tsuchitani, 1988; Joris, 1996). However, others have only observed onset firing neurons (Garcia-Pino et al., 2017). Another group has identified different firing types but concluded that onset firing is typical for principal LSO neurons (Franken et al., 2018). Therefore, the firing behavior in response to pure-tone stimulation at CF is an important variable for interpreting results.

Mice are high-frequency hearing animals and cover a hearing range of ~1-80 kHz (see Introduction). Here, mice were stimulated with pure tones through hollow ear bars, while the activity of isolated neurons was recorded extracellularly. Neurons in the lateral part of the superior olivary complex that were excited by ipsilateral stimulation and inhibited by contralateral stimulation were classified as LSO neurons (Fig.3.24 A).

In an initial step, I analyzed the CF of LSO neurons. The lowest CF recorded was 1.8 kHz and the highest 17.9 kHz ( $9.2 \pm 10.7$  kHz; mean  $\pm$  SD; Fig.3.24 B). The threshold varied from 5 dB to 84 dB with a mean of  $46 \pm 22$  dB. I used PSTHs, constructed from ten repetitions of CF stimulation at 20 dB above threshold, to describe the firing behavior of the neurons (Fig.3.24 C). The exemplary neuron shown in Fig.3.24 (C<sup>1</sup>), exhibited a prominent onset response, which involved two highly precise APs, and was followed by a sustained firing phase, with a ~10 times lower firing frequency. A very similar picture is drawn by the sample mean (Fig.3.24 C<sup>2</sup>). The onset of stimulation was reliably encoded by a maximal rate of  $767 \pm 158$  APs/s and was followed by notch of ~1 ms. Thereafter, the AP rate decreased to a

sustained level of  $160 \pm 142$  APs/s. This illustrates that the population of LSO neurons has an onset-dominated firing behavior. This was further subcategorized to onset firing behavior or sustained firing behavior, by employing an arbitrary threshold of 100 APs/s of the sustained rate. Plotting the onset rate versus the sustained rate highlighted three neurons with sustained rates  $< 100$  APs/s, amounting to 20 % (3/15 neurons; Fig.3.24 D). The remaining 80 % (12/15 neurons) were further classified as sustained firing LSO neurons. Fig.S.8 shows the average PSTHs of the two groups.

Together, the *in vivo* recorded LSO neurons present onset dominated firing behavior, with 20 % of the neurons being classified as onset firing neurons and 80 % as sustained firing neurons.

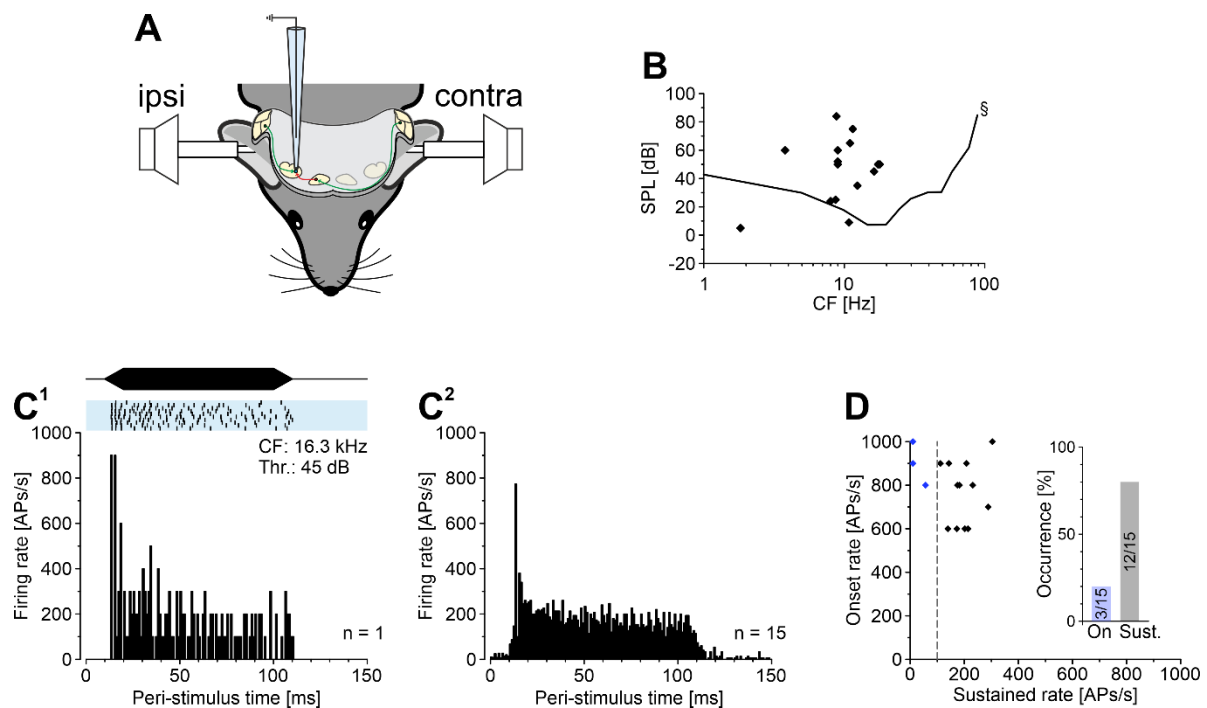


**Figure 3.24 LSO neurons display onset-dominated firing behaviors *in vivo*.**

**(A)** Cartoon depicting the *in vivo* recording setup. Sound stimulations were presented through hollow ear bars and extracellular recordings of putative LSO neurons were performed.

**(B)** The threshold and characteristic frequency (CF) plotted alongside a psychophysically measured mouse audiogram (§ redrawn from Markl & Ehret, 1973).

**(C)** Peri-stimulus time histograms (PSTHs) showing the firing behavior of LSO neurons. **C<sup>1</sup>** Top: spike raster plot of ten repeats, stimulated at CF and 20 dB above threshold (65 dB, contra stimulus = 0 dB) of an exemplary LSO neuron. The stimulus duration is indicated by the black ramped box. Bottom: PSTH of ten repeats, with a bin size of 1 ms. **C<sup>2</sup>** Mean, first peak aligned PSTH for  $n = 15$  neurons.

**(D)** Onset rate plotted against the sustained rate. The onset rate is defined as the maximal rate within the first 10 ms of stimulation, while the sustained rate is the average of the last 50 ms of stimulation. A value of 100 APs/s in the sustained rate was chosen as the cut-off to classify neurons as onset (On) or sustained firing (Sust.). The inset displays the relative abundance of each type, with numbers in the bars capturing the counts.

### 3.4.2 Enhanced ILD coding precision in stimulus onset

We used a classical ILD protocol to characterize the ILD coding capabilities of the neurons. The mice were stimulated ipsilaterally with a tone at CF and 20 dB above threshold, and the contralateral intensity varied between 0 and 90 dB. Similar to the *in vitro* experiments (e.g., Fig.3.13), the analysis focused on an onset phase and differentiated this from the total stimulation time (TST; for comparison with other studies, the onset was not excluded in the TST). Analyzing the AP rate as a function of ILD, revealed a monotonic rate decrease with decreasing ILD (Fig.3.25 A, and blue lines in Fig.3.25 B<sup>1</sup>&B<sup>2</sup>). In the next step, I determined two ILD measures, the dynamic range and the ILD<sub>50</sub> (Figs.3.25 C&D). The dynamic range was significantly smaller for the onset compared to the TST (TST: 40.4 ± 16.6; Onset 17.5 ± 0.9;  $p = 0.013$ ), arguing for an increased precision in the ILD coding (Fig.3.25 C). The ILD<sub>50</sub> describes the ILD that decreased the AP rate by half. This was significantly lower for the onset period compared to the TST (TST: 10.9 ± 15.2; Onset 1.6 ± 0.9;  $p = 0.034$ ; Fig.3.25 D). Thus, the onset APs encoded ILDs with a bias towards the midline compared to the TST. This decrease in ILD<sub>50</sub> was accompanied by a higher correlation with the ipsilateral stimulation intensity as quantified by  $\rho$  (TST: 0.15; On: 0.49; Fig.3.25 E). However  $\rho$  missed significance in both cases (TST:  $p = 0.64$ ; On:  $p = 0.07$ ; but see Tsai et al., 2010; Karcz et al., 2011).

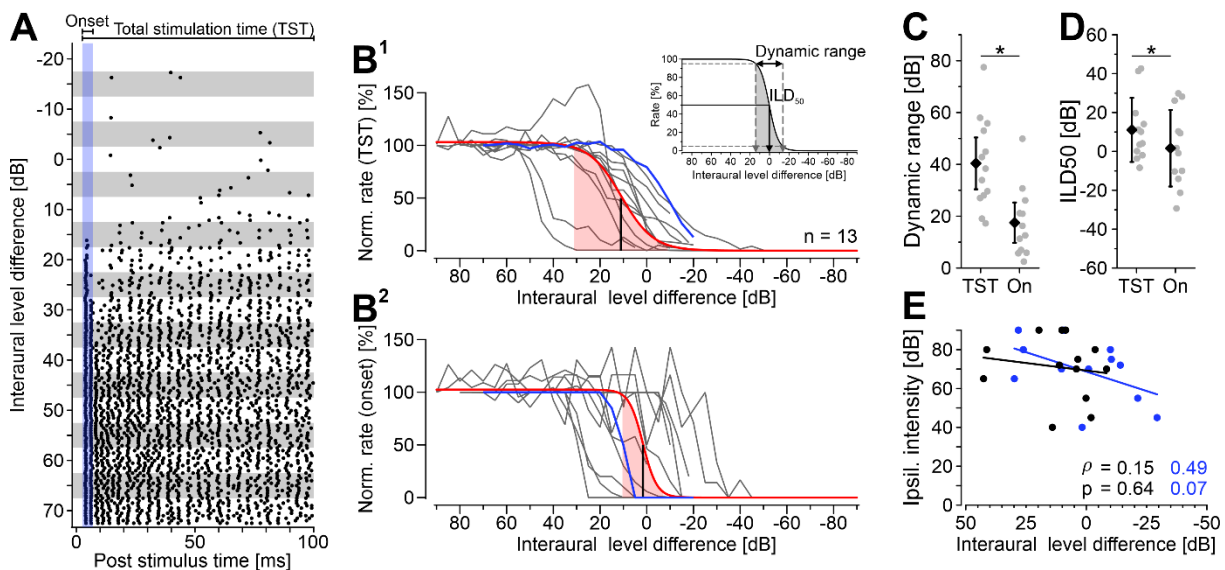


**Figure 3.25 Increased ILD coding precision in onset compared to total stimulation time.**

(A) Spike raster plot across the tested ILD range. The ipsilateral stimulation was fixed at 20 dB above threshold and the contralateral intensity ranged from 0-90 dB. Each ILD was tested ten times. The exemplary neuron was stimulated with an ipsilateral stimulation of 70 dB, resulting in ILD of 70 to -20 dB (tested in 5 dB steps). The blue box indicates the onset analysis period and was adjusted for each neuron. The total stimulation time (TST) started at the same point but continued until the end of stimulation.

(B) The normalized rate as function of ILD for the TST (B<sup>1</sup>) and for the onset rate (B<sup>2</sup>). The blue lines indicate the respective curves of the neuron in A, whereas the red lines show the average across  $n = 13$  neurons. Two ILD measures were extracted by sigmoid fitting from the ILD functions and are displayed for the average curve: ILD<sub>50</sub> (vertical black line) and the dynamic range (pink area). Inset in B<sup>1</sup>:

Illustration depicting the  $ILD_{50}$  and dynamic range computation.

**(D)** The dynamic range compared between the TST and the onset (On). Black diamond illustrates mean  $\pm$  SD and grey circles data of individual neurons. Statistics were evaluated by paired t-test,  $p = 0.013$ .

**(D)** Same as **D**, but for the  $ILD_{50}$ . Statistics were evaluated by paired t-test,  $p = 0.034$ .

**(E)** The ipsilateral stimulus intensity plotted against the  $ILD_{50}$  for the onset (blue) and the TST (black). Circles depict single neuron data and lines linear fits. Pearson correlation coefficients and the accompanying p-value are indicated in the plot.

---

These results demonstrate that LSO neurons compute ILDs more steeply at stimulus onset compared to TST. Combined with the higher firing rate at the onset, this supports an emphasize of ILD encoding at the beginning of stimulations.

### 3.4.3 LSO neurons encode the increase of stimulus transience with increased temporal precision

The *in vitro* experiments had shown a dominant role of stimulus envelope to initiate AP firing in LSO neurons, and transient stimulations were a necessity to allow LSO neurons to perform rate-based level-difference computations (section 3.3.6 & section 3.3.7). Neurons in the afferent pathway (BCs and MNTB neurons) can phase-lock their APs to SAM tones, providing temporally structured inputs to LSO neurons (Joris & Yin, 1998). The influence of increasing transience in the amplitude modulation on LSO neurons' coding is not known. To this end, I analyzed experiments where LSO neurons were stimulated with increasing transience in the sound envelope.

To analyze the capability of LSO neurons to follow envelope structure, tonal stimulations with a broadband noise carrier and different envelope modulations were presented to the ipsilateral ear. The stimulation protocol included three  $F_{pulse}$ s in combination with different  $F_{mod}$ s. The stimulation combinations are highlighted in Fig.3.26 (A). The  $F_{mod}$  was always  $\geq F_{pulse}$  and increasing  $F_{mod}$  led to increasing transience in the stimulus waveform (Fig.3.26 B). The stimulus conditions are denoted as, e.g., pulse20 | mod100, corresponding to  $F_{pulse}$  of 20 Hz and  $F_{mod}$  of 100 Hz. Stimulations lasted 400 ms and thus included eight cycles ( $F_{pulse} = 20$  Hz), 20 cycles ( $F_{pulse} = 50$  Hz) or 40 cycles ( $F_{pulse} = 100$  Hz) of the amplitude modulation.

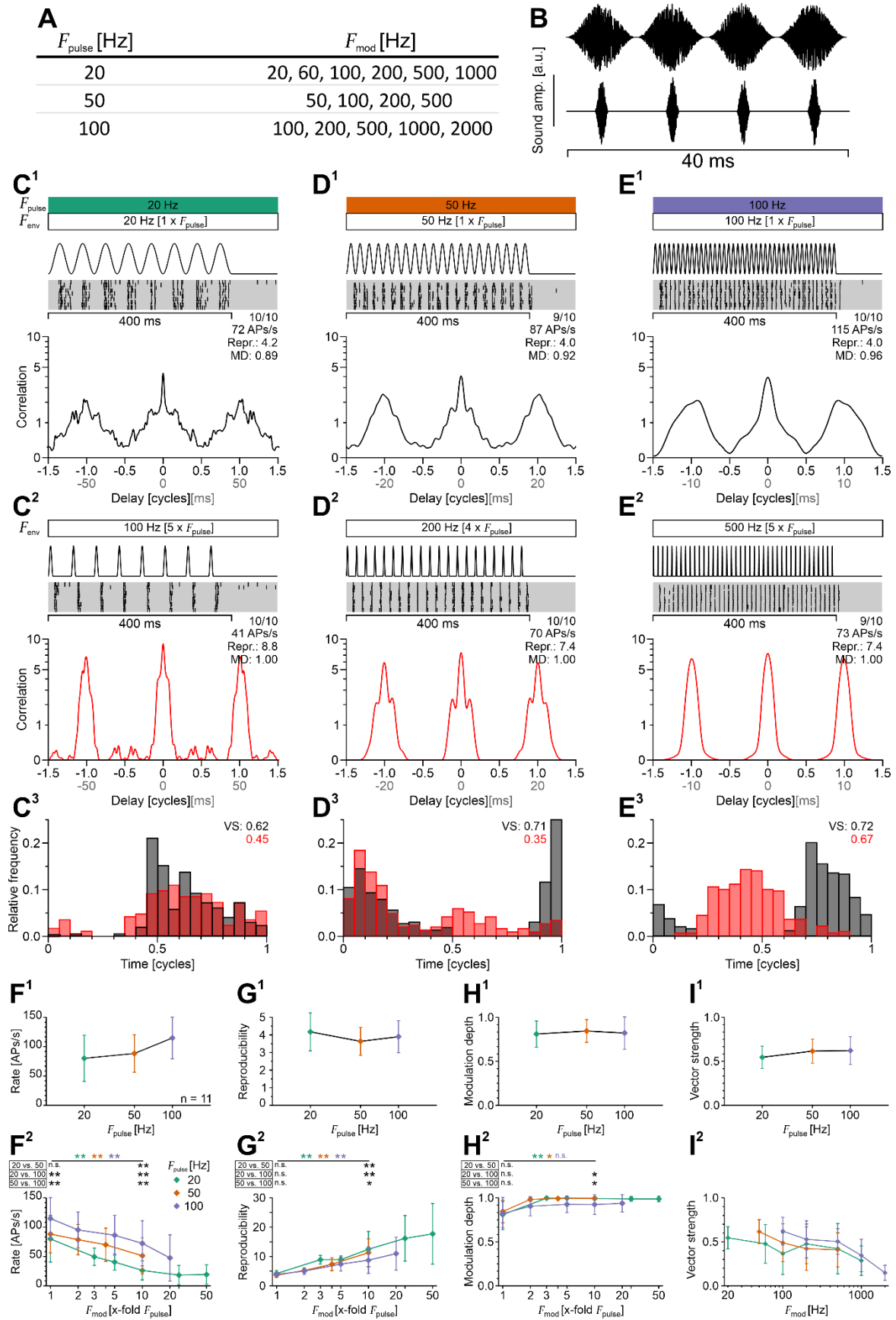


Figure 3.26 Stimulus transience increases temporal precision but decreases firing of LSO neurons *in vivo*.

**(A)** Overview of the tested sinusoidal stimulus conditions. The table lists 15 combinations of  $F_{pulse}$  and  $F_{mod}$  that were presented in an ipsilateral stimulation. The sinusoidal stimulations used a broadband noise carrier.

**(B)** Example waveforms for two representative conditions (top:  $F_{pulse} = 100$  Hz and  $F_{mod} = 100$  Hz, hereafter referred to as pulse100 | mod100; bottom: pulse100 | mod500), illustrating differences in pulse and modulation structure.

**(C)** Effect of increasing  $F_{mod}$  on LSO neuron spiking. **(C<sup>1</sup>)** The top panel presents the stimulus conditions and illustrates the stimulus envelope. The middle panel shows a spike raster plot for stimulation with pulse20 | mod20 of ten repeats. The bottom panel displays a SAC of the AP trains depicted above. The y-axis is scaled logarithmically to enhance the illustration of the sub-correlating space (correlation < 1), given that correlation can increase infinitely. The number of repeats (10/10), the AP rate, the reproducibility (repr.) and the modulation depth (MD) are presented in the top right corner. **C<sup>2</sup>** follows the structure of **C<sup>1</sup>** but for a stimulation with 5-fold increased  $F_{mod}$  (pulse20 | mod100). **C<sup>3</sup>** displays the phase histogram regarding  $F_{mod}$ , of the APs displayed in **C<sup>1</sup>** & **C<sup>2</sup>**. The vector strength (VS) is indicated.

**(D-E)** Same as **C** but for stimulations of pulse50 | mod50 (**D<sup>1</sup>**), pulse50 | mod200 (**D<sup>2</sup>**) and pulse100 | mod100 (**E<sup>1</sup>**), pulse100 | mod500 (**E<sup>2</sup>**) and the respective phase histograms in **D<sup>3</sup>** & **E<sup>3</sup>**.

**(F)** Quantifications of AP rates for 11 neurons under various stimulus conditions. **F<sup>1</sup>** illustrates rate modulation transfer function at  $F_{mod} = F_{pulse}$ . **F<sup>2</sup>** illustrates the effect of increasing  $F_{mod}$  on the AP rate. Diamonds represent median  $\pm$  MAD. The x-axis is scaled in x-fold  $F_{pulse}$ , which allows a comparison between stimulus conditions. Statistics were applied at overlapping stimulus conditions (1-fold  $F_{pulse}$  and 10-fold  $F_{pulse}$ ), using a Friedman test followed by a Wilcoxon signed rank test, due to non-normally distribution. Alpha levels were corrected for three-way comparison using Bonferroni correction. Details on statistics can be found in the supplement (Table S.14).

**(G-I)** Same as **F** but for the reproducibility (**G**; details on statistics in Table S.15), modulation depth (**H**; details on statistics in Table S.16), and vector strength (**I**). The data of the VS was normally distributed and thus display mean  $\pm$  SD. No statistical test was applied to the data in **I** as it is not analyzed as multiple of the  $F_{pulse}$ .

---

First, the AP rate was analyzed. For the exemplary neuron increased with increasing  $F_{pulse}$  from 72 APs/s at pulse20 | mod20 to 87 APs/s at pulse50 | mod50. The highest rate of 115 APs/s occurred at pulse100 | mod100 (Figs.3.26 C<sup>1</sup>-E<sup>1</sup>). This increase was evident on the ensemble level, with significant increases observed when comparing both pulse20 | mod20 and pulse50 | mod50 to pulse100 | mod100 (Fig.3.26 F<sup>1</sup>&F<sup>2</sup>). Increasing the transience of the stimulus by raising  $F_{mod}$  to 10x  $F_{pulse}$  resulted in a decrease of the AP rate at each  $F_{pulse}$  (Figs.3.26 C<sup>2</sup>-E<sup>2</sup> & F<sup>2</sup>). At these higher  $F_{mod}$ s the highest AP rate was again induced by  $F_{pulse} = 100$  Hz. The spike raster plots indicate that neuronal activity aligns with the stimulus envelope (Figs. 3.26 C<sup>1</sup>-E<sup>1</sup>), necessitating a temporal analysis. Temporal correlation was evaluated using three metrics: 1.) reproducibility (peak at delay 0 of the SAC), which analyzed consistency of AP patterns across trials, 2.) modulation depth (MD) to quantify distinctness in sound envelope cycles, and 3.) VS to measure phase-locking ability of neurons to the sound envelope.

The exemplary neuron reached high reproducibility for each stimulus condition across  $F_{pulse}$ s with values of 4.2 for pulse20 | mod20, and 4.0 for both pulse50 | mod50 and pulse100 | mod100 (Fig.3.26 C<sup>1</sup>-E<sup>1</sup>). Increasing transience by 4x or 5x boosted reproducibility by about 2-fold across  $F_{pulse}$  (Fig.3.26 C<sup>2</sup>-E<sup>2</sup>). At the ensemble level, a 10x higher  $F_{mod}$

significantly increased the reproducibility (Fig.3.26 G<sup>1</sup>-G<sup>2</sup>). The high reproducibility was accompanied in all stimulus conditions by high MDs, which sealed at values >0.9 for all conditions at  $F_{mod} > 2 \times F_{pulse}$  (Fig.3.26 H<sup>1</sup>-H<sup>2</sup>). The last metric (VS) requires a brief clarification: the VS is determined in relation to the phase of stimulation and can either be calculated on  $F_{pulse}$  or  $F_{mod}$ . To evaluate the neurons' ability to handle the transience of stimulation, the VS was calculated in relation to  $F_{mod}$ . For each  $F_{pulse}$ , the highest VS was reached at the lowest  $F_{mod}$ , i.e., at  $\text{pulse}20 \mid \text{mod}20$ ,  $\text{pulse}50 \mid \text{mod}50$  and  $\text{pulse}100 \mid \text{mod}100$ . A slight reduction in VS was noted across all  $F_{pulse}$ s up to a  $F_{mod}$  of 500 Hz. Thereafter the VS dropped more pronounced (Fig.3.26 C<sup>3</sup>-E<sup>3</sup> and Fig.3.26 I<sup>1</sup>-I<sup>2</sup>). This aligns with results from *in vitro* experiments (Fig.3.16 H).

The results of these experiments demonstrated an exceptional ability of LSO neurons to follow the stimulus envelope. An increase in the  $F_{pulse}$  led to a higher AP rate, while still conveying the temporal structure of the stimulus (at  $F_{pulse} = 100$  Hz). This highlights a remarkable capability to code temporal structure, such as for example in transient stimulation. This ability may be of functional importance to influence the impact of temporal disparities between excitation and inhibition. The subsequent experimental series aimed to determine, whether neurons remain capable of extracting ILDs reliably from transient stimulations.

#### 3.4.4 ILD coding is maintained with increasing stimulus transience

LSO neurons showed a lower dynamic range in ILD coding at the onset compared to the TST (Fig.3.25). The onset of pure-tone stimulation represents a transient signal, and LSO neurons follow transient stimulation even at a high repetition rate of 100 Hz (Fig.3.26). This raises the question of whether an increase in transience can still be used to employ ILD computation at such high repetition rates. To test this, we combined the pulse stimulation protocol with binaural stimulation.  $F_{pulse}$  was fixed to 100 Hz and three  $F_{mod}$ s of 100, 200 and 500 Hz were tested. The phases of the bilateral presented sounds were temporally aligned, such that no external delay existed.

The raster plots of an exemplary neuron are presented in Figs. 3.27 (A<sup>1</sup>-C<sup>1</sup>) for three  $F_{mod}$ s. The AP rate decreased with increasing  $F_{mod}$ :  $\text{pulse}100 \mid \text{mod}100$ : 107 APs/s,  $\text{pulse}100 \mid \text{mod}200$ : 79 APs/s,  $\text{pulse}100 \mid \text{mod}500$ : 42 APs/s (at ILD +45 dB, contralateral level = 0 dB; Fig.3.27 A<sup>1</sup>-C<sup>1</sup>). This recaptures the effects from the last experimental series (Fig.3.26). Furthermore, the raster plots suggest a similar decrease in the AP rate with increasing contralateral sound intensity (Figs.3.27 A<sup>2</sup>-C<sup>2</sup>), which was corroborated by an overlay of the sigmoidal ILD functions (Figs.3.27 A<sup>2</sup>-C<sup>2</sup> & D).

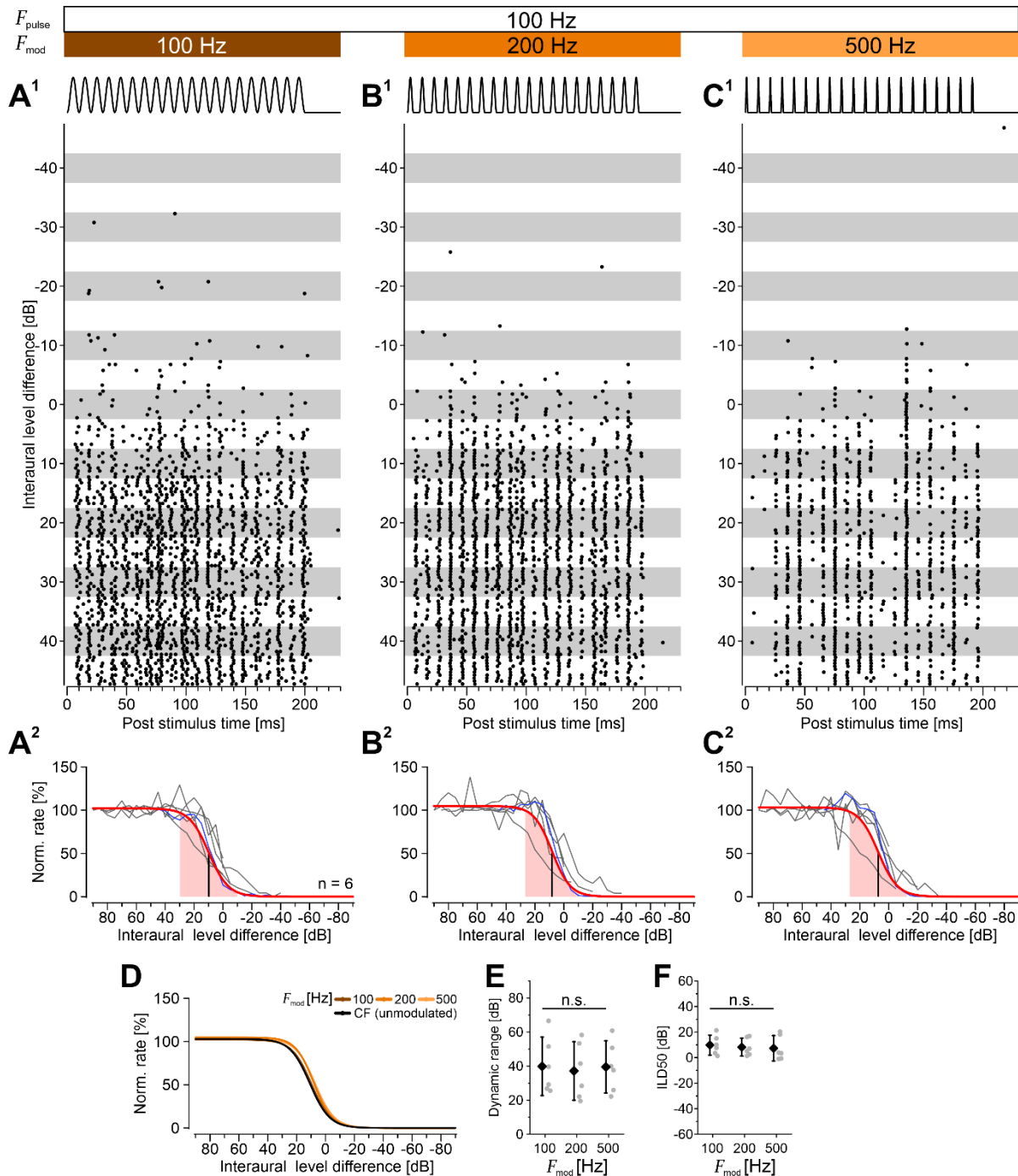


**Figure 3.27** ILD coding is maintained with increasing stimulus transience.

**(A)** ILD coding in a sinusoidal stimulation paradigm of P100\_E100. **A<sup>1</sup>** displays raster plots at 19 different ILDs, each condition presented ten times. Ipsilateral stimulation was fixed to 20 dB > threshold and contralateral intensity ranged from 0-90 dB. **A<sup>2</sup>** displays ILD functions for  $n = 6$  neurons (grey) and the mean ILD function (red). The blue curve depicts the data from the neurons presented in (**A<sup>1</sup>**).

**(B-C)** Similar as **A** but for stimulus condition of pulse100 | mod200 (**B**) and pulse100 | mod500 (**C**).

**(D)** Overlay of the three ILD function from **A-C** (brown to yellow) and the ILD function from the unmodulated stimulation as presented in Fig.3.25 (**B<sup>1</sup>**) (black).

**(E)** Quantification of the dynamic range for the three stimulation conditions. Black diamond display mean  $\pm$  SD. Statistics were evaluated by a one-way ANOVA (not significant).

**(F)** Same as **E**, but for the ILD<sub>50</sub>. There was again no significant effect found.

Analyzing the  $ILD_{50}$  and the dynamic range confirmed this trend by showing virtually identical values for both metrics. The dynamic range was at  $40 \pm 15$  dB (pulse100|mod100),  $37 \pm 15$  dB (pulse100|mod200), and  $40 \pm 13$  dB (pulse100|mod500; Fig.3.27 E). These values are also virtually identical to the dynamic range of the TST from ILD functions at CF ( $40 \pm 17$  dB, Fig.3.25 C). The  $ILD_{50}$  displayed values of  $-10 \pm 7$  dB,  $-8 \pm 6$  dB, and  $-7 \pm 9$  dB (pulse100|mod100, pulse100|mod200, and pulse100|mod500, respectively). Again, these values are similar to the  $ILD_{50}$  value at CF stimulations of  $-11 \pm 15$  dB (Fig.3.25 D).

Collectively, the experiments revealed that LSO neurons maintain a stable dynamic range and consistent  $ILD_{50}$  values across varying  $F_{mod}$ s during high-frequency pulse stimulation of 100 Hz. Although an increase in  $F_{mod}$  resulted in a decrease in the overall AP rate, the neurons demonstrated similar ILD tuning, as evidenced by the comparable dynamic range and  $ILD_{50}$  values under all conditions. These results indicate that increased stimulus transience does not negatively affect ILD coding at high repetition rates and robust ILD extraction is ensured.

## 4 Discussion

In this thesis, I studied synaptic integration mechanisms of LSO neurons in four aspects. First, I studied the synaptic innervation patterns of LSO neurons. Second, I determined the intrinsic biophysical membrane properties of LSO neurons, and studied AP initiation. Third, I used a semi-naturalistic synaptic integration protocol to stimulate LSO neurons in order to study synaptic integration of rate-based level differences and the integration of amplitude-modulated signals and its importance for temporal coding in the LSO. Fourth, I established a cooperation with the group of Dr. Conny Kopp-Scheinflug, where Luna Studer recorded LSO neurons *in vivo*. I analyzed this data to elucidate the behavioral importance of the *in vitro* findings. The results can be summarized as follows:

- I. Excitatory inputs onto LSO neurons have small  $SW_{exc}$  of 1 nS/input, and about 40 inputs converge. These are opposed by four inhibitory inputs, which have large  $SW_{inh}$  as shown in the literature (Gjoni, Zenke, et al., 2018; Müller, Sonntag, et al., 2019).
- II. LSO neurons demonstrated subthreshold membrane properties that are suited for fast signal integration along the tonotopic axis. The neurons showed predominantly onset firing behavior and exhibited biphasic APs, which are initiated in a slope-dependent manner.
- III. I presented an excitatory coincidence detection mechanism in the neurons. The  $SW_{exc}$  played a key role in shaping the excitatory integration, robustly transforming PL input patterns into an onset pattern for physiological  $SW_{exc}$ . This contrasted with *in vivo* findings, where only 20 % of the neurons were onset firing neurons. Moreover, the coincidence detection mechanism led to band-pass filtering behavior in sinusoidal activity. The mechanism underpinned a high sensitivity to stimulus transience, a finding that was corroborated by *in vivo* data.
- IV. To extract rate-based level difference, input activity required temporal correlation. The PL stimulations provided such transience in the onset, whereas the sustained phase was unsuitable for level-difference computation. Level-difference computation was possible with stimulus transience modeled in sinusoidal signal at a high repetition rate of 100 Hz. This finding was confirmed by *in vivo* data. Additionally, the stimulus transience shaped the coding of temporal disparities between excitation and inhibition.

## 4.1 Excitatory synaptic convergence in the LSO: integration of many weak inputs

The strength of excitatory inputs to a neuron are major determinants, whether APs are driven by individual inputs or require summation. Excitatory inputs of LSO neurons have been reported with considerable variability, in terms of input strength and number. Therefore, I conducted a detailed reevaluation of the excitatory innervations to LSO neurons, and constructed a characteristic EPSC template for DC experiments. The estimations of synaptic parameters are crucial as they form the basis for interpreting the DC experiments, where I systematically varied the input strength and input number.

My data indicated small  $SW_{exc}$  (median: 1 nS/input, Fig.3.1), consistent with optogenetic observations by Gjoni, Zenke, et al. (2018). However, 50 % of my recordings displayed a single, large stepwise increases in eEPSC amplitudes, while the other 50 % exhibited a linear increase eEPSC amplitudes with increasing stimulation intensity (Fig.3.1). A limitation of the optogenetic approach is that focal stimulation of synaptic terminals may activate individual boutons, potentially underestimating the full strength of unitary inputs (Gjoni, Aguet, et al. (2018); their Fig.5). Distal electrical fiber stimulations are less susceptible to this but carry their own limitation. Large stepwise increases in the eEPSC amplitudes may reflect the simultaneous activation of multiple converging inputs, possibly leading to an overestimation of unitary input strength. Small incremental increases are thus important to differentiate single inputs. This might explain the higher unitary eEPSC amplitudes reported by some studies (~200 pA by Felix and Magnusson, 2016, and Case et al., 2011) compared to 120 pA (mean) observed here. However, my results are in line with observations of Xiao et al. (2013) and Garcia-Pino et al. (2017), who estimated ~100 pA. A very recent study by Haragopal et al. (2025) estimated four converging excitatory inputs using electrical fiber stimulation. Yet, their functions of eEPSC amplitude versus stimulation intensity displayed a linear profile without distinct steps (their Fig.3). Collectively, these results support the interpretation that individual excitatory inputs to LSO neurons have a weak strength of ~100 pA or ~1 nS.

Reported maximal eEPSC values are similar across the studies (~1 nA, Felix & Magnusson, 2016; Garcia-Pino et al., 2017; Gjoni, Zenke, et al., 2018; Haragopal et al., 2025). This value is slightly higher than the maximal eEPSC values presented here (~750 pA) under improved recording conditions (including QX-314 in the internal solution, Fig.3.1 L). Estimates of convergence vary depending on the unitary strength and analysis method (e.g., simple division of  $\frac{\max eEPSC}{\min eEPSC}$ , or cluster analysis such as k-means based cluster analysis or a Gaussian mixture model). The upper end estimation for convergence, which I found here, is 30 inputs. The excitatory axonal innervations in the LSO show a fanlike arborization in transverse sections (Scheibel & Scheibel, 1974; Friauf & Ostwald, 1988), which makes it likely that some

inputs have been severed in the coronal sectioning procedure. Therefore, 30 inputs may still be a conservative estimate. To this end, I followed the suggestions by Gjoni, Zenke, and colleagues (2018) and used a number of 40 converging excitatory inputs, each contributing with a small  $SW_{exc}$  of 1 nS/input as a proxy for the physiological innervation pattern of BC inputs to LSO neurons (Fig.3.2).

The literature on inhibitory inputs from the MNTB to the LSO is more consistent. The  $SW_{inh}$  can vary largely between individual inputs and have a median  $SW_{inh}$  of about 8 nS (Müller, Sonntag, et al., 2019). The number of converging inputs is about 2-10 (mean ~4, Gjoni, Zenke, et al., 2018; Müller, Sonntag et al., 2019; Haragopal et al., 2025). Accordingly, I used four converging inhibitory inputs with a  $SW_{inh}$  of 8 nS/input as proxy for the physiological innervation pattern to LSO neurons (Fig.3.2).

The estimates of input strength and number yield a compound  $SW_{exc}$  ( $cSW_{exc}$ ) of 40 nS and a  $cSW_{inh}$  of 32 nS. Although they are similar in magnitude, their strength is distributed differently across inputs. The implication of this asymmetry for the integration of rate-based ILD cues and temporal disparities between excitatory and inhibitory inputs will be addressed in the following sections.

## 4.2 Passive and active membrane conductances tune LSO neurons for fast signal integration

Passive and active membrane properties shape the integration of synaptic signals, and determine the computational role of a neuron, whether it operates primarily as a differentiator or an integrator. I used a set of protocols at the beginning of each recording, which allowed me to analyze the membrane properties of LSO neurons. Such active and passive membrane properties vary along the LSO tonotopic axis in various animals, and I investigated this in mice.

The low  $R_{in}$  reported here (46 M $\Omega$ ; Fig.3.3) is a value that is highly comparable to data of others (30-60 M $\Omega$ , Walcher et al., 2011; Garcia-Pino et al., 2017; Fischer et al., 2018; Haragopal & Winters, 2023; one study reports drastically lower values: 18 M $\Omega$ , Choudhury et al., 2020). The  $R_{in}$  of LSO neurons aligns at the lower end, compared to other auditory neurons, such as BCs or MNTB neurons (BC: ~65 M $\Omega$ , Zhuang et al., 2017; Yildirim & Bal, 2018; MNTB neurons: 80 M $\Omega$  Choudhury et al., 2020). Mice have limited low-frequency hearing and they possess a small MSO. The neurons are reported to have very low  $R_{in}$  of about 25 M $\Omega$  (Fischl et al., 2016). Like the  $R_{in}$ , the  $\tau_{mem}$  values reported here (1.5 ms) are comparable to values reported by others (~1-2 ms, see references for  $R_{in}$ ). A very recent review supports these values and provides comparative insights across auditory brainstem neurons (Keine & Englitz, 2025).

The dataset presented here allowed me to perform a correlation analysis of the membrane properties with the neurons position along the LSO tonotopic axis. Such a correlation has been described in other small mammals, like rats (Barnes-Davies et al., 2004), and guinea pigs (Remme et al., 2014), but were not found here (Fig.3.3). Rats and guinea pigs are low-frequency hearing, while mice are high-frequency hearing animals (>1 kHz; Markl & Ehret, 1973; Lauer et al., 2011). If the found effects are caused by low-frequency sensitive LSO neurons (<1 kHz), these mechanisms would be obsolete in mice. The authors of both studies concluded that a lower  $R_{in}$ , in combination with the faster  $\tau_{mem}$  indicate an adaption for enhanced temporal processing of low-frequency tones in the LSO. The temporal processing of the envelope of high-frequency tones may be a reason for mice to exhibit fast membrane kinetics across the whole tonotopic axis.

I found that both, the  $R_{in}$  and the  $\tau_{mem}$  are significantly influenced by the  $V_{mem}$  (Fig.3.3). This indicates that the  $R_{in}$  is partly regulated by low-threshold active conductances. The interaction of two groups of low-threshold voltage-gated channels influence the  $R_{in}$  of auditory neurons: low-threshold Kv channels and HCN channels. The relative conductance of either channel at a given  $V_{mem}$  contributes to the  $R_{in}$  (Golding & Oertel, 2012, their Fig.3C shows an overlay of activation curves of such channels). Low threshold Kv channels, such as Kv1.1, Kv7.2/7.3, Kv11.3 have been shown in the LSO by immunohistochemical experiments (Kv1.1: Karcz et al., 2011) and by single cell patch-sequencing experiments (Kv1.1, Kv7.2/7.3, Kv11.3: Maraslioglu-Sperber et al., 2024). Among the second group, HCN channels, the HCN1 is the dominant subunit in LSO neurons (Leao et al., 2006; Kopp-Scheinflug et al., 2015). I found a significant correlation between the sag amplitude and  $R_{in}$ , as well as an interaction between the sag amplitude and  $V_{rest}$  (Fig.3.3), which further indicates the contribution of HCN channels. Differences in the presence of such channels along the LSO tonotopic axis are absent in mice for Kv1.1 channels (Karcz et al., 2011). In contrast, a gradient of Kv1.1 channels is reported in rats, with higher abundance in the lateral (low-frequency) part of the LSO (Barnes-Davies et al., 2004). For HCN channels, the interaction of sag amplitude with the location, can be used as a proxy for tonotopic differences. I found an absence of such correlation, indicating that HCN channels have a consistent contribution along the putative tonotopic axis in the mouse LSO (Fig.3.3). Conversely, such an interaction is present in the gerbil MSO (Baumann et al., 2013), but direct evidence for the mouse LSO and MSO are lacking. A comparative study on the contribution of low voltage-gated channels in sound processing in the LSO can provide insights into these species' differences (see Outlook for further details).

The steady-state membrane kinetics are major determinants of the sub-threshold resonance properties of the neuronal membrane (Richardson et al., 2003; Fischer et al., 2018) and are influenced by low threshold voltage gated conductances (Wang et al., 2024). The

resonance characteristics ( $Z_{inst}$ ,  $Z_{res}$ ,  $f_{res}$  and the Q factor) align well with earlier reports of membrane resonance properties in LSO neurons of mice (Fischer et al., 2018). Prior studies observed a tonotopic arrangement of LSO neurons exhibiting resonance properties (guinea pig: Remme et al., 2014). I did not find such an alignment here (Fig.3.4). From a functional perspective, the species difference, and the accompanying difference in sensitivity to low-frequency sound might be a reasonable explanation. The dataset presented here on resonance properties includes only ten neurons. Nonetheless, the conclusion is further supported by the absence of tonotopic effects of  $R_{in}$  and  $\tau_{mem}$ .

Differences in LSO neurons based on their transmitter phenotype suggest that excitatory neurons have a higher  $V_m$ , accompanied by a higher  $R_{in}$ , smaller  $\tau_{mem}$ , and smaller sag amplitude (Haragopal et al., 2023). Here I showed that the  $R_{in}$ ,  $\tau_{mem}$ , and the sag amplitude negatively correlate with  $V_m$  (Fig.3.3). This may indicate that the differences between putative excitatory and inhibitory LSO neurons, observed by Haragopal et al. (2023), are based on cellular mechanisms regulating  $V_m$ , rather than differences in the expression of low-threshold channels (e.g., Kv1.1, HCN1). This can be tackled by pharmacological isolation of the currents of low-threshold channels and determine their current density as well as the activation and inactivation kinetics. Single cell patch-sequencing experiments would allow to quantify differences in the expression profiles of such proteins, but also to identify target candidates that might play a role in regulating the  $V_{mem}$ .

Conclusively, sub-threshold membrane properties of LSO neurons are tuned for fast signal processing, involving low  $R_{in}$ , fast  $\tau_{mem}$  and membrane resonance properties. An absence of tonotopic arrangement of these properties, suggests similar tuning for ILD and ITD coding across the sound frequencies.

## 4.3 Regulation of excitability of LSO neurons

### 4.3.1 Extrinsic and intrinsic regulation of excitability in LSO neuron

Beyond their subthreshold membrane properties, I examined LSO neurons for their suprathreshold firing behaviour. A typical protocol to examine neuronal excitability is the step current protocol. LSO neurons responded predominantly with a phasic firing pattern, i.e., onset (single AP) or onset burst firing, characteristic of 'class three excitability' (Hodgkin, 1948; Izhikevich, 2006). A developmental regulation of the firing behavior is suggested by comparing the 93 % of onset firing neurons reported here at > P27 (Fig.3.5), to 60-80 % at P11 (recordings from the same lab; Ebbers et al., 2015, and Hirtz et al., 2011). Recent findings show variations in onset firing depending on neurotransmitter phenotype. In adult mice, excitatory LSO neurons exhibit onset firing in 50 % of cases, while inhibitory neurons do so in 76 % (Haragopal et al., 2023). Combining these values for comparison with my study yields

an average of 60 % (55/89 neurons), a value considerably lower compared to here. However, the extracellular  $\text{Ca}^{2+}$  concentration used here (2 mM) exceeded that used by Haragopal et al. (2025) (1.5 mM), and elevated extracellular  $\text{Ca}^{2+}$  concentration reduces neuronal excitability in MNTB neurons via an unresolved mechanism (Wang & Lu, 2023). Moreover, I used the rheobase from this protocol, to examine differences along the tonotopic axis (Fig.3.5). Like the passive membrane properties, the rheobase showed no such effects, suggesting similar excitability across the frequency range. Together, these findings warrant a systematic investigation of neuronal excitability and how extrinsic factors, like external  $\text{Ca}^{2+}$  concentration, modulate the excitability of LSO neurons.

#### 4.3.2 Rate-dependent AP threshold and spike initiation site in LSO neurons

'Class three excitability' often features a slope-dependent AP threshold, as demonstrated using ramped current protocols (McGinley & Oertel, 2006; review: Prescott et al., 2008). I showed that LSO neurons exhibit a slope-dependent AP threshold, with the lowest threshold between 200-500 Hz, just above rheobase (Fig.3.6). A conductance-based stimulation increased this frequency sensitivity towards 500 Hz, suggesting that non-linear current properties due to the conductance stimulation modulate dynamics of the slope-dependent threshold (Fig.3.8).

A phase-plane analysis revealed biphasic APs (Fig.3.7). These are described to be activations of Nav channels in the somatodendritic compartment and the AIS (Bean, 2007). The slope dependency of the  $V_{\text{thr}}$  suggests that slow input currents cause an inactivation of Nav channels in the somatodendritic compartment but can be employed by the AIS to initiate APs. Conversely, fast rising input signals can trigger somatodendritic spikes. Such a mechanism can be attributed to fast Nav channel inactivation in combination with the activation of low threshold Kv channels (Platkiewicz & Brette, 2011). The two-phasic, overshooting APs distinguish LSO neurons from BCs, octopus neurons, MNTB neurons (Yang et al., 2016, but see also Oertel, 1983 for BCs and Golding et al., 1995 for octopus cells), and MSO neurons (Scott et al., 2005), which show non-overshooting APs with a single phase. Single phasic APs are attributed to a low availability of somatic Nav conductances, which is described as a mechanism optimized for coincidence detection and temporally precise APs (Yang et al., 2016). T-stellate cells and fusiform neurons in the CN, as well as LOC neurons show two-phasic APs (Yang et al., 2016), like the LSO neurons reported here.

In the MSO, all-or-none APs are initiated in the AIS (Scott et al., 2007). During high-frequency activation, increasing Nav channel inactivation shifts the site of AP initiation to nodes of Ranvier, which is supported by thin, myelinated axons (Lehnert et al., 2014). This mechanism extends the dynamic range of rate coded ITDs. Furthermore, in MSO neurons, a negatively shifted inactivation of somatodendritic Nav channels enhances coincidence

detection of synaptic excitation (Scott et al., 2010). Similarly, in the avian analog of MSO neurons, the nucleus laminaris neurons, APs are initiated in the axon, distally from the soma (20-50  $\mu\text{m}$ ), which enhances coincidence detection (Kuba et al., 2006). The AIS enhances the transmission at high (modulation) frequencies, making it an important regulator for high-bandwidth, temporally precise information transfer (Lazarov et al., 2018). The impact of the AIS for AP initiation makes it a susceptible site for structural and functional plasticity. Such plasticity mechanisms regulate the excitability of avian nucleus magnocellularis neurons and support APs with high temporal precision (Kuba et al., 2010; review: Yamada & Kuba, 2016). A computational analysis of AIS plasticity demonstrated the AIS' role in the onset firing behavior of MSO neurons, thereby contributing to the coincidence detection mechanism (Jing et al., 2025). Plasticity mechanisms at the AIS, as well as its regulatory role for high-frequency information transfer, remain to be investigated in LSO neurons (see Outlook). Furthermore, how the soma-axon coupling influences synaptic integration in LSO neurons has not been studied in detail. One investigation points to a critical role for inhibitory synapses targeting the AIS in sharpening ITD functions, particularly for click stimulations (Franken et al., 2021). However, their two-compartment model only included AP initiation in the AIS and did not account for somatodendritic AP initiation.

#### 4.3.3 Molecular determinants of the AP waveform

Molecular determinants of the AP waveform further complicate the picture. Nav channel subtypes differ in activation and inactivation kinetics, shaping excitability (de Lera Ruiz & Kraus, 2015; Bennett et al., 2019). At P11, LSO neurons express *Scn1a* and *Scn8a* genes at high levels, encoding NaV1.1 and NaV1.6 proteins, respectively (Maraslioglu-Sperber et al., 2024). The Nav channel subtypes of mature LSO neurons are not known so far. This gap in knowledge limits our understanding of how these subtypes contribute to ILD and ITD processing in mature LSO neurons.

Rapid AP repolarization in auditory neurons is essential for high-frequency firing, which is mediated by high threshold Kv channels (Johnston et al., 2010; Kaczmarek & Zhang, 2017). In the LSO Kv3.3 channels are functionally important for this performance (Choudhury et al., 2020). However, its specific contribution to ILD and ITD processing in the LSO remains unexplored.

#### 4.3.4 Excitability of LSO neurons *in vitro* and *in vivo*

Importantly, the *in vitro* results of AP firing patterns (Fig.3.5) are not entirely reflected by the *in vivo* results reported here (Fig.3.24). In response to pure tone stimulations only 20 % of neurons showed onset responses, while the majority of 80 % showed sustained firing. Further differentiation into PL or chopper classes were not performed, although chopper firing is often

attributed to LSO neurons (Guinan, Guinan, et al., 1972; Tsuchitani, 1988). A study reporting *in vivo* whole-cell patch-clamp experiments of gerbil LSO neurons recently suggested that LSO principal neurons exhibit onset responses, while they attributed sustained firing to non-principal LSO neurons (Franken et al., 2018). Interestingly, both functional groups exhibited a voltage-sag in response to hyperpolarizing current pulses. Therefore, both groups would probably be considered principal neurons in *in vitro* studies. These functional classifications do not distinguish between the pre- and postsynaptic elements. Therefore, it is possibly that the postsynaptic neurons belong to a molecularly population but differ in their sensitivity to the synaptic inputs. The sustained response of LSO neurons is reduced by anesthesia depth, which further complicates functional allocation (Jing et al., 2021). The authors further report that the afferent auditory pathway is affected by the anesthesia depth, suggesting that the activity of LSO neurons is modulated two-fold: by the activity profile of its presynaptic partners and by intrinsic modulation due to the anesthetic depth.

#### 4.3.5 Concluding remarks on LSO neuron excitability

In conclusion, this section highlights multiple biophysical and molecular mechanisms that regulate LSO neuron excitability. These include developmentally regulated firing behaviors, compartment-specific Nav channel function, and slope-dependent threshold adaptations. Several key mechanisms, particularly those involving Nav channel subtype composition and AIS plasticity remain insufficiently understood. Furthermore, the interpretation of *in vitro* with *in vivo* results is challenging, as an onset firing response *in vitro* cannot simply be translated to onset firing *in vivo*.

### 4.4 Excitatory synaptic integration in LSO neurons

#### 4.4.1 Temporal differentiation by LSO neurons via excitatory coincidence detection

Coincidence detection of excitatory synaptic inputs is a well-established feature of several auditory neurons, such as BC (McGinley & Oertel, 2006), MSO neurons, and octopus cells (Golding & Oertel, 2012). In contrast LSO neurons have classically been seen as integrators, a feature seemingly inconsistent with coincidence detection. However, *in vivo* findings suggested that LSO neurons act as differentiators rather than integrators (Franken et al., 2018). So far, the role of excitatory coincidence detection for AP generation by LSO neurons has only been explored computationally (Ashida et al., 2016). As LSO neurons receive their canonical excitatory inputs from the ipsilateral CN, a coincidence detection mechanism is driven monaurally. In the following, I will discuss results that suffice the role of excitatory coincidence detection by LSO neurons and provide insights into how this coincidence detection might contribute to sound localization via temporal sensitivity.

A coincidence detection mechanism requires that asynchronous inputs fail to elicit APs, whereas synchronized inputs succeed in doing so. The degree of temporal dispersion between converging inputs therefore defines the temporal window within which coincidence detection can occur. Such temporal dispersion has been studied here, by modelling input activity that follows a sinusoidal activation and was compared to an idealized sinusoidal stimulation (Fig.3.8). The minimal  $F_{mod}$  required to elicit APs by LSO neurons was 50 Hz, corresponding to an input correlation within a 20 ms cycle. This was not different between the synaptic model and an idealized sinusoidal conductance, indicating that the intrinsic limitation by the slope-threshold restricts the AP generation. Noise added to sinusoidal stimuli has previously been described to elicit stochastic resonance in MSO neurons (Longtin, 1993; Gai et al., 2009). In such a situation, noise on top of sinusoidal stimulations elicits APs at preferential phases of the sinusoid. However, this phenomenon was not observed in the current study. As was detailed in the results (section 3.2.5), the 50 Hz sinusoid translates to a temporal jitter of 3.3 ms ( $\frac{20 \text{ ms}}{6}$ ). However, not all neurons were responsive to this value. Therefore, I will use a jitter of 1.6 ms (corresponding to a 100 Hz sinusoid) as the maximal temporal jitter that LSO neurons can reliably encode. The highest sensitivity of LSO neurons was reached at temporal jitter of 0.8 – 0.3 ms, resulting from sinusoids of 200 - 500 Hz (Fig.3.8). These findings suggest that the coincidence window of LSO neurons is relatively broad compared to MSO neurons. In the latter nucleus, the AP probability drops to zero if inputs from the two hemispheres are activated with a temporal delay of 0.5 ms. (Jercog et al., 2010; Pecka et al., 2010). This value calculates to a jitter of 0.17 ms (assuming a  $\pm 0.5$  ms window, or 1 ms full range), 10x shorter compared to LSO neuron reported here. In comparison, McGinley and Oertel (2006) report values for the temporal window of integration of 5.3 ms for BCs and 1.4 ms for octopus cells, which allow for temporal jitter values of 0.88 ms and 0.23 ms, respectively. These windows for coincidence detection are about 2-times and 8-times shorter compared to LSO neurons. Notably, first spike latency jitter upon pure-tone stimulation of BCs is about 0.58 ms, placing the highest sensitivity of LSO neurons in a similar range (Rhode & Smith, 1986).

Another finding from this experiment is that LSO neurons became less sensitive to stimuli following 1000 Hz modulations, with sensitivity declining further at 2000 Hz (Fig.3.8). This likely reflects the limited temporal integration capacity of the membrane, where the highly synchronized inputs ( $F_{mod} > 500$  Hz) are less effective at transferring charge compared to less synchronized ones, despite having the same conductance amplitude. This is similar in other auditory neurons like, ventral nucleus of the lateral lemniscus, DNLL and MNTB neurons, while the exceptional short  $\tau_{mem}$  of MSO neurons allows them to effectively convert synaptic inputs into rapid voltage changes (Kladsios et al., 2020), thereby minimizing temporal summation.

High  $F_{mod}$ s of 1000 Hz and 2000 Hz correspond to very small temporal jitter of 0.16 ms and 0.08 ms, respectively. Such small jitter in spike latency can be triggered in BCs by click stimulation (0.18 ms; Müller et al., 2023). Nevertheless, click stimulations trigger highly reliable APs in the neurons. The decrease in sensitivity to these highly synchronous inputs might therefore be compensated by recruiting a larger number of input neurons to successfully trigger APs in LSO neurons.

Together, these findings highlight that LSO neurons perform an excitatory coincidence detection, enabling them to selectively respond to correlated synaptic inputs while filtering out uncorrelated activity. This mechanism allows LSO neurons to act as temporal differentiators, responding preferentially to input patterns with precise timings. The SBCs, which provide these inputs, synchronize their activity to the sound envelope (Joris, Carney, et al., 1994; Müller, Jovanovic, et al., 2019) and exhibit the highest temporal correlation during rapidly changing sound events, such as click stimulations. Together, the excitatory coincidence detection mechanism enhances the sensitivity of LSO neurons to transient sound events. This feature permits the initiation of APs in response to rapidly changing input signals, and effectively suppresses slowly changing input signal.

#### 4.4.2 Onset response patterns are support by physiological $SW_{exc}$ , which prevents temporally random APs in the sustained part

##### 4.4.2.1 $SW_{exc}$ shape AP firing patterns of LSO neurons

A key objective of my study was to isolate the influence of synaptic parameter, such as input timings and  $SW$ , from that of the postsynaptic neuron. Using a synaptic input model, simulating the PL firing of excitatory SBC, I analyzed how the  $SW_{exc}$  influences synaptic integration in LSO neurons.

Under physiological conditions (1 nS/input), LSO neurons reliably generate APs at the stimulus onset, independent of stimulus level as modeled by  $f_{exc}$  (Fig.3.9). At the onset, multiple excitatory inputs are recruited at once, which triggers APs. In contrast, in the sustained part of stimulation, the small physiological  $SW_{exc}$  cause a dispersed conductance profile, which does not lead to APs in the sustained part, due to a depolarization block. This is evident by the adaptation of  $V_{thr}$  during this part of the stimulation (Fig.3.12). A release from this block is necessary to allow the neuron to trigger APs, which occurs when the synaptic noise is increased due to larger  $SW_{exc}$ . Similar effects were observed in a Hodgkin-Huxley model of BCs that were stimulated with PL stimuli (Rothman et al., 1993). The authors attribute the depolarization block to a combination of Nav channel inactivation together with low-threshold Kv channel activation. This is supported by findings of Svirkis et al. (2004), who show that Nav channel inactivation together with low threshold Kv channel activation synergistically

enhance coincidence detection in MSO neurons. The observation that stimulations with physiological  $SW_{exc}$  were not able to elicit sustained firing, was independent of  $f_{exc}$ . In other words, the increase in the excitatory level cannot be translated to an increased output of the neuron (Fig.3.9). A sustained firing threshold of 50 APs/s was only reached with  $SW_{exc}$ s exceeding 2.5 nS/input, and a threshold of 100 APs/s was reached with  $SW_{exc}$ s exceeding 4.7 nS/input. This suggests that low  $SW_{exc}$  effectively enforce onset firing pattern in LSO neurons, reliably transforming PL inputs into precisely timed onset spikes (Fig.5.1).

Gradually increasing the  $SW_{exc}$  increased the sustained rate, transitioning the onset response into a firing pattern that resembles a PL firing (Fig.3.9 and Fig.S.1). Furthermore, increasing synaptic noise, either by increasing the  $SW_{exc}$  or introducing heterogeneity (uniformly-distributed versus gamma-distributed  $SW_{exc}$ ; Fig.3.10) enhances sustained output. For larger  $SW_{exc}$  (>2 nS/input), the increased noise might cause the effect (Silver, 2010). For gamma-distributed  $SW_{exc}$ s, single inputs might trigger APs, instead of relying on the overall noise level. A similar observation was made in a biophysical model of BCs Spirou et al. (2023). Uniformly-distributed  $SW_{exc}$ s are arguably a simplified scenario, and there is most likely variation in the  $SW_{exc}$  between excitatory inputs. Only, in 50 % of the neurons, the gamma-distributed  $SW_{exc}$ s increased the dynamic range of the LSO neurons. This might partially contribute to the differences in AP pattern observed in *in vivo* and *in vitro* experiments. Spirou et al. (2023) furthermore showed that the bandwidth of information transfer is increased by few strong inputs, which explain their functional role. A scenario further discussed below (section 4.4.4)

#### 4.4.2.2 Pre- and postsynaptic gain modulation as mechanisms to regulate excitability

Notably, the onset spiking probability remained high and was invariant across  $SW_{exc}$  conditions. However, the sustained rate was modulated by the amplitude of noise in the excitatory conductance. A similar effect has been described in cortical pyramidal neurons, which increase their gain (minimal to maximal firing rate) in dependence of noise in the stimulus (Chance et al., 2002; Higgs et al., 2006). Gain modulation is an important feature in the auditory system, allowing to adapt to different auditory environments (Auerbach & Gritton, 2022). LSO neurons have been described to adapt their coding range to differences in the input statistics (Gleiss et al., 2019), suggesting that they exhibit mechanisms of gain modulation. An activity-dependent gain control mechanism in the LSO operates through postsynaptically released GABA, binding on presynaptic GABA<sub>B</sub> receptors, which differently reduces the release of synaptic vesicles for excitation and inhibition (Magnusson et al., 2008). This mechanism permits LSO neurons to rapidly adapt excitation-inhibition balance and possibly modify ILD sensitivity. How these changes affect the synaptic integration in an ongoing stimulation has not been tested by the authors. However, given that both  $SW_{exc}$  and

$SW_{inh}$  are reduced, this argues for a shift in neuronal computation from integration to temporal differentiation of transient signals. Co-released GABA from MTNB terminals activates presynaptic GABA<sub>A</sub> receptors, leading to a depolarization and increased the excitability of the terminals (Weisz et al., 2016). This enhanced excitability may facilitate the recruitment of additional synaptic inputs during ongoing activity, thereby enhancing inhibitory synaptic transmission. Furthermore, homeostatic increases of  $SW_{inh}$  are able to compensate for the loss of inhibitory inputs in a computational study (Ashida et al., 2021).

Postsynaptic mechanisms of gain control may involve mechanisms that regulate intrinsic properties, such as the  $R_{in}$  by the regulation of subthreshold active conductances (Wu & Kaczmarek, 2021; Kaczmarek, 2023). In animals exposed to prolonged noise, long-term changes are reported in MSO neurons and include a decreased  $R_{in}$ , probably due to upregulated HCN channels (Siveke et al., 2021). Moreover, HCN1 channels in the LSO, known to regulate  $R_{in}$ , are suppressed by nitric oxide, which hyperpolarizes the activation voltage and slows the kinetics (Kopp-Scheinflug et al., 2015). This suppression reduces the contribution to the resting conductances, thereby increasing  $R_{in}$  and neuronal excitability. A modulation of HCN channels has furthermore been suggested to underly a cAMP-mediated increase in excitability (Shaikh & Finlayson, 2005). Further mechanisms of gain modulation could include modulation of Kv1 conductances, as Kv1 together with HCN conductances dynamically regulate synaptic integration (Khurana et al., 2011) and Kv1 conductances are suggested to adjust the sensitivity to noisy input signals (Kuznetsova et al., 2008). The channels are not directly regulated by cyclic monoamines, but can be modulated through second messenger cascades, including a cAMP/PKA pathway (Winkhofer et al., 2003). Kv1 channel dynamics were also shown to influence  $V_{thr}$  adaptations in cortical neurons (Higgs & Spain, 2011). An adaptive threshold has been reported in a computational study to ‘*diversify neuronal operating modes*’ (temporal differentiation versus integration, Lubejko et al., 2019). Thereby Kv1 conductances may contribute to regulations of the AP rate in the sustained part, such as proposed in a model of auditory processing (Kaczmarek, 2023).

Together, pre- and postsynaptic gain modulation are mechanisms that allow LSO neurons to adapt different sound environments. By modulating their sensitivity to temporally varying inputs, these mechanisms could help LSO neurons to maintain reliable signal processing even in noisy environments. The fact, that changes in the  $SW_{exc}$  can be translated to increasing AP rates shows that presynaptic gain modulation carry the potential to influence the neuronal computation. Postsynaptic mechanisms of gain modulation are described for HCN channels. Kv channels are further candidates for gain modulation, but the molecular mechanism of such modulation remains to be studied in the auditory system (see Outlook).

#### 4.4.2.3 Temporal correlation of onset APs but random AP firing in the sustained part

My temporal analysis of APs showed that onset precision was highest for small  $SW_{exc}$  and lowest for large  $SW_{exc}$ , due to input latency jitter rather than intrinsic mechanisms (Fig.3.11). This enhances AP precision at transients in the input activity of LSO neurons and their inputs to CNIC and DNLL, and would suggest that LSO neurons deliver temporally coded inputs to these neurons (Greenberg et al., 2017; Ono et al., 2020). Furthermore, the APs triggered by large  $SW_{exc}$  were temporally uncorrelated, but could convey rate-coded input to the upstream neurons.

#### 4.4.2.4 Functional classification of primary-like DC experiments based on comparison with *in vivo* findings

The comparison between *in vitro* and *in vivo* results have already been subject of discussion (section 4.3.4). However, the input model, in combination with the DC stimulations, build a bridge between these observations. The predominant firing pattern elicited by stimulations with physiological  $SW_{exc}$  was onset firing behavior. In contrast, our *in vivo* results showed onset firing only in 20 % of neurons (Fig. 3.24). Another study reports onset firing responses in 100 % of neurons (Garcia-Pino et al., 2017). Adding to the previous discussion, I here showed that the  $SW_{exc}$  plays a critical role in adjusting the firing pattern (Fig.3.9 and Fig.S.1). Moreover, small  $SW_{exc}$  would also explain the low spontaneous firing rate of LSO neurons *in vivo*, compared to their presynaptic partner, the BCs (LSO neurons: 2.5 APs/s, Karcz et al., 2011; BC: 60 APs/s, Postolache et al., 2024). Considering the 60 APs/s as  $f_{exc}$  of the sustained part,  $SW_{exc} \leq 2$  nS/input would explain the ~30-fold reduction in the spontaneous rate in LSO neurons.

I showed that the  $SW_{exc}$  contributes majorly to the firing pattern of LSO neurons, effectively shifting an onset response, triggered by small  $SW_{exc}$  to a PL, triggered by large  $SW_{exc}$ . This shows that different  $SW_{exc}$  distributions can contribute to the different firing pattern observed in *in vivo* preparations (onset vs sustained firing). The gain modulated state of the neuron could further contribute to this. An investigation of dynamic gain control in LSO neurons would address this possibility and could help to explain differences in occurrence of onset and sustained firing neurons.

#### 4.4.3 Rate-modulation coding and band-pass filtering in LSO neurons in response to sinusoidal input activity and transients

Temporal coding abilities of auditory neurons are often assessed using SAM tones. In high CF neurons, phase locking to the stimulus fine structure is restricted, but these neurons can still convey temporal information via phase locking to the envelope of SAM tones (Joris, 2019). In this section, I will first discuss the encoding of sinusoidal envelopes in the LSO by excitatory

stimulations, before discussing excitation-inhibition interaction of temporally correlated inputs in a later section.

To analyze the rate and temporal coding of ongoing sinusoidal activity, I used stimuli with a 200-ms duration, in contrast to earlier experiments, which tested a single cycle. When stimulated with physiological  $SW_{exc}$  (1 nS/input), LSO neurons exhibited strong band-pass filtering. The AP rate was minimal at low  $F_{mod}$ s (5-20 Hz), peaked around 100 - 200 Hz, and declined rapidly at higher  $F_{mod}$ s (Fig.3.16). This stands in contrast to results from the *in vivo* experiments, in which low  $F_{mod}$ s are reliably encoded, albeit at a lower rate (Fig. 3.26; Joris & Yin, 1998). As previously discussed, the low-frequency filtering might be attributed to an excitatory coincidence detection mechanism as proposed in a modelling study (Ashida et al., 2016). Notably, Joris and Yin (1998) reports that LSO neurons exhibit a high-frequency limit between 500 and 1000 Hz in the rMTF, a phenomenon not observed in BCs and MNTB neurons. This should not be confused with tMTFs, for which all neurons show a low-pass filtering with a cutoff between 500-2000 Hz (Joris & Yin, 1998). A modeling study assigned the majority of rMTFs of LSO neurons as “peak & decrease” functions and attributed this effect to a coincidence detection mechanism (Ashida et al., 2016). The rMTFs of ANFs are flat (Joris & Yin, 1992). BCs and MNTB neurons exhibit rMTFs that often show a small peak at 200 – 500 Hz, but aside from this, they are also flat (Joris & Yin, 1998; Tolnai et al., 2008). The small peak has been attributed to a coincidence detection mechanism (Spirou et al., 2023). However, the  $SW_{exc}$  in BCs are substantially larger compared to the  $SW_{exc}$  in LSO neurons, which may lead to less pronounced bandpass filtering in BCs.

An important factor shaping the upper limit of synaptic filtering functions is the synaptic  $\tau_{decay}$  of the inputs. The corner frequency, beyond which the sinus modulation is attenuated can be approximated by  $f_{corner} = \frac{1}{2\pi\tau_{decay}}$  (e.g.: Linaro et al., 2018). This results in a corner frequency of about 530 Hz for a fast  $\tau_{decay}$  of 0.3 ms. At higher frequencies, the EPSP profile progressively changes to a disperse profile. Therefore, stimulations at higher  $F_{mod}$ s are more comparable to the sustained part of the PL stimulation in which the LSO neurons did not fire APs. This high-frequency limitation can be overcome when stimulated with larger  $SW_{exc}$  of 4 nS/input, which elicited a AP rate of about 40 APs/s (Fig.3.16). This resembles the sustained rate seen in response to PL inputs at this  $SW_{exc}$  (58 APs/s at  $f_{exc} = 200$  Hz; Fig. 3.9) and may reflect a transition from temporal integration of multiple inputs to single-input-driven APs. A similar effect would explain the rather flat rMTFs of BCs (and accordingly of MNTB neurons), given their larger synaptic inputs (commonly >1 nA/input, or ~15 nS; Cao and Oertel, 2010).

Together, these findings suggest that band-pass filtering in LSO neurons arises from a combination of coincidence detection, limiting APs in low-frequency sinusoidal signals, and high-frequency synaptic filtering, and both factors are shaped by the small  $SW_{exc}$  in LSO

neurons. This dual mechanism creates a narrow tuning window that favors  $F_{mod}$ s around 200 Hz. The adaptive threshold mechanism mentioned earlier plays a crucial role in shaping the band-pass filtering of bird auditory neurons (Fontaine et al., 2014). Considering that the temporal coding of LSO neurons relies on this band-pass filter, it would be valuable to investigate its impact on ILD and ITD coding within LSO neurons.

To further assess the effect of stimulus transients, I systematically increased the  $F_{mod}$ , while maintaining a fixed  $F_{pulse}$  of 100 Hz (Fig. 3.17). LSO neurons showed maximal responsiveness at 200 Hz, with reduced firing rates at both lower (100 Hz) and higher (500 and 1000 Hz)  $F_{mod}$ s. This again highlights the intrinsic high sensitivity of LSO neurons to stimulations at a  $F_{mod}$  of 200 Hz. At a  $F_{mod}$  of 1000 Hz, the rate-level function is shifted towards higher input frequencies, and the responsiveness is substantially decreased, which may be explained by the temporal integration limitations imposed by  $\tau_{mem}$  as discussed earlier (section 4.4.1). The *in vivo* experiments showed a decreasing AP rate with increasing stimulus transience, which was observed at all  $F_{pulse}$  tested (Fig.3.26). The mechanism behind this reduction might be the temporally limited time of effective auditory stimulation, for example, at a stimulation of 50 Hz  $f_{pulse}$  and 200 Hz  $F_{mod}$  the neuron is effectively only stimulated  $\frac{1}{4}$  of the time (5 ms stimulation which repeats every 20 ms). The experiment does not allow interference with the limited integration of excitation by  $F_{mod}$  of 1000 Hz, which reduces sensitivity.

The finding that LSO neurons exhibit the lowest threshold when input signals are not perfectly synchronized but have some degree of temporal jitter suggests that these neurons may be adapted to detect fluctuations in sound envelopes, present in natural auditory environments (Joris, 2022). Even clicks, the most transient auditory signals, elicit some degree of temporal jitter in BCs and MNTB neurons (Müller et al., 2023), which indicates that natural input to the LSO is rarely perfectly synchronized. Together, these results highlight the sensitivity of LSO neurons to temporally synchronized inputs, suggesting an adaptation for extracting temporal information from sound envelopes.

#### 4.4.4 Temporally precise coding of the frequency modulation and the phase-locking limit of LSO neurons

In the previous section, I discussed how the  $SW_{exc}$  influences the rate coding in response to sinusoidal activation of LSO neurons, which leads to the emergence of a band-pass filter. In this section, I will discuss the data in terms of its temporal precision and the accompanying tMTFs.

In response to sinusoidal conductance stimulations, LSO neurons exhibited a high degree of phase locking (Fig.3.16). Generally, the tMTFs showed low-pass filtering behavior, which was appreciable for  $SW_{exc}$  of 2 and 4 nS/input. The VS increased with  $F_{mod}$ s up to 500 Hz, which was followed by an abrupt decline. Therefore, the cutoff frequency of the filter can be

approximated to values between 500 and 1000 Hz. *In vivo* experiments indicated a very similar cutoff value of 800 Hz when presenting SAM tones (Joris, 1996). The cutoff value *in vivo* is bound by two major factors. The synaptic filtering has previously been discussed, which imposes a high-frequency limitation set by the  $\tau_{\text{decay}}$  of the synaptic currents. This is further restricted by membrane resonance properties of the postsynaptic neurons, and the suprathreshold resonance properties, which refer to the AP initiation limitations in following high frequencies (Hutcheon & Yarom, 2000; Fourcaud-Trocme et al., 2003). On the other hand, the high-frequency phase-locking limitations of the presynaptic neuron are essential. Their cutoff values will determine the highest  $F_{\text{mod}}$  at which synaptic inputs can follow the modulation. Low-pass filtering is a feature commonly seen in the tMTFs of auditory neurons in the afferent pathway to the LSO. At the level of ANFs, the cutoff frequency is at about 1 - 1.5 kHz, a value higher compared to the limits approximated here for LSO neurons (Rose et al., 1967; Joris & Yin, 1992). Similar high values are reached by BCs as well as MNTB neurons that project onto LSO neurons (Joris & Yin, 1998; Tolnai et al., 2008; Müller, Jovanovic, et al., 2019). Therefore, these neurons deliver phase-locked input to LSO neurons, and if the  $F_{\text{mod}}$  is high enough, the LSO neurons can reliably transform this into similarly precise APs.

Neurons in the afferent pathway can enhance phase locking with increased stimulus transience. Dreyer and Delgutte (2006) showed that ANFs respond with higher temporal precision to transposed tones than to SAM tones. The *in vitro* experiments with pulsed-sine stimulations at  $f_{\text{pulse}}$  of 100 Hz showed high VS values at  $F_{\text{mod}}$  of 100 Hz, which increased further with increasing transience at  $F_{\text{mod}}$ s of 200 and 500 Hz (Fig.3.17). The *in vivo* experiments with pulsed-sine tones also showed that LSO neurons exhibited increasing reproducibility (another measure of temporal precision; Kessler et al., 2021) with higher  $F_{\text{mod}}$ s (Fig.3.26). VS calculated on the  $F_{\text{mod}}$ , demonstrated that LSO neurons were able to track  $F_{\text{mod}}$ s of up to 500 Hz, with a decline at higher rates. This strong phase locking indicated that AP timings are confined to narrow temporal windows. This implies that the temporal window for excitation-inhibition interactions becomes narrower with increasing  $F_{\text{mod}}$  during transient stimulations, a hypothesis tested *in vitro* and discussed in a later section (section 4.5).

Furthermore, I observed that phase locking of LSO neurons depended on the  $SW_{\text{exc}}$ , with larger  $SW_{\text{exc}}$  decreasing temporal precision. Conversely, APs are triggered more reliably at preferential phases of the stimulus with smaller  $SW_{\text{exc}}$  (Fig.3.16). Similarly, BCs reduce the temporal jitter of APs (equivalent to the VS) when multiple subthreshold inputs converge (Xu-Friedman & Regehr, 2005a). In an accompanying paper (Xu-Friedman & Regehr, 2005b), the authors show that jitter increases when fewer, stronger inputs converge, aligning well with my data presented in Fig.3.16. Using a multi-compartment model, Spirou et al. (2023) showed

that small inputs onto BCs significantly increase phase locking of  $F_{mod}$ s up to 200 Hz, a phenomenon also observed here. Furthermore, they showed that large synapses (equivalent to large  $SW_{exc}$ ) in combination with small ones, increase phase locking at higher  $F_{mod}$ s (not specified). Although this seems to contrast with my data, it may be explained by small inputs enabling better sinusoidal tracking of  $V_{mem}$ , while large inputs could induce stochastic resonance, thereby enhancing phase locking (Gai et al., 2010). However, in the LSO, strong individual inputs can bypass the excitatory coincidence mechanism (section 4.3.1 and Fig.3.10), which would influence the coincidence detection mechanism.

Together, this section highlighted that LSO neurons have the intrinsic capability to increase phase locking from their excitatory inputs. The neurons are able to track fast envelope fluctuations, thereby shaping the temporal window for excitation-inhibition interactions. The enhancement in phase locking by small  $SW_{exc}$ , argues for an adaptation for temporally precise AP initiation, potentially optimized for the processing of fast envelope fluctuations of sounds. The interactions with inhibition will further be discussed in section 4.5.

#### 4.4.5 Concluding remarks on excitatory synaptic integration

The experiments on excitatory synaptic integration show several key mechanisms that enable LSO neurons to perform a temporal differentiation of excitatory input signals. A coincidence detection mechanism restricts APs to transiently increasing input activity, such as for fast sinusoidal activations or at the onset of PL stimulations. Physiologically small  $SW_{exc}$  contribute to transforming PL input activity to an onset response, effectively suppressing APs in the sustained rate. Dynamic gain modulation was discussed as an appealing mechanism for altering sensitivity to synaptic noise, which would enable adaptation to changing auditory environments. Furthermore, the coincidence detection mechanism sets the low-frequency limit of signal transmission in rMTFs of sinusoidal activation. In combination with a high-frequency limit at 500-1000 Hz, the rMTFs resemble band-pass filtering characteristics. The APs of LSO neurons exhibited very high temporal precision, which is further supported by small  $SW_{exc}$ . These temporally precise APs set the temporal window for excitation-inhibition interactions.

Together, these experiments highlight the role of LSO neurons as temporal differentiators, which makes them sensitive to sound signals that elicit a high degree of synchronization in the excitatory input neurons, such as transient sound signals. This supports the temporal encoding of sound envelope structure by LSO neurons.

## 4.5 Excitation-inhibition integration in LSO neurons

### 4.5.1 Precise ILD coding of transients *in vitro* and *in vivo* but contrasting results in the sustained part of integration

The encoding of binaural information by LSO neurons is classically attributed to the integration of excitatory and inhibitory inputs, with ILDs encoded via differences in their respective firing rate (Owrutsky et al., 2021). In this thesis, I directly tested this coding paradigm at the cellular level using PL stimulation patterns with varying  $f_{inh}$  to evaluate rate-based level-difference coding in LSO neurons.

In my study, I demonstrated that LSO neurons reliably encoded level differences at the onset of PL stimulations (Fig.3.13-Fig.3.15). This is consistent with rate-based models of ILD coding. However, in the sustained part, AP rates varied bidirectionally, depending on the input configuration. This contrasts with *in vivo* findings, where both onset and sustained responses reliably reflect ILD coding (Fig.3.25; see e.g., Tollin & Yin, 2002a). Notably, level-difference sensitivity was consistently higher at the stimulus onset than across the full stimulus duration, both *in vitro* and *in vivo*.

The onset of PL DC stimulation provides a transient cue for integration that allows LSO neurons to reliably initiate APs (Fig.3.9). The onset reliability decreases with an increasing inhibitory rate. However, the effectiveness of the reduction varied with the  $SW$  configurations (Fig.3.14). Specifically, onset reliability was most effectively suppressed when small  $SW_{exc}$  were paired with small  $SW_{inh}$ . Increasing the  $SW_{inh}$  increased the  $f_{inh}$  to reach the separability threshold for any combination with  $SW_{exc}$ . The  $SW_{exc}$  had a stronger effect, with the AP rate being less reliable reduced with larger  $SW_{exc}$  values (Fig.3.13 - Fig.3.15). This likely reflects reduced temporal overlap between excitation and inhibition when fewer, stronger synapses converge, allowing excitation to occasionally evade inhibition and trigger APs. Conversely, with increasing convergence, temporal summation improves synchronization between excitation and inhibition, enhancing the suppressive effect. Therefore, optimal ILD encoding at the onset appears to occur with small  $SW_{exc}$  and  $SW_{inh}$ , with many converging inputs. Thus, the physiological assumption of convergence of a few strong inhibitory inputs conflicts with this functional reasoning. However, when the onset APs were triggered by the physiological assumed weak  $SW_{exc}$  (1 nS/input), this effect was smallest, allowing the reliable encoding of onset level differences. These findings align with *in vivo* observations of LSO onset firing patterns, demonstrating that onset responses can be utilized for a rate-based ILD extraction (Fig.3.25; Garcia-Pino et al., 2017; Franken et al., 2021).

In contrast, the sustained part of stimulation revealed a complex and paradoxical interplay between excitation and inhibition. Crucially, my separability analysis revealed that there was virtually no useful information for level-difference computation in the sustained part (Fig.3.15).

These results indicate that cellular mechanisms of LSO neurons hinder the encoding of ILD information when temporally uncorrelated excitation interacts with inhibition. These paradoxical results conflict with *in vivo* literature (e.g.: Tsuchitani & Boudreau, 1969; Park et al., 1997; Tollin & Yin, 2002a; Tsai et al., 2010; Karcz et al., 2011; review: Friauf et al., 2019) and with our *in vivo* results (Fig.3.25). I will continue the discussion on a mechanistic basis to allow a functional interpretation.

Inhibition has been described to be able to enhance excitation in a narrow-timed window after inhibition (Dodla & Rinzel, 2006; Dodla et al., 2006). This effect is known as post-inhibitory facilitation (PIF), and was also observed in the LSO (Beiderbeck et al., 2018). I showed that LSO neurons undergo depolarization block during the sustained phase of excitatory stimulation with small  $SW_{exc}$  (Fig.3.12). This makes the neurons especially susceptible to PIF: the neurons are already in a depolarized state, which allows hyperpolarizing inhibition to release the depolarization block, and the neurons can then fire an AP. STAs of the inhibitory conductance (Fig.5.4) show that APs are often preceded by a transient decrease in  $G_{inh}$ , supporting this two-step PIF mechanism: hyperpolarization relieves depolarization block, followed by sufficient release from inhibition to allow AP initiation. These results support the hypothesis by Beiderbeck et al. (2018) that hyperpolarization decreases the  $V_{thr}$  for AP initiation and thereby induces PIF in LSO neurons.

The PIF mechanism is in line with the greatest facilitatory effect caused by large  $SW_{inh}$ . A single inhibitory input causes large hyperpolarization, supporting the PIF, and fewer inhibitory inputs reduce the likelihood of another input being active simultaneously. At intermediate levels of  $SW_{exc}$  (4 nS/input), transients in  $G_{exc}$  contribute to AP initiation, which can be blocked if inhibition is simultaneously active. The PIF effect and the inhibitory effect start to interact on the AP rate. When excitation induces high AP rates by stimulations with  $SW_{exc}$  of 10 nS/input, the inhibition becomes increasingly likely to interact temporally with AP initiation, and therefore, the inhibitory effect outweighs the PIF.

Decreasing the  $SW_{inh}$  (16 inputs with 2 nS/input) generally decreased the facilitatory effect and increased the inhibitory effect, which is in line with the argumentation above. This inhibition creates a more dispersed conductance profile, which generates a basin of hyperpolarization rather than transient inhibition. A key consideration is that the physiologically assumed  $SW$  might be overestimated. Both synapses, the CN-LSO, as well as the MNTB-LSO, undergo short-term depression when tonically stimulated (Brill et al., 2019; review: Friauf et al., 2015). The  $SW$ s have been determined by stimulation protocols with inter-stimulus intervals of 2 s, which avoids any short-term plasticity at these synapses (Müller, Sonntag, et al., 2019). This is different in *in vivo* situation, where synapses can be in a constant state of reduced synaptic transmission (Hermann et al., 2007). Therefore, the  $SW_{inh}$  with which LSO

neurons are bombarded during sustained stimulation might be overestimated here, possibly reducing the facilitatory effect, and thereby shifting the neurons to an onset-only coding regime. On the other hand, inhibitory MNTB-LSO inputs show a broad variability in their individual strength (Gjoni, Zenke, et al., 2018; Müller, Sonntag, et al., 2019). For a given LSO neuron, this indicates that some powerful inhibitory inputs can contribute highly to the PIF effect, while other weak ones contribute to the suppressive hyperpolarizing effect. Such heterogeneity in input strength is similar to findings in other systems, such as the cerebellum. Wu et al. (2024) demonstrated that variable-sized Purkinje cell inputs to the cerebellar nuclei influence both rate and timing of AP firing. These findings suggest that  $SW_{inh}$  heterogeneity may be a functional mechanism for regulating temporal coding and rate coding across different circuits.

Together, the above-discussed results present a paradoxical interaction of excitation and inhibition in the sustained part of synaptic integration, which raises the question: is this a bug or a feature for sound source localization? The cellular mechanisms that lead to the facilitatory effect might be less pronounced *in vivo* but argue that the neurons are onset firing neurons *in vivo*. These mechanisms allow for an ILD computation at the onset of the stimulus, such as observed by Franken et al. (2018) and Garcia-Pino et al. (2017). The facilitatory effect observed here has previously been described to increase ITD sensitivity in gerbils (Beiderbeck et al., 2018). Therefore, these mechanisms would allow a combined ILD and ITD integration of transient signals, such as at the onset of stimulation, and is also in line with time intensity trading by LSO neurons (Pollak, 1988; Grothe & Park, 1995; Park et al., 1996). However, these cellular mechanisms would hinder the extraction of ILD information present in the sustained part. Given the large dataset presented here, where 99 out of 106 neurons exhibited onset firing in response to step current stimulation, it seems unlikely that the sustained firing and onset firing LSO neurons observed *in vivo* belong to multiple cell classes, as proposed by Franken et al. (2018). Instead, the results suggest that they may belong to a single group, which might be in different states of excitability, and have a different sensitivity to the synaptic inputs, leading to an apparent switch between temporal differentiation and rate-based integration.

#### 4.5.2 Level-difference coding by transient stimulation

My results demonstrate that LSO neurons are tuned to fire APs in response to transient stimulations, like at the onset of PL stimulation patterns or by pulsed-sinusoidal stimulations (Fig.3.9 and Fig.3.17). These transient encoded APs can be employed for rate-based level differences between excitation and inhibition (Fig.3.13 and Fig.3.18).

The level-difference coding was tested at a  $F_{pulse}$  for three different  $F_{modS}$ , remodeling increasing transience of the stimulus (Fig.3.18). At all three  $F_{modS}$ , the AP rate of the neurons

gradually declined with increasing  $f_{inh}$ , reflecting classical rate-level coding. Therefore, ongoing rate-level coding is enabled when excitatory and inhibitory inputs show temporally correlated activity, such as in the pulsed-sinusoidal stimulations. The *in vivo* results do not entirely recapitulate these *in vitro* results. The extraction of ILD information was higher at the onset of pure-tone stimulations compared to the sustained part, however, ILD information was still conveyed in the sustained part (Fig.3.25). Furthermore, pulsed-sinusoidal stimulation with a broadband noise carrier confirmed that ILD information can be extracted from transient stimuli, with envelopes as short as 2 ms, reflecting a  $F_{mod}$  of 500 Hz (Fig.3.27).

The *in vitro* experiments suggest that temporal correlation is necessary in both excitatory inputs and inhibitory inputs to enable rate-level coding. Therefore, in this part, I will focus on the source of such correlated activity and the limitation on conveying a rate-based code by transient stimulation for level-difference computation. The *in vivo* experiments demonstrated that the correlation of LSO neurons' APs can be increased by increasing the transience of the stimulus, and the neurons were able to lock their APs to the transient stimulation, even at high  $F_{mod}$ s of up to 500 Hz (Fig.3.26). In other words, the APs were restricted to the temporal window set up by the envelope modulation. This implies that the innervating SBCs convey this high temporal precision, which depends on the stimulus structure. With increasing transience, the APs are restricted to a shorter temporal window. The temporal precision used for the pulsed level-difference experiments *in vitro* had a minimal temporal jitter of  $0.33 \text{ ms} \left( 500 \text{ Hz envelope; } \frac{2 \text{ ms phase duration}}{6} \right)$ , which is still three times higher compared to the jitter in BCs and MNTB neurons evoked by click stimulations (Müller et al., 2023). Therefore, the innervating pathway is capable of transmitting transient input signals to LSO neurons, and the temporal precision depends on the envelope structure of the auditory stimulus. In the *in vitro* experiments, inhibition was most effective when the  $F_{mod}$  was at 200 Hz (at an excitatory rate of 200 APs/s; Fig.3.18). At the same  $F_{mod}$ , the neurons were most sensitive to excitation, which argues for an intrinsic adaptation to this stimulus structure. Functionally, this implies that the degree of temporal jitter in the innervating neurons contributes to the ILD sensitivity of LSO neurons. This raises the question of whether the transience of the auditory signal may have a limiting effect on ILD coding. Irvine et al. (2001) systematically investigated the contribution of ITDs and ILDs on the binaural coding of LSO neurons. When stimulating with clicks *in vivo*, they found that the relative amplitude at either ear dominated the ILD computation of most neurons. For the remaining neurons, the ILD information is primarily extracted through temporal disparities between the excitatory and inhibitory inputs ("latency hypothesis", further described below). Their experiments suggest that a relative amplitude- (or input rate-) based computation is feasible. An attractive hypothesis is that differences in synchronization among input neurons may contribute to a functional gradient in LSO neurons, ranging from relative amplitude coding

to relative time coding sensitivity. Joris and Yin (1995) used click stimuli and tested varying ITDs and ILDs. They showed that a 5 dB increase in ILD decreased the probability of spiking by ~90 %. Further increasing the ILD resulted in a widening of the effective temporal window of inhibition. Franken et al. (2021) presents intracellular responses of an LSO neuron when stimulated with clicks with increasing sound level at either ear (their Fig.8 D). The successive increase in the IPSP amplitude with increasing contralateral level and the shift in onset latency of the IPSP suggest that an increased sound level shortens the latency (latency hypothesis) and increases the number of inhibitory inputs recruited to contribute to the compound IPSP.

Collectively, LSO neurons are highly sensitive to level-difference cues *in vitro* and *in vivo* of transient stimulations. Therefore, the synchronization of inputs to LSO neurons majorly contributes to the ILD extraction performance of LSO neurons. At the same time, increasingly transient signals enhance the neurons sensitive to the relative time differences between excitation and inhibition. I will discuss the coding of such temporal disparities in the next section.

#### 4.5.3 Stimulus structure defines the temporal window of effective inhibition

The importance of the relative timing of the excitatory and inhibitory inputs to ILD detectors has been proposed by many researchers (Galambos et al., 1959; Pollak, 1988; Tsuchitani, 1988, review: Tollin, 2003). The time differences in the envelopes reflect the adequate feature that creates temporal disparities in the inputs to LSO neurons (see Introduction). Moreover, the inputs to LSO neurons phase lock to the envelope structure of the inputs, thereby transmitting the temporal information of the envelope (Joris & Yin, 1998; Tolnai et al., 2008; Joris & van der Heijden, 2019; Müller, Jovanovic, et al., 2019).

Two major findings were observed in this study. First, amplitude-modulated input activity that followed a 100 Hz sinusoid elicited remarkably stable rate-level coding across a temporal range of up to 2 ms preceding inhibition (Fig.3.20). Second, the window of effective inhibition is majorly shaped by the amplitude modulation of the inputs (Fig.3.21, Fig.3.22, and Fig.3.23). These results reveal that the temporal correlation of the inputs is a major determinant for coding of temporal disparities in LSO neurons. This is the first report of the ITD coding capabilities of LSO neurons, with input activity correlating to different  $F_{mod}$ s tested directly on LSO neurons.

Several reports show that LSO neurons can perform a time-intensity trading (Pollak, 1988; Grothe & Park, 1995; Park et al., 1997), and the latency shifts depend on the envelope structure (Siveke et al., 2010). In my experiments, increasing the transience of the envelope (by increasing  $F_{mod}$ ) led to narrower trough width and steeper slopes of the trough functions (Fig.3.22), while level-difference coding remained remarkably stable across temporal disparities (Fig.3.20). These findings suggest that, although ILD sensitivity is robust, LSO

neurons become increasingly sensitive to the timing of inputs as transience increases. The steepening of the trough functions implies greater responsiveness to temporal shifts (Fig.3.23), thereby enhancing time-intensity trading under transient conditions. Moreover, this synchronization-based mechanism provides a concrete neuronal implementation of a key aspect of time-intensity trading models: when the contralateral sound level increases, it results in earlier and more synchronized inhibitory inputs, which produce both a latency shift and a rise in the inhibitory amplitude. Together, these results indicate that input synchronization plays a dual role in time-intensity trading by sharpening temporal resolution and amplifying the level-difference representation.

LSO neurons exhibit temporal coding sensitivity across a range of stimuli. *In vivo* recordings show strong ITD sensitivity to SAM tones (Joris & Yin, 1995; Batra et al., 1997), which can be remodeled using a coincidence counting model (Ashida et al., 2016). The modulation frequency imposes a high-frequency limitation for ITD coding at about 500 Hz. However, ITDs can reliably be extracted from click stimulations at this frequency (Beiderbeck et al., 2018). This underscores the role of stimulus transience in ITD coding of LSO neurons. For SAM tones, the repetition rate is 2 ms for 500 Hz with continuous stimulation, whereas clicks are transient stimulations of <100  $\mu$ s with no effective stimulation in the remaining time. My experiments bridge this gap by systematically increasing stimulus transience, linking SAM-like and click-like stimulation. While a 500 Hz SAM tone repeats every 2 ms with a continuous profile, a click is a highly transient signal (<100  $\mu$ s) followed by silence.

The ITD-coding capability of LSO neurons was highest when the inputs were not perfectly synchronized but showed some temporal jitter ( $\sim 0.8$  ms;  $F_{mod} = 200$  Hz;  $\frac{5 \text{ ms}}{6}$ ). This jitter level is about eight times higher than that observed in presynaptic neurons under click stimulation (Müller et al., 2023). However, in the experiments presented in Fig.3.21-Fig.3.23, the average conductance amplitudes were held constant across  $F_{mod}$ , which is realized by a smaller number of active inputs per cycle. As previously discussed, transient sound stimulation may recruit more inputs within a single stimulus phase, thereby increasing the conductance amplitudes of excitation and inhibition. Coupled with the observed narrowing of the ITD trough curves and the corresponding steepening of their flanks, these findings suggest that LSO neurons perform highly sensitive ITD coding under transient stimulation. In other word, for transient sounds, LSO neurons may depend more strongly on ITD coding, while for less transient sounds, the ILD information increases in importance.

#### 4.5.3.1 Limitations of the dynamic-clamp method in analyzing temporal coding of LSO neurons

Cellular mechanisms like PIF play a key role in shaping ITD sensitivity (Beiderbeck et al., 2018). Here, I will discuss two cellular mechanisms of temporal coding in LSO neurons, which are not captured by the DC method.

Inhibitory synapses are reported to target the AIS of LSO neurons, and a computational model showed the power in decreasing the AP probability of LSO neurons (Franken et al., 2021). As all currents are injected into the neuron's soma by the DC stimulations, such compartmentalized computations are probably overseen by the method used here. Another mechanism is dendritic integration, which shapes excitatory synaptic integration. Dendritic HCN-channels are described to locally decrease the  $R_{in}$  and thereby increase the importance for synchronized excitatory input activity (Leao et al., 2011). In the MSO, dendritic EPSPs are amplified by Nav channels, which are localized at the soma and proximal dendrites. However, their availability is low, caused by a negative shift in their inactivation voltage, but sufficient to amplify the dendritic EPSPs (Scott et al., 2010). Here, I presented results that argue for a high availability of somatodendritic Nav channels in LSO neurons (Fig.3.7). These may have profound effects on synaptic integration by boosting synchronous dendritic EPSPs, which could summate supralinearly at the soma. Such mechanisms have not been tested in LSO neurons but might be a further adaptation to enhance temporal coding of transient synchronous input activity.

#### 4.5.3.2 Functional implications of transient ITD coding by LSO neurons

Psychophysical studies showed lower '*just noticeable differences*' for more transient sounds (Bernstein & Trahiotis, 2002, 2009). They tested this by using high-frequency envelope-modulated tones with increasing transience, either by using transposed tones or raised-sine tones (similar to the pulsed tone used in my study). Furthermore, ITD sensitivity in the CNIC is thought to be inherited from LSO processing. CNIC neurons show ITD sensitivity to the envelope structure of both SAM and transposed tones (Griffin et al., 2005; Ono et al., 2020), and show highest ITD sensitivity for steep rising envelopes (Greenberg et al., 2017; Kim et al., 2020). This is in line with psychoacoustic findings (Klein-Hennig et al., 2011) and further supports the conclusion that synchronized, transient input activity to LSO neurons plays a key role in shaping envelope-based ITD coding.

#### 4.5.4 Concluding remarks on excitation-inhibition integration in LSO neurons

In conclusion, LSO neurons are highly tuned to the temporal structure of binaural inputs. A rate-based level difference computation can be performed on transient input activity. Randomly active inputs cannot be used for a rate difference analysis in the *in vitro* preparation,

while such coding is feasible in the sustained part of in vivo preparations. Furthermore, increasing stimulus transience enhances the sensitivity of the neuron to relative time difference cues. These mechanisms support a dual encoding strategy of transient input activity, enabling LSO neurons to integrate ILD and ITD information depending on the temporal dynamics of the stimulus. Such sensitivity may underlie the high perceptual acuity for spatial cues observed with transient sounds.

#### 4.6 Implications for binaural coding with cochlear implants

Profound hearing impairment affects about 1 million people in Germany ([www.schwerhoerigen-netz.de/statistiken](http://www.schwerhoerigen-netz.de/statistiken), retrieved June 3<sup>rd</sup>, 2025). Hearing can be partially restored through the use of cochlear implants (CochImpls). Since CochImpls are inserted at the base of the cochlea, they activate high-frequency regions, due to the tonotopic organization of the sensory epithelium. This implies that the LSO circuitry is the primary pathway for binaural processing of CochImpl patients. Typically, CochImpl patients rely on amplitude differences for azimuthal sound source localization. These can also be used by rats as an animal model to study the neural processing of ILDs provided by CochImpl stimulations (Buchholz et al., 2024). However, CochImpl patients show very poor ITD sensitivity (Laback et al., 2015). ITD information from CochImpls exists in two ways: 1) envelope ITDs, which are similar to acoustic envelope ITDs, and 2) ITDs in the electrical pulses that stimulate the ANFs. As I have discussed at multiple sites in my thesis, Müller et al. (2023) demonstrated that BCs and MNTB neurons respond to acoustic click trains with high temporal precision. This precision is further enhanced (*hyper-precision*) under electrical stimulation via CochImpls. The pulse ITDs, rather than envelope ITDs, from CochImpl stimulation have recently been shown to govern the binaural processing of azimuthal sound source localization of CochImpl-implanted rats (Schnupp et al., 2025). Müller et al. (2023) further shows that this *hyper-precision* paradoxically degrades ITD coding in LSO neurons by narrowing the dynamic ITD range, and the ITD coding can be restored by reintroducing temporal jitter in a model of binaural processing. Together, these findings strongly argue for the LSO as the site of pulse ITD coding of CochImpl stimulations. My experiments empirically show that the processing of ITDs in the LSO depends on the synchronization of inputs. The neurons are most sensitive when the inputs follow jitter in the range of several hundred  $\mu$ s. Thereby, I demonstrated that temporal jitter is an important information for LSO neurons to extract envelope ITD information, and input synchronization plays a key role in time-intensity trading. My results thereby provide empirical validation of the findings of Müller et al. (2023) and offer a mechanistic explanation. Together, my results strongly support the recent suggestions of Schnupp et al. (2025) to adjust bilateral CochImpls to transmit pulse ITD information.

## 4.7 Outlook

This work is the first to analyze synaptic integration of *in vivo*-like activation patterns related to sound source localization directly in LSO neurons. I discussed multiple aspects of how synaptic integration in LSO neurons is shaped and proposed several approaches for investigating the mechanistic and functional consequences in future studies. These are summarized below.

- I. How do subthreshold conductances, such as those mediated by Kv1 and HCN channels, contribute to species-specific differences in subthreshold membrane properties?
  - i. Are such differences species-specific adaptations for low-frequency and high-frequency coding LSO neurons?
  - ii. How do subthreshold active conductances influence differences observed between excitatory and inhibitory LSO neurons (Haragopal & Winters, 2023). Do these differences support different coding regimes in the two populations?
- II. Molecular and structural mechanisms influencing LSO neuron excitability are poorly studied, and their contribution to ILD coding is insufficiently understood. These questions can be specified as follows.
  - i. Biphasic APs suggest compartment-specific activation of Nav channels in LSO neurons (Fig.3.7). This raises the question of how these contribute to the coding of level differences? Does the soma-axon coupling influence the LSO neurons' preferential role as temporal differentiator or integrator? How do molecular determinants (Nav channel subtype) contribute to this phenomenon?
  - ii. How does AIS plasticity contribute to coding regime in LSO neurons, and what is its functional importance for sound source localization?
- III. I discussed several mechanisms of gain control in the auditory system. How such gain control influences synaptic integration in LSO neurons is poorly understood.
  - i. Are Kv1 channels mediators of postsynaptic gain modulation in LSO neurons?
  - ii. Does the synergistic modulation of HCN and Kv1 channels alter the excitability of LSO neurons?
  - iii. How does the gain-modulated state influence the transformation of a PL to an onset firing pattern?
- IV. The coincidence detection mechanism had a major influence on rMTFs. This raises the question of how such a mechanism alters sensitivity to ILDs and ITDs.

- i. Does coincidence detection enhance ILD and ITD processing in the LSO in noisy environments? This could be tested by prolonged noise stimulations and a subsequent analysis of the ability of LSO neurons to extract signal in noise.
- V. A major result from excitation-inhibition integration is that transient activity can reliably be used for level-difference coding in LSO neurons. The functional consequences of this could be tested by disrupting the transient onset activity by using an animal model lacking synaptic ribbons (Bassoon knock-out mice; [Buran et al., 2010](#)). These animals show a decreased onset encoding in the PL response of ANFs. This allows for interaction with temporal coding in the innervating pathway.
  - i. How much do transients in input activity contribute to level-difference computation in Bassoon knock-out mice?
  - ii. Can these mice utilize  $ITD_{env}$  for sound source localization? And do these mice exhibit limited coding of ILDs and ITDs in the LSO? This could be tested using the pulsed-sine modulation protocol of the *in vivo* experiments.
- VI. My findings strongly suggest that stimulus transience influences time-intensity trading in LSO neurons and may underlie the high spatial acuity of ITDs in envelope-modulated high-frequency sounds. This raises the following questions.
  - i. Does the  $F_{mod}$  contribute to time-intensity trading in LSO neurons?
  - ii. How does the  $F_{mod}$  in *in vivo* pulsed-sine stimulation influence the  $ITD_{env}$  sensitivity of LSO neurons?

Addressing these questions will deepen our understanding of synaptic integration of LSO neurons and clarify how their intrinsic properties and circuit-level properties shape binaural processing. In particular, such investigations could offer insights into the ongoing debate of the relative importance of temporal versus rate-based coding strategies in LSO neurons.

## 4.8 Conclusion

In this thesis, I provided a mechanistic framework for understanding how LSO neurons integrate excitation and inhibition to support sound source localization. I demonstrated that LSO neurons are tuned for fast, temporally precise synaptic integration, shaped by both passive and active membrane properties. The level-difference coding critically depended on the synchrony of converging inputs. While transient excitatory inputs reliably drive temporally precise APs and support ILD computation, sustained inputs fail to do so in the absence of temporal correlation. This highlights coincidence detection as a key mechanism in LSO neurons, enabling them to extract level-difference cues and temporal disparities of excitation and inhibition from rapid changes in signal envelopes. Thereby, my work provides a mechanistic reasoning for the high perceptual acuity of high-frequency transient sounds.

## 5 Index of Abbreviations

ACSF	Artificial cerebro spinal fluid
AMPA	$\alpha$ -amino-3-hydroxy-5-methyl-4-isoxazolepropionic acid
ANF	Auditory nerve fiber
AP	Action potential
AVCN	Anteroventral cochlear nucleus
BC	Bushy cell
CC	Current-clamp
CF	Characteristic frequency
CI	Correlation index
Cmem	Membrane capacitance
CN	Cochlear nucleus
CNIC	Central nucleus of the inferior colliculus
$cSW$	Compound synaptic weight
DC	Dynamic-clamp
DNLL	Dorsal nucleus of the lateral lemniscus
(e)EPSC	(evoked) excitatory postsynaptic current
EPSC	Excitatory postsynaptic conductance
EPSP	Excitatory postsynaptic potential
$f_{exc}$	Excitatory activation rate
FFT	Fast Fourier transformation
$f_{inh}$	Inhibitory activation rate
$F_{mod}$	Modulation rate
$F_{pref}$	Preferred frequency
$F_{pulse}$	Pulse rate
$f_{res}$	Resonance frequency
GBC	Globular bushy cell
$G_{exc}$	Excitatory conductance
$G_{inh}$	Inhibitory conductance
$G_{syn}$	Synaptic conductance
HCN	Hyperpolarization-activated cyclic nucleotide-gated
ILD	Interaural level difference
INLL	Intermediate nucleus of the lateral lemniscus
IPSC	Inhibitory postsynaptic current
IPSP	Inhibitory postsynaptic potential
ITD	Interaural time difference
$I_{thr}$	Current threshold
Kv channel	Voltage-gated potassium channel
LOC	Lateral olivocochlear
LSO	Lateral superior olive

MD	Modulation depth
MNTB	Medial nucleus of the trapezoid body
MSO	Medial superior olive
Nav channel	Voltage-gated sodium channel
NMDA	N-methyl-D-aspartate
PIF	Post-inhibitory facilitation
PSTH	Peri-stimulus time histogram
rMTF	Rate modulation transfer function
RS	Rayleigh statistics
SAC	Shuffled auto correlogram
SAM	Sinus amplitude modulation
SBC	Spherical bushy cell
SGN	Spiral ganglion neuron
STA	Spike-triggered average
$SW$	Synaptic weight
$SW_{exc}$	Excitatory synaptic weight
$SW_{inh}$	Inhibitory synaptic weight
tMTF	Temporal modulation transfer function
TST	Total stimulus time
$\tau_{decay}$	Decay time constant
$\tau_{mem}$	Membrane time constant
VAS	Ventral acoustic stria
VC	Voltage-clamp
$V_{mem}$	Membrane potential
$V_{rest}$	Resting membrane potential
VS	Vector strength
$V_{thr}$	Voltage threshold
Z	Impedance
$Z_{inst}$	Instantaneous impedance
$Z_{res}$	Resonant impedance

## 6 References

- Ashida, G., Kretzberg, J., & Tollin, D. J. (2016). Roles for Coincidence Detection in Coding Amplitude-Modulated Sounds. *PLoS Comput Biol*, 12(6), e1004997. <https://doi.org/10.1371/journal.pcbi.1004997>
- Ashida, G., Tollin, D. J., & Kretzberg, J. (2017). Physiological models of the lateral superior olive. *PLoS Comput Biol*, 13(12), e1005903. <https://doi.org/10.1371/journal.pcbi.1005903>
- Ashida, G., Tollin, D. J., & Kretzberg, J. (2021). Robustness of neuronal tuning to binaural sound localization cues against age-related loss of inhibitory synaptic inputs. *PLoS Comput Biol*, 17(7), e1009130. <https://doi.org/10.1371/journal.pcbi.1009130>
- Auerbach, B. D., & Gritton, H. J. (2022). Hearing in Complex Environments: Auditory Gain Control, Attention, and Hearing Loss. *Front Neurosci*, 16, 799787. <https://doi.org/10.3389/fnins.2022.799787>
- Banks, M. I., & Smith, P. H. (1992). Intracellular recordings from neurobiotin-labeled cells in brain slices of the rat medial nucleus of the trapezoid body. *J Neurosci*, 12(7), 2819-2837. <https://doi.org/10.1523/JNEUROSCI.12-07-02819.1992>
- Banna, H. U., Slayo, M., Armitage, J. A., Del Rosal, B., Vocale, L., & Spencer, S. J. (2024). Imaging the eye as a window to brain health: frontier approaches and future directions. *J Neuroinflammation*, 21(1), 309. <https://doi.org/10.1186/s12974-024-03304-3>
- Barnes-Davies, M., Barker, M. C., Osmani, F., & Forsythe, I. D. (2004). Kv1 currents mediate a gradient of principal neuron excitability across the tonotopic axis in the rat lateral superior olive. *Eur J Neurosci*, 19(2), 325-333. <https://doi.org/10.1111/j.0953-816x.2003.03133.x>
- Batra, R., Kuwada, S., & Fitzpatrick, D. C. (1997). Sensitivity to interaural temporal disparities of low- and high-frequency neurons in the superior olivary complex. I. Heterogeneity of responses. *J Neurophysiol*, 78(3), 1222-1236. <https://doi.org/10.1152/jn.1997.78.3.1222>
- Baumann, V. J., Lehnert, S., Leibold, C., & Koch, U. (2013). Tonotopic organization of the hyperpolarization-activated current (I<sub>h</sub>) in the mammalian medial superior olive. *Front Neural Circuits*, 7, 117. <https://doi.org/10.3389/fncir.2013.00117>
- Bean, B. P. (2007). The action potential in mammalian central neurons. *Nat Rev Neurosci*, 8(6), 451-465. <https://doi.org/10.1038/nrn2148>
- Beiderbeck, B., Myoga, M. H., Müller, N. I. C., Callan, A. R., Friauf, E., Grothe, B., & Pecka, M. (2018). Precisely timed inhibition facilitates action potential firing for spatial coding in the auditory brainstem. *Nat Commun*, 9(1), 1771. <https://doi.org/10.1038/s41467-018-04210-y>
- Benichoux, V., Rebillat, M., & Brette, R. (2016). On the variation of interaural time differences with frequency. *J Acoust Soc Am*, 139(4), 1810. <https://doi.org/10.1121/1.4944638>
- Bennett, D. L., Clark, A. J., Huang, J., Waxman, S. G., & Dib-Hajj, S. D. (2019). The Role of Voltage-Gated Sodium Channels in Pain Signaling. *Physiol Rev*, 99(2), 1079-1151. <https://doi.org/10.1152/physrev.00052.2017>

- Bernstein, L. R., & Trahiotis, C. (2002). Enhancing sensitivity to interaural delays at high frequencies by using "transposed stimuli". *J Acoust Soc Am*, *112*(3 Pt 1), 1026-1036. <https://doi.org/10.1121/1.1497620>
- Bernstein, L. R., & Trahiotis, C. (2009). How sensitivity to ongoing interaural temporal disparities is affected by manipulations of temporal features of the envelopes of high-frequency stimuli. *J Acoust Soc Am*, *125*(5), 3234-3242. <https://doi.org/10.1121/1.3101454>
- Bledsoe, S. C., Jr., Snead, C. R., Helfert, R. H., Prasad, V., Wenthold, R. J., & Altschuler, R. A. (1990). Immunocytochemical and lesion studies support the hypothesis that the projection from the medial nucleus of the trapezoid body to the lateral superior olive is glycinergic. *Brain Res*, *517*(1-2), 189-194. [https://doi.org/10.1016/0006-8993\(90\)91025-c](https://doi.org/10.1016/0006-8993(90)91025-c)
- Boudreau, J. C., & Tsuchitani, C. (1968). Binaural interaction in the cat superior olive S segment. *J Neurophysiol*, *31*(3), 442-454. <https://doi.org/10.1152/jn.1968.31.3.442>
- Brand, A., Behrend, O., Marquardt, T., McAlpine, D., & Grothe, B. (2002). Precise inhibition is essential for microsecond interaural time difference coding. *Nature*, *417*(6888), 543-547. <https://doi.org/10.1038/417543a>
- Brette, R., Rudolph, M., Carnevale, T., Hines, M., Beeman, D., Bower, J. M., Diesmann, M., Morrison, A., Goodman, P. H., Harris, F. C., Jr., Zirpe, M., Natschläger, T., Pecevski, D., Ermentrout, B., Djurfeldt, M., Lansner, A., Rochel, O., Vieville, T., Müller, E., . . . Destexhe, A. (2007). Simulation of networks of spiking neurons: a review of tools and strategies. *J Comput Neurosci*, *23*(3), 349-398. <https://doi.org/10.1007/s10827-007-0038-6>
- Brew, H. M., & Forsythe, I. D. (1995). Two voltage-dependent K<sup>+</sup> conductances with complementary functions in postsynaptic integration at a central auditory synapse. *J Neurosci*, *15*(12), 8011-8022. <https://doi.org/10.1523/JNEUROSCI.15-12-08011.1995>
- Brill, S. E., Janz, K., Singh, A., & Friauf, E. (2019). Considerable differences between auditory medulla, auditory midbrain, and hippocampal synapses during sustained high-frequency stimulation: Exceptional vesicle replenishment restricted to sound localization circuit. *Hear Res*, *381*, 107771. <https://doi.org/10.1016/j.heares.2019.07.008>
- Bronkhorst, A. W. (2015). The cocktail-party problem revisited: early processing and selection of multi-talker speech. *Atten Percept Psychophys*, *77*(5), 1465-1487. <https://doi.org/10.3758/s13414-015-0882-9>
- Brughera, A., Dunai, L., & Hartmann, W. M. (2013). Human interaural time difference thresholds for sine tones: the high-frequency limit. *J Acoust Soc Am*, *133*(5), 2839-2855. <https://doi.org/10.1121/1.4795778>
- Buchholz, S., Schnupp, J. W. H., Arndt, S., & Rosskoth-Kuhl, N. (2024). Interaural level difference sensitivity in neonatally deafened rats fitted with bilateral cochlear implants. *Sci Rep*, *14*(1), 30515. <https://doi.org/10.1038/s41598-024-82978-4>
- Buran, B. N., Strenzke, N., Neef, A., Gundelfinger, E. D., Moser, T., & Liberman, M. C. (2010). Onset coding is degraded in auditory nerve fibers from mutant mice lacking synaptic ribbons. *J Neurosci*, *30*(22), 7587-7597. <https://doi.org/10.1523/JNEUROSCI.0389-10.2010>

- Bures, Z., & Marsalek, P. (2013). On the precision of neural computation with interaural level differences in the lateral superior olive. *Brain Res*, 1536, 16-26. <https://doi.org/10.1016/j.brainres.2013.05.008>
- Caicedo, A., & Eybalin, M. (1999). Glutamate receptor phenotypes in the auditory brainstem and mid-brain of the developing rat. *Eur J Neurosci*, 11(1), 51-74. <https://doi.org/10.1046/j.1460-9568.1999.00410.x>
- Caird, D., & Klinke, R. (1983). Processing of binaural stimuli by cat superior olivary complex neurons. *Exp Brain Res*, 52(3), 385-399. <https://doi.org/10.1007/BF00238032>
- Campbell, N. (1909). The study of discontinuous phenomena. *Proceedings of the cambridge philosophical society*, 15(300), 250.
- Cant, N. B. (1984). The fine structure of the lateral superior olivary nucleus of the cat. *J Comp Neurol*, 227(1), 63-77. <https://doi.org/10.1002/cne.902270108>
- Cant, N. B., & Casseday, J. H. (1986). Projections from the anteroventral cochlear nucleus to the lateral and medial superior olivary nuclei. *J Comp Neurol*, 247(4), 457-476. <https://doi.org/10.1002/cne.902470406>
- Cao, X. J., & Oertel, D. (2010). Auditory nerve fibers excite targets through synapses that vary in convergence, strength, and short-term plasticity. *J Neurophysiol*, 104(5), 2308-2320. <https://doi.org/10.1152/jn.00451.2010>
- Cao, X. J., Shatadal, S., & Oertel, D. (2007). Voltage-sensitive conductances of bushy cells of the Mammalian ventral cochlear nucleus. *J Neurophysiol*, 97(6), 3961-3975. <https://doi.org/10.1152/jn.00052.2007>
- Case, D. T., Zhao, X., & Gillespie, D. C. (2011). Functional refinement in the projection from ventral cochlear nucleus to lateral superior olive precedes hearing onset in rat. *PLoS One*, 6(6), e20756. <https://doi.org/10.1371/journal.pone.0020756>
- Chance, F. S., Abbott, L. F., & Reyes, A. D. (2002). Gain modulation from background synaptic input. *Neuron*, 35(4), 773-782. [https://doi.org/10.1016/s0896-6273\(02\)00820-6](https://doi.org/10.1016/s0896-6273(02)00820-6)
- Cherry, E. C. (1953). Some Experiments on the Recognition of Speech, with One and with Two Ears. *The Journal of the Acoustical Society of America*, 25(5), 975-979. <https://doi.org/10.1121/1.1907229>
- Choudhury, N., Linley, D., Richardson, A., Anderson, M., Robinson, S. W., Marra, V., Ciampani, V., Walter, S. M., Kopp-Scheinpflug, C., Steinert, J. R., & Forsythe, I. D. (2020). Kv3.1 and Kv3.3 subunits differentially contribute to Kv3 channels and action potential repolarization in principal neurons of the auditory brainstem. *J Physiol*, 598(11), 2199-2222. <https://doi.org/10.1113/JP279668>
- Dagostin, A., & von Gersdorff, H. (2022). *Neural Maturation in the Murine Superior Olivary Complex* Abstracts of the 45th Annual MidWinter Meeting of the Association for Research in Otolaryngology,
- de Lera Ruiz, M., & Kraus, R. L. (2015). Voltage-Gated Sodium Channels: Structure, Function, Pharmacology, and Clinical Indications. *J Med Chem*, 58(18), 7093-7118. <https://doi.org/10.1021/jm501981g>

- Dietz, M., & Ashida, G. (2021). Computational Models of Binaural Processing. In R. Y. Litovsky, M. J. Goupell, R. R. Fay, & A. N. Popper (Eds.), *Binaural Hearing: With 93 Illustrations* (pp. 281-315). Springer. [https://doi.org/10.1007/978-3-030-57100-9\\_10](https://doi.org/10.1007/978-3-030-57100-9_10)
- Dietz, M., Bernstein, L. R., Trahiotis, C., Ewert, S. D., & Hohmann, V. (2013). The effect of overall level on sensitivity to interaural differences of time and level at high frequencies. *J Acoust Soc Am*, *134*(1), 494-502. <https://doi.org/10.1121/1.4807827>
- Dodla, R., & Rinzel, J. (2006). Enhanced neuronal response induced by fast inhibition. *Phys Rev E Stat Nonlin Soft Matter Phys*, *73*(1 Pt 1), 010903. <https://doi.org/10.1103/PhysRevE.73.010903>
- Dodla, R., Svirskis, G., & Rinzel, J. (2006). Well-timed, brief inhibition can promote spiking: postinhibitory facilitation. *J Neurophysiol*, *95*(4), 2664-2677. <https://doi.org/10.1152/jn.00752.2005>
- Dreyer, A., & Delgutte, B. (2006). Phase locking of auditory-nerve fibers to the envelopes of high-frequency sounds: implications for sound localization. *J Neurophysiol*, *96*(5), 2327-2341. <https://doi.org/10.1152/jn.00326.2006>
- Ebbers, L., Satheesh, S. V., Janz, K., Rüttiger, L., Blosa, M., Hofmann, F., Morawski, M., Griesemer, D., Knipper, M., Friauf, E., & Nothwang, H. G. (2015). L-type Calcium Channel Cav1.2 Is Required for Maintenance of Auditory Brainstem Nuclei. *J Biol Chem*, *290*(39), 23692-23710. <https://doi.org/10.1074/jbc.M115.672675>
- Ehrlich, I., Löhrike, S., & Friauf, E. (1999). Shift from depolarizing to hyperpolarizing glycine action in rat auditory neurones is due to age-dependent Cl<sup>-</sup> regulation. *J Physiol*, *520 Pt 1*(Pt 1), 121-137. <https://doi.org/10.1111/j.1469-7793.1999.00121.x>
- Faisal, A. A., Selen, L. P., & Wolpert, D. M. (2008). Noise in the nervous system. *Nat Rev Neurosci*, *9*(4), 292-303. <https://doi.org/10.1038/nrn2258>
- Felix, R. A., 2nd, & Magnusson, A. K. (2016). Development of excitatory synaptic transmission to the superior paraolivary and lateral superior olivary nuclei optimizes differential decoding strategies. *Neuroscience*, *334*, 1-12. <https://doi.org/10.1016/j.neuroscience.2016.07.039>
- Fettiplace, R. (2017). Hair Cell Transduction, Tuning, and Synaptic Transmission in the Mammalian Cochlea. *Compr Physiol*, *7*(4), 1197-1227. <https://doi.org/10.1002/cphy.c160049>
- Finlayson, P. G., & Caspary, D. M. (1991). Low-frequency neurons in the lateral superior olive exhibit phase-sensitive binaural inhibition. *J Neurophysiol*, *65*(3), 598-605. <https://doi.org/10.1152/jn.1991.65.3.598>
- Fisch, J. O. (2021). *Synaptic integration of sound localizing neurons: a dynamic-clamp analysis* Master thesis at University of Kaiserslautern. Kaiserslautern, Germany.
- Fischer, L., Leibold, C., & Felmy, F. (2018). Resonance Properties in Auditory Brainstem Neurons. *Front Cell Neurosci*, *12*, 8. <https://doi.org/10.3389/fncel.2018.00008>
- Fischl, M. J., Burger, R. M., Schmidt-Pauly, M., Alexandrova, O., Sinclair, J. L., Grothe, B., Forsythe, I. D., & Kopp-Scheinpflug, C. (2016). Physiology and anatomy of neurons in the medial superior olive of the mouse. *J Neurophysiol*, *116*(6), 2676-2688. <https://doi.org/10.1152/jn.00523.2016>

- Fontaine, B., MacLeod, K. M., Lubejko, S. T., Steinberg, L. J., Koppl, C., & Pena, J. L. (2014). Emergence of band-pass filtering through adaptive spiking in the owl's cochlear nucleus. *J Neurophysiol*, *112*(2), 430-445. <https://doi.org/10.1152/jn.00132.2014>
- Ford, M. C., Alexandrova, O., Cossell, L., Stange-Marten, A., Sinclair, J., Kopp-Scheinpflug, C., Pecka, M., Attwell, D., & Grothe, B. (2015). Tuning of Ranvier node and internode properties in myelinated axons to adjust action potential timing. *Nat Commun*, *6*, 8073. <https://doi.org/10.1038/ncomms9073>
- Fourcaud-Trocme, N., Hansel, D., van Vreeswijk, C., & Brunel, N. (2003). How spike generation mechanisms determine the neuronal response to fluctuating inputs. *J Neurosci*, *23*(37), 11628-11640. <https://doi.org/10.1523/JNEUROSCI.23-37-11628.2003>
- Franken, T. P., Bondy, B. J., Haimes, D. B., Goldwyn, J. H., Golding, N. L., Smith, P. H., & Joris, P. X. (2021). Glycinergic axonal inhibition subserves acute spatial sensitivity to sudden increases in sound intensity. *Elife*, *10*. <https://doi.org/10.7554/eLife.62183>
- Franken, T. P., Joris, P. X., & Smith, P. H. (2018). Principal cells of the brainstem's interaural sound level detector are temporal differentiators rather than integrators. *Elife*, *7*. <https://doi.org/10.7554/eLife.33854>
- Friauf, E., Fischer, A. U., & Fuhr, M. F. (2015). Synaptic plasticity in the auditory system: a review. *Cell Tissue Res*, *361*(1), 177-213. <https://doi.org/10.1007/s00441-015-2176-x>
- Friauf, E., Krächan, E. G., & Müller, N. I. C. (2019). Lateral Superior Olive. In *The Oxford Handbook of the Auditory Brainstem* (pp. 329-394). Oxford University Press. <https://doi.org/10.1093/oxfordhb/9780190849061.013.10>
- Friauf, E., & Ostwald, J. (1988). Divergent projections of physiologically characterized rat ventral cochlear nucleus neurons as shown by intra-axonal injection of horseradish peroxidase. *Exp Brain Res*, *73*(2), 263-284. <https://doi.org/10.1007/BF00248219>
- Gai, Y., Doiron, B., Kotak, V., & Rinzel, J. (2009). Noise-gated encoding of slow inputs by auditory brain stem neurons with a low-threshold K<sup>+</sup> current. *J Neurophysiol*, *102*(6), 3447-3460. <https://doi.org/10.1152/jn.00538.2009>
- Gai, Y., Doiron, B., & Rinzel, J. (2010). Slope-based stochastic resonance: how noise enables phasic neurons to encode slow signals. *PLoS Comput Biol*, *6*(6), e1000825. <https://doi.org/10.1371/journal.pcbi.1000825>
- Galambos, R., Schwartzkopff, J., & Rupert, A. (1959). Microelectrode study of superior olivary nuclei. *Am J Physiol*, *197*, 527-536. <https://doi.org/10.1152/ajplegacy.1959.197.3.527>
- Garcia-Pino, E., Gessele, N., & Koch, U. (2017). Enhanced Excitatory Connectivity and Disturbed Sound Processing in the Auditory Brainstem of Fragile X Mice. *J Neurosci*, *37*(31), 7403-7419. <https://doi.org/10.1523/JNEUROSCI.2310-16.2017>
- Gjoni, E., Aguet, C., Sahlender, D. A., Knott, G., & Schneggenburger, R. (2018). Ultrastructural basis of strong unitary inhibition in a binaural neuron. *J Physiol*, *596*(20), 4969-4982. <https://doi.org/10.1113/JP276015>
- Gjoni, E., Zenke, F., Bouhours, B., & Schneggenburger, R. (2018). Specific synaptic input strengths determine the computational properties of excitation-inhibition integration in

- a sound localization circuit. *J Physiol*, 596(20), 4945-4967. <https://doi.org/10.1113/JP276012>
- Gleiss, H., Encke, J., Lingner, A., Jennings, T. R., Brosel, S., Kunz, L., Grothe, B., & Pecka, M. (2019). Cooperative population coding facilitates efficient sound-source separability by adaptation to input statistics. *PLoS Biol*, 17(7), e3000150. <https://doi.org/10.1371/journal.pbio.3000150>
- Glendenning, K. K., Hutson, K. A., Nudo, R. J., & Masterton, R. B. (1985). Acoustic chiasm II: Anatomical basis of binaurality in lateral superior olive of cat. *J Comp Neurol*, 232(2), 261-285. <https://doi.org/10.1002/cne.902320210>
- Goldberg, J. M., & Brown, P. B. (1969). Response of binaural neurons of dog superior olivary complex to dichotic tonal stimuli: some physiological mechanisms of sound localization. *J Neurophysiol*, 32(4), 613-636. <https://doi.org/10.1152/jn.1969.32.4.613>
- Golding, N. L., & Oertel, D. (2012). Synaptic integration in dendrites: exceptional need for speed. *J Physiol*, 590(22), 5563-5569. <https://doi.org/10.1113/jphysiol.2012.229328>
- Golding, N. L., Robertson, D., & Oertel, D. (1995). Recordings from slices indicate that octopus cells of the cochlear nucleus detect coincident firing of auditory nerve fibers with temporal precision. *J Neurosci*, 15(4), 3138-3153. <https://doi.org/10.1523/JNEUROSCI.15-04-03138.1995>
- Goupell, M. J., Stecker, G. C., Williams, B. T., Bilokon, A., & Tollin, D. J. (2024). The Rapid Decline in Interaural-Time-Difference Sensitivity for Pure Tones Can Be Explained by Peripheral Filtering. *J Assoc Res Otolaryngol*, 25(4), 377-385. <https://doi.org/10.1007/s10162-024-00949-y>
- Greenberg, D., Monaghan, J. J. M., Dietz, M., Marquardt, T., & McAlpine, D. (2017). Influence of envelope waveform on ITD sensitivity of neurons in the auditory midbrain. *J Neurophysiol*, 118(4), 2358-2370. <https://doi.org/10.1152/jn.01048.2015>
- Griffin, S. J., Bernstein, L. R., Ingham, N. J., & McAlpine, D. (2005). Neural sensitivity to interaural envelope delays in the inferior colliculus of the guinea pig. *J Neurophysiol*, 93(6), 3463-3478. <https://doi.org/10.1152/jn.00794.2004>
- Grothe, B., Leibold, C., & Pecka, M. (2019). The Medial Superior Olivary Nucleus. In *The Oxford Handbook of the Auditory Brainstem* (pp. 301-328). Oxford University Press. <https://doi.org/10.1093/oxfordhb/9780190849061.013.9>
- Grothe, B., & Park, T. J. (1995). Time can be traded for intensity in the lower auditory system. *Naturwissenschaften*, 82(11), 521-523. <https://doi.org/10.1007/BF01134488>
- Grothe, B., Pecka, M., & McAlpine, D. (2010). Mechanisms of sound localization in mammals. *Physiol Rev*, 90(3), 983-1012. <https://doi.org/10.1152/physrev.00026.2009>
- Guinan, J. J., Guinan, S. S., & Norris, B. E. (1972). Single Auditory Units in the Superior Olivary Complex: I: Responses to Sounds and Classifications Based on Physiological Properties. *International Journal of Neuroscience*, 4(3), 101-120. <https://doi.org/10.3109/00207457209147165>
- Guinan, J. J., Norris, B. E., & Guinan, S. S. (1972). Single Auditory Units in the Superior Olivary Complex: II: Locations of Unit Categories and Tonotopic Organization. *International Journal of Neuroscience*, 4(4), 147-166. <https://doi.org/10.3109/00207457209164756>

- Haragopal, H., Mellott, J. G., Dhar, M., Kanel, A., Mafi, A., Tokar, N., & Winters, B. D. (2023). Tonotopic distribution and inferior colliculus projection pattern of inhibitory and excitatory cell types in the lateral superior olive of mice. *J Comp Neurol*, 531(14), 1381-1388. <https://doi.org/10.1002/cne.25515>
- Haragopal, H., Voytek, M. J., & Winters, B. D. (2025). Synaptic drive onto inhibitory and excitatory principal neurons of the mouse lateral superior olive. *eNeuro*. <https://doi.org/10.1523/ENEURO.0106-25.2025>
- Haragopal, H., & Winters, B. D. (2023). Principal neuron diversity in the murine lateral superior olive supports multiple sound localization strategies and segregation of information in higher processing centers. *Commun Biol*, 6(1), 432. <https://doi.org/10.1038/s42003-023-04802-5>
- Hardman, R. M., & Forsythe, I. D. (2009). Ether-a-go-go-related gene K<sup>+</sup> channels contribute to threshold excitability of mouse auditory brainstem neurons. *J Physiol*, 587(Pt 11), 2487-2497. <https://doi.org/10.1113/jphysiol.2009.170548>
- Hartmann, W. M. (2021). Localization and Lateralization of Sound. In *Binaural Hearing* (pp. 9-45). Springer. [https://doi.org/10.1007/978-3-030-57100-9\\_2](https://doi.org/10.1007/978-3-030-57100-9_2)
- Hartmann, W. M., & Macaulay, E. J. (2014). Anatomical limits on interaural time differences: an ecological perspective. *Front Neurosci*, 8, 34. <https://doi.org/10.3389/fnins.2014.00034>
- Hassfurth, B., Magnusson, A. K., Grothe, B., & Koch, U. (2009). Sensory deprivation regulates the development of the hyperpolarization-activated current in auditory brainstem neurons. *Eur J Neurosci*, 30(7), 1227-1238. <https://doi.org/10.1111/j.1460-9568.2009.06925.x>
- Held, H. (1893). Die centrale Gehörleitung. *Arch Anat Physiol*, 17, 201–248.
- Helfert, R. H., & Schwartz, I. R. (1987). Morphological features of five neuronal classes in the gerbil lateral superior olive. *Am J Anat*, 179(1), 55-69. <https://doi.org/10.1002/aja.1001790108>
- Hermann, J., Pecka, M., von Gersdorff, H., Grothe, B., & Klug, A. (2007). Synaptic transmission at the calyx of Held under in vivo like activity levels. *J Neurophysiol*, 98(2), 807-820. <https://doi.org/10.1152/jn.00355.2007>
- Higgs, M. H., Slee, S. J., & Spain, W. J. (2006). Diversity of gain modulation by noise in neocortical neurons: regulation by the slow afterhyperpolarization conductance. *J Neurosci*, 26(34), 8787-8799. <https://doi.org/10.1523/JNEUROSCI.1792-06.2006>
- Higgs, M. H., & Spain, W. J. (2011). Kv1 channels control spike threshold dynamics and spike timing in cortical pyramidal neurones. *J Physiol*, 589(Pt 21), 5125-5142. <https://doi.org/10.1113/jphysiol.2011.216721>
- Hirtz, J. J., Boesen, M., Braun, N., Deitmer, J. W., Kramer, F., Lohr, C., Müller, B., Nothwang, H. G., Striessnig, J., Lührke, S., & Friauf, E. (2011). Cav1.3 calcium channels are required for normal development of the auditory brainstem. *J Neurosci*, 31(22), 8280-8294. <https://doi.org/10.1523/JNEUROSCI.5098-10.2011>

- Hodgkin, A. L. (1948). The local electric changes associated with repetitive action in a non-medullated axon. *J Physiol*, 107(2), 165-181. <https://doi.org/10.1113/jphysiol.1948.sp004260>
- Hutcheon, B., & Yarom, Y. (2000). Resonance, oscillation and the intrinsic frequency preferences of neurons. *Trends Neurosci*, 23(5), 216-222. [https://doi.org/10.1016/s0166-2236\(00\)01547-2](https://doi.org/10.1016/s0166-2236(00)01547-2)
- Irvine, D. R., Park, V. N., & McCormick, L. (2001). Mechanisms underlying the sensitivity of neurons in the lateral superior olive to interaural intensity differences. *J Neurophysiol*, 86(6), 2647-2666. <https://doi.org/10.1152/jn.2001.86.6.2647>
- Izhikevich, E. M. (2006). *Dynamical Systems in Neuroscience*. MIT Press. <https://doi.org/10.7551/mitpress/2526.001.0001>
- Jercog, P. E., Svirskis, G., Kotak, V. C., Sanes, D. H., & Rinzel, J. (2010). Asymmetric excitatory synaptic dynamics underlie interaural time difference processing in the auditory system. *PLoS Biol*, 8(6), e1000406. <https://doi.org/10.1371/journal.pbio.1000406>
- Jing, A., Xi, S., Fransazov, I., & Goldwyn, J. H. (2025). Axon initial segment plasticity caused by auditory deprivation degrades time difference sensitivity in a model of neural responses to cochlear implants. *J Comput Neurosci*. <https://doi.org/10.1007/s10827-025-00902-9>
- Jing, Z., Pecka, M., & Grothe, B. (2021). Ketamine-xylazine anesthesia depth affects auditory neuronal responses in the lateral superior olive complex of the gerbil. *J Neurophysiol*, 126(5), 1660-1669. <https://doi.org/10.1152/jn.00217.2021>
- Johnston, J., Forsythe, I. D., & Kopp-Scheinflug, C. (2010). Going native: voltage-gated potassium channels controlling neuronal excitability. *J Physiol*, 588(Pt 17), 3187-3200. <https://doi.org/10.1113/jphysiol.2010.191973>
- Joris, P. X. (1996). Envelope coding in the lateral superior olive. II. Characteristic delays and comparison with responses in the medial superior olive. *J Neurophysiol*, 76(4), 2137-2156. <https://doi.org/10.1152/jn.1996.76.4.2137>
- Joris, P. X. (2019). Neural binaural sensitivity at high sound speeds: Single cell responses in cat midbrain to fast-changing interaural time differences of broadband sounds. *J Acoust Soc Am*, 145(1), EL45. <https://doi.org/10.1121/1.5087524>
- Joris, P. X. (2022). In praise of adventitious sounds. *Hear Res*, 425, 108592. <https://doi.org/10.1016/j.heares.2022.108592>
- Joris, P. X., Carney, L. H., Smith, P. H., & Yin, T. C. (1994). Enhancement of neural synchronization in the anteroventral cochlear nucleus. I. Responses to tones at the characteristic frequency. *J Neurophysiol*, 71(3), 1022-1036. <https://doi.org/10.1152/jn.1994.71.3.1022>
- Joris, P. X., Louage, D. H., Cardoen, L., & van der Heijden, M. (2006). Correlation index: a new metric to quantify temporal coding. *Hear Res*, 216-217, 19-30. <https://doi.org/10.1016/j.heares.2006.03.010>
- Joris, P. X., & Smith, P. H. (2008). The volley theory and the spherical cell puzzle. *Neuroscience*, 154(1), 65-76. <https://doi.org/10.1016/j.neuroscience.2008.03.002>

- Joris, P. X., Smith, P. H., & Yin, T. C. (1994). Enhancement of neural synchronization in the anteroventral cochlear nucleus. II. Responses in the tuning curve tail. *J Neurophysiol*, 71(3), 1037-1051. <https://doi.org/10.1152/jn.1994.71.3.1037>
- Joris, P. X., & Trussell, L. O. (2018). The Calyx of Held: A Hypothesis on the Need for Reliable Timing in an Intensity-Difference Encoder. *Neuron*, 100(3), 534-549. <https://doi.org/10.1016/j.neuron.2018.10.026>
- Joris, P. X., & van der Heijden, M. (2019). Early Binaural Hearing: The Comparison of Temporal Differences at the Two Ears. *Annu Rev Neurosci*, 42, 433-457. <https://doi.org/10.1146/annurev-neuro-080317-061925>
- Joris, P. X., & Yin, T. C. (1992). Responses to amplitude-modulated tones in the auditory nerve of the cat. *J Acoust Soc Am*, 91(1), 215-232. <https://doi.org/10.1121/1.402757>
- Joris, P. X., & Yin, T. C. (1995). Envelope coding in the lateral superior olive. I. Sensitivity to interaural time differences. *J Neurophysiol*, 73(3), 1043-1062. <https://doi.org/10.1152/jn.1995.73.3.1043>
- Joris, P. X., & Yin, T. C. (1998). Envelope coding in the lateral superior olive. III. Comparison with afferent pathways. *J Neurophysiol*, 79(1), 253-269. <https://doi.org/10.1152/jn.1998.79.1.253>
- Kaczmarek, L. K. (2023). Modulation of potassium conductances optimizes fidelity of auditory information. *Proc Natl Acad Sci U S A*, 120(12), e2216440120. <https://doi.org/10.1073/pnas.2216440120>
- Kaczmarek, L. K., & Zhang, Y. (2017). Kv3 Channels: Enablers of Rapid Firing, Neurotransmitter Release, and Neuronal Endurance. *Physiol Rev*, 97(4), 1431-1468. <https://doi.org/10.1152/physrev.00002.2017>
- Kandler, K., & Friauf, E. (1995). Development of glycinergic and glutamatergic synaptic transmission in the auditory brainstem of perinatal rats. *J Neurosci*, 15(10), 6890-6904. <https://doi.org/10.1523/JNEUROSCI.15-10-06890.1995>
- Karcz, A., Hennig, M. H., Robbins, C. A., Tempel, B. L., Rübsamen, R., & Kopp-Scheinpflug, C. (2011). Low-voltage activated Kv1.1 subunits are crucial for the processing of sound source location in the lateral superior olive in mice. *J Physiol*, 589(Pt 5), 1143-1157. <https://doi.org/10.1113/jphysiol.2010.203331>
- Keine, C., & Englitz, B. (2025). Cellular and synaptic specializations for sub-millisecond precision in the mammalian auditory brainstem. *Front Cell Neurosci*, 19, 1568506. <https://doi.org/10.3389/fncel.2025.1568506>
- Kessler, D., Carr, C. E., Kretzberg, J., & Ashida, G. (2021). Theoretical Relationship Between Two Measures of Spike Synchrony: Correlation Index and Vector Strength. *Front Neurosci*, 15, 761826. <https://doi.org/10.3389/fnins.2021.761826>
- Khurana, S., Remme, M. W., Rinzel, J., & Golding, N. L. (2011). Dynamic interaction of Ih and IK-LVA during trains of synaptic potentials in principal neurons of the medial superior olive. *J Neurosci*, 31(24), 8936-8947. <https://doi.org/10.1523/JNEUROSCI.1079-11.2011>

- Kim, D. O., Carney, L., & Kuwada, S. (2020). Amplitude modulation transfer functions reveal opposing populations within both the inferior colliculus and medial geniculate body. *J Neurophysiol*, 124(4), 1198-1215. <https://doi.org/10.1152/jn.00279.2020>
- Kim, G., & Kandler, K. (2003). Elimination and strengthening of glycinergic/GABAergic connections during tonotopic map formation. *Nat Neurosci*, 6(3), 282-290. <https://doi.org/10.1038/nn1015>
- Kim, Y., Kim, J. S., & Kim, G. W. (2018). A Novel Frequency Selectivity Approach Based on Travelling Wave Propagation in Mechanoluminescence Basilar Membrane for Artificial Cochlea. *Sci Rep*, 8(1), 12023. <https://doi.org/10.1038/s41598-018-30633-0>
- Kladisios, N., Fischer, L., & Felmy, F. (2020). Minimal Number of Required Inputs for Temporally Precise Action Potential Generation in Auditory Brainstem Nuclei. *Front Cell Neurosci*, 14, 592213. <https://doi.org/10.3389/fncel.2020.592213>
- Klein-Hennig, M., Dietz, M., Hohmann, V., & Ewert, S. D. (2011). The influence of different segments of the ongoing envelope on sensitivity to interaural time delays. *J Acoust Soc Am*, 129(6), 3856-3872. <https://doi.org/10.1121/1.3585847>
- Klug, J., Schmors, L., Ashida, G., & Dietz, M. (2020). Neural rate difference model can account for lateralization of high-frequency stimuli. *J Acoust Soc Am*, 148(2), 678. <https://doi.org/10.1121/10.0001602>
- Koka, K., Read, H. L., & Tollin, D. J. (2008). The acoustical cues to sound location in the rat: measurements of directional transfer functions. *J Acoust Soc Am*, 123(6), 4297-4309. <https://doi.org/10.1121/1.2916587>
- Kopp-Scheinflug, C., Dehmel, S., Dörrscheidt, G. J., & Rübsamen, R. (2002). Interaction of excitation and inhibition in anteroventral cochlear nucleus neurons that receive large endbulb synaptic endings. *J Neurosci*, 22(24), 11004-11018. <https://doi.org/10.1523/JNEUROSCI.22-24-11004.2002>
- Kopp-Scheinflug, C., Fuchs, K., Lippe, W. R., Tempel, B. L., & Rübsamen, R. (2003). Decreased temporal precision of auditory signaling in Kcna1-null mice: an electrophysiological study in vivo. *J Neurosci*, 23(27), 9199-9207. <https://doi.org/10.1523/JNEUROSCI.23-27-09199.2003>
- Kopp-Scheinflug, C., Pigott, B. M., & Forsythe, I. D. (2015). Nitric oxide selectively suppresses IH currents mediated by HCN1-containing channels. *J Physiol*, 593(7), 1685-1700. <https://doi.org/10.1113/jphysiol.2014.282194>
- Kuba, H., Ishii, T. M., & Ohmori, H. (2006). Axonal site of spike initiation enhances auditory coincidence detection. *Nature*, 444(7122), 1069-1072. <https://doi.org/10.1038/nature05347>
- Kuba, H., Oichi, Y., & Ohmori, H. (2010). Presynaptic activity regulates Na(+) channel distribution at the axon initial segment. *Nature*, 465(7301), 1075-1078. <https://doi.org/10.1038/nature09087>
- Kuenzel, T., Borst, J. G., & van der Heijden, M. (2011). Factors controlling the input-output relationship of spherical bushy cells in the gerbil cochlear nucleus. *J Neurosci*, 31(11), 4260-4273. <https://doi.org/10.1523/JNEUROSCI.5433-10.2011>

- Kuenzel, T., Nerlich, J., Wagner, H., Rübnsamen, R., & Milenkovic, I. (2015). Inhibitory properties underlying non-monotonic input-output relationship in low-frequency spherical bushy neurons of the gerbil. *Front Neural Circuits*, 9, 14. <https://doi.org/10.3389/fncir.2015.00014>
- Kuznetsova, M. S., Higgs, M. H., & Spain, W. J. (2008). Adaptation of firing rate and spike-timing precision in the avian cochlear nucleus. *J Neurosci*, 28(46), 11906-11915. <https://doi.org/10.1523/JNEUROSCI.3827-08.2008>
- Laback, B., Egger, K., & Majdak, P. (2015). Perception and coding of interaural time differences with bilateral cochlear implants. *Hear Res*, 322, 138-150. <https://doi.org/10.1016/j.heares.2014.10.004>
- Lauer, A. M., Connelly, C. J., Graham, H., & Ryugo, D. K. (2013). Morphological characterization of bushy cells and their inputs in the laboratory mouse (*Mus musculus*) anteroventral cochlear nucleus. *PLoS One*, 8(8), e73308. <https://doi.org/10.1371/journal.pone.0073308>
- Lauer, A. M., Slee, S. J., & May, B. J. (2011). Acoustic basis of directional acuity in laboratory mice. *J Assoc Res Otolaryngol*, 12(5), 633-645. <https://doi.org/10.1007/s10162-011-0279-y>
- Lazarov, E., Dannemeyer, M., Feulner, B., Enderlein, J., Gutnick, M. J., Wolf, F., & Neef, A. (2018). An axon initial segment is required for temporal precision in action potential encoding by neuronal populations. *Sci Adv*, 4(11), eaau8621. <https://doi.org/10.1126/sciadv.aau8621>
- Leao, K. E., Leao, R. N., Sun, H., Fyffe, R. E., & Walmsley, B. (2006). Hyperpolarization-activated currents are differentially expressed in mice brainstem auditory nuclei. *J Physiol*, 576(Pt 3), 849-864. <https://doi.org/10.1113/jphysiol.2006.114702>
- Leao, K. E., Leao, R. N., & Walmsley, B. (2011). Modulation of dendritic synaptic processing in the lateral superior olive by hyperpolarization-activated currents. *Eur J Neurosci*, 33(8), 1462-1470. <https://doi.org/10.1111/j.1460-9568.2011.07627.x>
- Leao, R. M. (2019). The ion channels and synapses responsible for the physiological diversity of mammalian lower brainstem auditory neurons. *Hear Res*, 376, 33-46. <https://doi.org/10.1016/j.heares.2018.12.011>
- Lehnert, S., Ford, M. C., Alexandrova, O., Hellmundt, F., Felmy, F., Grothe, B., & Leibold, C. (2014). Action potential generation in an anatomically constrained model of medial superior olive axons. *J Neurosci*, 34(15), 5370-5384. <https://doi.org/10.1523/JNEUROSCI.4038-13.2014>
- Li, K., Chan, C. H. K., Rajendran, V. G., Meng, Q., Roskoth-Kuhl, N., & Schnupp, J. W. H. (2019). Microsecond sensitivity to envelope interaural time differences in rats. *J Acoust Soc Am*, 145(5), EL341. <https://doi.org/10.1121/1.5099164>
- Lim, D., & Capranica, R. R. (1994). Measurement of temporal regularity of spike train responses in auditory nerve fibers of the green treefrog. *J Neurosci Methods*, 52(2), 203-213. [https://doi.org/10.1016/0165-0270\(94\)90131-7](https://doi.org/10.1016/0165-0270(94)90131-7)
- Linaro, D., Biro, I., & Giugliano, M. (2018). Dynamical response properties of neocortical neurons to conductance-driven time-varying inputs. *Eur J Neurosci*, 47(1), 17-32. <https://doi.org/10.1111/ejn.13761>

- Lindsey, B. G. (1975). Fine structure and distribution of axon terminals from the cochlear nucleus on neurons in the medial superior olivary nucleus of the cat. *J Comp Neurol*, 160(1), 81-103. <https://doi.org/10.1002/cne.901600106>
- Longtin, A. (1993). Stochastic resonance in neuron models. *Journal of Statistical Physics*, 70(1-2), 309-327. <https://doi.org/10.1007/bf01053970>
- Lubejko, S. T., Fontaine, B., Soueidan, S. E., & MacLeod, K. M. (2019). Spike threshold adaptation diversifies neuronal operating modes in the auditory brain stem. *J Neurophysiol*, 122(6), 2576-2590. <https://doi.org/10.1152/jn.00234.2019>
- Magnusson, A. K., Park, T. J., Pecka, M., Grothe, B., & Koch, U. (2008). Retrograde GABA signaling adjusts sound localization by balancing excitation and inhibition in the brainstem. *Neuron*, 59(1), 125-137. <https://doi.org/10.1016/j.neuron.2008.05.011>
- Maki, K., & Furukawa, S. (2005). Acoustical cues for sound localization by the Mongolian gerbil, *Meriones unguiculatus*. *J Acoust Soc Am*, 118(2), 872-886. <https://doi.org/10.1121/1.1944647>
- Manis, P. B., & Marx, S. O. (1991). Outward currents in isolated ventral cochlear nucleus neurons. *J Neurosci*, 11(9), 2865-2880. <https://doi.org/10.1523/JNEUROSCI.11-09-02865.1991>
- Maraslioglu-Sperber, A., Pizzi, E., Fisch, J. O., Kattler, K., Ritter, T., & Friauf, E. (2024). Molecular and functional profiling of cell diversity and identity in the lateral superior olive, an auditory brainstem center with ascending and descending projections. *Front Cell Neurosci*, 18, 1354520. <https://doi.org/10.3389/fncel.2024.1354520>
- Mardia, K. V., & Jupp, P. E. (1999). *Directional Statistics*. John Wiley & Sons, Ltd. <https://doi.org/10.1002/9780470316979>
- Markl, H., & Ehret, G. (1973). Die Hörschwelle der Maus (*Mus musculus*). *Zeitschrift für Tierpsychologie*, 33(3-4), 274-286. <https://doi.org/10.1111/j.1439-0310.1973.tb02096.x>
- McGinley, M. J., & Oertel, D. (2006). Rate thresholds determine the precision of temporal integration in principal cells of the ventral cochlear nucleus. *Hear Res*, 216-217, 52-63. <https://doi.org/10.1016/j.heares.2006.02.006>
- Mellott, J. G., Dhar, M., Mafi, A., Tokar, N., & Winters, B. D. (2022). Tonotopic distribution and inferior colliculus projection pattern of inhibitory and excitatory cell types in the lateral superior olive of Mongolian gerbils. *J Comp Neurol*, 530(2), 506-517. <https://doi.org/10.1002/cne.25226>
- Mikiel-Hunter, J., Kotak, V., & Rinzel, J. (2016). High-Frequency Resonance in the Gerbil Medial Superior Olive. *PLoS Comput Biol*, 12(11), e1005166. <https://doi.org/10.1371/journal.pcbi.1005166>
- Moore, M. J., & Caspary, D. M. (1983). Strychnine blocks binaural inhibition in lateral superior olivary neurons. *J Neurosci*, 3(1), 237-242. <https://doi.org/10.1523/JNEUROSCI.03-01-00237.1983>
- Müller, M., Hu, H., Dietz, M., Beiderbeck, B., Ferreiro, D. N., & Pecka, M. (2023). Temporal hyper-precision of brainstem neurons alters spatial sensitivity of binaural auditory

- processing with cochlear implants. *Front Neurosci*, 16, 1021541. <https://doi.org/10.3389/fnins.2022.1021541>
- Müller, M. K., Jovanovic, S., Keine, C., Radulovic, T., Rübsamen, R., & Milenkovic, I. (2019). Functional Development of Principal Neurons in the Anteroventral Cochlear Nucleus Extends Beyond Hearing Onset. *Front Cell Neurosci*, 13, 119. <https://doi.org/10.3389/fncel.2019.00119>
- Müller, N. I. C., Sonntag, M., Maraslioglu, A., Hirtz, J. J., & Friauf, E. (2019). Topographic map refinement and synaptic strengthening of a sound localization circuit require spontaneous peripheral activity. *J Physiol*, 597(22), 5469-5493. <https://doi.org/10.1113/JP277757>
- Myoga, M. H., Lehnert, S., Leibold, C., Felmy, F., & Grothe, B. (2014). Glycinergic inhibition tunes coincidence detection in the auditory brainstem. *Nat Commun*, 5, 3790. <https://doi.org/10.1038/ncomms4790>
- Nielsen, T. A., DiGregorio, D. A., & Silver, R. A. (2004). Modulation of glutamate mobility reveals the mechanism underlying slow-rising AMPAR EPSCs and the diffusion coefficient in the synaptic cleft. *Neuron*, 42(5), 757-771. <https://doi.org/10.1016/j.neuron.2004.04.003>
- Oertel, D. (1983). Synaptic responses and electrical properties of cells in brain slices of the mouse anteroventral cochlear nucleus. *J Neurosci*, 3(10), 2043-2053. <https://doi.org/10.1523/JNEUROSCI.03-10-02043.1983>
- Oertel, D., Cao, X.-J., & Recio-Spinoso, A. (2019). The Cochlear Nuclei. In *The Oxford Handbook of the Auditory Brainstem* (pp. 95-122). Oxford University Press. <https://doi.org/10.1093/oxfordhb/9780190849061.013.4>
- Ono, M., Bishop, D. C., & Oliver, D. L. (2020). Neuronal sensitivity to the interaural time difference of the sound envelope in the mouse inferior colliculus. *Hear Res*, 385, 107844. <https://doi.org/10.1016/j.heares.2019.107844>
- Osen, K. K. (1969). Cytoarchitecture of the cochlear nuclei in the cat. *J Comp Neurol*, 136(4), 453-484. <https://doi.org/10.1002/cne.901360407>
- Owruksy, Z. L., Benichoux, V., & Tollin, D. J. (2021). Binaural Hearing by the Mammalian Auditory Brainstem: Joint Coding of Interaural Level and Time Differences by the Lateral Superior Olive. In *Binaural Hearing* (pp. 113-144). Springer. [https://doi.org/10.1007/978-3-030-57100-9\\_5](https://doi.org/10.1007/978-3-030-57100-9_5)
- Park, T. J., Grothe, B., Pollak, G. D., Schuller, G., & Koch, U. (1996). Neural delays shape selectivity to interaural intensity differences in the lateral superior olive. *J Neurosci*, 16(20), 6554-6566. <https://doi.org/10.1523/JNEUROSCI.16-20-06554.1996>
- Park, T. J., Monsivais, P., & Pollak, G. D. (1997). Processing of interaural intensity differences in the LSO: role of interaural threshold differences. *J Neurophysiol*, 77(6), 2863-2878. <https://doi.org/10.1152/jn.1997.77.6.2863>
- Pecka, M., Brand, A., Behrend, O., & Grothe, B. (2008). Interaural time difference processing in the mammalian medial superior olive: the role of glycinergic inhibition. *J Neurosci*, 28(27), 6914-6925. <https://doi.org/10.1523/JNEUROSCI.1660-08.2008>

- Pecka, M., & Encke, J. (2020). Coding of Spatial Information. In *The Senses: A Comprehensive Reference* (pp. 713-731). Elsevier. <https://doi.org/10.1016/b978-0-12-809324-5.24243-0>
- Pecka, M., Siveke, I., Grothe, B., & Lesica, N. A. (2010). Enhancement of ITD coding within the initial stages of the auditory pathway. *J Neurophysiol*, *103*(1), 38-46. <https://doi.org/10.1152/jn.00628.2009>
- Pilati, N., Linley, D. M., Selvaskandan, H., Uchitel, O., Hennig, M. H., Kopp-Scheinflug, C., & Forsythe, I. D. (2016). Acoustic trauma slows AMPA receptor-mediated EPSCs in the auditory brainstem, reducing GluA4 subunit expression as a mechanism to rescue binaural function. *J Physiol*, *594*(13), 3683-3703. <https://doi.org/10.1113/JP271929>
- Platkiewicz, J., & Brette, R. (2011). Impact of fast sodium channel inactivation on spike threshold dynamics and synaptic integration. *PLoS Comput Biol*, *7*(5), e1001129. <https://doi.org/10.1371/journal.pcbi.1001129>
- Pollak, G. D. (1988). Time is traded for intensity in the bat's auditory system. *Hear Res*, *36*(2-3), 107-124. [https://doi.org/10.1016/0378-5955\(88\)90054-8](https://doi.org/10.1016/0378-5955(88)90054-8)
- Postolache, M., Connelly Graham, C. J., Burke, K., Lauer, A. M., & Xu-Friedman, M. A. (2024). Effects of Age on Responses of Principal Cells of the Mouse Anteroventral Cochlear Nucleus in Quiet and Noise. *eNeuro*, *11*(8). <https://doi.org/10.1523/ENEURO.0215-24.2024>
- Prescott, S. A., De Koninck, Y., & Sejnowski, T. J. (2008). Biophysical basis for three distinct dynamical mechanisms of action potential initiation. *PLoS Comput Biol*, *4*(10), e1000198. <https://doi.org/10.1371/journal.pcbi.1000198>
- Prinz, A. A., Abbott, L. F., & Marder, E. (2004). The dynamic clamp comes of age. *Trends Neurosci*, *27*(4), 218-224. <https://doi.org/10.1016/j.tins.2004.02.004>
- Puil, E., Gimbarzevsky, B., & Miura, R. M. (1986). Quantification of membrane properties of trigeminal root ganglion neurons in guinea pigs. *J Neurophysiol*, *55*(5), 995-1016. <https://doi.org/10.1152/jn.1986.55.5.995>
- Pyott, S. J., & von Gersdorff, H. (2020). Auditory Afferents: Sound Encoding in the Cochlea. In *The Senses: A Comprehensive Reference* (pp. 487-500). Elsevier. <https://doi.org/10.1016/b978-0-12-805408-6.00030-0>
- Rayleigh, L. (1909). XII. On our perception of sound direction. *The London, Edinburgh, and Dublin Philosophical Magazine and Journal of Science*, *13*(74), 214-232. <https://doi.org/10.1080/14786440709463595>
- Reiss, L. A., & Young, E. D. (2005). Spectral edge sensitivity in neural circuits of the dorsal cochlear nucleus. *J Neurosci*, *25*(14), 3680-3691. <https://doi.org/10.1523/JNEUROSCI.4963-04.2005>
- Remme, M. W., Donato, R., Mikiel-Hunter, J., Ballestero, J. A., Foster, S., Rinzel, J., & McAlpine, D. (2014). Subthreshold resonance properties contribute to the efficient coding of auditory spatial cues. *Proc Natl Acad Sci U S A*, *111*(22), E2339-2348. <https://doi.org/10.1073/pnas.1316216111>

- Rhode, W. S., Oertel, D., & Smith, P. H. (1983). Physiological response properties of cells labeled intracellularly with horseradish peroxidase in cat ventral cochlear nucleus. *J Comp Neurol*, 213(4), 448-463. <https://doi.org/10.1002/cne.902130408>
- Rhode, W. S., & Smith, P. H. (1986). Encoding timing and intensity in the ventral cochlear nucleus of the cat. *J Neurophysiol*, 56(2), 261-286. <https://doi.org/10.1152/jn.1986.56.2.261>
- Richardson, M. J., Brunel, N., & Hakim, V. (2003). From subthreshold to firing-rate resonance. *J Neurophysiol*, 89(5), 2538-2554. <https://doi.org/10.1152/jn.00955.2002>
- Rietzel, H.-J., & Friauf, E. (1998). Neuron types in the rat lateral superior olive and developmental changes in the complexity of their dendritic arbors. *The Journal of Comparative Neurology*, 390(1), 20-40. [https://doi.org/10.1002/\(sici\)1096-9861\(19980105\)390:1<20::Aid-cne3>3.0.Co;2-s](https://doi.org/10.1002/(sici)1096-9861(19980105)390:1<20::Aid-cne3>3.0.Co;2-s)
- Robinson, H. P., & Kawai, N. (1993). Injection of digitally synthesized synaptic conductance transients to measure the integrative properties of neurons. *J Neurosci Methods*, 49(3), 157-165. [https://doi.org/10.1016/0165-0270\(93\)90119-c](https://doi.org/10.1016/0165-0270(93)90119-c)
- Romero, G. E., & Trussell, L. O. (2022). Central circuitry and function of the cochlear efferent systems. *Hear Res*, 425, 108516. <https://doi.org/10.1016/j.heares.2022.108516>
- Rose, J. E., Brugge, J. F., Anderson, D. J., & Hind, J. E. (1967). Phase-locked response to low-frequency tones in single auditory nerve fibers of the squirrel monkey. *J Neurophysiol*, 30(4), 769-793. <https://doi.org/10.1152/jn.1967.30.4.769>
- Rosen, S. (1992). Temporal information in speech: acoustic, auditory and linguistic aspects. *Philos Trans R Soc Lond B Biol Sci*, 336(1278), 367-373. <https://doi.org/10.1098/rstb.1992.0070>
- Rothman, J. S., Young, E. D., & Manis, P. B. (1993). Convergence of auditory nerve fibers onto bushy cells in the ventral cochlear nucleus: implications of a computational model. *J Neurophysiol*, 70(6), 2562-2583. <https://doi.org/10.1152/jn.1993.70.6.2562>
- Rutherford, M. A., von Gersdorff, H., & Goutman, J. D. (2021). Encoding sound in the cochlea: from receptor potential to afferent discharge. *J Physiol*, 599(10), 2527-2557. <https://doi.org/10.1113/JP279189>
- Sakitt, B. (1973). Indices of discriminability. *Nature*, 241(5385), 133-134. <https://doi.org/10.1038/241133a0>
- Sanes, D. H. (1990). An in vitro analysis of sound localization mechanisms in the gerbil lateral superior olive. *J Neurosci*, 10(11), 3494-3506. <https://doi.org/10.1523/JNEUROSCI.10-11-03494.1990>
- Sanes, D. H., & Rubel, E. W. (1988). The ontogeny of inhibition and excitation in the gerbil lateral superior olive. *J Neurosci*, 8(2), 682-700. <https://doi.org/10.1523/JNEUROSCI.08-02-00682.1988>
- Sayles, M., Füllgrabe, C., & Winter, I. M. (2013). Neurometric amplitude-modulation detection threshold in the guinea-pig ventral cochlear nucleus. *J Physiol*, 591(13), 3401-3419. <https://doi.org/10.1113/jphysiol.2013.253062>

- Scheibel, M. E., & Scheibel, A. B. (1974). Neuropil organization in the superior olive of the cat. *Exp Neurol*, 43(2), 339-348. [https://doi.org/10.1016/0014-4886\(74\)90175-7](https://doi.org/10.1016/0014-4886(74)90175-7)
- Schnupp, J. W. H., Buchholz, S., Buck, A. N., Budig, H., Khurana, L., & Roskoth-Kuhl, N. (2025). Pulse timing dominates binaural hearing with cochlear implants. *Proc Natl Acad Sci U S A*, 122(16), e2416697122. <https://doi.org/10.1073/pnas.2416697122>
- Scott, L. L., Hage, T. A., & Golding, N. L. (2007). Weak action potential backpropagation is associated with high-frequency axonal firing capability in principal neurons of the gerbil medial superior olive. *J Physiol*, 583(Pt 2), 647-661. <https://doi.org/10.1113/jphysiol.2007.136366>
- Scott, L. L., Mathews, P. J., & Golding, N. L. (2005). Posthearing developmental refinement of temporal processing in principal neurons of the medial superior olive. *J Neurosci*, 25(35), 7887-7895. <https://doi.org/10.1523/JNEUROSCI.1016-05.2005>
- Scott, L. L., Mathews, P. J., & Golding, N. L. (2010). Perisomatic voltage-gated sodium channels actively maintain linear synaptic integration in principal neurons of the medial superior olive. *J Neurosci*, 30(6), 2039-2050. <https://doi.org/10.1523/JNEUROSCI.2385-09.2010>
- Shaikh, A. G., & Finlayson, P. G. (2005). Excitability of auditory brainstem neurons, in vivo, is increased by cyclic-AMP. *Hear Res*, 201(1-2), 70-80. <https://doi.org/10.1016/j.heares.2004.10.005>
- Sharp, A. A., O'Neil, M. B., Abbott, L. F., & Marder, E. (1993). Dynamic clamp: computer-generated conductances in real neurons. *J Neurophysiol*, 69(3), 992-995. <https://doi.org/10.1152/jn.1993.69.3.992>
- Silver, R. A. (2010). Neuronal arithmetic. *Nat Rev Neurosci*, 11(7), 474-489. <https://doi.org/10.1038/nrn2864>
- Siveke, I., Leibold, C., Kaiser, K., Grothe, B., & Wiegrebe, L. (2010). Level-dependent latency shifts quantified through binaural processing. *J Neurophysiol*, 104(4), 2224-2235. <https://doi.org/10.1152/jn.00392.2010>
- Siveke, I., Myoga, M. H., Grothe, B., & Felmy, F. (2021). Ambient noise exposure induces long-term adaptations in adult brainstem neurons. *Sci Rep*, 11(1), 5139. <https://doi.org/10.1038/s41598-021-84230-9>
- Smith, P. H., Joris, P. X., & Yin, T. C. (1993). Projections of physiologically characterized spherical bushy cell axons from the cochlear nucleus of the cat: evidence for delay lines to the medial superior olive. *J Comp Neurol*, 331(2), 245-260. <https://doi.org/10.1002/cne.903310208>
- Sommer, I., Lingenhohl, K., & Friauf, E. (1993). Principal cells of the rat medial nucleus of the trapezoid body: an intracellular in vivo study of their physiology and morphology. *Exp Brain Res*, 95(2), 223-239. <https://doi.org/10.1007/BF00229781>
- Spirou, G. A., Kersting, M., Carr, S., Razzaq, B., Yamamoto Alves Pinto, C., Dawson, M., Ellisman, M. H., & Manis, P. B. (2023). High-resolution volumetric imaging constrains compartmental models to explore synaptic integration and temporal processing by cochlear nucleus globular bushy cells. *Elife*, 12. <https://doi.org/10.7554/eLife.83393>

- Stancu, M., Wohlfrom, H., Hess, M., Grothe, B., Leibold, C., & Kopp-Scheinflug, C. (2024). Ambient sound stimulation tunes axonal conduction velocity by regulating radial growth of myelin on an individual, axon-by-axon basis. *Proc Natl Acad Sci U S A*, 121(11), e2316439121. <https://doi.org/10.1073/pnas.2316439121>
- Stange-Marten, A., Nabel, A. L., Sinclair, J. L., Fischl, M., Alexandrova, O., Wohlfrom, H., Kopp-Scheinflug, C., Pecka, M., & Grothe, B. (2017). Input timing for spatial processing is precisely tuned via constant synaptic delays and myelination patterns in the auditory brainstem. *Proc Natl Acad Sci U S A*, 114(24), E4851-E4858. <https://doi.org/10.1073/pnas.1702290114>
- Stecker, G. C., Bernstein, L. R., & Brown, A. D. (2021). Binaural hearing with temporally complex signals. In *Binaural Hearing: With 93 Illustrations* (pp. 145-180). Springer. [https://doi.org/10.1007/978-3-030-57100-9\\_6](https://doi.org/10.1007/978-3-030-57100-9_6)
- Sterenborg, J. C., Pilati, N., Sheridan, C. J., Uchitel, O. D., Forsythe, I. D., & Barnes-Davies, M. (2010). Lateral olivocochlear (LOC) neurons of the mouse LSO receive excitatory and inhibitory synaptic inputs with slower kinetics than LSO principal neurons. *Hear Res*, 270(1-2), 119-126. <https://doi.org/10.1016/j.heares.2010.08.013>
- Stevens, S. S., & Newman, E. B. (1936). The Localization of Actual Sources of Sound. *The American Journal of Psychology*, 48(2). <https://doi.org/10.2307/1415748>
- Stotler, W. A. (1953). An experimental study of the cells and connections of the superior olivary complex of the cat. *J Comp Neurol*, 98(3), 401-431. <https://doi.org/10.1002/cne.900980303>
- Street, S. E., & Manis, P. B. (2007). Action potential timing precision in dorsal cochlear nucleus pyramidal cells. *J Neurophysiol*, 97(6), 4162-4172. <https://doi.org/10.1152/jn.00469.2006>
- Svirskis, G., Kotak, V., Sanes, D. H., & Rinzel, J. (2004). Sodium along with low-threshold potassium currents enhance coincidence detection of subthreshold noisy signals in MSO neurons. *J Neurophysiol*, 91(6), 2465-2473. <https://doi.org/10.1152/jn.00717.2003>
- Taberner, A. M., & Liberman, M. C. (2005). Response properties of single auditory nerve fibers in the mouse. *J Neurophysiol*, 93(1), 557-569. <https://doi.org/10.1152/jn.00574.2004>
- Tolbert, L. P., & Morest, D. K. (1982). The neuronal architecture of the anteroventral cochlear nucleus of the cat in the region of the cochlear nerve root: electron microscopy. *Neuroscience*, 7(12), 3053-3067. [https://doi.org/10.1016/0306-4522\(82\)90229-9](https://doi.org/10.1016/0306-4522(82)90229-9)
- Tollin, D. J. (2003). The lateral superior olive: a functional role in sound source localization. *Neuroscientist*, 9(2), 127-143. <https://doi.org/10.1177/1073858403252228>
- Tollin, D. J., & Yin, T. C. (2002a). The coding of spatial location by single units in the lateral superior olive of the cat. I. Spatial receptive fields in azimuth. *J Neurosci*, 22(4), 1454-1467. <https://doi.org/10.1523/JNEUROSCI.22-04-01454.2002>
- Tollin, D. J., & Yin, T. C. (2002b). The coding of spatial location by single units in the lateral superior olive of the cat. II. The determinants of spatial receptive fields in azimuth. *J Neurosci*, 22(4), 1468-1479. <https://doi.org/10.1523/JNEUROSCI.22-04-01468.2002>

- Tollin, D. J., & Yin, T. C. (2005). Interaural phase and level difference sensitivity in low-frequency neurons in the lateral superior olive. *J Neurosci*, *25*(46), 10648-10657. <https://doi.org/10.1523/JNEUROSCI.1609-05.2005>
- Tolnai, S., Hernandez, O., Englitz, B., RübSamen, R., & Malmierca, M. S. (2008). The medial nucleus of the trapezoid body in rat: spectral and temporal properties vary with anatomical location of the units. *Eur J Neurosci*, *27*(10), 2587-2598. <https://doi.org/10.1111/j.1460-9568.2008.06228.x>
- Tsai, J. J., Koka, K., & Tollin, D. J. (2010). Varying overall sound intensity to the two ears impacts interaural level difference discrimination thresholds by single neurons in the lateral superior olive. *J Neurophysiol*, *103*(2), 875-886. <https://doi.org/10.1152/jn.00911.2009>
- Tsuchitani, C. (1977). Functional organization of lateral cell groups of cat superior olivary complex. *J Neurophysiol*, *40*(2), 296-318. <https://doi.org/10.1152/jn.1977.40.2.296>
- Tsuchitani, C. (1982). Discharge patterns of cat lateral superior olivary units to ipsilateral tone-burst stimuli. *J Neurophysiol*, *47*(3), 479-500. <https://doi.org/10.1152/jn.1982.47.3.479>
- Tsuchitani, C. (1988). The inhibition of cat lateral superior olive unit excitatory responses to binaural tone bursts. I. The transient chopper response. *J Neurophysiol*, *59*(1), 164-183. <https://doi.org/10.1152/jn.1988.59.1.164>
- Tsuchitani, C., & Boudreau, J. C. (1969). Stimulus level of dichotically presented tones and cat superior olive S-segment cell discharge. *J Acoust Soc Am*, *46*(4), 979-988. <https://doi.org/10.1121/1.1911818>
- Vitten, H., Reusch, M., Friauf, E., & Löhre, S. (2004). Expression of functional kainate and AMPA receptors in developing lateral superior olive neurons of the rat. *J Neurobiol*, *59*(3), 272-288. <https://doi.org/10.1002/neu.10326>
- Von Békésy, G. (1960). *Experiments in hearing*. McGraw-Hill.
- Wade, N. J., & Deutsch, D. (2008). Binaural Hearing—Before and After the Stethophone. *Acoustics Today*, *4*(3). <https://doi.org/10.1121/1.2994724>
- Wahl-Schott, C., & Biel, M. (2009). HCN channels: structure, cellular regulation and physiological function. *Cell Mol Life Sci*, *66*(3), 470-494. <https://doi.org/10.1007/s00018-008-8525-0>
- Walcher, J., Hassfurth, B., Grothe, B., & Koch, U. (2011). Comparative posthearing development of inhibitory inputs to the lateral superior olive in gerbils and mice. *J Neurophysiol*, *106*(3), 1443-1453. <https://doi.org/10.1152/jn.01087.2010>
- Wang, H., & Lu, Y. (2023). High calcium concentrations reduce cellular excitability of mouse MNTB neurons. *Brain Res*, *1820*, 148568. <https://doi.org/10.1016/j.brainres.2023.148568>
- Wang, L., & Colburn, H. S. (2012). A modeling study of the responses of the lateral superior olive to ipsilateral sinusoidally amplitude-modulated tones. *J Assoc Res Otolaryngol*, *13*(2), 249-267. <https://doi.org/10.1007/s10162-011-0300-5>
- Wang, R., Gu, H., & Zhang, X. (2024). Dynamics of interaction between IH and IKLT currents to mediate double resonances of medial superior olive neurons related to sound

- localization. *Cogn Neurodyn*, 18(2), 715-740. <https://doi.org/10.1007/s11571-023-10024-6>
- Weiss, T. F., & Rose, C. (1988). A comparison of synchronization filters in different auditory receptor organs. *Hear Res*, 33(2), 175-179. [https://doi.org/10.1016/0378-5955\(88\)90030-5](https://doi.org/10.1016/0378-5955(88)90030-5)
- Weisz, C. J., Rubio, M. E., Givens, R. S., & Kandler, K. (2016). Excitation by Axon Terminal GABA Spillover in a Sound Localization Circuit. *J Neurosci*, 36(3), 911-925. <https://doi.org/10.1523/JNEUROSCI.1132-15.2016>
- Williams, I. R., Filimontseva, A., Connelly, C. J., & Ryugo, D. K. (2022). The lateral superior olive in the mouse: Two systems of projecting neurons. *Front Neural Circuits*, 16, 1038500. <https://doi.org/10.3389/fncir.2022.1038500>
- Williams, I. R., & Ryugo, D. K. (2024). Bilateral and symmetric glycinergic and glutamatergic projections from the LSO to the IC in the CBA/CaH mouse. *Front Neural Circuits*, 18, 1430598. <https://doi.org/10.3389/fncir.2024.1430598>
- Winkhofer, M., Matthias, K., Seifert, G., Stocker, M., Sewing, S., Herget, T., Steinhäuser, C., & Saaler-Reinhardt, S. (2003). Analysis of phosphorylation-dependent modulation of Kv1.1 potassium channels. *Neuropharmacology*, 44(6), 829-842. [https://doi.org/10.1016/s0028-3908\(03\)00070-4](https://doi.org/10.1016/s0028-3908(03)00070-4)
- Winter, I. M., & Palmer, A. R. (1990). Responses of single units in the anteroventral cochlear nucleus of the guinea pig. *Hear Res*, 44(2-3), 161-178. [https://doi.org/10.1016/0378-5955\(90\)90078-4](https://doi.org/10.1016/0378-5955(90)90078-4)
- Wong, N. F., Brongo, S. E., Forero, E. A., Sun, S., Cook, C. J., Lauer, A. M., Müller, U., & Xu-Friedman, M. A. (2025). Convergence of Type 1 Spiral Ganglion Neuron Subtypes onto Principal Neurons of the Anteroventral Cochlear Nucleus. *J Neurosci*, 45(6). <https://doi.org/10.1523/JNEUROSCI.1507-24.2024>
- Wu, J., & Kaczmarek, L. K. (2021). Modulation of Neuronal Potassium Channels During Auditory Processing. *Front Neurosci*, 15, 596478. <https://doi.org/10.3389/fnins.2021.596478>
- Wu, S., Wardak, A., Khan, M. M., Chen, C. H., & Regehr, W. G. (2024). Implications of variable synaptic weights for rate and temporal coding of cerebellar outputs. *Elife*, 13. <https://doi.org/10.7554/eLife.89095>
- Wu, S. H., & Kelly, J. B. (1992). Synaptic pharmacology of the superior olivary complex studied in mouse brain slice. *J Neurosci*, 12(8), 3084-3097. <https://doi.org/10.1523/JNEUROSCI.12-08-03084.1992>
- Xiao, L., Michalski, N., Kronander, E., Gjoni, E., Genoud, C., Knott, G., & Schneggenburger, R. (2013). BMP signaling specifies the development of a large and fast CNS synapse. *Nat Neurosci*, 16(7), 856-864. <https://doi.org/10.1038/nn.3414>
- Xu-Friedman, M. A., & Regehr, W. G. (2005a). Dynamic-clamp analysis of the effects of convergence on spike timing. I. Many synaptic inputs. *J Neurophysiol*, 94(4), 2512-2525. <https://doi.org/10.1152/jn.01307.2004>

- Xu-Friedman, M. A., & Regehr, W. G. (2005b). Dynamic-clamp analysis of the effects of convergence on spike timing. II. Few synaptic inputs. *J Neurophysiol*, *94*(4), 2526-2534. <https://doi.org/10.1152/jn.01308.2004>
- Yamada, R., & Kuba, H. (2016). Structural and Functional Plasticity at the Axon Initial Segment. *Front Cell Neurosci*, *10*, 250. <https://doi.org/10.3389/fncel.2016.00250>
- Yang, Y., Adowski, T., Ramamurthy, B., Neef, A., & Xu-Friedman, M. A. (2015). High-speed dynamic-clamp interface. *J Neurophysiol*, *113*(7), 2713-2720. <https://doi.org/10.1152/jn.00543.2014>
- Yang, Y., Ramamurthy, B., Neef, A., & Xu-Friedman, M. A. (2016). Low Somatic Sodium Conductance Enhances Action Potential Precision in Time-Coding Auditory Neurons. *J Neurosci*, *36*(47), 11999-12009. <https://doi.org/10.1523/JNEUROSCI.1475-16.2016>
- Yildirim, C., & Bal, R. (2018). ERG Channels Regulate Excitability in Stellate and Bushy Cells of Mice Ventral Cochlear Nucleus. *J Membr Biol*, *251*(5-6), 711-722. <https://doi.org/10.1007/s00232-018-0048-5>
- Yin, T. C., & Chan, J. C. (1990). Interaural time sensitivity in medial superior olive of cat. *J Neurophysiol*, *64*(2), 465-488. <https://doi.org/10.1152/jn.1990.64.2.465>
- Yin, T. C. T., Smith, P. H., & Joris, P. X. (2019). Neural Mechanisms of Binaural Processing in the Auditory Brainstem. *Compr Physiol*, *9*(4), 1503-1575. <https://doi.org/10.1002/cphy.c180036>
- Yu, W. M., & Goodrich, L. V. (2014). Morphological and physiological development of auditory synapses. *Hear Res*, *311*, 3-16. <https://doi.org/10.1016/j.heares.2014.01.007>
- Zhuang, X., Sun, W., & Xu-Friedman, M. A. (2017). Changes in Properties of Auditory Nerve Synapses following Conductive Hearing Loss. *J Neurosci*, *37*(2), 323-332. <https://doi.org/10.1523/JNEUROSCI.0523-16.2016>
- Zhuang, X., Wong, N. F., Sun, W., & Xu-Friedman, M. A. (2020). Mechanisms and Functional Consequences of Presynaptic Homeostatic Plasticity at Auditory Nerve Synapses. *J Neurosci*, *40*(36), 6896-6909. <https://doi.org/10.1523/JNEUROSCI.1175-19.2020>

## 7 Supplementary Information

Table S.1 Stimulus parameters used for primary-like-like activation shown in Fig.3.9.

The steady-state amplitude of the stimulus function ( $R_{ss}$ ) was varied to increase the activation rate ( $f_{exc}$ ).

$R_{ss}$	target $f_{exc}$	resulting $f_{exc}$
38	50	51.3
95	100	101.5
160	150	155.3
223	200	202.4
298	250	253.3
380	300	305.1
465	350	353.0
560	400	401.1
672	450	452.6
800	500	505.6

Table S.2 Stimulus parameters used for primary-like activation shown in Fig.3.13.

The steady-state amplitude of the stimulus function ( $R_{ss}$ ) was varied to increase the activation rate ( $f_{exc}$  &  $f_{inh}$ ).

$R_{ss}$	target $f_{exc}$	resulting $f_{exc}$
380	300	305.0

$R_{ss}$	target $f_{inh}$	resulting $f_{inh}$
50	50	51.0
100	100	102.0
150	150	155.7
200	200	202.8
250	250	253.7
300	300	304.5

Table S.3 Stimulus parameters used for sinusoidal activation shown in Fig.3.16.

The amplitude of the stimulus function ( $A_{sin}$ ) was varied to increase the activation rate ( $f_{exc}$ ).

$F_{mod}$	$A_{sin}$	targed $f_{exc}$	resulting $f_{exc}$
5	512	200	199.7
10	512	200	199.2
20	512	200	199.5
50	512	200	200.0
100	512	200	199.7
200	506	200	199.4
500	486	200	199.6
1000	468	200	201.4
2000	466	200	198.3

Table S.4 Stimulus parameters used for sinusoidal activation shown in Fig.3.17.

The amplitude of the stimulus function ( $A_{sin}$ ) was varied to increase the activation rate ( $f_{exc}$ ).

$F_{mod}$	$F_{pulse}$	$A_{sin}$	target $f_{exc}$	resulting $f_{exc}$
100	100	226	100	99.3
100	100	512	200	201.0
100	100	876	300	300.0
100	100	1360	400	399.5
100	100	2000	500	499.1
200	100	234	50	52.8
200	100	515	100	100.2
200	100	866	150	149.6
200	100	1380	200	202.1
200	100	2002	250	253.3
500	100	222	20	19.7
500	100	480	40	41.0
500	100	812	60	58.3
500	100	1240	80	79.3
500	100	1860	100	102.0
1000	100	210	10	10.0
1000	100	456	20	20.6
1000	100	720	30	29.7
1000	100	1020	40	39.5
1000	100	1380	50	49.1

Table S.5 Stimulus parameters used for sinusoidal activation shown in Fig.3.18.

The amplitude of the stimulus function ( $A_{sin}$ ) was varied to increase the activation rate ( $f_{exc}$  &  $f_{inh}$ ).

$F_{mod}$	$F_{pulse}$	$A_{sin}$	target $f_{exc}$	resulting $f_{exc}$
100	100	226	100	99.6
100	100	512	200	199.7
100	100	876	300	299.9
200	100	234	50	51.8
200	100	515	100	100.9
200	100	866	150	150.2
500	100	222	20	20.1
500	100	480	40	40.0
500	100	812	60	59.0
1000	100	210	10	10.0
1000	100	456	20	20.3
1000	100	720	30	29.8
$F_{mod}$	$F_{pulse}$	$A_{sin}$	target $f_{inh}$	resulting $f_{inh}$
100	100	226	100	99.3
100	100	512	200	201.0
100	100	876	300	300.0
100	100	1360	400	399.5
100	100	2000	500	499.1
200	100	234	50	52.8
200	100	515	100	100.2
200	100	866	150	149.6
200	100	1380	200	202.1
200	100	2002	250	253.3
500	100	222	20	19.7
500	100	480	40	41.0
500	100	812	60	58.3
500	100	1240	80	79.3
500	100	1860	100	102.0
1000	100	210	10	10.0
1000	100	456	20	20.6
1000	100	720	30	29.7
1000	100	1020	40	39.5
1000	100	1380	50	49.1

**Table S.6 Statistical summary tables of Fig.3.8 (E)**

The number of APs per stimulus (median  $\pm$  MAD) for the sinusoidal conductance stimulation and the synaptic model stimulation at nine different  $F_{mod}$ s. Statistics were evaluated by Wilcoxon-signed-rank test, due to non-normal distributed data. Significances are indicated as: n.s. ( $p \geq 0.05$ ), \* ( $p < 0.05$ ), \*\* ( $p < 0.01$ ), \*\*\* ( $p < 0.001$ ). Numbers in brackets provide p values.

$F_{mod}$ [Hz] ( $f_{exc} = 200$ APs/s)	5	10	20	50	100	200	500	1000	2000
Sinusoidal conductance	0 $\pm$ 0	0 $\pm$ 0	0 $\pm$ 0	0 $\pm$ 0	0 $\pm$ 0	0.11 $\pm$ 0.11	0.49 $\pm$ 0.49	0.18 $\pm$ 0.18	0 $\pm$ 0
Synaptic model	0 $\pm$ 0	0 $\pm$ 0	0 $\pm$ 0	0 $\pm$ 0	0.1 $\pm$ 0.1	0.13 $\pm$ 0.13	0.19 $\pm$ 0.19	0.09 $\pm$ 0.09	0 $\pm$ 0
Significance	n.s.	n.s.	n.s.	n.s.	n.s.	n.s.	* <b>(0.016)</b>	** <b>(0.008)</b>	n.s.

$F_{mod}$ [Hz] ( $f_{exc} = 500$ APs/s)	5	10	20	50	100	200	500	1000	2000
Sinusoidal conductance	0 $\pm$ 0	0 $\pm$ 0	0 $\pm$ 0	0 $\pm$ 0	0.15 $\pm$ 0.15	0.95 $\pm$ 0.94	1 $\pm$ 0	1 $\pm$ 0	1 $\pm$ 0
Synaptic model	0 $\pm$ 0	0 $\pm$ 0	0 $\pm$ 0	0 $\pm$ 0	0.45 $\pm$ 0.45	1 $\pm$ 0.5	1 $\pm$ 0	1 $\pm$ 0	0.24 $\pm$ 0.24
Significance	n.s.	n.s.	n.s.	n.s.	n.s.	n.s.	n.s.	n.s.	*** <b>(0.0001)</b>

**Table S.7 Statistical summary tables of Fig.3.8 (F)**

The entrainment threshold (median  $\pm$  MAD) for the sinusoidal conductance stimulation and the synaptic model stimulation at nine different  $F_{mod}$ s. Statistics were evaluated by Wilcoxon-signed-rank test. Significances are indicated as: n.s. ( $p \geq 0.05$ ), \* ( $p < 0.05$ ), \*\* ( $p < 0.01$ ), \*\*\* ( $p < 0.001$ ). Numbers in brackets provide p values.

$F_{mod}$ [Hz]	100	200	500	1000	2000
Sinusoidal conductance	5 $\pm$ 0	2.5 $\pm$ 0	1 $\pm$ 0	0.5 $\pm$ 0	0.25 $\pm$ 0
Synaptic model	5 $\pm$ 0	2.5 $\pm$ 0	1 $\pm$ 0	0.5 $\pm$ 0	0.5 $\pm$ 0
Significance	n.s.	n.s.	n.s.	* <b>(0.028)</b>	** <b>(0.003)</b>

**Table S.8 Statistical summary table of Fig.3.10 (D)**

The sustained rate for uniformly distributed  $SW_{exc}$  ( $uSW_{exc}$ ) and gamma-distributed  $SW_{exc}$  ( $jSW_{exc}$ ) (mean  $\pm$  SD) at ten different  $f_{exc}$ . Statistics were evaluated by paired t-test. Significances are indicated as: n.s. ( $p \geq 0.05$ ), \* ( $p < 0.05$ ), \*\* ( $p < 0.01$ ), \*\*\* ( $p < 0.001$ ). Numbers in brackets provide p values.

$f_{exc}$ [APs/s]	50	100	150	200	250	300	350	400	450	500
$uSW_{exc}$	$0 \pm 0$	$0.8 \pm 2.1$	$1.2 \pm 2.1$	$1.7 \pm 3.9$	$4.6 \pm 6.5$	$5.4 \pm 10.3$	$8.7 \pm 11.6$	$7.3 \pm 11.2$	$8.9 \pm 14.8$	$8.8 \pm 15.2$
$jSW_{exc}$	$0.8 \pm 1.6$	$2.9 \pm 4.6$	$9.1 \pm 12.9$	$9.4 \pm 11.5$	$15.9 \pm 19.7$	$18.4 \pm 24.8$	$19.6 \pm 26.1$	$22 \pm 26.9$	$24.8 \pm 34.9$	$14.2 \pm 23.2$
Significance	n.s.	n.s.	n.s.	* (0.026)	* (0.035)	* (0.031)	n.s.	* (0.022)	* (0.043)	n.s.

**Table S.9 Statistical summary table of Fig.3.12 (E)**

The  $\Delta_{thr}$  for five  $SW_{exc}$  (median  $\pm$  MAD) at ten different  $f_{exc}$ . Statistics were evaluated by one sample Wilcoxon signed-rank test. Significances are indicated as: n.s. ( $p \geq 0.05$ ), \* ( $p < 0.05$ ), \*\* ( $p < 0.01$ ), \*\*\* ( $p < 0.001$ ). Numbers in brackets provide p values.

$f_{exc}$ [APs/s]	50	100	150	200	250	300	350	400	450	500
<b><math>SW_{exc}: 10</math> nS/input</b>										
$\Delta_{thr}$	-1.6 $\pm$ 1	-1.4 $\pm$ 1	-0.9 $\pm$ 1.1	-1.6 $\pm$ 1.3	-0.6 $\pm$ 1.7	-0.6 $\pm$ 1.9	-0.5 $\pm$ 2	0.1 $\pm$ 2.8	0.4 $\pm$ 3.4	0.3 $\pm$ 4.1
Significance	*	**	n.s.	*	n.s.	n.s.	n.s.	n.s.	n.s.	n.s.
	<b>(0.027)</b>	<b>(0.004)</b>		<b>(0.049)</b>						
<b><math>SW_{exc}: 4</math> nS/input</b>										
$\Delta_{thr}$	-0.1 $\pm$ 1.4	0.2 $\pm$ 1.2	0.3 $\pm$ 1	0.6 $\pm$ 1.1	1.1 $\pm$ 1.2	1.7 $\pm$ 1.8	2.4 $\pm$ 2.3	3.7 $\pm$ 2.1	2.9 $\pm$ 3.7	3.6 $\pm$ 2.8
Significance	n.s.	n.s.	n.s.	n.s.	n.s.	n.s.	n.s.	n.s.	n.s.	n.s.
<b><math>SW_{exc}: 2</math> nS/input</b>										
$\Delta_{thr}$	0 $\pm$ 0.9	1.4 $\pm$ 1	2.6 $\pm$ 1.6	2.5 $\pm$ 1.7	3.9 $\pm$ 1.6	3.4 $\pm$ 1.9	4 $\pm$ 2.1	5.2 $\pm$ 2.1	5.3 $\pm$ 2.3	5.9 $\pm$ 2.6
Significance	n.s.	*	*	n.s.	*	*	n.s.	n.s.	n.s.	*
		<b>(0.031)</b>	<b>(0.039)</b>		<b>(0.039)</b>	<b>(0.039)</b>				<b>(0.047)</b>
<b><math>SW_{exc}: 1</math> nS/input</b>										
$\Delta_{thr}$	0 $\pm$ 0	1.4 $\pm$ 1	2.6 $\pm$ 1.6	2.5 $\pm$ 1.7	3.9 $\pm$ 1.6	3.4 $\pm$ 1.9	4 $\pm$ 2.1	5.2 $\pm$ 2.1	5.3 $\pm$ 2.3	5.9 $\pm$ 2.6
Significance	n.s.	n.s.	n.s.	n.s.	n.s.	n.s.	*	*	n.s.	*
							<b>(0.016)</b>	<b>(0.031)</b>		<b>(0.031)</b>
<b><math>SW_{exc}: 0.1</math> nS/input</b>										
$\Delta_{thr}$	N.D.	N.D.	N.D.	N.D.	N.D.	N.D.	N.D.	N.D.	N.D.	N.D.

**Table S.10 Statistical summary table of Fig.3.14 (C<sup>1</sup>)**

The MI for three  $SW_{inh}$  and  $SW_{exc}$  of 10 nS/input (mean  $\pm$  SD) at seven  $f_{inh}$ . Statistics were evaluated by one sample two-tailed t-test. Significances are indicated as: n.s. ( $p \geq 0.05$ ), \* ( $p < 0.05$ ), \*\* ( $p < 0.01$ ), \*\*\* ( $p < 0.001$ ). Numbers in brackets provide p values.

$f_{inh}$ [APs/s]	0	50	100	150	200	250	300
$SW_{exc}$ : 10 nS/input		$SW_{inh}$ : 8 nS/input					
MI	0 $\pm$ 0	0 $\pm$ 0.1	0 $\pm$ 0.2	0 $\pm$ 0.2	-0.1 $\pm$ 0.2	-0.2 $\pm$ 0.2	-0.3 $\pm$ 0.2
Significance		n.s.	n.s.	n.s.	n.s.	n.s.	* <b>(0.0156)</b>
$SW_{exc}$ : 10 nS/input		$SW_{inh}$ : 4 nS/input					
$\Delta$ thr	0 $\pm$ 0	0 $\pm$ 0.1	-0.1 $\pm$ 0.1	-0.1 $\pm$ 0.2	-0.2 $\pm$ 0.3	-0.3 $\pm$ 0.2	-0.3 $\pm$ 0.2
Significance		n.s.	n.s.	n.s.	n.s.	** <b>(0.0054)</b>	* <b>(0.0146)</b>
$SW_{exc}$ : 10 nS/input		$SW_{inh}$ : 2 nS/input					
$\Delta$ thr	0 $\pm$ 0	-0.2 $\pm$ 0.1	-0.1 $\pm$ 0.1	-0.2 $\pm$ 0.2	-0.3 $\pm$ 0.2	-0.3 $\pm$ 0.2	-0.4 $\pm$ 0.2
Significance		*** <b>(0.0001)</b>	* <b>(0.0243)</b>	* <b>(0.0283)</b>	** <b>(0.0039)</b>	* <b>(0.0124)</b>	*** <b>(0.0006)</b>

**Table S.11 Statistical summary table of Fig.3.14 (C<sup>2</sup>)**

The MI for three  $SW_{inh}$  and  $SW_{exc}$  of 4 nS/input (mean  $\pm$  SD) at seven  $f_{inh}$ . Statistics were evaluated by one sample two-tailed t-test. Significances are indicated as: n.s. ( $p \geq 0.05$ ), \* ( $p < 0.05$ ), \*\* ( $p < 0.01$ ), \*\*\* ( $p < 0.001$ ). Numbers in brackets provide p values.

$f_{inh}$ [APs/s]	0	50	100	150	200	250	300
$SW_{exc}$ : 4 nS/input		$SW_{inh}$ : 8 nS/input					
MI	0 $\pm$ 0	-0.1 $\pm$ 0.2	0.1 $\pm$ 0.3	0.1 $\pm$ 0.4	0.2 $\pm$ 0.4	0.1 $\pm$ 0.4	-0.1 $\pm$ 0.4
Significance		n.s.	n.s.	n.s.	n.s.	n.s.	n.s.
$SW_{exc}$ : 10 nS/input		$SW_{inh}$ : 4 nS/input					
$\Delta$ thr	0 $\pm$ 0	0.1 $\pm$ 0.2	-0.1 $\pm$ 0.3	0 $\pm$ 0.5	-0.1 $\pm$ 0.4	-0.1 $\pm$ 0.5	-0.3 $\pm$ 0.4
Significance		n.s.	n.s.	n.s.	n.s.	n.s.	n.s.
$SW_{exc}$ : 10 nS/input		$SW_{inh}$ : 2 nS/input					
$\Delta$ thr	0 $\pm$ 0	0 $\pm$ 0.1	0.1 $\pm$ 0.4	0 $\pm$ 0.4	-0.1 $\pm$ 0.5	-0.2 $\pm$ 0.5	-0.4 $\pm$ 0.4
Significance		n.s.	n.s.	n.s.	n.s.	n.s.	<b>* (0.0309)</b>

**Table S.12 Statistical summary table of Fig.3.14 (C<sup>3</sup>)**

The MI for three  $SW_{inh}$  and  $SW_{exc}$  of 1 nS/input (mean  $\pm$  SD) at seven  $f_{inh}$ . Statistics were evaluated by one sample two-tailed t-test. Significances are indicated as: n.s. ( $p \geq 0.05$ ), \* ( $p < 0.05$ ), \*\* ( $p < 0.01$ ), \*\*\* ( $p < 0.001$ ). Numbers in brackets provide p values.

$f_{inh}$ [APs/s]	0	50	100	150	200	250	300
$SW_{exc}$ : 1 nS/input	$SW_{inh}$ : 8 nS/input						
MI	0 $\pm$ 0	0.2 $\pm$ 0.2	0.4 $\pm$ 0.2	0.7 $\pm$ 0.3	0.6 $\pm$ 0.3	0.6 $\pm$ 0.3	0.3 $\pm$ 0.3
Significance		* (0.0136)	** (0.0016)	*** (0.0003)	** (0.0016)	*** (0.0004)	* (0.0171)
$SW_{exc}$ : 1 nS/input	$SW_{inh}$ : 4 nS/input						
$\Delta$ thr	0 $\pm$ 0	0.3 $\pm$ 0.3	0.1 $\pm$ 0.3	0.1 $\pm$ 0.6	0.2 $\pm$ 0.4	0.2 $\pm$ 0.5	-0.1 $\pm$ 0.5
Significance		* (0.0105)	n.s.	n.s.	n.s.	n.s.	n.s.
$SW_{exc}$ : 1 nS/input	$SW_{inh}$ : 2 nS/input						
$\Delta$ thr	0 $\pm$ 0	0 $\pm$ 0.4	0.1 $\pm$ 0.5	0 $\pm$ 0.6	0.3 $\pm$ 0.7	-0.2 $\pm$ 0.4	-0.2 $\pm$ 0.5
Significance		n.s.	n.s.	n.s.	n.s.	n.s.	n.s.

**Table S.13 Statistical summary table of Fig.3.18 (F&H)**

The MI-0.75 values for the combinations of three  $F_{mod}$ s and two  $f_{exc}$  (mean  $\pm$  SD). A two-way ANOVA followed by paired t-tests was performed, and alpha levels were corrected for three-way comparison using Bonferroni correction. Significances are indicated as: n.s. ( $p \geq 0.017$ ), \* ( $p < 0.017$ ), \*\* ( $p < 0.003$ ), \*\*\* ( $p < 0.0003$ ). Numbers in brackets provide p values.

$f_{exc}$ [APs/s]	200			300		
$F_{mod}$ [Hz]	100	200	300	100	200	300
AP rate [APs/s]	184 $\pm$ 44	141 $\pm$ 63	202 $\pm$ 45	232 $\pm$ 66	247 $\pm$ 72	280 $\pm$ 82
Significance						
		** (6e-4)	** (7e-4)		n.s.	n.s.
		n.s.			** (0.001)	
			*** (2e-4)			
				*** (5e-8)		
					** (6e-4)	

**Table S.14 Statistical summary table of Fig.3.26 ( $F^2$ )**

The AP rate for the combinations of three  $F_{pulse}$ s and three  $F_{mod}$ s (median  $\pm$  MAD). A Friedman test was followed by a Wilcoxon signed rank test, and alpha levels were corrected for three-way comparison using Bonferroni correction. Significances are indicated as: n.s. ( $p \geq 0.017$ ), \* ( $p < 0.017$ ), \*\* ( $p < 0.003$ ), \*\*\* ( $p < 0.0003$ ). Numbers in brackets provide p values.

$F_{pulse}$	20	50	100	20	50	100
$F_{mod}$	20	50	100	200	500	1000
Rate [APs/s]	80 $\pm$ 39.5	88.3 $\pm$ 32	114.8 $\pm$ 35.5	26.3 $\pm$ 16.3	51.3 $\pm$ 30.8	72.5 $\pm$ 38.5
Significance						

**Table S.15 Statistical summary table of Fig.3.26 ( $G^2$ )**

The reproducibility for the combinations of three  $F_{pulse}$ s and three  $F_{mod}$ s (median  $\pm$  MAD). A Friedman test was followed by a Wilcoxon signed rank test, and alpha levels were corrected for three-way comparison using Bonferroni correction. Significances are indicated as: n.s. ( $p \geq 0.017$ ), \* ( $p < 0.017$ ), \*\* ( $p < 0.003$ ), \*\*\* ( $p < 0.0003$ ). Numbers in brackets provide p values.

$F_{pulse}$	20	50	100	20	50	100
$F_{mod}$	20	50	100	200	500	1000
Reproducibility	4.2 $\pm$ 1.1	3.6 $\pm$ 0.8	3.9 $\pm$ 0.9	12.5 $\pm$ 6.1	11.3 $\pm$ 4.7	8.7 $\pm$ 4.5
Significance						

Table S.16 Statistical summary table of Fig.3.26 (H<sup>2</sup>)

The modulation depth rate for the combinations of three  $F_{pulse}$ s and three  $F_{mod}$ s (median  $\pm$  MAD). A Friedman test was followed by a Wilcoxon signed rank test, and alpha levels were corrected for three-way comparison using Bonferroni correction. Significances are indicated as: n.s. ( $p \geq 0.017$ ), \* ( $p < 0.017$ ), \*\* ( $p < 0.003$ ), \*\*\* ( $p < 0.0003$ ). Numbers in brackets provide p values.

$F_{pulse}$	20	50	100	20	50	100
$F_{mod}$	20	50	100	200	500	1000
Modulation depth	0.9 $\pm$ 0.1	0.9 $\pm$ 0.1	0.9 $\pm$ 0.1	1 $\pm$ 0	1 $\pm$ 0	1 $\pm$ 0
Significance						
	n.s.		n.s.	n.s.		* (0.016)
	n.s.			* (0.016)		
	** (2.0e-3)			* (3.9e-3)		
	n.s.					

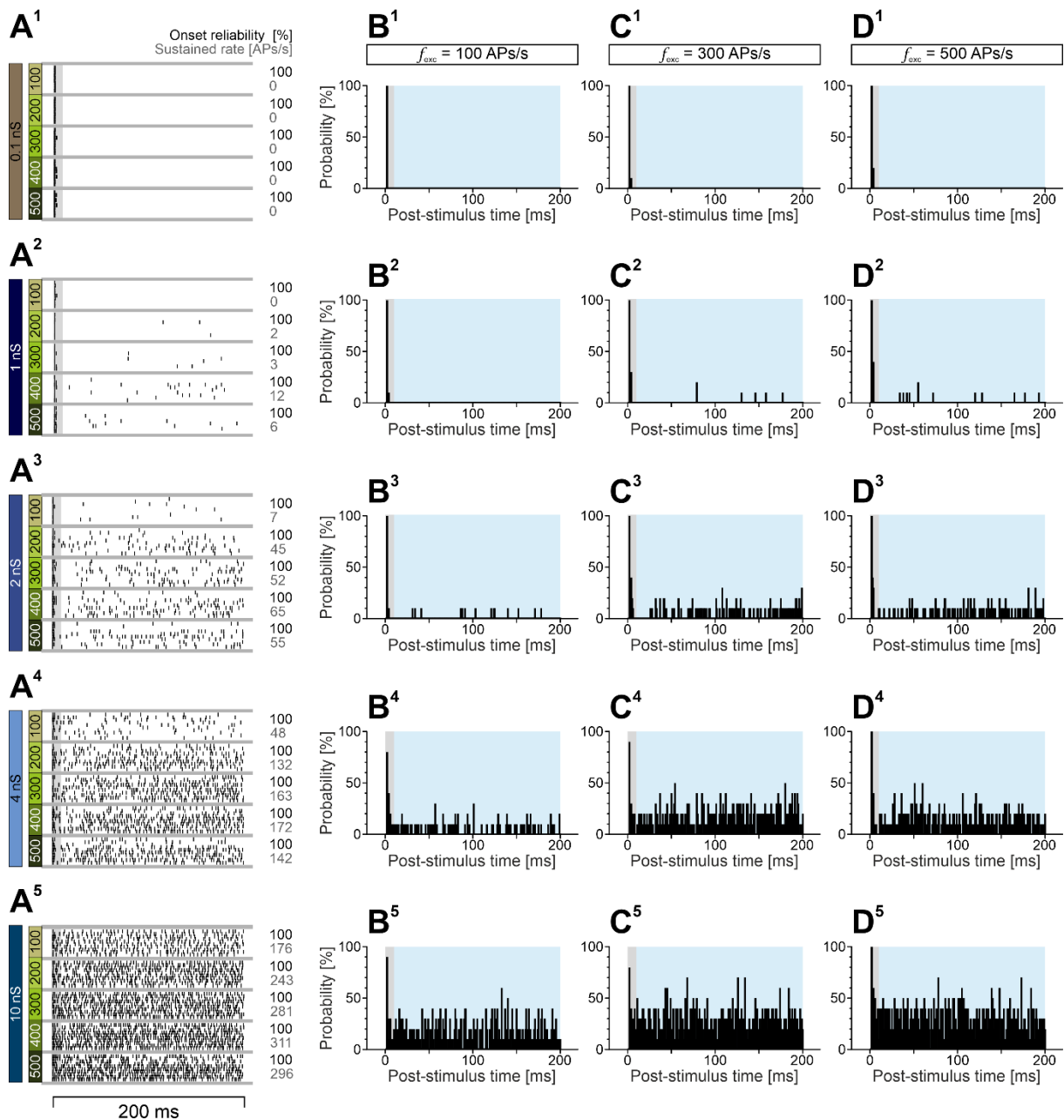


**Figure 7.1** Firing behavior of a single neuron at different  $SW_{exc}$ .

(A) Raster plots of AP occurrence for five  $SW_{exc}$  configurations (0.1 nS/input (A<sup>1</sup>), 1 nS/input (A<sup>2</sup>), 2 nS/input (A<sup>3</sup>), 4 nS/input (A<sup>4</sup>), 10 nS/input (A<sup>5</sup>)). The raster plots are depicted for five  $f_{exc}$  for each  $SW_{exc}$  configuration and the number on the right depict the onset reliability and the sustained rate.

(B) Post-stimulus time histograms show the probability of AP occurrence throughout the stimulus time. Three PSTHs at different  $f_{exc}$  are drawn for each  $SW_{exc}$  ( $f_{exc} = 100$  APs/s (B<sup>1-5</sup>),  $f_{exc} = 300$  APs/s (C<sup>1-5</sup>),  $f_{exc} = 500$  APs/s (D<sup>1-5</sup>)). The bin size was 1 ms.

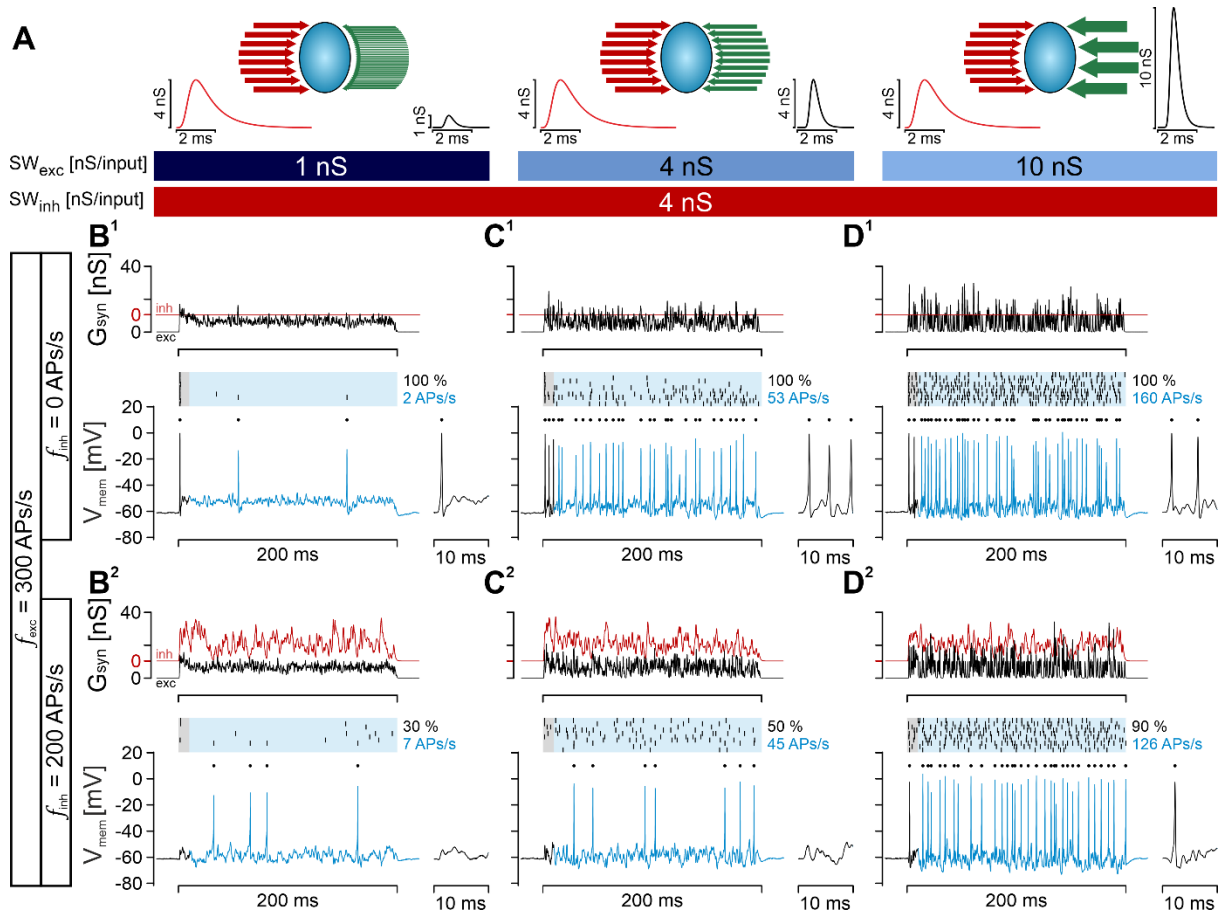


Figure 7.2 Integration of excitation and inhibition during primary-like activation with  $SW_{inh}$  of 4 nS/input.

(A-D) Same as Fig.3.13 (A-D) but for a  $SW_{inh}$  of 4 nS/input and three  $SW_{exc}$  of 1, 4 and 10 nS/input.

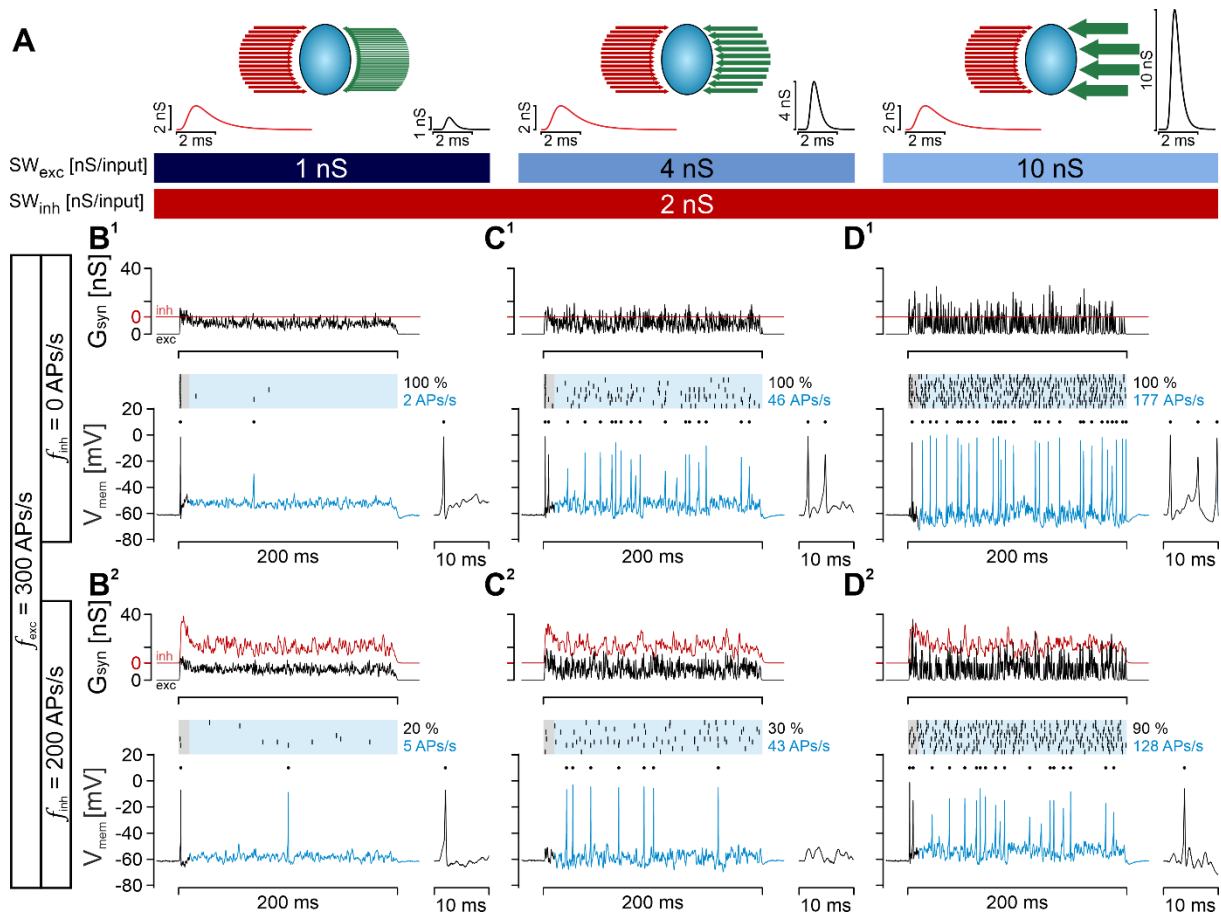


Figure 7.3 Integration of excitation and inhibition during primary-like activation with  $SW_{inh}$  of 4 nS/input.

(A-D) Same as Fig.3.13 (A-D) but for a  $SW_{inh}$  of 4 nS/input and three  $SW_{exc}$  of 1, 4 and 10 nS/input.ms.

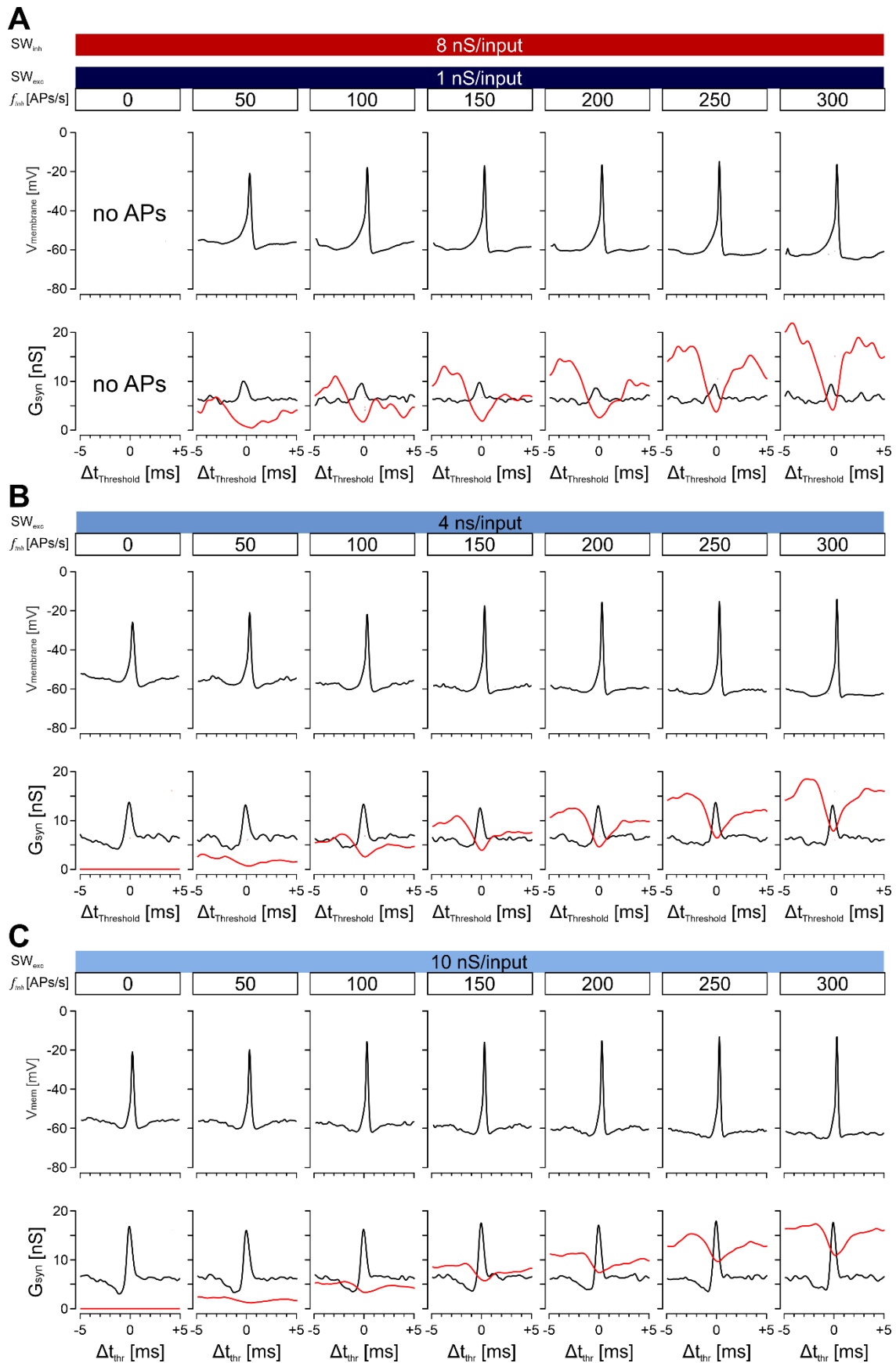


Figure 7.4 Spike triggered averages of primary-like excitation and inhibition.

- (A)** Spike triggered average curves of the  $V_{\text{mem}}$  (top panel),  $G_{\text{exc}}$  and  $G_{\text{inh}}$  (bottom panel, black and red, respectively) for seven levels of inhibition. The  $SW_{\text{exc}}$  was 1 nS/input, and  $SW_{\text{inh}}$  8 nS/input. The curves are aligned at the time of the AP threshold ( $t_{\text{thr}}$ ) and the x-axis scaled accordingly.
- (B)** Same as **A**, but for a  $SW_{\text{exc}}$  of 4 nS/input.
- (C)** Same as **A**, but for a  $SW_{\text{exc}}$  of 10 nS/input.



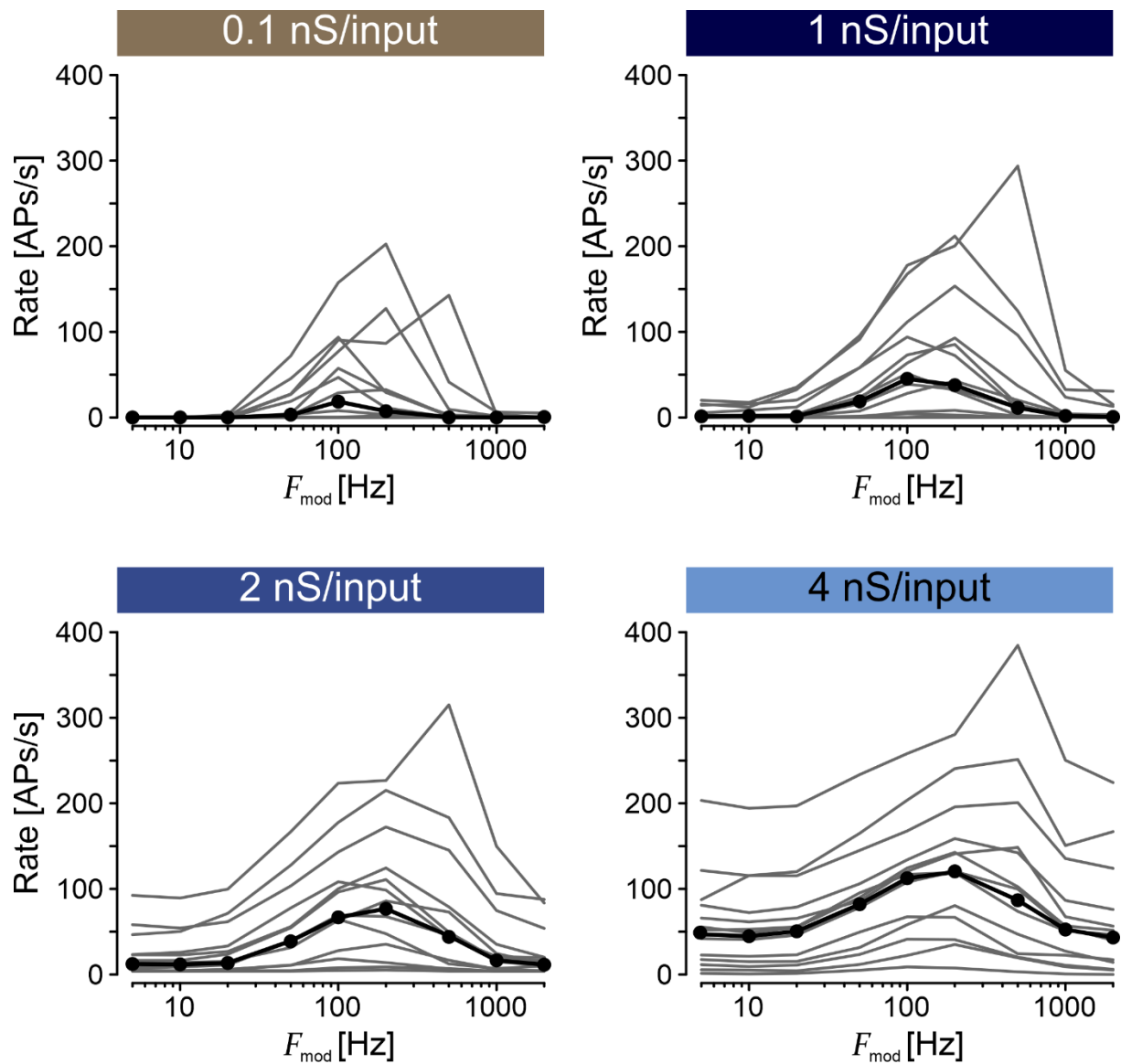


Figure 7.6 Rate modulation transfer functions at four  $SW_{exc}$ .

(A-D) The AP rate as a function of  $F_{mod}$  for four  $SW_{exc}$  (0.1 nS/input (A), 1 nS/input (B), 2 nS/input (C), and 4 nS/input (D)). The grey lines show the rMTFs for 14 neurons. Black dots and lines show the median of the 14 neurons.

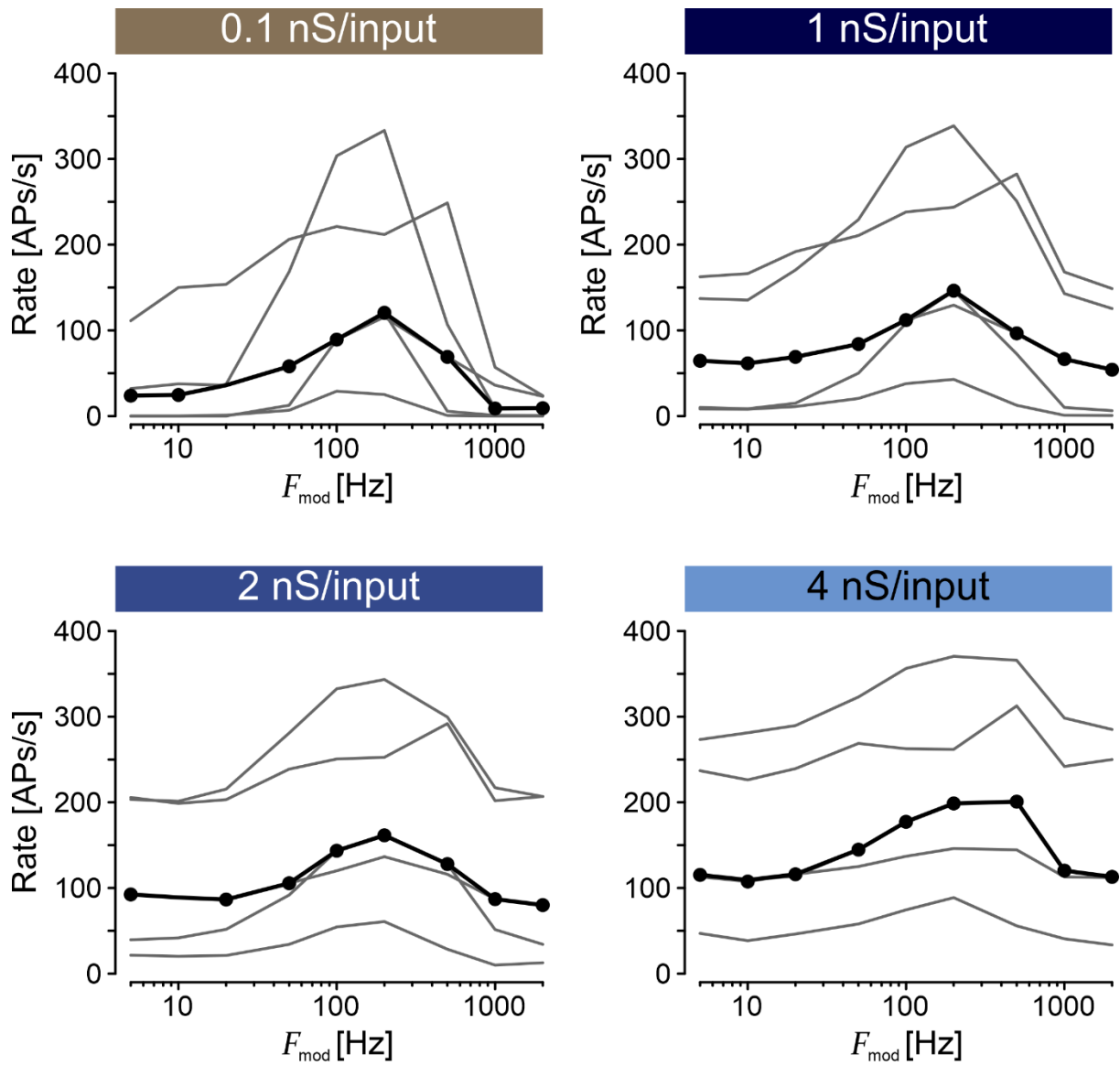


Figure 7.7 Rate modulation transfer functions at four  $SW_{exc}$  of multi firing neurons.

(A-D) The AP rate as a function of  $F_{mod}$  for four  $SW_{exc}$  (0.1 nS/input (A), 1 nS/input (B), 2 nS/input (C), and 4 nS/input (D)). The grey lines show the rMTFs for 14 neurons. Black dots and lines show the median of the 5 neurons.

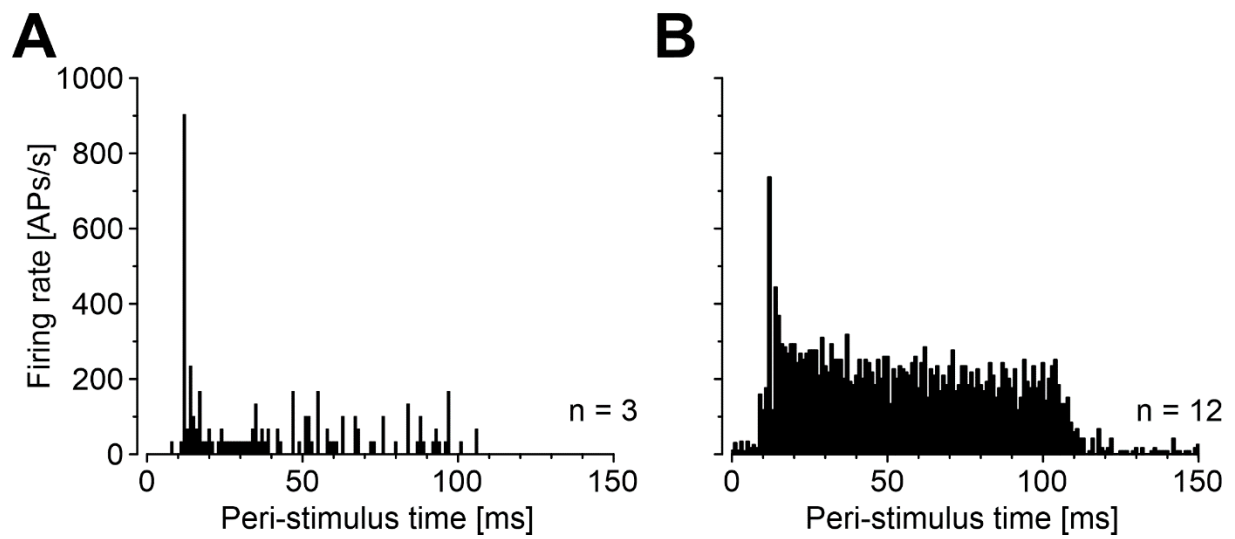


Figure 7.8 PSTHs of onset firing neurons and sustained firing neurons.

(A) The mean, peak aligned PSTH of three onset neurons. The classification of onset and sustained firing neurons is defined in Fig.3.24.

(B) Same as A but for sustained firing neurons.

## 8 Curriculum vitae

### Jonas Martin Fisch (M.Sc.)

#### Institute address:

University of Kaiserslautern-Landau  
Department of Biology, Animal Physiology group  
Erwin-Schrödinger-Straße 13  
67663 Kaiserslautern

#### Education

---

- 2021 – **University of Kaiserslautern, PhD Student**  
2025
  - Animal Physiology
  - Supervision: Prof. Dr. Eckhard Friauf
- 2018 – **University of Kaiserslautern, Master of Science**  
2021 **Specialization Neurobiology**
  - Master Thesis: "Synaptic integration of sound localizing neurons: a dynamic-clamp analysis"
  - Supervisor: Prof. Dr. Eckhard Friauf
- 2019 – **University at Buffalo, Student internship**  
2020
  - Learning the dynamic-clamp technique in Prof. Dr. Matthew Xu-Friedman's laboratory
- 2014 – **University of Kaiserslautern, Bachelor of Science**  
2018
  - Bachelor Thesis: "Modulation of inhibitory synapses in the auditory brainstem using pentobarbital",
  - Supervisor: Prof. Dr. Eckhard Friauf
- 2014 **University of Homburg**
  - Two-week practical course in bacteriology and hygiene
- 2014 **Hofenfelsgymnasium Zweibrücken**
  - Qualification for university entrance

## Publications

---

- Fischer AU, Müller NIC, Deller T, Del Turco D, **Fisch JO**, Griesemer D, Kattler K, Maraslioglu A, Roemer V, Xu-Friedman MA, Walter J and Friauf E (2019) GABA is a modulator, rather than a classical transmitter, in the medial nucleus of the trapezoid body-lateral superior olive sound localization circuit. *The Journal of Physiology* 597.8:2269-2295. doi: 10.1113/JP277566
- Müller NIC, Paulußen I, Hofmann LN, **Fisch JO**, Singh A and Friauf E (2022) Development of synaptic fidelity and action potential robustness at an inhibitory sound localization circuit: effects of otoferlin-related deafness. *The Journal of Physiology*, 600.10:2461-2497. doi: 10.1113/JP280403
- Maraslioglu A, Pizzi E, **Fisch JO**, Kattler K, Ritter T, Friauf E (2024) Molecular and functional profiling of cell diversity and identity in the lateral superior olive, an auditory brainstem center with ascending and descending projections. *Frontiers in Cellular Neuroscience*. doi: 10.3389/fncel.2024.1354520
- Vahdat Z, Gambrell O, **Fisch JO**, Friauf E, Singh A (2025) Interfering synaptic transmission from the stochastic dynamics of the quantal content: An analytical approach. *PLOS Computational Biology*. doi: 10.1371/journal.pcbi.1013067

## Conferences

---

- **Fisch J**, Friauf E (2024) The influence of synaptic noise on action potential generation and temporal filtering in lateral superior olive neurons of the auditory brainstem: a dynamic-clamp study, Poster Presentation, Society for Neuroscience meeting, Chicago, IL, USA
- **Fisch J**, Friauf E (2023) Effect of synaptic noise on level and temporal coding in lateral superior olive neurons, Poster Presentation, Annual midwinter meeting of the ARO, Orlando, FL, USA
- **Fisch J**, Friauf E (2022) Integration of in vivo like inputs in the lateral superior olive: a dynamic-clamp study, Poster Presentation, Annual midwinter meeting of the ARO, USA (online)
- **Fisch J**, Freche N, Xu-Friedman M, Friauf E (2021) Synaptic integration in the lateral superior olive analyzed via dynamic-clamp, Poster Presentation, Göttinger meeting of the German Neuroscience Society, Göttingen, Germany (online)
- **Fisch J**, Maraslioglu A, Friauf E (2019) The modulatory effect of pentobarbital in the auditory brainstem: evidence against GABAergic synapses in the lateral superior olive, Poster Presentation, Göttinger meeting of the German Neuroscience Society, Göttingen, Germany
- **Fisch J**, Lion L (2025) Wired for motion: perspectives on motor control. Symposia organization for the Göttingen meeting of the German Neuroscience Society, Göttingen, Germany

## Scientific Community Engagement

---

- **2023 – present (as of 2025)** **Section speaker in the German Neuroscience Society**
  - Representative for the young German neuroscience society
- **2021** **Co-Organizer of the NeuroCon 2021 - Science+**
  - Conference tailored to the interest of young neuroscientists

## Talks

---

- **Fisch J (2023)** Synaptic integration in sound localization, annual meeting of the biology department of the university of Kaiserslautern, Thallichtenberg, Germany
- **Fisch J (2020)** The dynamic-clamp to study synaptic integration, annual meeting of the biology department of the university of Kaiserslautern, Germany (online)
- **Fisch J (2020)** Auditory brainstem synapses: measurements and models of resilient synapses, Class in front of modeling students, University of Delaware, Newark, DE, USA

## Teaching Experience

---

- 2023 **Teaching assistant, German Neuroscience Society patch-seq workshop**  
Methods course on patch-seq data acquisition and data handling
- 2021 **Supervision of 9-weeks advanced practical course**  
Teaching patch-clamp technique to three master students
- 2021 – present **Teaching assistant, lecture-accompanying practical course**  
Teaching “Hearing course”
- 2021 **Laboratory supervision, Bachelor thesis I**
- 2021 **Laboratory supervision, Bachelor thesis II**

## Languages

---

German: Native

English: Fluent

French: Intermediate

Spanish: beginner

---

Kaiserslautern, 12/06/2025, Jonas Fisch

## 9 Acknowledgements

An dieser Stelle ist es mir noch geboten allen Personen, die mich auf den Weg meiner Dissertation begleitet haben zu danken. Hier gilt es erstmal zu sagen: Merci!

An erster Stelle gilt es meiner Promotionskommission zu danken. Vielen Dank Stefan Kins, dass du den Vorsitz der Promotionskommission übernimmst. Vielen Dank an meinen Zweitgutachter Felix Felmy. Ich freue mich immer, dich und deinem Team an Konferenzen zu treffen, an Postern den aktuellen Stand eurer Projekte zu diskutieren, und neben der Wissenschaft auch einfach mal die Zeit mit dir und/oder deiner Gruppe zu genießen. Du hast ein tolles Team, mit dem ich mich immer freue, die Konferenzen zu erobern.

Mir ist es eine riesige Freude, auch dir zu danken Eck! Du hast mir im Bachelor eine Chance gegeben, die Laborarbeit kennenzulernen, im Master eine Möglichkeit gegeben, mich zu etablieren, und in der Promotion die Geduld gehabt, damit ich mich beweisen durfte. Von dir gefordert zu werden, habe ich selten als Last angesehen, auch wenn es mal anstrengender wurde. Ich habe unfassbar viel von dir gelernt! Die zahlreichen Stunden freitags im Eck-Büro waren nicht nur den wissenschaftlichen Diskurs wert, sondern die Zeit, die du dir genommen hast, habe ich auch als Wertschätzung meiner Arbeit angesehen. Vielen Dank für sieben (seit Bachelor) anstrengende, aber vor allem spannende Jahre.

Es war mir immer eine große Hilfe eine gute Stimmung beizubehalten, wozu die Unterstützung aller Mitstreiterinnen und Mitstreiter an der Uni, inklusive und vor allem den wissenschaftlichen Mitarbeiterinnen, und des Junior Professors beigetragen haben. Vielen Dank an dieser Stelle an Kornelia, Tina, und Jan! Jennifer, dir will ich hier ganz besonders danken, du warst eine riesige Hilfe im Labor! Es hat wirklich Spaß gemacht mit euch allen zu arbeiten.

Ein Einfaches Danke ist auch keineswegs ausreichend, um der Unterstützung zu danken, die ich von anderen Doktoranden erfahren habe. An aller erster Stelle steht hier Ayse! Du trägst eine große Schuld daran, dass ich mich heute in der Wissenschaft so wohl fühle! Du hast mich immer unterstützt und Geduld gezeigt, mich im Labor zu ermuntern. Ich bin einfach unfassbar dankbar für die gemeinsamen Zeiten. Du bist meine Wissenschaftsmama und ich freue mich immer noch über jede Minute, die wir telefonieren.

Kira, Lina, Erika, Simon, Theta, Dennis, Nicos und Elisa, von und mit euch zu lernen, Zeit zu genießen und zu blödeln, hat die Zeit im Labor sich anfühlen lassen wie ein zweites zu Hause. Ich freu mich immer euch beim Döner oder auf Konferenzen zu treffen.

Lena und Rouven, danke, dass ihr mich durch die Promotion begleitet, ihr habt die Zeit im Zug immer wie im Flug vergehen lassen und ich habe jede Kaffeepause mit euch extrem genossen.

Aber natürlich will ich auch meiner Familie, meinen Freunden, und vor allem meiner Freundin Luisa danken!

Mama und Papa, ihr habt mich immer in meinen Entscheidungen unterstützt und diese nie hinterfragt. Ihr habt mir Freude, Neugierde und Resilienz mit auf den Weg gegeben, ohne die ich es niemals bis an diese Stelle geschafft hätte. Vielen Dank für eure bedingungslose Unterstützung und den besten Rückhalt den man sich von einer Familie nur wünschen kann.

Vielen dank an all meine Freunde, und meine Geschwister, die mich immer auf ganz schnellem Weg den Alltagsstress vergessen lassen.

Luisa, dir muss ich am meisten danken! Du bietest mir immer Verständnis, ohne viele Worte, Motivation, wenn mir die Kraft fehlt, Inspiration im Alltag, und vor allem aber eine Freundin, mit der ich jeden Tag genieße. Vielen Dank, du machst mich zu einem besseren Menschen und ich freue mich auf ganz viele weiteren Abenteuer, die wir in Zukunft meistern! Ich liebe dich über alles!

The electronic supplementary information is made available through the publication server of the University of Kaiserslautern-Landau (KLUEDO):

<https://kluedo.ub.rptu.de>

---